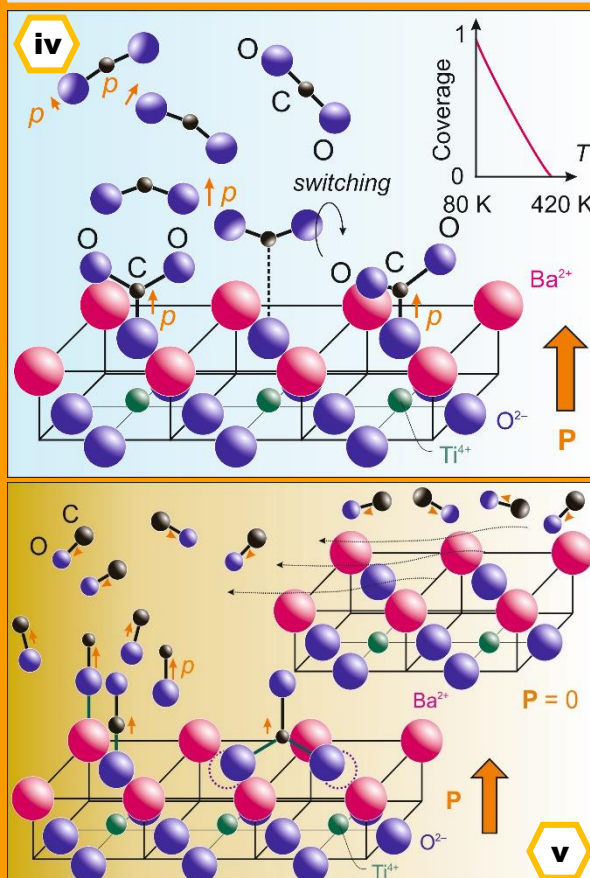
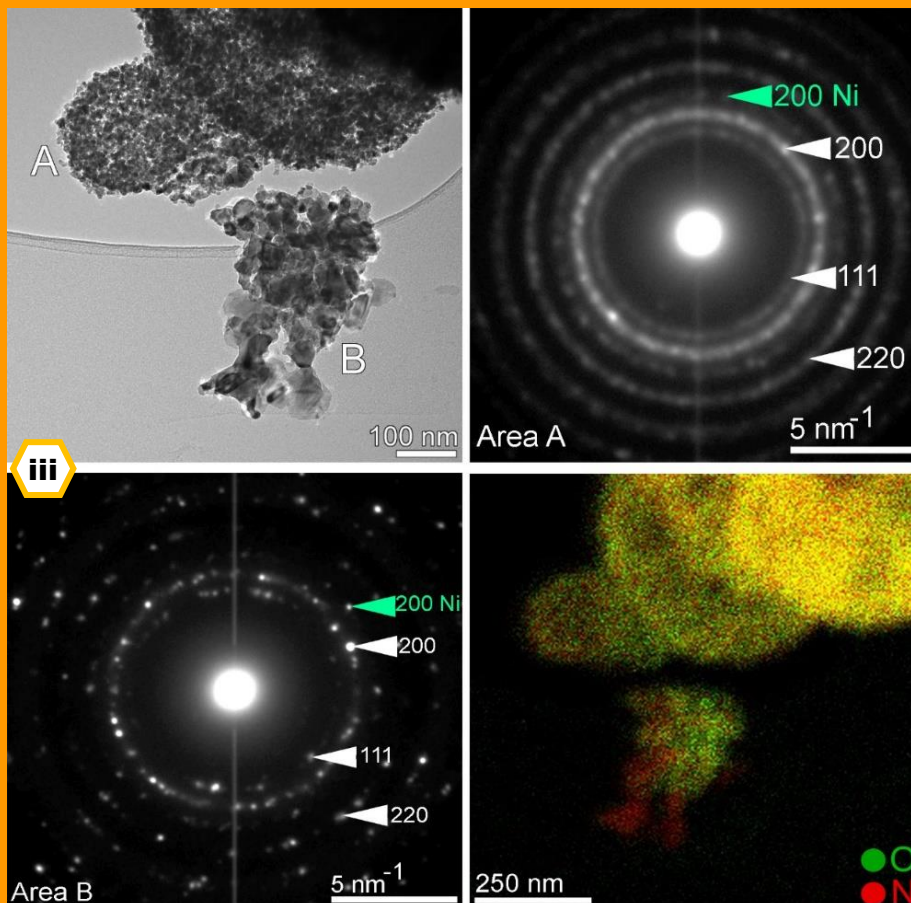
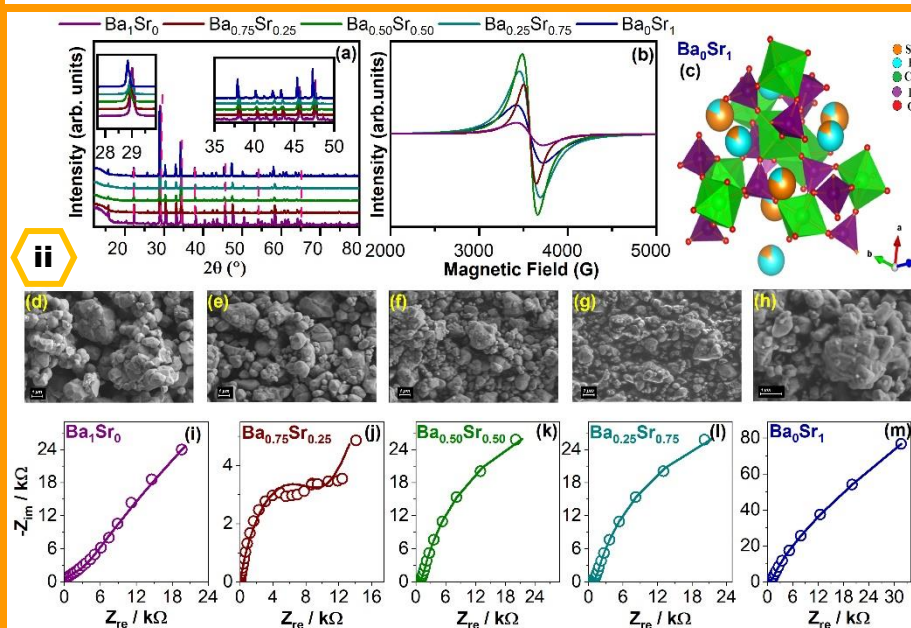
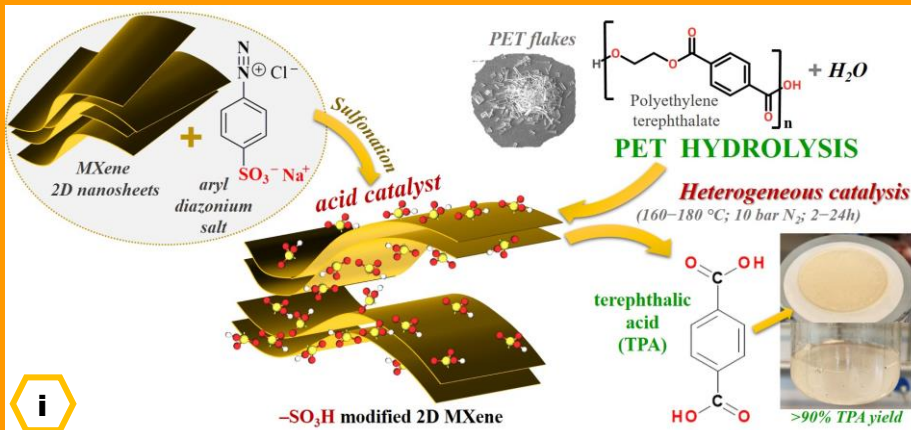


**National Institute of
Materials Physics**

ANNUAL REPORT 2024

**Ministry of Education
and Research**



National Institute of Materials Physics

ANNUAL REPORT 2024

Cover page – Figures reproduced/adapted from:

- i. I.M. Chirica, A.G. Mirea, T. Şuteu, A. Kuncser, Ş. Neaţu, M. Florea, M.W. Barsoum, F. Neaţu, *Acid-modified, Ti_3C_2 -based MXene as catalysts for upcycling polyethylene terephthalate*, ACS Sustain. Chem. Eng. 12 (2024) 9766–9776.
- ii. Z. Mighri, I.D. Yildirim, L.N. Leonat, O. El Khouja, E. Erdem, H. Nasri, A.C. Galca, A.M. Rostas, *Hybrid supercapacitors based on X-site Ba(II) ions substituted by Sr(II) in Langbeinite-type phosphates*, Materialia 36 (2024) 10214.
- iii. C.G. Mihalcea, M. Stefan, C. Ghica, O.G. Florea, A. Stanoiu, C.E. Simion, S. Somacescu, D. Ghica, *In-depth insight into the structural properties of nanoparticulate NiO for CO sensing*, Appl. Surf. Sci. 651 (2024) 159252.
- iv. A.-C. Iancu, A. Nicolaev, N.G. Apostol, L.E. Abramiuc, C.M. Teodorescu, *Reversible oxidation of ethylene on ferroelectric BaTiO₃(001): An X-ray photoelectron spectroscopy study*, Heliyon 10 (2024) e35072.
- v. A.-C. Iancu, G.A. Lungu, C.A. Tache, C.M. Teodorescu, *Ferroelectric-enabled significant carbon dioxide molecular adsorption on BaTiO₃(001)*, Mater. Adv. 5 (2024) 8798–8811.

Research Laboratories

LABORATORY 10

“Functional Nanostructures”

Head of laboratory: Dr. Silviu POLOȘAN, Senior Researcher rank 1 (silv@infim.ro)

Personnel: 36 members – 11 × SR1, 1 × SR2, 10 × SR3, 3 × SR, 10 × RA, and 1 × technician (*SR stands for Senior Researcher; RA stands for Research Assistant).

Beyond its scientific endeavours, the group actively participates in educational and training initiatives.

27 team members hold PhD titles in physics (12), chemistry (2), chemical engineering (6), biochemistry (3), materials engineering (1), energy engineering (1), biotechnology (1), and biomechanics (1). Additionally, the team includes 7 PhD students and 1 MSc student.

Main research directions:

The group deals with nanostructures and nanostructured materials preparation and development of applications. Both chemical/electrochemical (chemical bath deposition, electrochemical deposition with and without a template, chemical vapor deposition) and physical (sputtering, thermal evaporation in vacuum, electrospinning and forcespinning) methods are employed for nanostructures and nanostructured materials preparation. Different types of materials are used, including here metals, metal oxides, organometallic compounds and polymers. The nanostructures developed by this approach are used as building blocks for different types of functional devices (*e.g.*, transistors or diodes, biosensors, actuators). Several specific examples follow:

- ✿ Nanostructures and devices based on nanostructures – physical and chemical methods are employed for preparing nanostructures. Electrochemical or chemical deposition is used for preparing nanowires of zinc oxide with diameters down to 10 nm. Thermal oxidation of metal foils is used for obtaining metal oxide nanowires with diameters down to 20 nm. Further, the nanowires can be employed as building blocks for electronic devices such as diodes and transistors using microlithographic (photolithography and electron beam lithography). Devices complexity can be employed (*e.g.*, core shell devices can be fabricated) by covering the nanowires with thin-films employing methods such as magnetron sputtering or thermal evaporation. Chemical vapor deposition is employed for preparing thin nanostructured films such as metal oxides or graphene.
- ✿ Materials for applications in optics, optoelectronics and photonics for devices which include diodes and transistors for light emitting applications, glasses or modular composition fibres for photonic applications.
- ✿ Biosensors and biomedical devices based on nanostructures or on devices containing nanostructures as building blocks.

Nanostructures and nanostructured materials can be exploited successfully in biosensors, mainly due to the high specific surface but also due to other specific functionalities induced by the low dimensionality. Electrochemical sensors are developed based on nanostructured materials and are functionalized with different types of biomolecules in such a way in which both the desired sensitivity and selectivity are obtained. In this context, different types of substrates and configurations of functionalization are investigated with the goal of optimizing device performances. Novel applications are considered, including wearable sensors for physiologic parameters monitoring. Several specific examples follow:

- ✿ Submicrometer fibres; biomimetic devices based on microfiber web electrodes. In our group, methods of fabricating polymer submicrometric fibres were developed namely: electrospinning and forcespinning. By further functionalization, transparent and flexible electrodes based on metal covered polymer fibre webs are obtained. These electrodes

can be applied on a wide range of substrates including here materials such as textiles and paper and can become the functional element of devices such as biosensors or for applications such as artificial muscles. Functionality can be increased by covering with electroactive polymers, leading to devices with highly superior performances when compared to classic architectures.

- ✿ Biocompatible materials represent another research direction of the group, several approaches being developed, including both biopolymeric fibres (collagen or cellulose), natural membranes (eggshell membrane) or nanostructured materials such as hydroxyapatite. Further functionalization includes covering with different compounds or nanostructures or doping and leads to multiple fields of applications, the main one being that of medical devices.

The research directions of Lab. 10 are mostly interconnected for developing devices with direct applications. Equipment for fabricating fibres by means of electrospinning and forcespinning were designed and developed in the laboratory with the support of the engineers from the application department.

Relevant infrastructure:

The activity of Lab. 10 relies on several fully-equipped chemistry and electrochemistry laboratories (dedicated to different types of applications) as well as clean room infrastructure, essential for devices fabrication:

- ✿ Electron-beam nanolithography equipment with Raith Elphy systems with laser interferometers and Hitachi S3400 and Zeiss Merlin compact electron microscopes;
- ✿ Lithography/Mask Alignment EVG@620 NT system with nanoimprint capabilities;
- ✿ CVD equipment for preparation of carbon-based nanostructures;
- ✿ CVD equipment for deposition of semiconducting materials;
- ✿ Laboratory for optical characterization including UV – Vis absorption spectrometers (Carry 5 and Perkin Elmer 35), photoluminescence spectrometers (Edinburgh and Perkin Elmer LS55), near field photoluminescence microscope, plasmonic resonance spectrometer with potentiostat;
- ✿ Liquid chromatography equipment with mass spectroscopy;
- ✿ Laboratory for cytocompatibility testing, including cell culture facilities and multi-parametric analysis methods (flow cytometry, spectrophotometry, fluorescence microscopy).

Available services:

- ✿ Scanning electron microscopy characterization of materials (micromorphology, composition);
- ✿ Optical characterization by means of optical spectroscopy;
- ✿ Development of equipment for producing micrometric and submicrometric fibres by means of electrospinning and forcespinning.

Main results:

- ✿ 6 research projects (2 × PNRR; 2 × PCE; 1 × PED; and 1 × PD);
- ✿ 35 articles published in Web of Science®-indexed journals with impact factor (of which 14 with main author from Lab. 10);
- ✿ 1 EPO patent application;
- ✿ 1 OSIM granted patent;
- ✿ 9 OSIM patent applications.

Highlights:

- 🍷 Electronic and optical properties of ZnO nanowires/graphene nanohybrids [see **J. Alloys Compd.** 976 (2024) 173109];
- 🍷 Multiferroic materials based on M-hexaferrites [see **J. Alloys Compd.** 983 (2024) 173897];
- 🍷 Submicron electrospun polymeric fibres coated with palladium for wearable sensors [see **ACS Appl. Polym. Mater.** 6 (2024) 2274–2283 & **Talanta** 280 (2024) 126684];
- 🍷 Metallic thin films with various applications obtained by innovative techniques [see **J. Magnes. Alloy** 12 (2024) 3115–3134];
- 🍷 Hydroxyapatites for biological and environmental applications [see **Mater. Chem. Phys.** 324 (2024) 129690; **Micron** 184 (2024) 103661 & **Ceram. Int.** 50B (2024) 1742–1755];
- 🍷 Electrospun nanofibers and fibrillary scaffold for electrochemical cell biomarkers detection [see **Smart Mater. Struct.** 33 (2024) 015009 & **Microchimica Acta** 191 (2024) 435].

LABORATORY 20

“Complex Heterostructures and Multifunctional Materials”

HeCoMat

Head of laboratory: Dr. George STAN, Senior Researcher rank 1 (george.stan@infim.ro)

Personnel: 33 members – 9 × SR1, 3 × SR2, 8 × SR3, 2 × SR, 7 × RA, 2 × sub-engineer/engineer, and 2 × technician.

Beyond its scientific endeavours, the group actively participates in educational and training initiatives.

23 team members hold PhD titles in physics (19), chemistry (2), electrical engineering (2), and materials engineering (1), including 1 PhD supervisor. Additionally, the team includes 4 PhD students and 2 MSc students.

Main research directions:

- 🌀 Ferroelectric materials and related structures for electronic, optoelectronic and sensing applications (including non-volatile memories, UV and IR detectors, piezoelectric devices);
- 🌀 Materials and devices with application in microelectronics, photovoltaic conversion and light/particle detection (including field-effect transistors, hybrid perovskite and chalcogenide solar cells, and silicon-based particle detectors);
- 🌀 Superconducting and magnetic materials, strongly correlated electron systems;
- 🌀 Dielectric and ferroelectric materials for microwave devices (*e.g.*, dielectric resonators, ferroelectric varactors, filters, antennas);
- 🌀 Materials for healthcare applications.

Relevant infrastructure:

HeCoMat possesses a noteworthy infrastructure, covering the entire technological chain from the preparation of materials in the form of powders, bulk and thin layers and their complex physico-chemical characterization, to the integration of the optimized materials into functional devices. Amongst the most important systems and equipment one can mention:

- 🌀 SURFACE SCIENCE pulsed laser deposition (PLD) work station (**Fig. 20–1a**) equipped with: 2 deposition chambers, each with 4-target carousels; a KrF excimer laser with 248 nm wavelength, repetition rate of 1 – 10 Hz, and maximum energy of 700 mJ; control of laser fluence; substrate heating up to 1000 °C; control of working gases pressure; *in-situ* reflection high-energy electron diffraction (RHEED) capabilities. One reaction chamber is used to deposit ferroelectric layers based on perovskites and other metal oxides (*e.g.*, doped ZnO, HfO₂), whilst the other chamber is used to prepare superconductor thin-films.
- 🌀 SURFACE SCIENCE hybrid system for thin-films synthesis from temperature-sensitive materials by (i) matrix assisted pulsed laser evaporation (MAPLE) and (ii) PLD, constituted of: a deposition chamber with *in-situ* freezing facilities for targets (*e.g.*, frozen suspensions of organic materials or inorganic nanoparticles in a support matrix); a KrF excimer laser with 248 nm wavelength, 1 – 10 Hz repetition rate, and 700 mJ maximum power; maximum heating temperature of the substrate: 500 °C – MAPLE & 700 °C – PLD.
- 🌀 Multi-cathode radio-frequency (RF), direct current (DC) and pulsed direct current (p-DC) magnetron sputtering (MS) systems with various facilities: bias, etching and heating (up to 800 °C) of substrates; vacuum load-lock for sample transfer; vacuum systems (down to ~10⁻⁶ Pa); computerized control and process automation. The latest MS

equipment, AJA PHASE II J, purchased in 2016, is shown in **Fig. 20-1b**. Each MS system in Laboratory 20 is dedicated to a distinct class of materials: metallic contacts; semiconductor and dielectric materials; biocompatible materials.

- ❁ Chemistry laboratory for the preparation of powders, bulk materials and thin-films by chemical (wet) methods, equipped with high-temperature annealing furnaces; spin-coating systems; fume hoods, aggregate mills; weighting scales; in-house made glove-boxes; glassware; *etc.*
- ❁ Doctor blade/Slot-die MTI system for large area deposition equipped with 100 mm width adjustable micrometre applicator, a slot-die head and an adjustable speed syringe pump. Additionally, two in-house built Doctor blade/Slot-die systems are also available.
- ❁ Spray pyrolysis facilities.
- ❁ Professional Glove-box MBraun with two chambers (3 and 4 gloves), with integrated spin-coater and closed cycle gas purification system capable of maintaining an atmosphere with H₂O and O₂ under 0.1 ppm and with a solvent filter.
- ❁ Laboratory for the preparation of piezoelectric and superconducting materials, polycrystals and single crystals.
- ❁ Ceramic materials 3D printing laboratory, equipped with a NORDSON EFD, EV series, robocasting (direct ink writing) printing system, with Ultimius V dispenser; an ANTON PARR MCR302e modular rheometer; and a THINKY ARE-250 ceramic mixing & degassing machine.



Fig. 20-1a PLD workstation assembly, SURFACE SCIENCE, for the deposition of ferroelectric thin-films.



Fig. 20-1b RF, DC and p-DC magnetron sputtering system, AJA PHASE II, for the deposition of semiconductor thin-films.

- ❁ X-ray diffraction systems for structure analysis of thin-films (a RIGAKU SmartLab 3 kW/2017 from room-temperature to 1100 °C and a BRUKER D8 Advance/2006) and powders (ANTON PAAR XRDynamic500 – from 600 °C to –180°C and a BRUKER D8 Advance/2007).
- ❁ Optical and structural characterization systems, including a (i) variable angle spectroscopic ellipsometer (WOOLLAM) with wavelength range 200 – 1700 nm (6.2 – 0.73 eV), angle of incidence (35 – 90°), automated sample translation stage (for mapping) 150 mm × 150 mm, and an Instec temperature control stage (-160 – 600 °C) and (ii) a near infrared (NIR), infrared (midIR) and far infrared (farIR) Fourier transform infrared (FTIR) JASCO spectrometry platform, encompassing the 12000 – 50 cm⁻¹ spectral range. VASE Woollam can be used in the following modes: (i) reflection ellipsometry on semiconductor/dielectric thin-films or multilayers (inferred sample parameters: thicknesses, refractive index, extinction coefficient, absorption coefficient,

dielectric function, band gap, critical point energies, electrical parameters for degenerate semiconductors – resistivity/conductivity, carrier density, scattering time, carrier mobility, phase transition in the temperature range -160 – 600 °C); and (ii) transmission ellipsometry on uniaxial/biaxial crystals, glasses and glass ceramics (derived sample parameters: linear birefringence and linear dichroism, Verdet constant/ Faraday rotation).

- ❁ Surface investigation by scanning probe microscopy (SPM) in contact or non-contact mode with piezoelectric (PFM), magnetic (MFM) or conductive (C-AFM) response.
- ❁ Electrical measurements laboratory, including: 2 LAKE SHORE cryo-probers for electrical measurements in the temperature range of 10 – 400 K; one with vertical magnetic field up to 2.5 T, and one with horizontal magnetic field up to 1.5 T, each with at least 3 micro-manipulated arms with contact needles allowing electrical measurements from liquid helium to 400 K under various electric/magnetic fields and illumination conditions; 4 cryostats, covering a temperature range between 10 – 800 K; DLTS (deep-level transient spectroscopy) and TSC (thermally stimulated current) systems for the investigation of electrically active defects (charge carrier traps) in materials and MOS-like structures; set-up for pyroelectric measurements; ferritesters; various instruments for measuring currents, resistances and voltages (electrometers, nanovoltmeters, Lock-In amplifiers); voltage and current sources; RLC bridges; and impedance analysers. These facilities are used to perform complex characterization of electrical (hysteresis loops; C-V and I-V characteristics; impedance spectroscopy; defect spectroscopies; *etc.*) and superconductive properties (electron transport, thermodynamics, magnetic-field penetration depth measurements); determination of the d_{33} piezoelectric coefficient; Kelvin probe and Hall measurements.
- ❁ Solar cells testing laboratory (**Fig. 20-2**), with two Newport LED solar simulators (aperture 50 mm × 50 mm), VeraSol-2 AAA Class and a MiniSol ABA Class), with AM 1.5G solar spectrum and adjustable power coupled with a Keithley source 2601. A system for measuring the Quantum Efficiency (EQE and IPCE) with accessories, working in the 250 – 2500 nm spectral range, is available.
- ❁ Microwave dielectric materials and devices testing laboratory, including:
 - Vector Network Analyser PNA 8361A from Agilent (0.01 – 67 GHz) for two-ports complex S parameters. It uses electronic calibrator Agilent N4694-60001 in the range of 0.01 – 67 GHz. For access, 1.9 mm, 2.9 mm, 2.4mm, 3.5 mm, SMA or N connectors or adaptors are used.
 - Vector Network Analyser PNA-X N5245A from Agilent (0.1 – 50 GHz standalone) with 4 ports and dual sources. It allows measurements of the S and X non-linear parameters. By using the millimetre wave extensions, the system covers a wide frequency band up to 500 GHz. Each extension pair allows the measurement of the two-ports parameter of waveguide devices. The millimetre wave extensions are from Agilent/OML (N5260A V10 VNA2, WR-10, 75-110 GHz; N5260A V06 VNA2, WR-06, 110-170 GHz; N5260A V05 VNA2, WR-05, 140-220 GHz; N5260A V03 VNA2, WR-03, 220-325 GHz; N5260A V02.2 VNA2, WR-02.2, 325-500 GHz).
 - Anechoic chamber with internal dimensions 3040 mm × 4100 mm × 2800 mm, for antenna characterizations (*e.g.*, directivity parameter) in the range of 0.9 – 40 GHz.
 - Microprobe station for direct *on-wafer* measurements of two-ports in the frequency range 0.1 – 67 GHz by using GSG probes with 150 µm and 100 µm pitches.
 - THz-TDS spectrometer from AISPEC Pulse IRS 2000 Pro, operating in the range of 200 GHz – 5 THz.

- ✿ In the framework of collaborative research activities, HeCoMat can access other NIMP infrastructures, such as: TEM and SEM equipment; XPS characterization (including at Elettra Synchrotron Trieste); magnetic measurements (SQUID, PPMS); other optical spectroscopy techniques (Raman, UV-Vis-NIR, luminescence); clean-room (photolithography, dry etching); and *in-vitro* preliminary biological testing of materials.

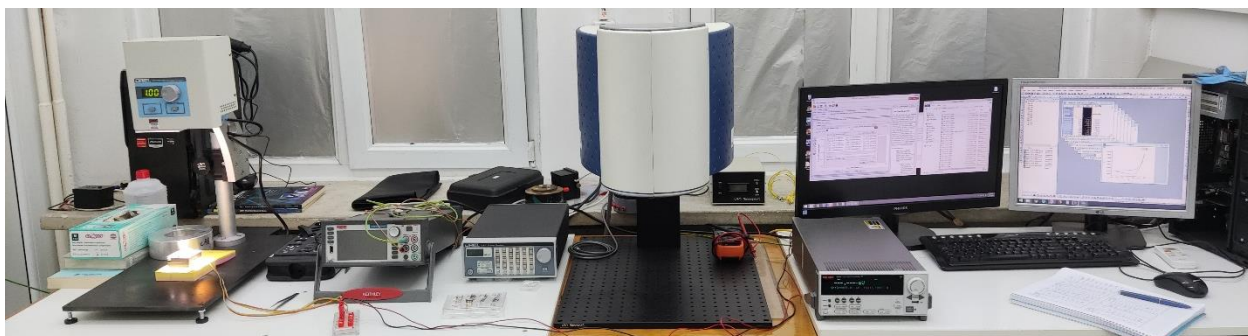


Fig. 20-2 Solar cells testing laboratory.

Available services:

- ✿ Preparation of materials (nano-powders; bulk ceramics; fabrication of thin-films by various techniques, including chemical methods, CVD and PVD techniques);
- ✿ Investigation of charge carrier traps by DLTS and TSC;
- ✿ Electric characterization of materials in a wide temperature range, under electric and magnetic fields;
- ✿ Investigation of pyroelectric properties;
- ✿ Fabrication and characterization of materials by electrochemistry;
- ✿ Fabrication and characterization of perovskite solar cells;
- ✿ Fabrication and characterization of microelectronic devices (*e.g.*, FET, MOS);
- ✿ Characterization of microwave, millimetre waves and terahertz materials and devices;
- ✿ Antenna characterization (antenna directivity) in anechoic chamber in the frequency band from 900 MHz to 40 GHz;
- ✿ Electromagnetic design for microwaves devices/structures by using high accuracy software packages such as CST Studio Suite, Ansoft HFSS, and Ansoft Designer;
- ✿ Deposition of biocompatible (ceramic and glass) coatings on metallic implants;
- ✿ Characterizations by (a) reflection ellipsometry on semiconductor/dielectric thin-films or multilayers (thicknesses, refractive index, extinction coefficient, absorption coefficient, dielectric function, band gap, critical point energies, electrical parameters for degenerate semiconductors – resistivity/conductivity, carrier density, scattering time, carrier mobility, phase transition in the temperature range -160 – 600 °C); and (b) transmission ellipsometry on uniaxial/biaxial crystals, glasses and glass ceramics (optical constants, linear birefringence and linear dichroism, Verdet constant/ Faraday rotation).
- ✿ XRD characterizations for crystalline phase identification and their quantitative analysis; determination of the lattice parameters, average size of crystallites, macro- and micro-strains, preferred orientation, *etc*; analysis of homo- and hetero-epitaxial structures; X-ray reflectometry analyses for inferring the thickness, density and roughness of the surface and interfaces of amorphous and crystalline layers and multilayers; *etc*.
- ✿ FTIR spectroscopy analyses in transmission, specular reflectance (including at grazing incidence), attenuated total reflectance – ATR (RT – 180 °C), diffuse reflectance – DRIFT (RT – 500 °C) and integrating sphere modes.
- ✿ Morpho-compositional analyses by HR-SEM – EDXS;
- ✿ Surface characterization of materials by AFM, PFM, MFM, and C-AFM.

Main results:

- 🌀 12 research projects (1 × PD; 1 × PCE; 1 × PED; 1 × PTE; 3 × CERN; 1 × SEE; 1 × RONAQCI; 1 × Sectorial; 1 × M-ERA.NET; and 1 × PNRR);
- 🌀 34 articles published in Web of Science®-indexed journals with impact factor (of which 14 with main author from Lab. 20);
- 🌀 3 OSIM granted patents;
- 🌀 7 OSIM patent applications.

Highlights:


- 🌀 Successful execution of the economic contract with Swarm European Services, focused on research in memristors for cryptographic key applications.
- 🌀 Successful completion of the EEA-Norway funded project PERLA-PV, which aimed to develop cost-effective, large-area printing technologies for perovskite solar cells (PSCs) while addressing toxicological and environmental concerns associated with hazardous elements and solvents in the fabrication process. PERLA-PV brought together five research institutions: National Institute of Materials Physics (Romania, coordinator), University of Oslo (Norway), Reykjavik University (Iceland), Horia Hulubei National Institute for R&D in Physics and Nuclear Engineering (Romania), and Trittech Group (WATTROM, Romania, SME end-user). The project focused on: (1) Developing scalable printing technologies for large-area deposition of all PSC layers; (2) Engineering perovskite compositions to diminish degradation effects and enhance stability of PSCs while implementing environmentally friendly solvent strategies; (3) Investigating degradation mechanisms in PSCs through experimental and theoretical studies of materials and interfaces to enhance device durability.

Key outcomes of PERLA-PV include the development of fully printable, cost-effective PSC fabrication techniques, which are readily scalable for industrial production & the knowledge gained on the chemistry, physical properties, and charge transport mechanism in PSCs. The project successfully produced large-area perovskite solar cells and mini-photovoltaic panels, with fully printing-like and cost-effective techniques for all of the different layers in a PSC (inorganic, hybrid, and organic compounds). The printing technologies developed in PERLA-PV are readily scalable to an industrial level, representing a significant achievement for both the scientific community and industry by advancing fundamental knowledge and practical applications in the field. PERLA-PV resulted in 10 scientific articles, 1 patent, and functional PSC devices and photovoltaic modules. Project details, reports, and outputs are freely accessible at <https://perla-pv.ro/>. Recognizing its impact, the project was selected among the top five EEA projects with notable results.

- 🌀 We demonstrated the ferroelectric switching at both the nanoscale and macroscopic levels by producing $\text{Ba}_{0.8}\text{Sr}_{0.2}\text{TiO}_3$ ceramics down to 77 nm – an achievement not previously reported for this composition. The study [see **Prog. Solid State Chem.** **74** (2024) 100457] showed a significant decrease in permittivity and a stable Curie temperature. Grain size reduction was attained through spark plasma sintering of nanopowders (mean particle size ≈ 70 nm) under varying conditions. Submicron-structured samples exhibited stronger ferroelectric properties than ultrafine ceramics, which can be explained by a multiphase coexistence model and “dilution” effects from non-ferroelectric boundaries. These findings expand the understanding of grain-size-dependent phenomena in BaTiO_3 -based systems and offer new perspectives for optimizing lead-free, fine-grained ferroelectric ceramics for high-performance energy storage, sensing, and actuation applications.

- Advances toward energy-efficient neuromorphic computing were made with the demonstration of a novel ferroelectric memristor based on an epitaxial HZO/SrTiO_{3-δ}/Si structure. The device operates at low-voltage (≤ 2 V), exhibits ultra-low energy consumption (~ 8 fJ per event), and supports multi-level conductance states. Structural and electrical characterizations confirm robust ferroelectricity and synaptic plasticity. By incorporating a semiconductor electrode, this approach enhances device stability and scalability, addressing key challenges in ferroelectric non-volatile memories. These findings contribute to the development of brain-inspired hardware with power-efficient, bio-realistic learning capabilities [see **Adv. Funct. Mater.** **34** (2024) **2311767**].
- Research was focused on the critical analysis of the wetting properties and photocatalytic efficiency of engineered glass surfaces coated with TiO₂ nanoparticles for self-cleaning applications. The TiO₂ layers were obtained using a simple spraying method, a technique well-suited for industrial processing of large-area substrates, regardless of the material type (plastic, metal, glass, or ceramic). Its cost-effectiveness stems from the accessibility and easy maintenance of its components. As highlighted in our study, the self-cleaning functionality of TiO₂ layers is predominantly influenced by their surface topography. We demonstrated that optimizing spraying pressure during deposition and adjusting post-annealing temperatures effectively enhances these properties. Our results showed an impressive 100% cleaning efficiency in both thick and thin TiO₂ films while maintaining optical transparency between 60% and 80% in the visible spectrum. Furthermore, we established the dual capability of these engineered TiO₂ surfaces for high-efficiency cleaning and effective disinfection. These findings offer valuable insights for the development of advanced materials applicable in construction, automotive, healthcare, solar energy, and environmental protection [see **Ceram. Int.** **50B** (2024) **42264–42275**];
- Efforts to combine osteogenic and piezoelectric stimuli within hydroxyapatite (HA) and barium titanate (BT) ceramic couples have been pursued for a new generation of synthetic bone graft substitutes. In a multi-parameter study, we demonstrated that in a conventional sintering regime, the reactivity of BT-HA mixture constituents cannot be avoided at temperatures exceeding 800 °C, regardless of their ratio, crystalline quality, or particle size. This not only resulted in a decline in piezoelectric properties but also led to poor cytocompatibility. To address this, a simple and cost-effective solution was proposed and validated: deposition of HA coatings on the surface of pre-sintered BT discs using industrial-ready radio-frequency magnetron sputtering technology. This approach proved to be highly promising for successfully and uncompromisingly coupling the piezoelectric and osteogenic properties of ceramics [see **Ceram. Int.** **50** (2024) **29711–29728**].
- We explored new manganites for room-temperature micro-scale magnetic cooling, highlighting two promising compositions. La_{0.67}Ba_{0.13}K_{0.20}MnO₃ prepared by the Pechini method, showed a relatively large magnetic entropy change (MCE) and relative cooling power (RCP) of 4.23 Jkg⁻¹K⁻¹ and 225 Jkg⁻¹, respectively, at a magnetic transition temperature (T_c) of 316 K under a 5 T applied magnetic field [see **J. Alloys Compd.** **976** (2024) **173257**]. Similarly, La_{0.8}K_{0.1}Pb_{0.1}MnO₃ bulk perovskite, synthesized by flash combustion reaction followed by a sintering process at 1200 °C, exhibited a high and sharp peak in MCE of 5.5 Jkg⁻¹K⁻¹ and RCP of 219 Jkg⁻¹, at a T_c of 289 K, also under 5 T [see **J. Mater. Sci.–Mater. Electron.** **35** (2024) **2138**].
- We investigated the impact of sulfurization and thermal treatment on the microstructure and composition of quinary/quaternary chalcogenide light absorbers

for photovoltaics, obtained via solution-based approaches: (i) using spin-coating of quasi-protic molecular ink, we examine the solubility limits of cobalt in $\text{Cu}_2\text{ZnSnS}_4$ [see **Appl. Surf. Sci. 672 (2024) 160848**]; (ii) employing co-electrodeposition, we identified the most suitable additive for obtaining $\text{Cu}_2\text{CoSnS}_4$ at fixed applied potential [see **J. Electroanal. Chem. 959 (2024) 118177**]; and (iii) through spray pyrolysis, we explored the effect of different substrate temperatures on the formation of single-phase $\text{Cu}_2\text{BaSnS}_4$ [see **Materialia 36 (2024) 102178**].

 We conducted an exhaustive characterization of potassium phosphates for energy storage obtained by solid-state reaction. Our findings revealed that copper-based chromium phosphates exhibit the most efficient charge mobility and the highest a.c. conductivity compared to those with nickel or cobalt [see **J. Alloys Compd. 1009 (2024) 176870**]. Furthermore, substituting Ba^{2+} by Sr^{2+} in $\text{KBa}_{1-x}\text{Sr}_x\text{Cr}_2(\text{PO}_4)_3$ Langbeinite-type phosphate led to the highest specific capacitance of 3.86 F/g for $\text{KBa}_{0.5}\text{Sr}_{0.5}\text{Cr}_2(\text{PO}_4)_3$, with an energy density of 343 mWh/kg and a power density of 30.9 kW/kg. This composition also presented the lowest impedance, highlighting its potential for energy storage applications [see **Materialia 36 (2024) 102147**].

LABORATORY 30

“Magnetism and Superconductivity”

ECMS

Head of laboratory: Dr. Victor KUNCSEK, Senior Researcher rank 1, Habil. (kuncser@infim.ro)

Personnel: 34 members – 7 × SR1, 7 × SR2, 7 × SR3, 3 × SR, 3 × RA, 2 × technological development engineer (1 × TDE2 and 1 × TDE3), 1 engineer, and 4 × technician.

Beyond its scientific endeavours, the group actively participates in educational and training initiatives.

27 team members hold PhD titles in physics and chemistry, including 2 PhD supervisors coordinating 1 – 2 PhD students annually. In addition, the team includes 3 PhD students.

Main research directions:

- ✿ Fundamental and applied research in the field of magnetic and magneto-functional materials for actuator and sensoristic applications as well as in the field of superconductivity, mainly targeting materials with superconducting properties with potential for practical applications. The research process covers all stages, from preparation (bulk materials, thin-films or nanostructures) to structural and electronic characterization, completed with a deep analysis of the magnetic and superconducting properties, respectively.
- ✿ Related to the magnetic behaviour, mainly the functionalities mediated by magnetic reconfiguration controlled by temperature, magnetic and electric fields, applied or from interface interactions, are envisaged. The research is focused especially on the study of 0D, 1D and 2D nanostructures. In the case of magneto-functional structures, magnetic systems of nanoparticles, thin-films and multilayers, materials for colossal magnetoresistance (CMR), giant magnetoresistance (GMR) and tunnelling magnetoresistance (TMR), soft and hard magnetic materials, Heusler compounds with spin polarization, heterogeneous multiferroic systems, magneto-caloric materials, diluted magnetic oxides/semiconductors, thermo-electric systems, *etc* are envisaged. In addition, bulk materials, advanced hybrid systems and composites/nanocomposites destined to operate in extreme conditions such as the ones in fusion and fission reactors, particle accelerators and in space, are investigated. Interactions at the interface and functionalities induced by them in nanostructured hybrid systems such as soft magnet/hard magnet (exchange-spring), ferromagnet/antiferromagnet (exchange-bias), ferromagnet-ferroelectric (magneto-electric coupling) represent other fields of interest related to fundamental and applicative aspects of smart multi-functional systems. In specific cases, the experimental studies are completed by theoretical studies approaching electronic configurations based on Density Functional Theory (DFT) and magnetic configurations based on finite-element simulation programs.
- ✿ Related to the superconducting behaviour, studies of vortex matter, dynamics and pinning and nano-engineering of artificial pinning centres for high-magnetic field applications are envisaged. Exploration of fields of applicability of these materials and related ones considering, beyond superconductivity, other that may be important for applications, such as mechanical, biological, optical are also considered. The studied materials are mainly cuprate high temperature superconductors Y (rare earth) $\text{Ba}_2\text{Cu}_3\text{O}_7$ (RE123) with nano-engineered pinning centres, Bi- and La-based superconducting cuprates, MgB_2 (with various additions for increasing pinning properties), iron-based pnictide and chalcogenide multicomponent superconductors and low temperature (classic) metallic and intermetallic superconductors. Other

materials of interest are CeO_2 , SrTiO_3 , LiPdPtB , PdO , boron/carbide composites, selected steels, and archaeological ceramic materials. Most of the materials are obtained in the laboratory in various forms: powders, polycrystalline bulk samples, single crystals, wires/tapes, nanostructures, heterostructures and nanocomposites. The group uses advanced techniques for obtaining or processing materials: conventional powder synthesis in controlled atmosphere, cryochemistry or energy milling, crystal growth in flux or by melting zone, growth of thin films by laser ablation, sintering by spark plasma, lamination, arc melting, *etc.*

Relevant infrastructure:

Amongst important research equipment, considering preparation facilities as well as characterization ones, the following can be listed:

- ✿ Spark plasma sintering, hot pressing sintering, microwave sintering (**Fig. 30-1**);
- ✿ Melt-spinning and various ball mills;
- ✿ Nanoparticle preparation systems by hydrothermal / solvothermal synthesis in autoclave and centrifugation for separation by sizes);
- ✿ RF/DC sputtering deposition system for magnetic thin-films and multilayers with 4 sources and base pressure in the range of 10^{-9} mbar;
- ✿ Facility for inducing thermal transfer in radiofrequency magnetic field to determine specific absorption rates in dispersed nanoparticle systems;
- ✿ Thermogravimetric and differential scanning calorimetry systems;
- ✿ Vibrating Sample Magnetometry system in magnetic fields up to 9 Tesla;
- ✿ Mossbauer spectrometers with different accessories to perform measurements at variable temperatures (4.5 K – 1000 K) and in applied fields, *via* the detection of gamma radiation / X- rays / conversion electrons (the only group in Romania active in Mossbauer Spectroscopy) (**Fig. 30-1**);
- ✿ Complex system for measurements of physical properties (PPMS) with magnetic fields up to 14, DynaCool System in up to 9 T and a SQUID type magnetometer (**Fig. 30-1**) working in 7 T down to 2 K from Quantum Device with the corresponding facility for liquid He production (18 L/24 h);
- ✿ Magnetic texturing of thin-films is investigated by vectorial MOKE magnetometry;
- ✿ For high temperature domain, the laboratory possesses a Laser Flash Analyser system that allows the determination of thermal diffusivity, specific heat and thermal conductivity of the volume materials or multilayers (3 layers, including liquids) in the range 25 – 1100 °C, a dilatometer (Netzsch 402 C, 2015) to determine thermal expansion coefficients (25 – 1600 °C) and an equipment (Netzsch, Nemesis 2015) to determine electrical conductivity and Seebeck coefficient (25 – 800 °C);
- ✿ In order to determine the composition in bulk / powder systems, an X-ray fluorescence device is available, while for very low concentrations/quantities the group possesses an inductively coupled plasma mass spectrometer (ICP-MS) (**Fig. 30-1**), with an extension for thin film analysis by laser ablation (LA), the last one being acquired in 2019;
- ✿ Mechanical properties are determined in quasistatic regime up to 1700 °C, using a recently-acquired equipment (INSTRON).



Fig. 30-1 ICP-MS with LA for thin-films (upper left), Mossbauer spectrometers with closed circuit He cryostats (lower left) and SQUID device – Quantum Design, of high sensitivity (middle). Spark plasma sintering plant (FCT Systeme GmbH) used to obtain high density bulk materials (right).

Available services:

- ✿ Preparation of metallic and intermetallic compounds in the geometry of thin-films, ribbons or bulk;
- ✿ Synthesis of materials that are important for applications using state-of-the-art powder metallurgy techniques;
- ✿ Lyophilization from frozen materials;
- ✿ Treatment of powders and thin-films at high pressures and temperatures in non-corrosive gas atmosphere (hydrogen, nitrogen, methane, carbon dioxide, helium) and measurement of the formation kinetics and thermodynamics of the materials obtained by gas-solid reaction;
- ✿ High sensitivity magnetometry to characterize the magnetic properties of the elements (bulk, powders and nano-powders, ribbons and nanocomposites, 0-, 1- and 2-dimensional nanostructures);
- ✿ Characterization of the thermodynamic and transport properties (thermal, electric) of the materials in a large temperature domain;
- ✿ Determination of the Debye temperature, specific heat and entropy variation of solid materials in the temperature range of 2 – 300 K and in a magnetic field between 0 and 14 T;
- ✿ Determination of thermal conductivity of solid materials in the temperature range of 2 – 300 K and in a magnetic field between 0 and 14 T;
- ✿ Complex characteristics and specific local configurations and magnetic interactions in materials containing iron, evidenced by all techniques of Mossbauer spectroscopy;
- ✿ Specific temperature-dependent properties evidenced by modern differential thermal analysis methods, differential calorimetry and mass spectrometry;
- ✿ Atomistic simulation within the DFT of the materials for advanced applications and finite element micromagnetic modelling;
- ✿ Preparation/processing by various techniques of powders, single-crystals, thin films/heterostructures/nanostructures, bulks, composites;
- ✿ Magnetic and transport measurements on superconducting materials;
- ✿ Analysis of experimental data obtained on superconductors with the determination and modelling of critical parameters (critical temperature, critical current density, irreversibility field, pinning force and pinning mechanisms, trapped field, vortex pinning energies, Debye temperature, and others);

- ✿ Mechanical measurements in quasistatic regime up to 1700 °C (bending/compression of hard materials);
- ✿ Analysis of mechanical properties and correlation with fractography aspects;
- ✿ Targets fabrication for thin film deposition.

The group also develops materials and technologies for a number of applications: superconducting thin layers and coated conductors from high critical temperature cuprates containing nano-engineered pinning centres; superconducting MgB₂ wires/tapes in metallic sheath; MgB₂-based magnetic storage devices, magnetic concentrators and magnetic shieldings; MgB₂-based powders, coatings and bulks for biomedical applications; boron-based super-hard materials for tools and extreme high temperature applications, integrated multifunctional devices.

Main results:

- ✿ 17 research projects (1 × SOL; 1 × SEE; 4 × EURATOM; 4 × PED; 1 × PCE; 2 × TE; 2 × PD; 1 × SNFR; and 1 × INUMMAT);
- ✿ 34 articles published in Web of Science®-indexed journals with impact factor (of which 19 with main author from Lab. 30);
- ✿ 1 OSIM granted patent;
- ✿ 9 OSIM patent applications.

Highlights:

- ✿ Design and characterization of novel RE-free based exchange spring magnetic nanocomposites with enhanced magnetic performances [see **Sci. Rep. (2024) 17029**];
- ✿ Investigation of the magnetic behaviour and exchange bias effects in Fe-FeO-ZnO nanocomposites [see **Results Phys. 58 (2024) 107469**];
- ✿ Investigations of image potential states of 2D materials [see **Appl. Mater. Today 39 (2024) 102304**];
- ✿ Investigation of local structure and magnetic interactions in non-stoichiometric Mg_{0.5}Ca_{0.5}Fe₂O₄ nanoferrites by magnetometry and Mössbauer spectroscopy [see **Ceram. Int. 50 (2024) 6025**];
- ✿ Magnetocaloric properties of bulk perovskite manganites [see **J. Mater. Sci.-Mater. Electron. 35 (2024) 2138**];
- ✿ Evidence of skyrmion phase in Fe-Co-Si systems obtained by mechanochemical activation [see **Physica B Condens. Matter 688 (2024) 416153**].

LABORATORY 40

“Surface and Interface Science”

Head of laboratory: Dr. Cristian Mihail TEODORESCU, Senior Researcher rank 1, Habil. (teodorescu@infim.ro)

Personnel: 22 members – 2 × SR1, 4 × SR2, 6 × SR3, 1 × TDE3, 4 × SR, 3 × RA, and 2 × technician. Beyond its scientific endeavours, the group actively participates in educational and training initiatives.

17 team members hold PhD titles in physics (12), chemistry (1), materials engineering (3), and electronics (1), including 1 PhD supervisor. Additionally, the team includes 3 PhD students in physics.

Main research directions:

- ✿ Surface and interface analysis by photoelectron spectroscopies (XPS–ESCA, ARUPS, spin-resolved PES, PED) *in situ* electron diffraction (LEED, RHEED), AES, scanning tunnelling microscopy and spectroscopy STM–STS, photoelectron spectromicroscopy, low energy and photoemission electron microscopy (LEEM–PEEM);
- ✿ Surfaces, thin-films and heterostructure preparation by molecular beam epitaxy (MBE);
- ✿ Theoretical aspects of ferroic systems.

New subjects:

- ✿ Analysis of ferroelectric surfaces, band bending in heterostructures;
- ✿ Molecular reactions at ferroelectric surfaces;
- ✿ In plane conduction properties of 2D systems on ferroelectric surfaces;
- ✿ ‘2D nanoreactors’, molecular reactions with reactants stabilized between graphene layers and substrates;
- ✿ Spin asymmetry in band structure of 2D systems;
- ✿ Photocatalysts with internal junctions;
- ✿ Multiferroic structures with indirect exchange or coupling through charge accumulation;
- ✿ Theoretical developments in the area of ferroic thin-films (ferroelectric, ferromagnetic);
- ✿ Ferromagnetic and ferroelectric domains;
- ✿ Development of new devices operating in ultrahigh vacuum (effusion cells, evaporators, manipulators);
- ✿ Development of software packages for data analysis.

Relevant infrastructure:

- ✿ A complex cluster for surface and interface science (Specs, **Fig. 40–1**), composed by: (i) a chamber for photoelectron spectroscopy (XPS, ESCA, UPS, AES); (ii) a molecular beam epitaxy (MBE) chamber with *in situ* follow-up by low energy electron diffraction (LEED) and reflection high energy electron diffraction (RHEED) and residual gas analysis; (iii) a chamber for scanning tunnelling microscopy and spectroscopy (STM/STS) and non-contact atomic force microscopy (AFM) with atomic resolution; (iv) load-lock and storage of samples in ultrahigh vacuum;
- ✿ An installation for X-ray photoelectron spectroscopy with possibilities of restricted area analyses (lateral resolution 2 μm) and automated change of samples / measuring areas, coupled to a reaction cell at high pressures and temperatures (Kratos, **Fig. 40–2**);
- ✿ A complex cluster for surface and interface science (Specs, **Fig. 40–3**), delocalized actually on the SuperESCA beamline at the Elettra synchrotron radiation facility in Trieste (Combined Spectroscopy and Microscopy on a Synchrotron – CoSMoS),

composed by: (i) a chamber for photoelectron spectroscopy (XPS, ESCA, UPS, AES) with angle and spin resolution (ARPES, XPD, ARUPS, SR-UPS); (ii) a molecular beam epitaxy (MBE) chamber with *in situ* follow-up by low energy electron diffraction (LEED) and reflection high energy electron diffraction (RHEED) and residual gas analysis; (iii) a chamber for scanning tunnelling microscopy and spectroscopy (STM/STS); (iv) load-lock and storage of samples in ultrahigh vacuum. This installation has allocated each semester from Elettra 5 days of „in-house research” beamtime and 6 days of beamtime allocated based on research projects, reserved only from projects from Romania. In addition to synchrotron radiation beamtime, photoelectron spectroscopy using laboratory sources, or other experiments STM/STS, LEED, RHEED, Auger, *etc* are possible at any time, provided the personnel is able to travel at Elettra;

- ❁ An installation for low energy and photoemission electron microscopy: LEEM – PEEM, micro LEED, micro ARUPS (Specs). The installation is able to perform simultaneous imaging (*i.e.*, without scanning) of surfaces by using low energy electrons or photoelectrons produced by UV radiation. In the LEEM mode, the lateral resolution is about 5 nm, and in the PEEM mode about 50 nm. The advantages of using this installation are: (i) the possibility to record immediate imaging, to realize movies, to follow-up in real-time surface modifications; (ii) the fact that one uses low energy electrons makes this method suitable for delicate surfaces, which otherwise would be damaged by high energy electrons such as the ones used in scanning electron microscopy (SEM); (iii) one may obtain structural or electronic structure (densities of states, dispersion laws) information on nanometre scale.
- ❁ Setup for extended X-ray absorption fine structure (EXAFS). Excitations: Mo $K_{\alpha 1}$ (17479.34 eV), W $L_{\alpha 1}$ (8397.6 eV), power 3 kW (40 kV, 75 mA); Ge(220), Ge(400), Ge(840) monochromators; detectors: proportional counters, scintillation detectors; measurement in transmission or fluorescence; simulation and analysis software. Produced by Rigaku, Tokyo, Japan.
- ❁ Magneto-optical Kerr effect microscope with possibilities of in-plane and out-of-plane magnetic fields up to 1 T, resolution 500 nm.

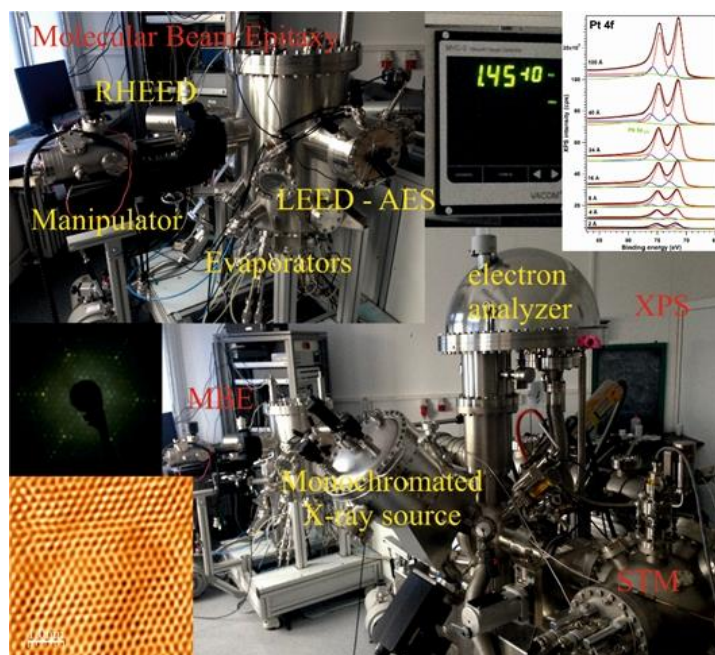


Fig. 40–1 The first cluster of surfaces and interfaces (the “multi-method system” coupled to MBE), located at NIMP. With red, the principal components are denoted (XPS, STM, MBE). With yellow, the main devices. Other photographs from this panel plot the working pressures, the quality of XPS spectra, LEED and STM images.

Produced by Specs, Berlin, Germany.

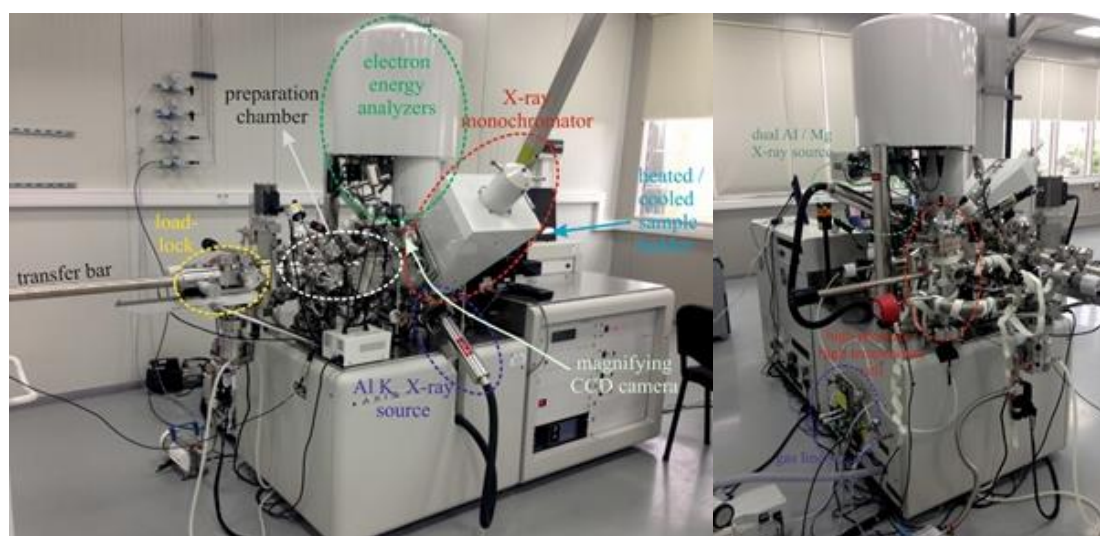


Fig. 40-2 The installation for photoelectron spectroscopy with possibilities of analysis on micrometre areas and provided with a cell for sample treatment at elevated pressures and temperatures (4 bar / 1000 °C). Produced by Kratos, Manchester, United Kingdom.

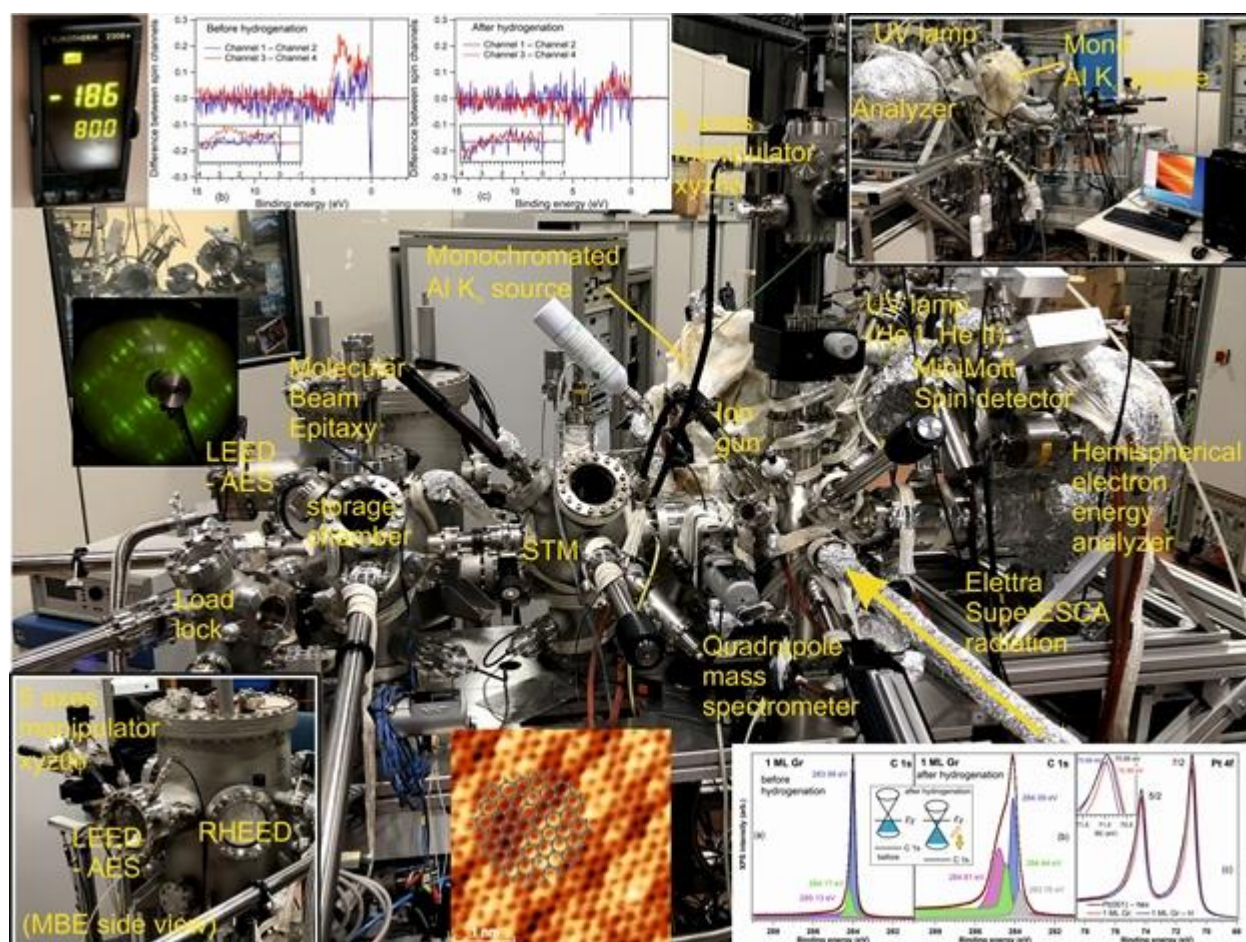


Fig. 40-3 The CoSMoS (combined spectroscopy and microscopy on a synchrotron) cluster coupled to the SuperESCA beamline at Elettra, Trieste. Produced by Specs, Berlin, Germany.

Available services:

- ☀ Photoelectron spectroscopy-based techniques: X-ray photoelectron spectroscopy (XPS) and diffraction (XPD), ultraviolet photoelectron spectroscopy (UPS), angle-resolved UPS (ARUPS), spin-resolved ARUPS;
- ☀ Auger electron spectroscopy (AES) and diffraction (AED);

- ✿ Low energy electron diffraction (LEED) and reflection high energy electron diffraction (RHEED) characterization of surfaces;
- ✿ Scanning tunnelling microscopy (STM) and spectroscopy (STS) at variable temperature;
- ✿ Non-contact atomic force microscopy (AFM) with atomic resolution;
- ✿ Sample depth-profiling by ion sputtering assisted by XPS or AES;
- ✿ Surface cleaning and synthesis of epitaxial thin-films by molecular beam epitaxy (MBE);
- ✿ Thermally-programmed desorption of molecules from surfaces by residual gas analysis (RGA);
- ✿ Low energy electron microscopy (LEEM) and photoemission electron microscopy (PEEM), micro-LEED and micro-ARUPS;
- ✿ Extended X-ray absorption fine structure (EXAFS).

Main results:

- ✿ 4 research projects (1 × PCE; 1 × TE; 1 × ELI; and 1 × IOSIN);
- ✿ 36 articles published in Web of Science®-indexed journals with impact factor (of which 7 with main author from Lab. 40);
- ✿ 1 OSIM granted patent;
- ✿ 3 OSIM patent applications.

Highlights:

- ✿ Evidence of the interplay between substrate polarization and reversible molecular adsorption/desorption processes for CO on BaTiO₃(001) [see Mater. Adv. 5 (2024) 5709–5723], C₂H₄/BaTiO₃(001) [see Heliyon 5 (2024) 5709–5723] and CO₂/BaTiO₃(001) [see Mater. Adv. 5 (2024) 8798–8811]. In the latter case, the carbon coverage was nearly one monolayer, which is a promising result for using barium titanate in carbon capture, utilization and storage (CCUS) technologies.
- ✿ Evidence of surface spin asymmetry of O 2p states in SrTiO₃(001) [see Physica Scripta 99 (2024) 105925] and in SrTiO₃(011) [see J. Chem. Phys. 162 (2025) 054707]. In the latter case the spin asymmetry is considerably larger, since the surface O₂ layer must have a lower negative ionization state in order to stabilize the surface, according to Tasker's criteria.
- ✿ Theory of Floquet topological insulators with time-reversal symmetry broken by light irradiation (FTI) with spin-orbit coupling [see Phys. Rev. B 109 (2024) 075121] and of related Floquet topological spin filters based on an FTI realized by irradiating a honeycomb lattice with circularly polarized light, in the presence of intrinsic spin-orbit coupling [see Phys. Rev. B 110 (2024) L241113].

LABORATORY 50

“Theoretical Physics and Computational Modeling”

Head of laboratory: Dr. Valeriu MOLDOVEANU, Senior Researcher rank 1 (valim@infim.ro)

Personnel: 6 members – 1 × SR1, 1 × SR2, 3 × SR3, 1 × SR, and 1 × RA.

Beyond its scientific endeavours, the group actively participates in educational and training initiatives.

All 6 team members hold PhD titles in physics.

Main research directions:

- 🌀 Topological and transport properties of 2D materials and lattices;
- 🌀 Hybrid quantum systems for nano-electronics and nano-optomechanics;
- 🌀 Correlation effects in 2D lattices and artificial molecules.

Main results:

- 🌀 4 articles published in Web of Science®-indexed journals with impact factor (of which 2 with main author from Lab. 50).

Highlights:

- 🌀 Stacking model of a 3D higher-order topological insulator. We presented a 3D tight-binding model for a higher-order topological system, built by stacking square diatomic Chern insulator layers. Our analysis highlighted the role of chiral and antiunitary symmetries in shaping electron-hole symmetry and energy spectrum degeneracy. By exploring different geometries – bulk, slab, and nanowire – we revealed the emergence of zero-energy surface states and chiral hinge states that support a 3D quantum anomalous Hall effect. Notably, we demonstrated that hinge state localization, determined by the number of layers, gives rise to fractional Hall plateaus in a four-terminal transport setup. Our findings provide valuable insights into realizing 3D Chern insulators in platforms such as magnetic topological materials, photonic crystals, and topoelectrical circuits [see **Phys. Rev. Res.** **6** (2024) 023168];
- 🌀 QED-DFT-TP approach to cavity-quantum dot arrays. In two recent articles we adapted the so-called QED-DFT-TP theoretical method to investigate the equilibrium properties and the excitation spectrum of a square quantum dot array embedded in a cylindrical cavity. We first report the modelling of the equilibrium properties of a two-dimensional electron gas (2DEG) in a square lateral superlattice of quantum dots in a GaAs heterostructure subject to an external homogeneous perpendicular magnetic field and a far-infrared circular cylindrical photon cavity with one quantized TE₀₁₁ mode. We accomplished this with a DFT model of the 2DEG delivering the current and the charge densities. The densities are used in the para- and the diamagnetic electron-photon interactions that are updated within each iteration of the DFT-calculation. With basis states constructed as a tensor product of the electron DFT-states (orbitals) and the eigenstates of the cavity-photon number operator we thus obtain states and energy spectra of the Coulomb and photon interacting 2DEG self-consistently. This approach allows us to include the electron-photon interaction to high order and observe the complex formation of Rabi-resonances in the reciprocal space of the superlattice. Fundamental to our method to describe the electron-photon to any order is the choice of the TE₀₁₁ cylindrical cavity mode which spatial symmetry conforms with the complex symmetry of the superlattice in an external magnetic field. The electron-photon

coupling polarizes the charge density and tends to reduce the Coulomb exchange effects as the coupling strength increases. In the 2nd article we added a time-dependent excitation to the same system and model the magnetically active photon processes controlling the ratio of virtual and real para- and diamagnetic transitions. The real-time excitation method provides results beyond the traditional linear response regime [see **Phys. Rev. B 109 (2024) 235306** & **Phys. Rev. B 110 (2024) 205301**].

LABORATORY 60

“Optical Processes in Nanostructured Materials”

Head of Laboratory: Dr. Mihaela BAIBARAC, Senior Researcher rank 1, Habil. (barac@infim.ro)

Personnel: 28 members – 8 × SR1, 3 × SR2, 5 × SR3, 3 × SR, and 9 × RA.

Beyond its scientific endeavours, the group actively participates in educational and training initiatives.

21 team members hold PhD titles in physics (20) and chemistry (1), including 1 PhD supervisor. Additionally, the team includes 7 PhD students.

Main research directions:

- ✿ Optical properties of composite materials based on macromolecular compounds and carbon nanoparticles (graphene, including graphene oxide and reduced graphene oxide, carbon nanotubes, fullerene) and phosphorene, respectively, for applications in the field of eco-nanotechnologies, health and energy storage (supercapacitors, rechargeable batteries);
- ✿ Photoluminescence of 2D inorganic materials (including dichalcogenides) and their applications in information technology, sensors and energy storage;
- ✿ Optical properties of plasmonic materials, quantum dots and their applications in the fields of eco-nano-technologies and the pharmaceutical field;
- ✿ Optical properties of the inorganic micro/nano-particles for applications in the fields of heritage and optoelectronics.

Relevant infrastructure:

- ✿ An UV-VIS-NIR spectrophotometer, Lambda 950 model, from Perkin Elmer;
- ✿ A FTIR spectrophotometer, Vertex 80 model, from Bruker;
- ✿ A FT-Raman spectrophotometer, MultiRam model, from Bruker (**Fig. 60-1**);
- ✿ A Fluorolog FL-3.2.2.1 model with upgrade for the NIR range, from Horiba Jobin Yvon;
- ✿ A triple Raman spectrophotometer T64000 model, from Horiba Jobin Yvon, equipped with the lasers for the excitation in visible range;
- ✿ A FTIR imaging microscope SPOTLIGHT 400 from Perkin Elmer;
- ✿ A thermoluminescence reader Harshaw TLD 3500;
- ✿ A system for photoconductivity and I-V characteristics;
- ✿ A Scanning Near Field Optical Microscope (Multiview 4000 SNOM/SPM system from Nanonics) coupled with Atomic Force Microscope (AFM);
- ✿ A Fluoromax 4P with quantum efficiency and colorimetry options, for luminophores characterization, o system to measure surface/interfacial tension, contact angle and density;
- ✿ A Langmuir-Blodgett instruments, KSV 2000 system and KSV 5003 model;
- ✿ A potentiostat/galvanostat, Voltalab 80, from Radiometer Analytical;
- ✿ A multi-channel potentiostat/galvanostat, Origaflex model, from Origalys;
- ✿ An equipment for deposition by vacuum evaporation of organic materials;
- ✿ A broadband dielectric spectroscopy system from Novocontrol;
- ✿ An infrared spectro-microscope, Carry 600, from Agilent Scientific;
- ✿ A surface plasmons resonance (SPR) equipment from Reichert (**Fig. 60-2**);
- ✿ A hybrid Magnetron Sputtering – Pulsed Laser Deposition equipment for thin-films (**Fig. 60-3**);
- ✿ A Physical Vapor Transport equipment for transition metal dichalcogenides (**Fig. 60-4**).

Available services:

- ✿ Development of composite materials based on the conducting and insulating polymers and carbon nanoparticles of the type carbon nanotubes, graphene oxide, reduced graphene oxide, graphene quantum dots, fullerene and carbon nanohorns;
- ✿ Development of organic/inorganic hybrid materials based on conducting polymers and inorganic nanoparticles of the type ZnO, ZnS, CdS, TiO₂;
- ✿ Chemical and electrochemical functionalization of 2D materials (reduced graphene oxide, phosphorene, *etc*) with the organic and macromolecular compounds;
- ✿ Synthesis of transition metal dichalcogenides (TDMs) of the type MoS₂, WS₂, *etc*;
- ✿ The preparation of the surface-enhanced Raman scattering (SERS) supports of the type of rough metallic (Ag, Au, Cu) films, the colloidal suspensions of the metallic nanoparticles and the graphene sheets decorated with metallic nanoparticles;
- ✿ Deposition of thin layers using magnetron sputtering and Langmuir Blodgett;
- ✿ Realization of organic/organic and organic/inorganic structures by vacuum evaporation and from solution;
- ✿ Controlled crystallization of thin-films in various atmospheres;
- ✿ Functionalization of metallic surfaces for development of optical sensors *via* surface plasmons resonance;
- ✿ Analyses by the UV-VIS-NIR and IR absorption spectroscopy, Raman scattering, surface-enhanced Raman scattering (SERS), surface-enhanced infrared absorption (SEIRA) spectroscopy, photoluminescence, atomic force microscopy and broad-band dielectric spectroscopy;
- ✿ Structural characterization and phase identification in crystalline materials;
- ✿ Contact angle analysis for assessment of hydrophobic/hydrophile properties;
- ✿ Measurements of surface/interface tension and of the density of liquids;
- ✿ Colorimetry and quantum yield measurements for the characterization of phosphors;
- ✿ Calculated absorption coefficient of inorganic and macromolecular chain with density-functional theory (DFT);
- ✿ Electrochemical analysis by cyclic voltammetry, chronoamperometry, chronopotentiometry, electrochemical impedance spectroscopy, Tafel polarizations;
- ✿ Surface nano-patterning by UV Nano Imprint lithography (UV-NIL);
- ✿ Characterization of organic heterostructures for opto-electronic devices;
- ✿ Galvanostatic charge-discharge measurements for the testing nanomaterials as electrode active materials in supercapacitors and rechargeable batteries;
- ✿ The preparation of electrodes with the application in the field of the electrochemical sensors;
- ✿ Analysis concerning the stability of the drugs in the presence of UV light and various chemical agents by UV-VIS spectroscopy, photoluminescence, Raman scattering and FTIR spectroscopy.



Fig. 60-1 MultiRam FT-Raman spectrophotometer from Bruker.



Fig. 60-2 Surface Plasmon Resonance equipment from Reichert.



Fig. 60-3 Hybrid Magnetron Sputtering – Pulsed Laser Deposition equipment for thin-films.



Fig. 60-4 Physical Vapor Transport equipment for transition metal dichalcogenides.

Main results:

- ✿ 7 research projects (4 × M-ERA.NET; 2 × PED; and 1 × PNRR). In addition, Lab. 60's is involved in 2 COST actions;
- ✿ 26 articles published in Web of Science®-indexed journals with impact factor (of which 16 with main author from Lab. 60);
- ✿ 1 EPO patent application;
- ✿ 4 OSIM granted patents;
- ✿ 4 OSIM patent applications.

Highlights:

- ✿ Rare-earth doped GdF₃ nanocrystals in silicate glass matrix: Crystallization processes and photoluminescence properties [see Ceram. Int. 50 (2024) 37518];
- ✿ MAPLE-deposited perylene diimide derivative based layers for optoelectronic applications [see Nanomaterials 14 (2024) 1733];
- ✿ Fabrication of direct FLG\MoS₂ heterostructures [see Mater. Chem. Phys. 322 (2024) 129530];
- ✿ Carbonaceous structures-based composites for applications for applications in the fields of biomedical, energy storage and conversion, and fire-retardant building materials [see J. Therm. Anal. Calorim. 149 (2024) 2805; Polymers 16 (2024) 53; & Materials 17 (2024) 6127].

LABORATORY 70

“Atomic Structures and Defects in Advanced Materials”

LASDAM

Head of laboratory: Dr. Corneliu GHICA, Senior Researcher rank 1 (cghica@infim.ro)

Personnel: 25 members – 2 × SR1, 9 × SR2, 3 × SR3, 3 × SR, 5 × RA, and 3 × engineer.

Beyond its scientific endeavours, the group actively participates in educational and training initiatives.

19 team members hold PhD titles in physics (18) and chemistry (1). Additionally, the team includes 3 PhD students.

Main research directions:

Fundamental research

- Atomic scale structure-functionality correlations in advanced materials (nanostructures, thin-films, ceramics and special alloys);
- Paramagnetic point defects, either intrinsic or induced by impurities or radiations in insulators and wide-bandgap semiconductors;

Applied research

- Investigation of the physical-chemical mechanisms underpinning the detection process in nanostructured materials for gas sensing applications;
- Dielectric and semiconductor thin-films for microelectronic applications of interest for environment, security, space, biomedicine, food safety;
- Cellular and non-cellular *in vitro* interactions and biomedical applications of inorganic nanomaterials and hybrid nanostructures;
- Nanostructured materials for post-Li-ion solid-state batteries;
- AI-based algorithms for TEM-generated data analysis.

Main research infrastructure:

- Aberration-corrected analytical transmission electron microscope (HRTEM/HRSTEM) provided with EDS and EELS microanalytical facilities for sub-Ångström resolution imaging and atomic-resolution elemental mapping;
- High-resolution analytical electron microscope for electron tomography, *in situ* and *operando* experiments by specimen heating/cooling/electrical biasing;
- SEM-FIB dual analytical system used for morpho-structural and microanalytical investigations (SEM, EDS, EBSD) as well as for ion beam micro- and nano-processing;
- Continuous wave (cw) X-band (9.8 GHz) EPR spectrometer with variable temperature (VT) accessories in the 80 – 500 K range; cw Q-band (34 GHz) EPR spectrometer with ENDOR (Electron-Nuclear Double Resonance) and VT accessories (5 – 300 K);
- Pulse X-band (9.7 GHz) EPR spectrometer equipped with pulse ENDOR, pulse ELDOR (Electron-Electron Double Resonance) and VT accessories (5 – 300 K);
- Automatic liquid He plant completed with a helium recovery system; computer-controlled gas mixing station and associated electrical measurements chains for materials testing under controlled atmosphere;
- Chemical reactor and autoclave for hydrothermal and co-precipitation chemical synthesis;
- Magnetron sputtering installation for thin-films deposition, with *in situ* characterization/monitoring by Auger electron spectroscopy (AES), low-energy electron diffraction (LEED) and ellipsometry;

- ❁ Installation for rapid thermal annealing, oxidation and nitriding; horizontal furnace with 3 temperature zones for thermal treatments and physical vapor deposition (PVD);
- ❁ Measurement chains for electrical, ferroelectric and photoelectric characterization, Hall effect and magnetoresistance measurements.



Fig. 70-1 (a) JEM ARM200F aberration-corrected analytical transmission electron microscope; (b) Bruker EPR spectrometer in CW Q-band with ENDOR accessory; (c) Setup for electrical measurements under controlled atmosphere gas mixing station; (d) Magnetron sputtering installation for thin-films deposition, equipped with *in situ* AES, LEED, and ellipsometry.

Available services:

- ❁ SEM morphological characterization of advanced materials;
- ❁ TEM characterization of nanostructured materials, thin-films, ceramics, alloys;
- ❁ Chemical elemental composition and elemental mapping by SEM-EDS and STEM-EDS;
- ❁ Multifrequency EPR characterization of bulk and nanostructured insulating and semiconductor materials: nature, concentration, localization, formation mechanism and stability of the paramagnetic centres in materials; chemical processes, structural or magnetic transitions;
- ❁ Controlled simulation of toxic and explosive gas environments (CO, CH₄, NO₂, H₂S, NH₃, SO₂) for gas sensors testing and calibration; temperature-voltage calibration for the optimization of power consumption for substrates and gas sensors.
- ❁ Growth of thin-films and multilayers by magnetron sputtering;
- ❁ Rapid thermal annealing (RTA) and controlled oxidation (RTO) at temperatures within 200 – 1250 °C, heating rates up to 200 °C/s in gas flow (N₂, O₂, Ar, H₂) and thermal treatments using the horizontal furnace with 3 temperature zones up to 1200 °C in vacuum or flow of Ar, N₂;
- ❁ Electrical characterization under dark/illumination conditions, Hall effect measurements and modelling of experimental curves current-voltage (I-V) at varying

temperature, in DC and AC, capacity-voltage (C-V), capacity-frequency (C-f), capacity-time (C-t), polarization-voltage (P-V), I-T and R-T; spectral characteristics of the photocurrent (I- λ) in modulated and continuous illumination; Hall measurements: V-I curves as a function of current, magnetic field and temperature.

LASDAM operates as Partner Facility within CERIC-ERIC (<https://www.ceric-eric.eu/>) on behalf of NIMP, the Romanian Representing Entity in the ERIC along with research institutes and universities in Austria, Croatia, Czech Republic, Hungary, Italy, Poland, or Slovenia.

Main results:

- ✿ 6 research projects (1 \times M-ERA.NET; 1 \times PCE; 1 \times PED; and 3 \times TE);
- ✿ 45 articles published in Web of Science®-indexed journals with impact factor (of which 13 with main author from Lab. 70);
- ✿ 1 OSIM granted patent;
- ✿ 6 OSIM patent applications.

Highlights:

- ✿ p-type NiO semiconductor nanopowders have been explored as a potential material for CO sensing. A combination of EPR, XPS, HRTEM, and electrical measurements under *in situ* heating or *operando* conditions on nanopowders synthesized at various temperatures have been used to investigate the role of oxygen vacancies and paramagnetic Ni³⁺ ions in the sensing mechanism. The morpho-structural, spectroscopic, and gas-sensing data illustrate the complex interplay between nanoparticle size, morphology, and the shallow defects near the grain surface, which are correlated with the thermal history of the samples [see **Appl. Surf. Sci. 651 (2024) 159252**].
- ✿ Trilayer Al₂O₃/Ge/Al₂O₃ memory structure was fabricated by magnetron sputtering and analysed with respect to the influence of annealing on the charging-discharging mechanism. The behaviour of the capacitance-voltage (C-V) characteristics as a function of the annealing temperature is explained in correlation with the structure and morphology of the films. The best memory performances were obtained for samples annealed at an intermediate temperature of 600 °C, with a maximum memory window of 5.6 V and retention time with only 2% charge loss after 10⁸ s [see **ACS Applied Electron. Mater. 6 (2024) 978-986**].
- ✿ Selectively grown 2D MoS₂ coatings consisting of 1, 2 or 3 atomic monolayers, on Mo patterned substrates was achieved by a MO-CVD method, where MoO₃ from an oxidized Mo pattern and S powder served as growth precursors. Devices for measuring the photosensitivity of the selectively grown 2D MoS₂, with electrostatic doping controlled by the field effect, were fabricated directly by contacting the large Mo pads of the finger contact structures as source-drain electrodes and using the doped Si substrates as gate electrodes. By field effect control, high $\Delta I_{ph}/I_{dark}$ photosensitivity of 10⁵ % was obtained with a V_{sd} of 0.5 V and V_g of -5 V, under 4.5 \times 10⁻⁴ mW/cm² 650 nm monochromatic light [see **ACS Appl. Nano Mater. 7 (2024) 5051-5062**].
- ✿ A short-wavelength infrared (SWIR) photosensitive coating based on SiGeSn nanocrystals embedded in a HfO₂ amorphous matrix has been achieved by magnetron co-sputtering deposition, showing a spectral photosensitivity extended to 2000 nm. Microstructural and spectroscopic investigations, combined with photoelectrical measurements, confirmed that the addition of Si improves the thermal stability of SiGeSn NCs with respect to similar results obtained with GeSn NCs. Furthermore, the use of HfO₂ instead of SiO₂ matrix results in better passivation of NCs, increasing the SWIR

photosensitivity for optoelectronic applications at room-temperature [see **Sci. Rep. 14 (2024) 3532**].

- ✿ High-resolution TEM investigations have revealed a novel growth mechanism for epitaxial ZrO₂ thin films on highly misfit substrates, by domain matching epitaxy. The strain imposed by a (111)-cut Nb:SrTiO₃ substrate determines the epitaxial growth of a 8 nm thin film of ZrO₂ in a metastable rhombohedral phase with ferroelectric properties for CMOS compatible applications [see **Energy Environ. Mater. 7 (2024) e12500**].
- ✿ Deep learning methods are being developed for a fast and reliable analysis of large amounts of data provided by multiple TEM techniques. A fully automated software, based on You Look Only Once (YOLO) type neural networks for data segmentation and identification, as well as on EasyOCR deep learning Python, has been developed for real-time analysis of nanoparticle size and shape distribution.

LABORATORY 80

“Catalytic Materials and Catalysis”

MATCA

Head of laboratory: Dr. Mihaela FLOREA, Senior Researcher rank 1, Habil. (mihaela.florea@infim.ro)

Personnel: 6 members – 3 × SR1, 2 × SR3, and 1 × RA.

Beyond its scientific endeavours, the group actively participates in educational and training initiatives.

6 team members, including 1 PhD supervisor and 1 PhD student.

The MATCA group possesses expertise in the materials preparation with various properties, tailored to suit the applications for which they are designed.

Main research directions:

- ✿ Pioneering advancements in catalytic and photocatalytic materials, addressing pressing challenges in sustainability, energy, and environmental protection. With a strong focus on the development, preparation, and characterization of heterogeneous catalytic materials, the group explores innovative solutions that enhance efficiency and performance in key chemical transformations.
- ✿ A significant part of their research is devoted to catalytic reactions, encompassing selective oxidation and hydrogenation processes that enable the synthesis of high-value compounds. Their work extends to the development of polymers derived from renewable and alternative resources, fostering sustainable materials for industrial applications. Moreover, MATCA researchers are at the forefront of depolymerization technologies, seeking efficient methods to break down plastics and contribute to circular economy strategies. In parallel, they investigate the reduction of volatile organic compounds (VOCs), aiming to minimize environmental pollutants and improve air quality.
- ✿ Photocatalysis represents another core research direction, harnessing solar energy to drive essential chemical reactions. The group is actively engaged in water splitting for green hydrogen production, a key component in the transition to clean energy. Additionally, their studies on photocatalytic CO₂ transformation and artificial photosynthesis explore ways to convert carbon dioxide into valuable fuels and chemicals, offering innovative approaches to carbon capture and utilization.
- ✿ In the field of energy, the MATCA team focuses on the synthesis of advanced materials for electrocatalysis in fuel cells. Their work aims to enhance the performance and durability of fuel cell components, contributing to the development of efficient, next-generation energy technologies that support decarbonization efforts.

Relevant infrastructure:

Lab. 80 has an infrastructure covering various methods of catalytic material preparation and physico-chemical characterization. Among the important infrastructures one can mention:

- ✿ Chemistry laboratory (**Fig. 80–1**) equipped with all necessary small equipment's for catalytic materials synthesis (ovens working in air or vacuum, rotavapors, magnetic stirrers, autoclaves for hydrothermal treatments, chemical niche, apparatus for milliQ water production, centrifuge, balances) and catalytic reactors (in house reactors for solid-gas phase and liquid-solid phase reactions);

- Thermo-programmed desorption and reduction equipment (TPD-TPR) – for determining the adsorption capacity and redox properties (**Fig. 80-2**);
- Spectroscopy analysis: UV-Vis and Raman portable (**Fig. 80-2**);
- Thermal analysis – to study the relationship between a sample property and its temperature as the sample is heated or cooled in a controlled manner (**Fig. 80-2**);
- Analysis of the reaction products – gas chromatograph with three detectors (TCD, FID, and BID) gas chromatograph coupled with mass spectrometer (**Fig. 80-2**);
- Adsorption analyser with high performance capabilities - utilized to quantify the surface area, pore size, and pore volume of powders and particulate materials. The equipment is outfitted with a chemisorption feature that expands the scope of its application to encompass both physical and chemical adsorption. This enables the characterization of catalyst texture and active surface properties in catalyst supports, sensors, and several other materials. By including an automated injection loop, the TCD analytical range can be expanded through the utilization of pulse chemisorption;
- Catalytic flow reactor – is a highly advanced modular laboratory system for determining in real time the selectivity and activity of catalysts for different catalytic applications through different configurations and options.

The group has access to other infrastructures located at NIMP, through collaborative research activities, such as: SEM; TEM; XPS; optical spectroscopies (Raman, UV-Vis-NIR, FTIR); X-ray diffraction; ICP-MS; photoluminescence.

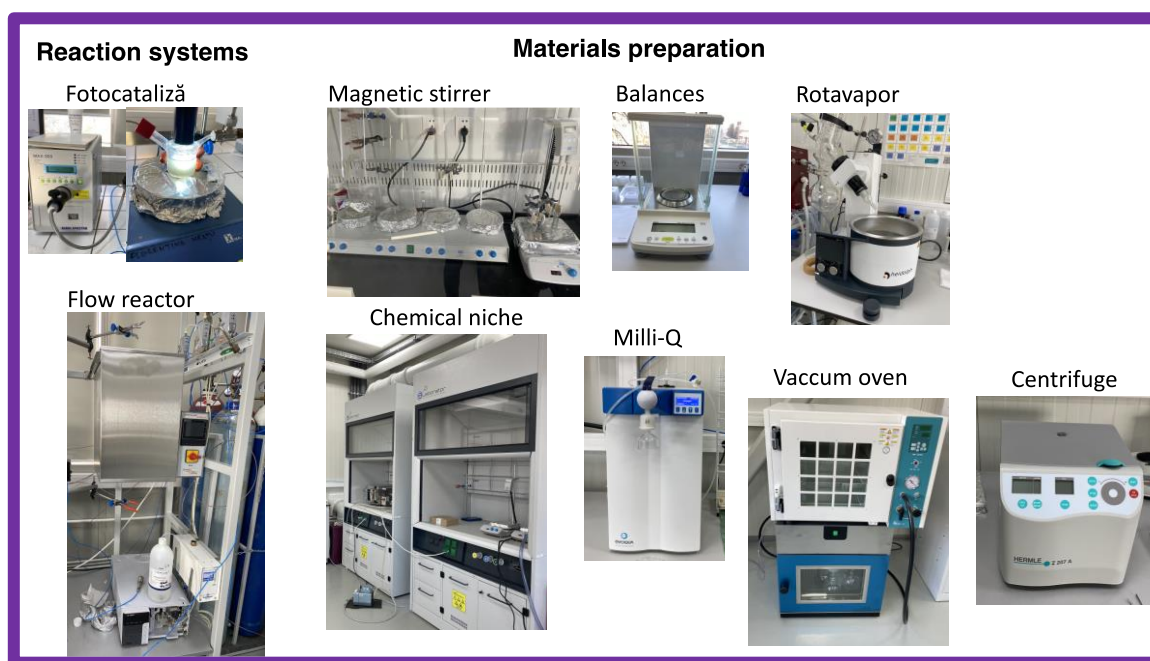


Fig. 80-1 Chemistry laboratory.

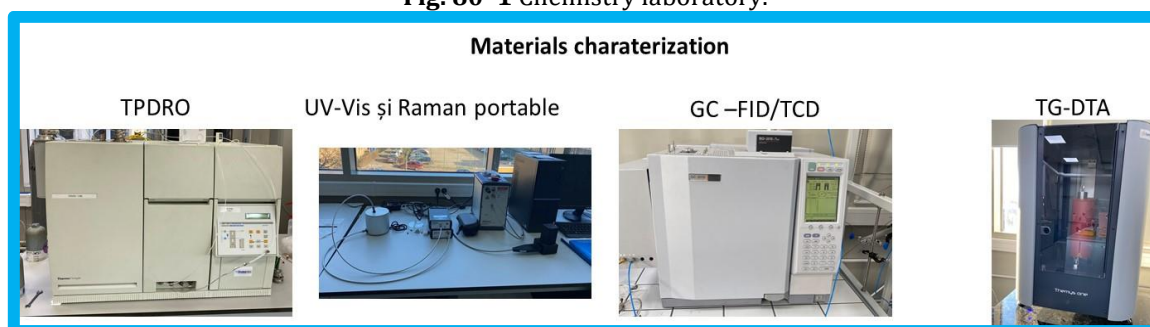


Fig. 80-2 Equipment for materials characterization and analysis.

Available services:

- ✿ Catalytic materials preparation;
- ✿ Gas-solid and gas-liquid catalytic reaction;
- ✿ H₂ production through water splitting;
- ✿ Surface characterization;
- ✿ Structural and textural characterization of the catalytic materials;
- ✿ Investigation of acid-base and redox properties;
- ✿ Determination of acid and basic properties (qualitatively and quantitatively).

Main results:

- ✿ 2 research projects (1 × PTE and 1 × PCE);
- ✿ 9 articles published in Web of Science®-indexed with high-impact factor (of which 3 with the main author from Lab. 80).

Highlights:

- ✿ The development of active and selective materials for low-temperature oxidative activation of methane into value-added products remains a key challenge for the scientific community. We are actively involved in designing catalysts for selective methane oxidation to formaldehyde using molecular oxygen over MXene-based catalysts at low-temperature and ambient-pressure conditions. Moreover, the dynamics of the structural and surface changes that these systems go through during catalysis were studied at the Swiss Light Source (SLS) synchrotron under O₂ and/or CH₄ environments at different temperatures. As expected, the surface is “alive” and reversible surface modifications were observed, indicating the presence of a possible “memory” phenomenon. This was done in collaboration with Dr. L. Artiglia's group from the Paul Scherrer Institute, Switzerland;
- ✿ Making 1D filaments of materials containing Ti, C, and O to split water under photocatalytic conditions and create H₂ gas is a straightforward, low-cost, and economically viable strategy, thanks to a collaboration with a team of researchers at Drexel University, led by Prof. M. Barsoum and a team from the University of Strasbourg, France, led by Dr. D. Constantin. This partnership will continue into 2025;
- ✿ New photocatalytic systems based on i-MXene-semiconductor composites for hydrogen production via photocatalytic water splitting reaction are the main focus of the PCE-funded project;
- ✿ Plastics are indispensable materials for packaging and many products from our daily life, and their recycling is essential to ensure a circular economy. Therefore, we developed acidic heterogeneous catalysts for upcycling of polyethylene terephthalate (PET) to terephthalic acid (TPA) and ethylene glycol by hydrolysis. Through this study, we obtained acid-modified MXene catalysts that can break down PET at a temperature of 180 °C, which is 40 °C lower than the temperature required by other already used catalysts under comparable reaction conditions. Moreover, our catalysts are stable at least for 3 cycles. These findings suggest that both the acidity of the catalysts and the 2D features are important for the depolymerization of PET and, thus, acid-modified MXenes can be promoted as valuable catalysts for upcycling PET [see **ACS Sustain. Chem. Eng.** **12** (2024) 9766–9776].

Through their multidisciplinary approach, the MATCA research group is driving innovation in catalytic science, bridging fundamental research with practical applications that promote sustainability, cleaner energy solutions, and environmental resilience.

Advances in Materials and Devices for Electronics, Photonics & Optoelectronics

The interface structural, electronic and optical properties of ZnO nanowires/Graphene nanohybrid (ZnO NWs/G): Experimental and theoretical DFT investigations

I. Boukhoubza¹, M. Achehboune², I. Derkaoui³, M.M. Apostol^{1,4}, M.A. Basyooni^{5,6}, M. Khenfouch⁷, L. Nedelcu¹, I. Enculescu¹, E. Matei¹

- 1) *National Institute of Materials Physics, 077125, Măgurele, Romania*
- 2) *Laboratoire de Physique du Solide, Namur Institute of Structured Matter, University of Namur, 5000, Namur, Belgium*
- 3) *Laboratory of Solid-State Physics, Faculty of Sciences Dhar el Mahraz, University Sidi Mohammed Ben Abdellah, 30 000, Fez, Morocco*
- 4) *Faculty of Chemical Engineering and Biotechnologies, National University of Science and Technology Politehnica Bucharest, 011061, Bucharest, Romania*
- 5) *Department of Nanotechnology and Advanced Materials, Graduate School of Applied and Natural Science, Selçuk University, 42030, Konya, Turkey*
- 6) *Science and Technology Research and Application Centre (BITAM), Necmettin Erbakan University, 42090, Konya, Turkey*
- 7) *Laboratory of Materials, Electrical Systems, Energy and Environment (LMS3E), Department of Physics, Faculty of Applied Sciences, Ibn Zohr University, 86153, Agadir, Morocco*

A ZnO/Graphene (G) heterostructure is a promising material combination, as both components exhibit excellent optoelectronic properties, enabling diverse applications in photocatalysis, supercapacitors, sensors, and solar cells [1–3]. Moreover, the strong electronic combination between the nanostructured ZnO and the low dimensionality carbon material in a nanohybrid system can dramatically change the ZnO band structure. By tuning the process parameters for the ZnO growing on top of a graphene covered substrate, the morphology/aspect ratio, the orientation, and the density of the resulting ZnO nanostructures can be controlled [4]. In this work [5], a ZnO nanowires/G nanohybrid was synthesized by a three steps approach. Copper substrates were covered with graphene by chemical vapor deposition, further ZnO nanowires were electrochemically deposited on the as-grown graphene on copper and finally a transfer process was employed for moving the heterostructure onto a SiO₂/Si substrate *via* electrochemical delamination (Fig. 1).

XRD and Raman measurements (Fig. 2a,b) revealed that the ZnO nanowires crystallize in a wurtzite structure with a preferred orientation along the *c*-axis (002), perpendicular to the graphene. This process results in the formation of a nanohybrid heterostructure. Fig. 2c shows SEM images of ZnO nanowires grown on G/Cu substrates, revealing uniform and dense, completely covering the substrate. The nanowires have diameters of 20–40 nm and lengths of 100–300 nm. Most exhibit a hexagonal cross-section, with their orientations influenced by the wavy graphene structure formed during CVD growth. Despite the challenges of depositing materials on graphene's hydrophobic surface, electrochemical deposition enabled successful ZnO nanowire growth. Fig. 2d illustrates the transferred ZnO nanowires/graphene layer onto SiO₂/Si after delamination from Cu and PMMA removal, preserving its uniform architecture and maintaining high-quality graphene over a large area [5].

To further understand the interaction between the graphene surface and adsorbed ZnO molecules, charge density difference calculations were performed for three adsorption positions: bridge, top, and hollow sites (Fig. 2e). The charge redistribution, shown by yellow (charge loss) and sky-blue (charge gain) lobes, indicates significant electron transfer between ZnO molecules and the graphene monolayer. The Bader charge analysis reveals transferred charges of −0.245 |e|, −0.545 |e|, and −0.338 |e| for the bridge, top, and hollow sites, respectively, with the top site being the preferred adsorption site due to the strongest interaction.

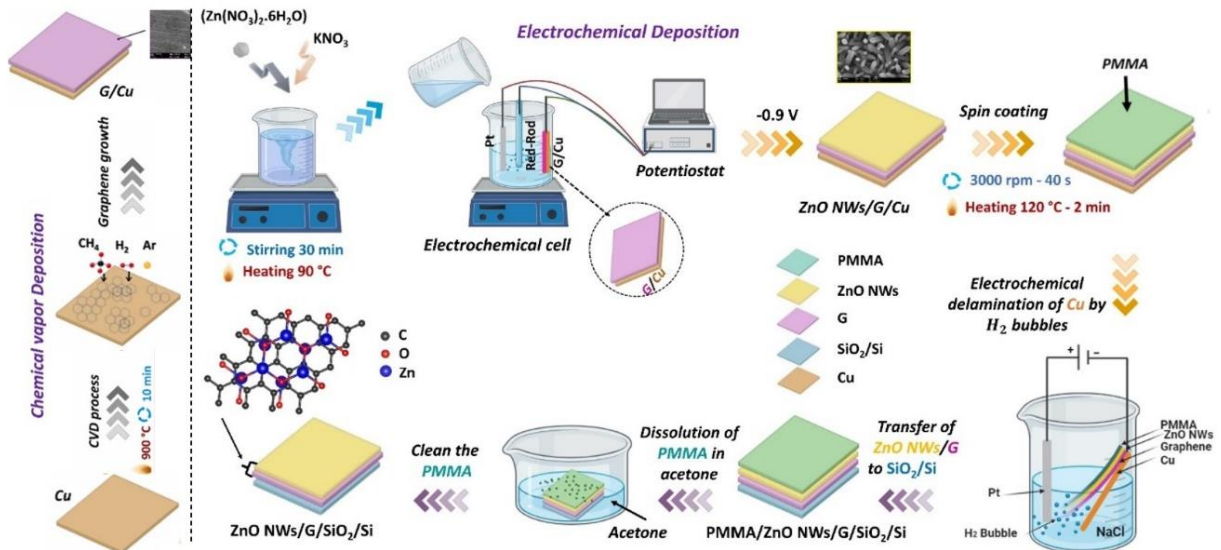


Fig. 1: Synthesis process of ZnO NWs/G/SiO₂/Si nanohybrid. Reproduced from Ref. [5].

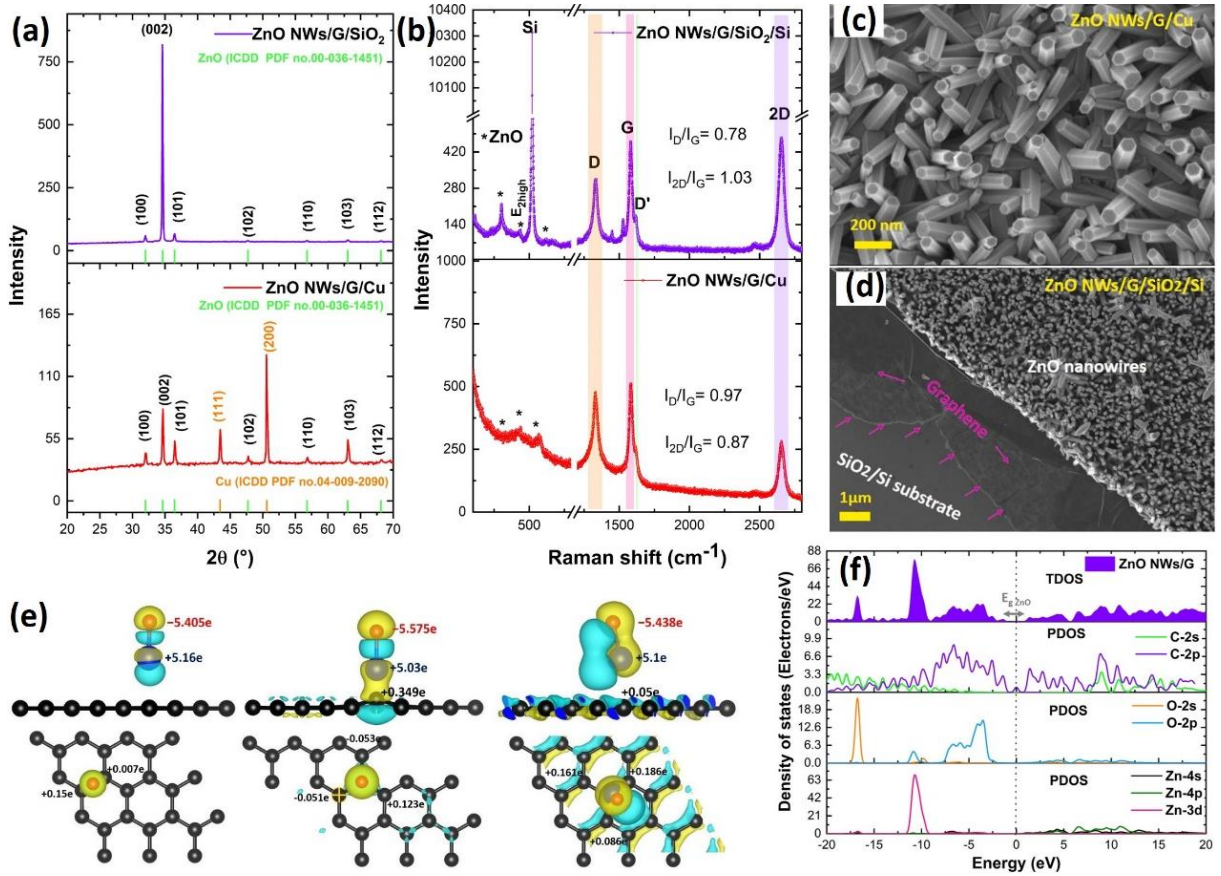


Fig. 2: (a) XRD patterns, (b) Raman spectra and (c) (d) SEM images of the ZnO NWs/G/Cu and ZnO NWs/G/SiO₂/Si nanohybrid; (e) model structures of ZnO adsorption on G; (f) total and partial density of states (DOS) of ZnO NWs/G. Reproduced from Ref. [5].

The total density of states (TDOS) and partial density of states (PDOS) reveal that the valence band is mainly influenced by Zn 3d and O and C 2p and 2s orbitals, while the conduction band is dominated by C 2p and 2s, O 2p, and Zn 4s and 3d orbitals. The introduction of the graphene monolayer modifies the electronic properties in the range of -20 to 20 eV, resulting in new transition defects near the Fermi level. These defects are attributed to electron transitions from graphene to ZnO due to carbon-related defects (Fig. 2f).

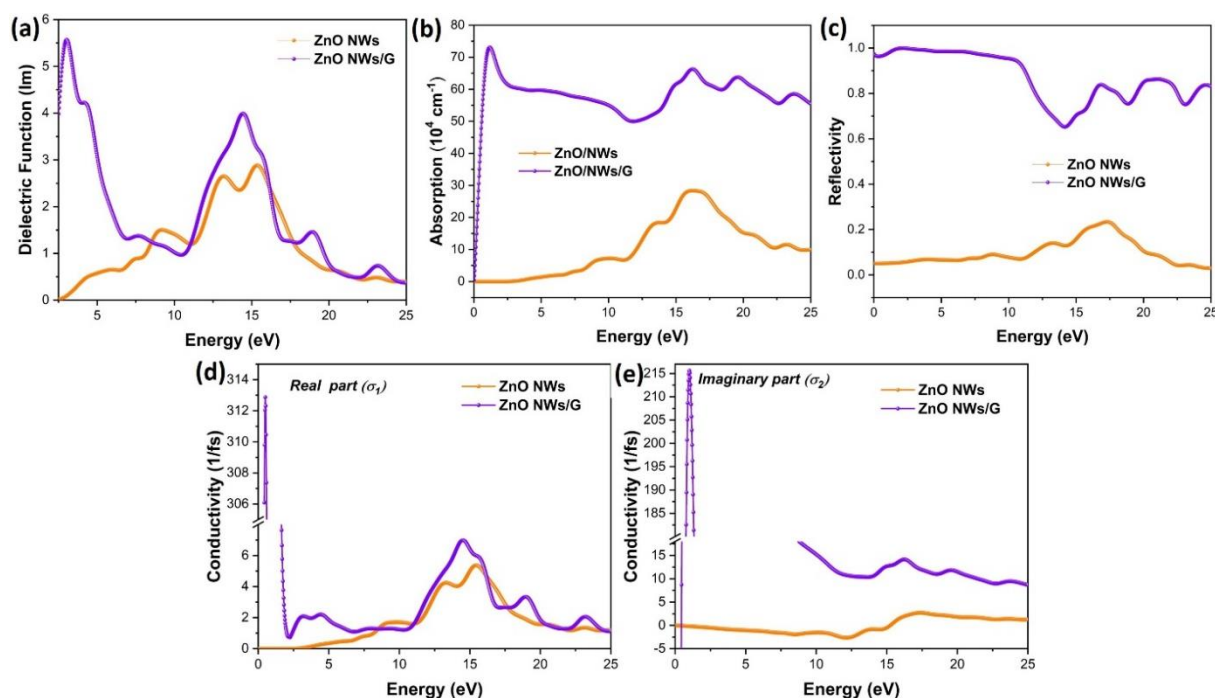


Fig. 3: Optical properties: (a) imaginary part of the dielectric function, (b) absorption, (c) reflectivity; the calculated (d) real part and (e) imaginary part of the complex optical conductivity of ZnO NWs and ZnO NWs/G nanohybrid. Reproduced from Ref. [5].

Further, using the DFT study, under GGA-PBE+ U and DFT-D2 methods, the optical properties of ZnO NWs/G, such as the complex dielectric function, reflectivity, absorption coefficient and optical conductivity were calculated (Fig. 3a–e). The adsorption energy shows that the structure of the ZnO top site on graphene layer is more stable. Further, it was found that ZnO NWs/G nanohybrids have an enhancement in optical properties and optical conductivity in the UV and visible light ranges compared to ZnO. We believe that this study [5] provides a solid foundation for understanding the potential of ZnO NWs/G nanohybrids in optoelectronic devices, particularly for sensor applications, and will inspire further research in this field.

References:

- [1] E.R. Ezeigwe, M.T. Tan, P.S. Khiew, C.W. Siong, *One-step green synthesis of graphene/ZnO nanocomposites for electrochemical capacitors*, *Ceram. Int.* 41(2015) 715–724.
- [2] J. Wu, M. Gong, *ZnO/graphene heterostructure nanohybrids for optoelectronics and sensors*, *J. Appl. Phys.* 130 (2021) 070905.
- [3] M.M. Tavakoli, R. Tavakoli, P. Yadav, J. Kong, *A graphene/ZnO electron transfer layer together with perovskite passivation enables highly efficient and stable perovskite solar cells*, *J. Mater. Chem. A*, 7 (2019) 679–686.
- [4] I. Boukhoubza, E. Matei, A. Jorio, M. Enculescu, I. Enculescu, *Electrochemical deposition of ZnO nanowires on CVD-graphene/copper substrates*, *Nanomaterials* 12 (2022) 2858.
- [5] I. Boukhoubza, M. Achehboune, I. Derkaoui, M.M. Apostol, M.A. Basyooni, M. Khenfouch, L. Nedelcu, I. Enculescu, E. Matei, *The interface structural, electronic and optical properties of ZnO nanowires/Graphene nanohybrid (ZnO NWs/G): Experimental and theoretical DFT investigations*, *J. Alloys Compd.* 976 (2024) 173109.

Structural and magneto-optical investigations of citrate sol-gel derived barium hexaferrite nanocrystalline powder

M. Secu¹, C.E. Secu¹, E. Matei¹, C. Negrila¹, V. Turchenko², S. Polosan¹

1) National Institute of Materials Physics, 077125, Măgurele, Romania

2) Joint Institute for Nuclear Research, 141980, Dubna, Russia

In this work [1], magneto-optical measurements enabled the identification of Fe^{2+} and Fe^{3+} in the R and S blocks of $\text{BaFe}_{12}\text{O}_{19}$ M-hexaferrite powder, which was obtained by sol-gel processing followed by thermal annealing at 900 °C for 3 hours. The ferromagnetic phase is evidenced by the spin-majority configuration (Fe^{3+}) due to their unpaired electrons between d-d orbitals, while the Fe^{2+} in the low spin possesses diamagnetic behaviour strongly dependent on the surrounded crystal field. Additionally, the irradiation with gamma rays changes the ratio between $\text{Fe}^{2+}/\text{Fe}^{3+}$, mainly on the surface of $\text{BaFe}_{12}\text{O}_{19}$ nanocrystals. These changes were confirmed by X-ray photoelectron spectroscopy (XPS) measurements, which showed that the concentration of Fe^{2+} increased from 69% to 82%, while the concentration of Fe^{3+} decreased from 31% to 18%. The thermoluminescent measurements revealed similar changes in the Fe^{3+} in Fe^{2+} conversion by electron capturing during irradiation, which is released as a red emission following recombination processes. These changes are attributed to the increase in Fe–O bonds along the c-axis, primarily resulting from the breaking of a part of these bonds.

The X-ray diffraction (XRD) analysis (Fig. 1) confirmed changes in the parameters of the $\text{BaFe}_{12}\text{O}_{19}$ hexagonal structure [1,2]. Furthermore, the XRD patterns of the sol-gel powder revealed the formation of the hexagonal structure of $\text{BaFe}_{12}\text{O}_{19}$ after thermal annealing at 900 °C, along with traces of Fe_2O_3 resulting from the raw powders during the synthesis process (Fig. 1).

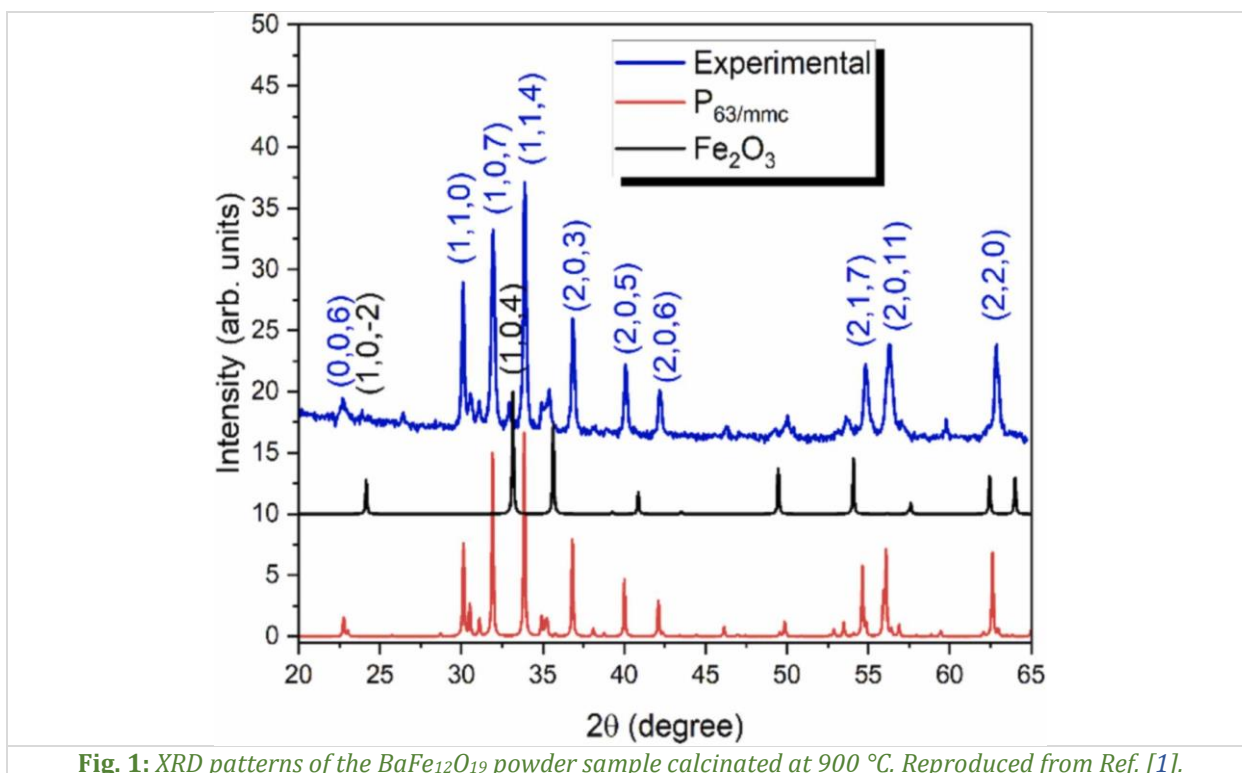


Fig. 1: XRD patterns of the $\text{BaFe}_{12}\text{O}_{19}$ powder sample calcinated at 900 °C. Reproduced from Ref. [1].

The high-resolution transmission electron microscopy (HR-TEM) allowed for the validation of the crystalline phase and provided detailed insights into the shape and distribution of the particles. The sample consisted of $\text{BaFe}_{12}\text{O}_{19}$ nanoparticles exhibiting both rod-like and irregular shapes. The irregularly shaped nanoparticles tend to have larger dimensions, typically below 100 nm, while the rod-shaped nanoparticles have a diameter of less than 50 nm (Fig. 2a). The phase was identified by indexing the selected area electron diffraction pattern (SAED). The planes corresponding to the $\text{BaFe}_{12}\text{O}_{19}$ (space

group $P6_3/mmc$) phase were identified, in agreement with XRD patterns [1,3]. Moreover, this has also been confirmed by indexing the FFT pattern corresponding to high-resolution images of the nanoparticles, where the crystalline planes were clearly visible [1,4]. In each case, the axis parallel to the electron beam has been identified, and the FFT pattern was compared to the SAED simulation performed on a crystal with the same orientation. The two patterns showed excellent agreement (Fig. 2b).

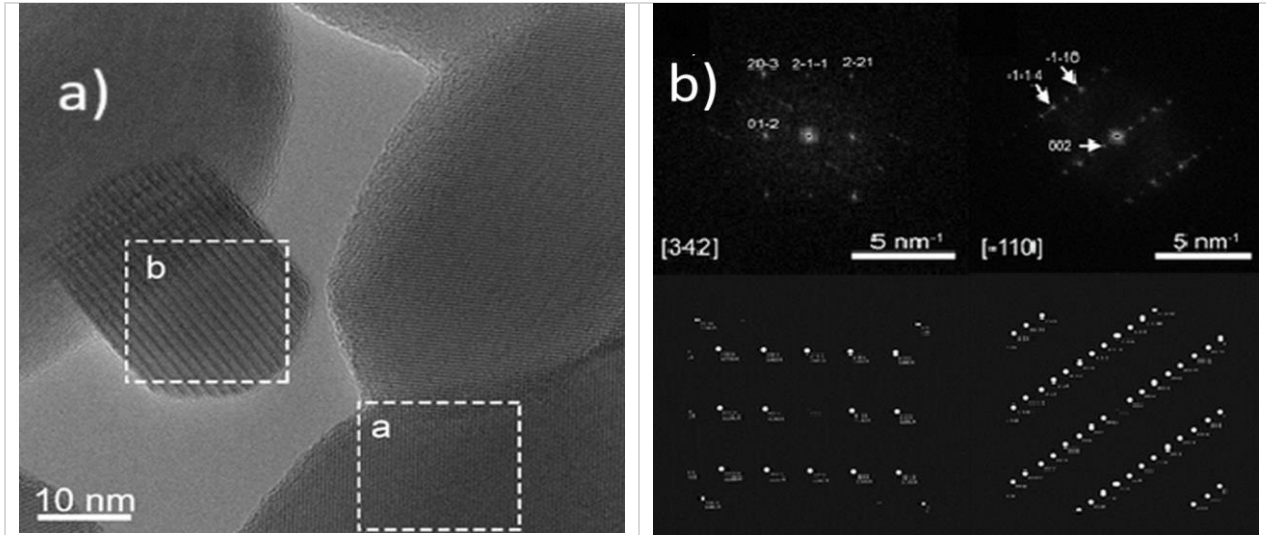


Fig. 2: (a) HRTEM image of the $BaFe_{12}O_{19}$ nanoparticles; (b) FFT transforms taken in the two regions indicated on the HR image. Reproduced from Ref. [1].

New features are revealed in the XPS spectra of the Fe 2p and Fe 3p regions after gamma-ray irradiation (Fig. 3a,b). The Fe 3p binding energy is reduced by more than 1 eV, accompanied by a considerable decrease in peak width. A minor shift is also observed for the Fe 2p lines (Fig. 3a). The irradiation caused the reduction of Fe^{3+} ions to Fe^{2+} ions, and both the energy shift and the decrease in peak broadening are apparent, resulting from the change in the Fe^{3+} to Fe^{2+} ion ratio.

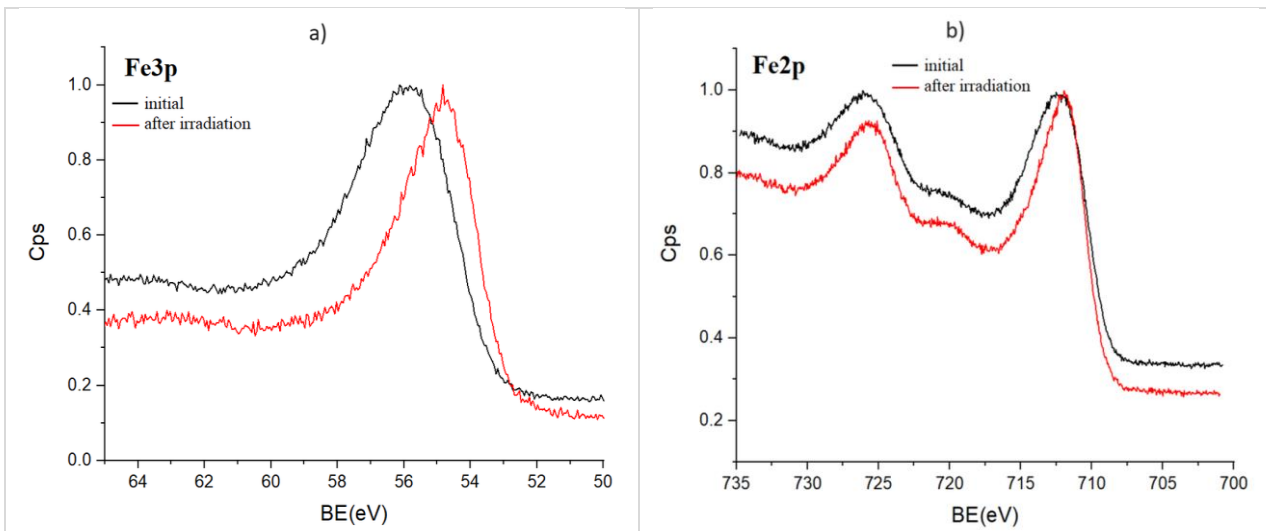
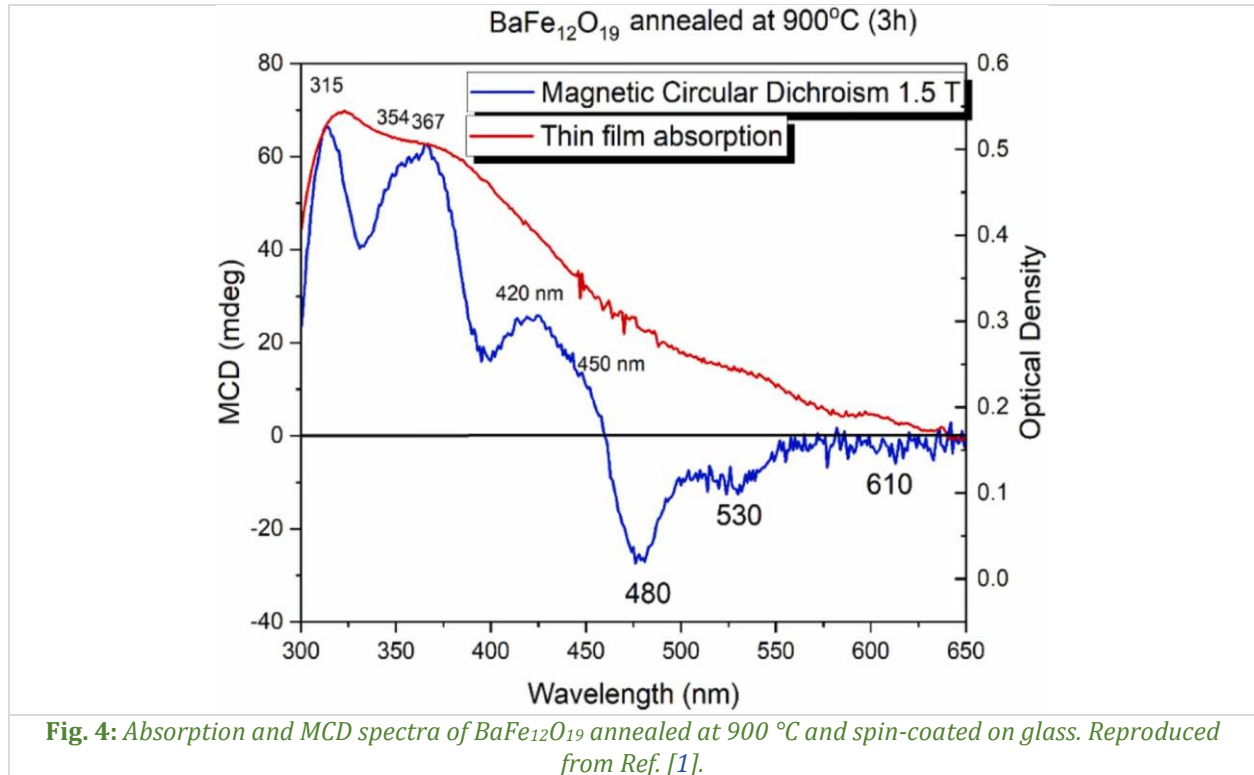


Fig. 3: The XPS spectra of (a) Fe 2p and (b) Fe 3p core electron levels recorded for the $BaFe_{12}O_{19}$ powder sample before and after gamma-ray irradiation. Adapted from Ref. [1].

The magnetic circular dichroism (MCD) spectra confirmed the presence of ferromagnetic phases. The spin-majority configuration (Fe^{3+}) is given by the paramagnetic transition from 530 nm (2.34 eV) seconded by the ligand-to-metal charge transfer (LMCT) between the oxygen atoms p-orbital to Fe in an octahedral position, centred at 480 nm (Fig. 4). After the gamma-irradiation of the $BaFe_{12}O_{19}$ powder,

thermoluminescence measurements confirmed the conversion of Fe^{3+} to Fe^{2+} by electron capture, releasing a red photon during the thermally activated recombination processes. This reduction process leads to the breaking of some $\text{Fe}^{3+}(\text{i})\text{--O}^{2-}\text{--Fe}^{3+}(\text{j})$ bonds (where $\text{j}=1, 2, 3, 4, 5$) and the creation of hole centres (*e.g.*, O^{2-} near the Fe^{3+} ion), which, in turn, weakens the superexchange interactions responsible for the magnetic properties of $\text{BaFe}_{12}\text{O}_{19}$.



References:

- [1] M. Secu, C.E. Secu, E. Matei, C. Negrila, V. Turchenko, C. Radu, S. Polosan, *Structural and magneto-optical investigations of citrate sol-gel derived barium hexaferrite nanocrystalline powder*, J. Alloys Compd. 983 (2024) 173897.
- [2] V. Turchenko, V.G. Kostishyn, S. Trukhanov, F. Damay, F. Porcher, M. Balasoiu, N. Lupu, B. Bozzo, I. Fina, A. Trukhanov, J. Waliszewski, K. Recko, S. Polosan, *Crystal and magnetic structures, magnetic and ferroelectric properties of strontium ferrite partially substituted with In ions*, J. Alloys Compd. 821 (2020) 153412.
- [3] V. Turchenko, V.G. Kostishin, S. Trukhanov, F. Damay, M. Balasoiu, B. Bozzo, I. Fina, V.V. Burkhovetsky, S. Polosan, M.V. Zdorovetsj, A.L. Kozlovskiy, K.A. Astapovich, A. Trukhanov, *Structural features, magnetic and ferroelectric properties of $\text{SrFe}_{10.8}\text{In}_{1.2}\text{O}_{19}$ compound*, Mater. Res. Bull. 138 (2021) 111236.
- [4] A.V. Trukhanova, V.A. Turchenkoc, V.G. Kostishin, F. Damay, F. Porcher, N. Lupu, B. Bozzo, I. Fina, S. Polosan, M.V. Silibin, M.M. Salemm, D.I. Tishkevich, S.V. Trukhanov, *The origin of the dual ferroic properties in quasi-centrosymmetrical $\text{SrFe}_{12-x}\text{In}_x\text{O}_{19}$ hexaferrites*, J. Alloys Compd. 886 (2021) 161249.

Electronic synapses based on an epitaxial $\text{SrTiO}_{3-\delta}/\text{Hf}_{0.5}\text{Zr}_{0.5}\text{O}_2$ ferroelectric memristor integrated on silicon

A. Dimoulas^{1,2}, N. Siannas², C. Zacharaki², P. Tsipas^{1,2}, D.J. Kim², W. Hamouda², C. Istrate¹, L. Pintilie¹, M. Schmidbauer², C. Dubourdieu²

1) National Institute of Materials Physics, 077125, Măgurele, Romania

2) Institute of Nanoscience and Nanotechnology, National Centre for Scientific Research DEMOKRITOS, 15341, Athens, Attiki, Greece

A long-term goal of the research community is to develop energy-efficient systems using in-memory or brain-inspired neuromorphic computing. Non-volatile memories (NVMs), such as OxRAM, PCM, and CBRAM, are promising candidates for this purpose. Ferroelectric NVMs, being voltage-driven, offer the potential for ultra-low power computing platforms. Among different types of ferroelectric memories, the ferroelectric tunnel junction (FTJ) is attractive due to its simple structure and non-destructive readout. FTJs function as voltage-driven memristors, with conductance states modulated by the ferroelectric polarization. However, challenges exist, such as the instability of ferroelectricity in thin HZO films and high programming voltages. This work [1] proposes a novel ferroelectric field-effect diode, with a thin HZO layer, that promises low voltage operation, low energy consumption, and improved reliability. The device uses a doped oxide semiconductor as the bottom electrode, offering advantages over resistive metallic oxides, and demonstrates synaptic behaviours with low energy consumption, comparable to biological synapses.

A memristor based on a metal/ferroelectric/semiconductor configuration using a thin epitaxial HZO layer (~5 nm) is demonstrated, with synaptic plasticity, including symmetric potentiation/depression, pair pulse facilitation, and spike-timing dependent plasticity across several time scales (ns to ms) [1]. The key element of the design is an ultrathin n-type $\text{SrTiO}_{3-\delta}$ semiconductor (10 – 20 nm), grown epitaxially on Si(001), which not only serves as an electrode but also enables epitaxy for HZO. This structure enhances the device's functionality by facilitating non-volatile conductance modulation *via* the ferroelectric field effect. The motion of oxygen vacancies in $\text{SrTiO}_{3-\delta}$ improves the dynamic range of the synapses during potentiation and depression over 50 μs and ensures retention. These synapses operate with low voltage (≤ 2 V) and ultra-low energy consumption (~8 fJ per programming event), similar to biological synapses.

The HZO films were grown on epitaxial $\text{SrTiO}_{3-\delta}/\text{Si}$ substrates using molecular beam epitaxy (MBE), with $\text{SrTiO}_{3-\delta}$ intentionally oxygen-deficient to function as an n-type semiconductor bottom electrode. High-resolution transmission electron microscopy (HRTEM) verified the orthorhombic ferroelectric phase of HZO and its domain-matching epitaxy with $\text{SrTiO}_{3-\delta}$. Fast Fourier transform (FFT) analysis highlighted the near-coincidence lattice matching, reducing the effective lattice mismatch and promoting high-quality epitaxial growth. These findings support the structural integrity and functional properties of the fabricated devices. (Fig. 1).

The P-V and I-V characteristics of epitaxial devices ($50 \times 50 \mu\text{m}^2$) at 1 kHz, in both pristine and wake-up states, are shown in Fig. 2a,b. A remnant polarization of ~14 $\mu\text{C}/\text{cm}^2$ is achieved, with a low coercive voltage (~1 V), enabling programming below 2 V. Fig. 2c presents I-V characteristics in polarization upward and downward states, with an $I_{\text{ON}}/I_{\text{OFF}}$ ratio of 3 at $V_{\text{read}} = +0.4$ V. Due to the relatively thick HZO barrier (~5 nm, ~2 eV), direct tunneling currents remain low (~0.1 – 1 pA/ μm^2). Resistance memory loops (Fig. 2d) were recorded using 1 ms pulses of varying amplitudes, with resistance extracted as $R = V_{\text{read}}/I$. The resistance ratio is ~200%, with over 16 stable intermediate states, corresponding to 4-bit memory. Switching occurs near 1 V, in line with the coercive voltage, confirming a ferroelectric-driven mechanism (Fig. 2).

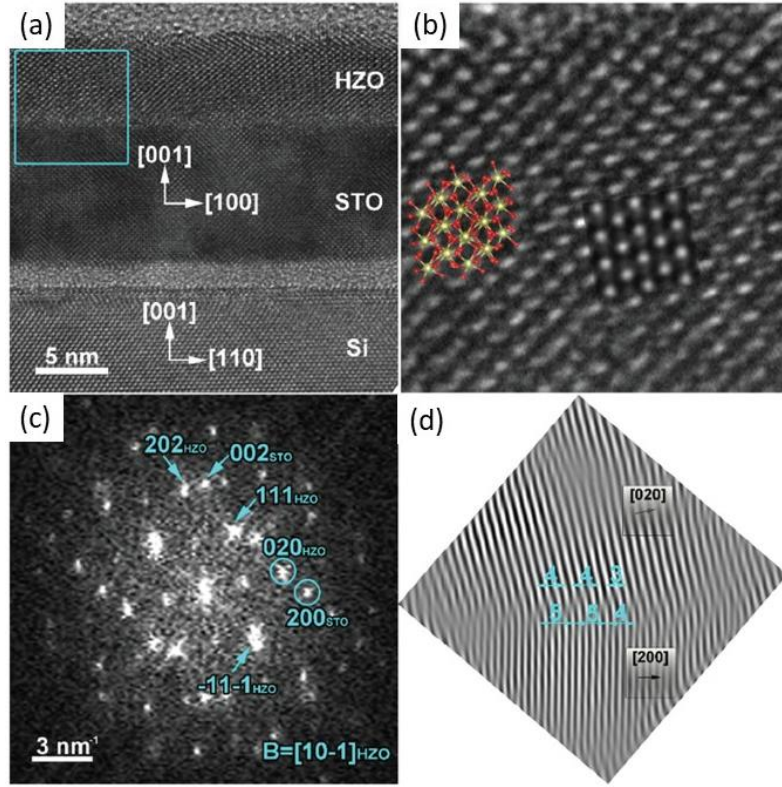


Fig. 1: (a) HRTEM cross-section image of the stack; (b) magnified view of an HZO crystallite with the atomic structural model of the orthorhombic phase in the $[101]$ zone axis superimposed, along with the simulated HRTEM image at a defocus of -30 nm and a thickness of 40 nm; (c) Fast Fourier Transform (FFT) pattern from the area marked by the blue square in (a), containing both HZO and STO thin films, along with an additional FFT pattern (top left) from an HZO crystallite viewed along the $[101]$ zone axis; (d) Fourier-filtered micrograph using (020) HZO and (200) STO reflections indexed in the FFT image in (c). Reproduced from Ref. [1].

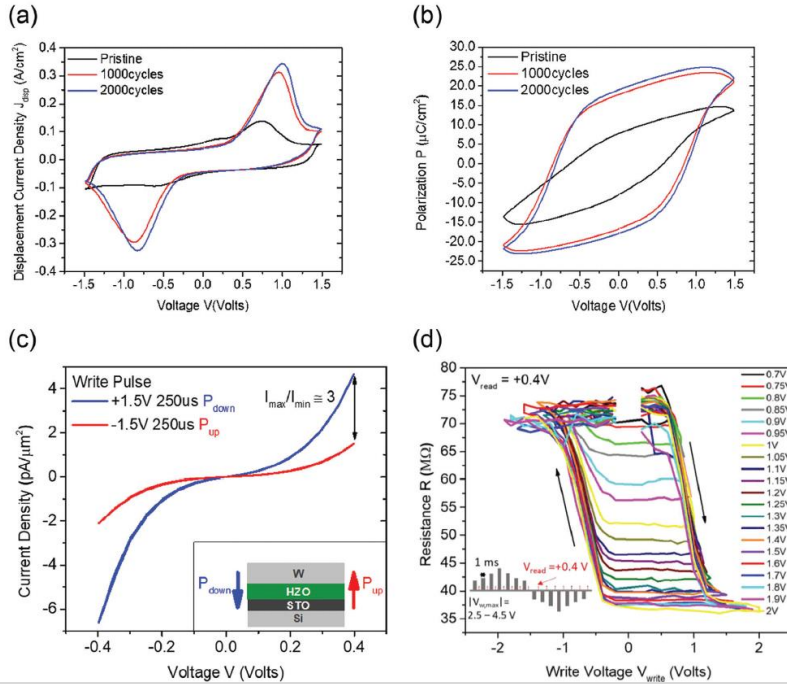
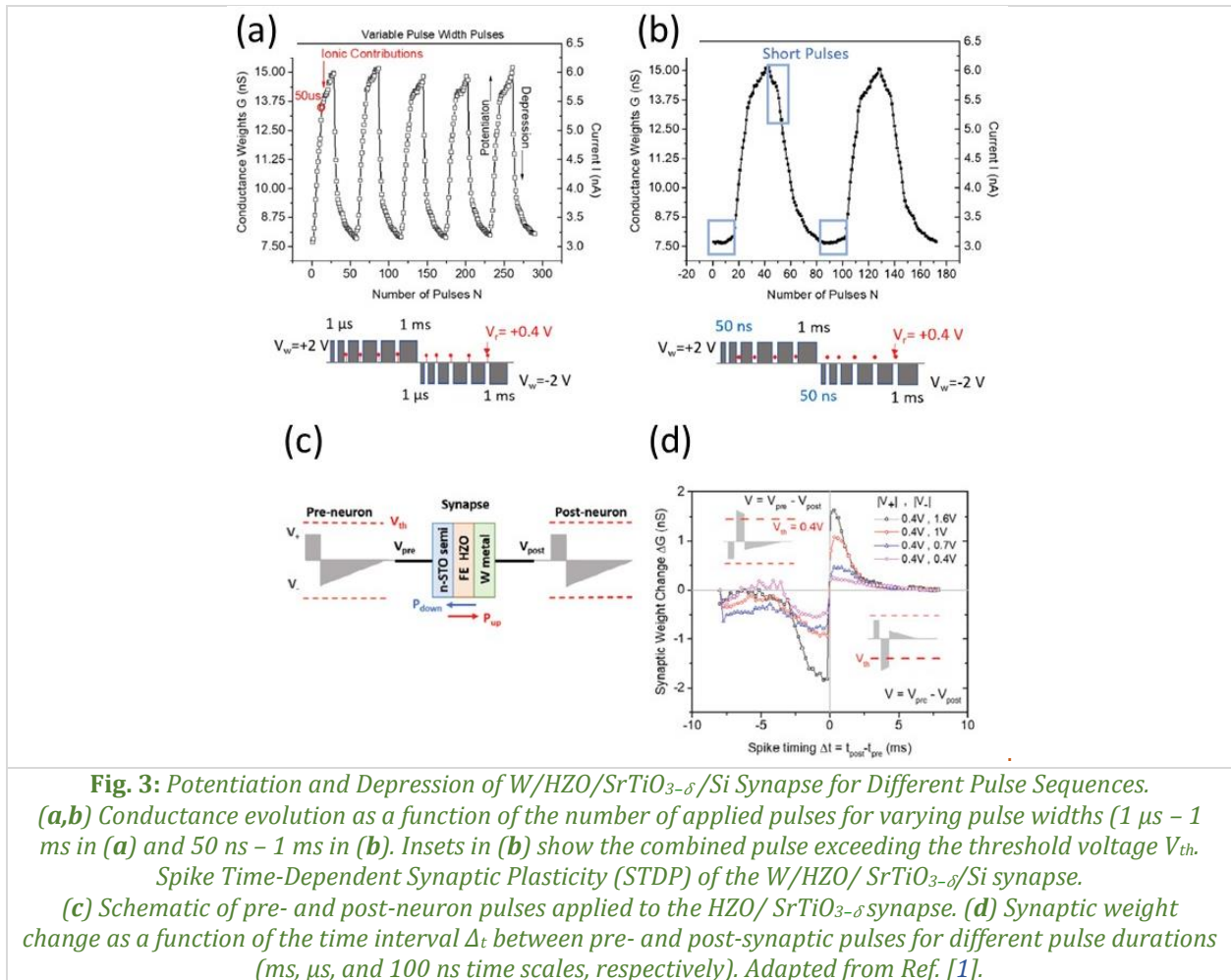


Fig. 2: Ferroelectric properties and resistance states of the W/HZO/SrTiO_{3-δ}/Si memristive device: (a,b) Displacement current and polarization versus applied voltage at 1 kHz. (c) I-V characteristics for two polarization states of the ferroelectric film. (d) Resistance variation under pulses with amplitudes ranging from 0.7 to 2.0 V (inset), demonstrating multiple intermediate states. V_{read} ($+0.4$ V) is the applied voltage for resistance measurement. Reproduced from Ref. [1].

Fig. 3a,b presents the evolution of conductance as a function of the number of applied pulses for different programming schemes. When pulses with the same amplitude (+2 and -2 V) but increasing width are applied, a large number of intermediate states are accessible during potentiation, while depression remains more limited, resulting in asymmetry. Extending the pulse width range to 50 ns improves symmetry (Fig. 3b), highlighting the importance of pulse sequence optimization.

At short timescales (up to 50 μ s), potentiation is influenced by frequency dispersion related to the ferroelectric switching dynamics. Beyond 50 μ s, conductance increase slows down, likely due to ionic effects in the HZO/SrTiO_{3- δ} system. Using identical pulses instead of variable-width pulses is preferable for circuit design but has rarely been demonstrated in HZO-based devices. Here, it is shown that W/HZO/SrTiO_{3- δ} /Si synapses can achieve multiple stable states with identical pulses and near-ideal characteristics (Fig. 3). The HZO/SrTiO_{3- δ} ferroelectric memristors exhibit Spike Timing Dependent Plasticity (STDP), where synaptic strengthening or weakening depends on the timing between pre- and post-neuron spikes. When the time separation (Δt) between pulses is small, their overlap leads to polarization switching, causing changes in synaptic weights (Fig. 3c,d). This effect is observed across different pulse widths, demonstrating that STDP can be observed not only at biological timescales (\sim ms) but also at much shorter timescales (\approx 10 – 100 ns) [1].



Reference:

- [1] N. Siannas, C. Zacharaki, P. Tsipias, D.J. Kim, W. Hamouda, C. Istrate, L. Pintilie, M. Schmidbauer, C. Dubourdieu, A. Dimoulas, *Electronic synapses enabled by an epitaxial SrTiO_{3- δ} /Hf_{0.5}Zr_{0.5}O₂ ferroelectric field-effect memristor integrated on silicon*, Adv. Funct. Mater. 34 (2024) 2311767.

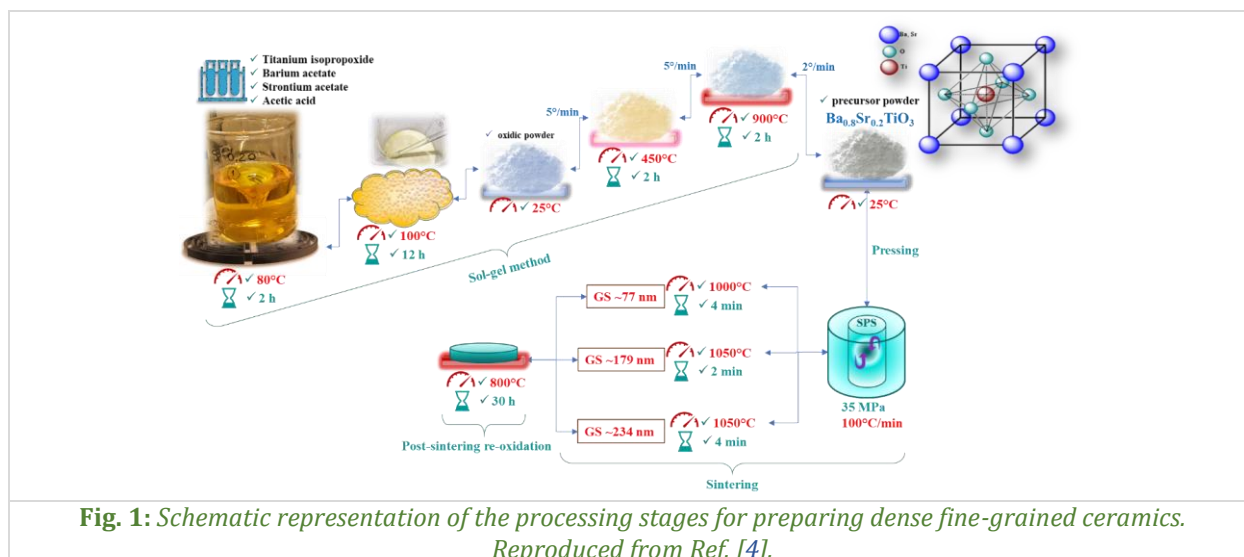
Downscaling grain size toward the nanometre range – A key-factor for tuning the crystalline structure, phase transitions, dielectric and ferroelectric behaviour in $\text{Ba}_{0.8}\text{Sr}_{0.2}\text{TiO}_3$ ceramics

R.E. Pătru¹, C.A. Stanciu^{2,3}, V.A. Surdu², E.M. Soare^{2,4}, R.D. Trușcă², B.S. Vasile², A.I. Nicoară², L. Trupină¹, I. Pasuk¹, M. Botea¹, N. Horchidan⁵, L. Mitoșeriu⁵, L. Pintilie¹, I. Pintilie¹, A.C. Ianculescu²

- 1) National Institute of Materials Physics, 077125, Măgurele, Romania
- 2) Department Science & Engineering of Oxide Materials and Nanomaterials, Faculty of Chemical Engineering and Biotechnologies, National University of Science and Technology Politehnica Bucharest, 011061, Bucharest, Romania
- 3) National Institute for Lasers, Plasma and Radiation Physics, 077125, Măgurele, Romania
- 4) Institute of Physical Chemistry “Ilie Murgulescu”, Romanian Academy, 060021, Bucharest, Romania
- 5) Department of Exact & Natural Sciences, “Alexandru Ioan Cuza” University, 700506, Iași, Romania

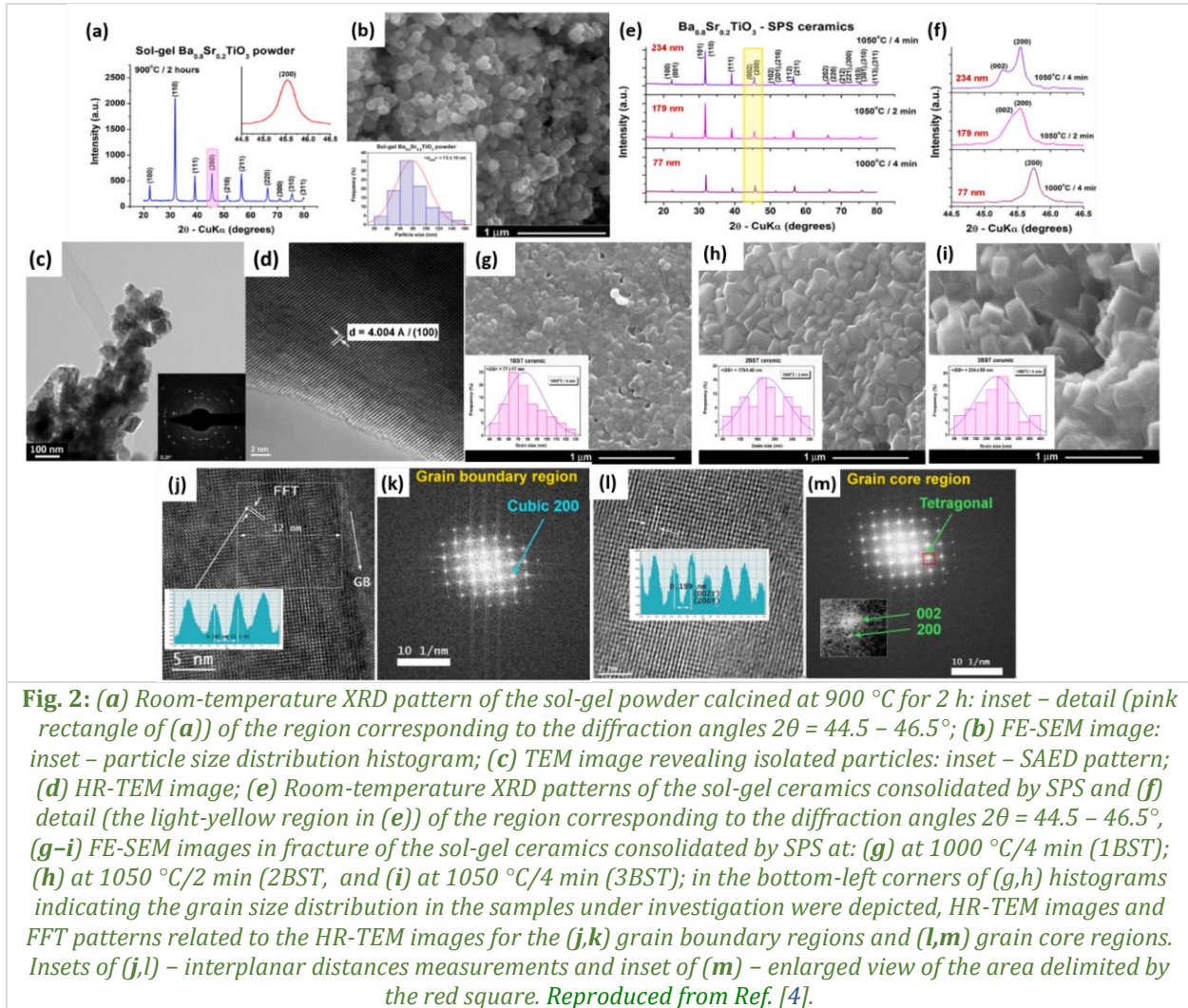
To address scale and temperature-dependent properties, ferroelectric BaTiO_3 (BT) and BT-based solid solutions have been investigated [1–3]. However, the specific effects of grain size on $\text{Ba}_{0.8}\text{Sr}_{0.2}\text{TiO}_3$ where strontium substitution shifts the ferroelectric–paraelectric transition to lower temperatures, remain unclear. Conflicting reports exist on whether the Curie temperature increases or decreases with decreasing grain size. This uncertainty highlights the need for a detailed investigation into how finely tuned fabrication processes and grain size manipulation can optimize ferroelectric and dielectric properties of these promising materials.

In this study [4], fine-grained $\text{Ba}_{0.8}\text{Sr}_{0.2}\text{TiO}_3$ ceramics were synthesized starting from a high-quality nanopowder produced by an acetate sol-gel process. The preparation method is schematically illustrated in Fig. 1. Three different sintering regimes were employed: the first sample (1BST) was sintered at 1000 °C for 4 minutes, the second (2BST) at 1050 °C for 2 minutes, and the third (3BST) at 1050 °C for 4 minutes.



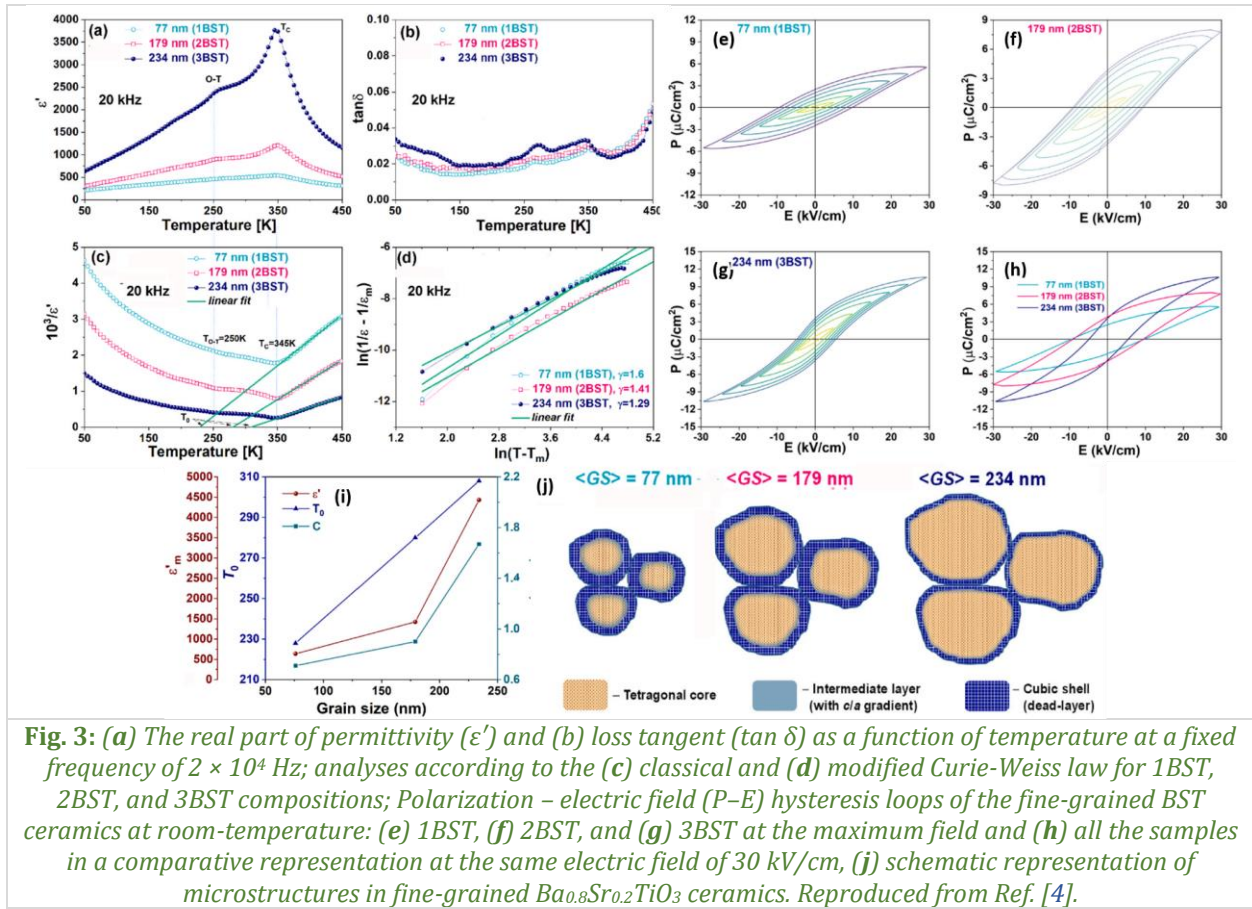
X-ray diffraction (XRD) analysis confirmed that the ceramics are single-phase BST. However, detailed Rietveld refinements indicated that a diphasic model – incorporating both cubic and tetragonal modifications – best fitted the experimental data. As the sintering temperature and time increased, the grain size grew, and the proportion of the tetragonal phase increased from 67.3% in 1BST to 89.9% in

3BST, accompanied by an enhancement in tetragonality (c/a ratio). Field-emission scanning electron microscopy (FE-SEM) revealed that 1BST, sintered at 1000 °C for 4 minutes, exhibited a dense, uniform microstructure with nearly spherical grains averaging 77 nm. In contrast, the 2BST and 3BST samples, sintered at 1050 °C for longer durations, yielded larger, well-faceted grains with average sizes of 179 nm and 234 nm, respectively. All maintained unimodal grain size distributions. High-resolution transmission electron microscopy (HR-TEM) further demonstrated that individual grains are structurally heterogeneous, showing pseudo-cubic “dead” layers at the grain boundaries and more relaxed tetragonal cores – a finding that supports the “brick-wall” model. This composite-like grain structure is believed to influence the observed scaling of dielectric properties with grain size in these ferroelectric ceramics (Fig. 2).



The dielectric properties of the dense fine-grained $\text{Ba}_{0.8}\text{Sr}_{0.2}\text{TiO}_3$ ceramics were investigated over a wide frequency range of $10^2 - 10^6$ Hz (Fig. 3). The significant grain size reduction was found to affect the permittivity and the nature of the phase transitions. The Curie temperature of 345 K remains constant across all samples. By systematically reducing the grain size, the ferroelectric–paraelectric (T–C) transition becomes broader, while the lower-temperature orthorhombic – tetragonal and rhombohedral–orthorhombic transformations (O–T and R–O) are flattened and can even vanish in ultrafine grains. Tetragonal and cubic phase coexistence is achieved in the proximity of room-temperature. Although the maximum permittivity decreases in the ultrafine ceramic and the Maxwell–Wagner relaxation becomes more evident at high temperatures and low frequencies, the dielectric losses remain low (below 5% for 1BST). Analysis using modified Curie–Weiss laws reveals that, as the grain size grows, both the Curie–Weiss temperature and the Curie constant increase, whereas the diffuseness of the transition diminishes. These findings are consistent with a composite-like structural

model, where non-ferroelectric (cubic) boundary regions grow in relative volume as the grain size shrinks, diluting the overall ferroelectric response.



A “brick-wall” model with cubic grain boundary regions and tetragonal grain cores is proposed. When the grain size decreases into the nanometre range, the increasing amount of cubic modification causes an increasing trend in the volume of the unit cell related to this phase. Unlike undoped BaTiO_3 , the Curie temperature (T_C) in $\text{Ba}_{0.8}\text{Sr}_{0.2}\text{TiO}_3$ remains unaffected by grain size within the 77 – 234 nm range. This is a result of competing factors – internal stresses that tend to lower T_C vs. the larger unit cell volume of the cubic boundary phase that tends to increase it – leading to a net balance and a stable T_C . All fine-grained BST ceramics exhibit switchable spontaneous polarization. As the grain size increases, the maximum polarization rises, while the coercive field decreases, reflecting enhanced tetragonality in the larger-grained samples.

References:

- [1] V. Buscaglia, C.A. Randall, *Size and scaling effects in barium titanate. An overview*, J. Eur. Ceram. Soc. 40 (2020) 3744–3758.
- [2] V.A. Lukacs, M. Airimioaei, L. Padurariu, L.P. Curecheriu, C.E. Ciomaga, A. Bencan, G. Drazic, M. Avakian, J.L. Jones, G. Stoian, M. Deluca, R. Brunner, A. Rotaru, L. Mitoseriu, *Phase coexistence and grain size effects on the functional properties of BaTiO_3 ceramics*, J. Eur. Ceram. Soc. 42 (2022) 2230–2247,
- [3] W. Cai, C. Fu, J. Gao, H. Chen, *Effects of grain size on domain structure and ferroelectric properties of barium zirconate titanate ceramics*, J. Alloys Compd. 480 (2009) 870–873.
- [4] R.E. Pătru, C.A. Stanciu, V.A. Surdu, E.M. Soare, R.D. Truşcă, B.S. Vasile, A.I. Nicoară, L. Trupină, I. Pasuk, M. Botea, N. Horchidan, L. Mitoseriu, L. Pintilie, I. Pintilie, A.C. Ianculescu, *Downscaling grain size toward the nanometre range – A key-factor for tuning the crystalline structure, phase transitions, dielectric and ferroelectric behaviour in $\text{Ba}_{0.8}\text{Sr}_{0.2}\text{TiO}_3$ ceramics*, Prog. Solid State Chem. 74 (2024) 100457.

2D image potential states of 2D materials

B. Borca¹, H.J.W. Zandvliet²

1) *National Institute of Materials Physics, 077125, Măgurele, Romania*

2) *Physics of Interfaces and Nanomaterials, MESA+ Institute, University of Twente, 7500 AE, Enschede, Netherlands*

Image Potential States (IPS) are quantized two-dimensional (2D) unoccupied electronic states that are formed in front of the surface of a material due to the attractive electrostatic force between an electron and its induced image charge within the material located symmetrically with respect to the surface. The quantized energy levels of IPS follow a Rydberg-like series and the binding energy decreases for higher-order states as the electron is farther from the surface. The IPS have a free-electron like dispersion parallel to the surface and are described by:

$$E_n = \frac{R_H}{16(n + a)^2} + \frac{\hbar^2}{2m^*} k_{\parallel}^2$$

where E_n is the energy of the n -th level of the Rydberg-like series, R_H is the Rydberg constant, n the quantum number, a ($a \in [0, 0.5]$) is the quantum defect that corrects the penetration of the wavefunction into the bulk, m^* is the effective mass and k_{\parallel} the momentum component parallel to the surface. Experimentally, IPS are mainly investigated by Inverse Photoemission Spectroscopy (IPES), Two-Photon Photoemission (2PPE) or multi-Photon Photoemission (mPPE) and scanning tunnelling microscopy and spectroscopy (STM/STS) techniques. Time- and angle-resolved (TR and AR) photoemission methods allow the detection of the binding energy, lifetime, effective mass, and the dispersion of the unoccupied states, discriminating between surface states, interface states or IPS.

IPS states are important in understanding surface physics, charge dynamics, and phenomena such as field emission, electron scattering, charge transfer, charge injection, and work function.

In 2D materials, IPS exhibit unique characteristics influenced by the reduced dimensionality and electronic properties of these systems, offering important information for potential applications especially for nanoscale electronic and optoelectronic devices.

The work published in Ref. [1] based on a collaboration with Professor Harold J.W. Zandvliet, review recent developments in the detection and analysis of IPS in single- and multilayered 2D materials, heterostructures and nanostructures thereof (Fig. 1), addressing several issues that can have an effect on IPS, including the preparation method, quality of the material, defects, interfacial interactions, and interactions with the substrate.

The review highlighted the utilization of IPS spectra to characterize:

- i. single-layer 2D materials (such as graphene, h-BN, Xenes, MXenes, chalcogenides) deposited or transferred on various substrates;
- ii. single-layer 2D materials with various materials (such as NaCl, Se, S, O, Au, Cu, Co) intercalated at the interface with the substrate;
- iii. heterostructures of hybrid 2D materials;
- iv. heterostructures of 2D self-assembled monolayers of organic molecules and 2D materials;
- v. nanostructures of 2D materials, such as nanoislands and nanoribbons.

The article [1] summarizes IPS studies that provide valuable information on the coupling strength between the 2D layer and the substrate; the appearance of new interfacial electronic states; the decoupling from the substrate by intercalation or insulating layers; the effects of functionalization, doping, and defects; the lateral modulation of electronic properties; and the size, and lateral confinement effects of quantum dots or nanoislands.

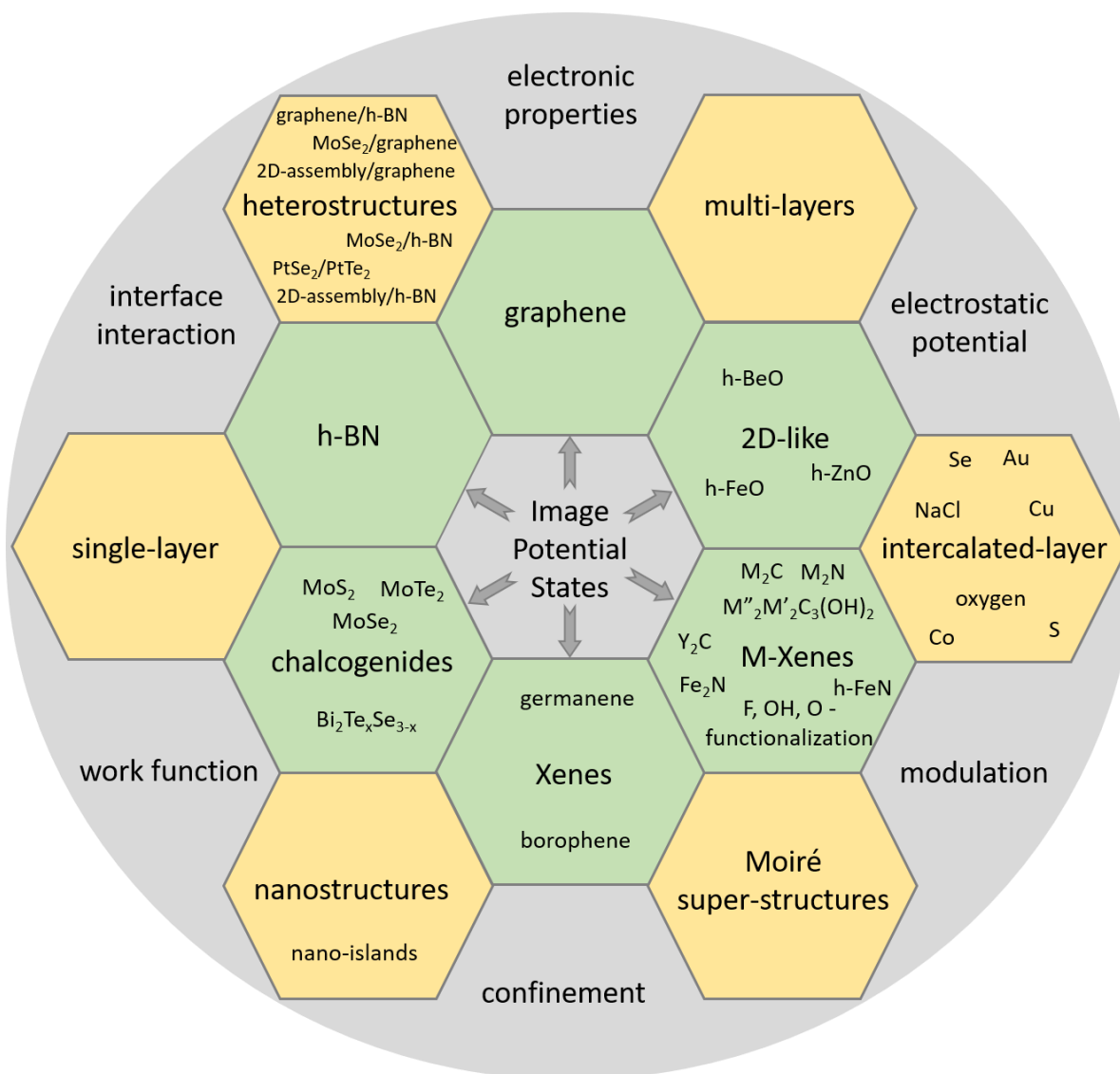


Fig. 1: Schematic representation of the reviewed 2D systems. Figure taken from Ref. [1] under the Creative Commons license CC BY-NC 4.0.

A free-standing 2D material is expected to exhibit, owing to its two surfaces, mirror-symmetry-induced splitting of the IPS to two IPS series for each side of the material. When a single layer of a 2D material is deposited on a substrate, the mirror symmetry is broken and usually only a single series of IPS peaks is observed. These IPS, which are trapped in a potential well in front of the surface of the 2D material, are modified by interfacial interactions. Therefore, IPS typically serve as a testimony of the interaction with the substrate. A lattice parameter mismatch of the 2D material with the substrate, frequently leads to a moiré superstructure. These moiré structures can result in a lateral modulation of the interfacial interaction that leads to a modulation of the electronic states, IPS, and work function. These electronically corrugated 2D materials can serve as templates for heterostructures with complex properties. Furthermore, nanoislands and quantum dots of 2D materials often lead to laterally confined IPS and quantum dots. In Ref. [1] are included the above-mentioned issues for the materials schematized in Fig. 1.

Reference:

- [1] B. Borca, H.J.W. Zandvliet, *Image potential states of 2D materials*, Appl. Mater. Today 39 (2024) 102304.

Magnetic behaviours of exchange-biased Fe(FM)–FeO(AFM)–ZnO nanocomposites of different iron concentrations prepared under non-identical conditions with annealing in a reducing atmosphere

V. Mihalache

National Institute of Materials Physics, 077125, Măgurele, Romania

The exchange bias (EB) is an important effect used in technological applications such as spin-based electronic devices including magnetic sensors (*e.g.*, spin valves) and magnetic media for (ultra)high-density data storage (*e.g.*, read-heads). Enhancement of the coercivity (of fine particles) to improve the performance of materials for permanent magnets is another application of the EB effect.

Depending on the preparation technique, the composites or the mixtures of (FM) (or ferrimagnetic, FIM) and antiferromagnetic (AFM) nanoparticles can be classified into three representative groups: mechanical milling, reduction (or overoxidation), and methods such as drying (colloidal) suspensions of the particles. (1) The main challenges of composites or mixtures produced using these techniques are the minimal or absent exchange bias and the tendency of the particles to coarsen. The solution for EB systems similar to Fe-FeO would be to use the method of partial reduction (by annealing in a reducing atmosphere) of the FeO to Fe nanoparticles embedded in the nonmagnetic/nonreactive (oxide) environment, which ensures (i) disordering at FM/AFM interfaces with stronger exchange coupling and (ii) prevention of magnetic nanoparticle agglomeration and excessive coarsening. (2) Another poorly addressed aspect is the influence of different processing parameters on the EB effect or the quality of exchange coupling between the AFM and FM spins at the FM/AFM interfaces. (3) There are few systematic investigations of the FM component (apart from having its spins pinned by AFM in an EB system) in terms of its coexistence in different magnetic regimes (*e.g.*, superparamagnetic, blocked or multidomain) and relatively broad particle size and coercivity (H_c) distribution. (4) Another unaddressed aspect refers to the origin of H_c suppression in an EB system at room-temperature (RT) (or above T_n) after cycling the field-cooled (FC) hysteresis loop. (5) There are no (systematic) studies on the Fe-FeO-ZnO EB systems.

All the issues mentioned above were addressed in our studies [1,2]. The complex systems of randomly oriented EB interfaces, *i.e.*, the composites of nanosized AFM FeO, FM α -Fe, and ZnO, were prepared under non-identical conditions involving the reduction of sol-gel-derived precursors of various Zn:Fe atomic ratios (0.97:0.03, 0.8:0.2, and 0.4:0.6) in a hydrogen-containing atmosphere (Table 1). We investigated the magnetic behaviour of exchange-biased Fe(FM)-FeO(AFM)-ZnO nanocomposites and explored their relationship with the processing conditions, particularly in terms of the system stability, including FM/AFM interfaces. To interpret the EB effect in these complex systems, we applied a spin-glass (SG)-like model.

The main findings of the study [1] are summarized below:

- a. ZnO can serve as a suitable nonmagnetic/nonreactive environment in EB systems, preventing the agglomeration and coarsening of Fe (and FeO) particles at the preparation stage.
- b. A superposition of superparamagnetic and ferromagnetic behaviours in the was observed in the M vs. H (Fig. 1a–d) and M vs. T (Fig. 1e) curves for all samples. This was assigned to the coexistence of low-coercivity multidomain and superparamagnetic Fe particles alongside high-coercivity Fe in the blocked state (Fig. 1f).
- c. All samples exhibited the EB effect (Fig. 2a–d), ascribed to the exchange coupling between the AFM and FM spins at the FeO/Fe interfaces. The EB field and coercivity enhancement reached values as high as 243 Oe and 223 Oe, respectively (Fig. 2e).
- d. A larger loop shift and coercivity enhancement were observed in samples prepared under conditions of higher non-equilibrium. These promote the formation of unstable/disordered FeO and Fe phases, resulting in FeO/Fe interfaces with stronger exchange coupling. This trend can be seen by comparing Figs. 2a and 2d with Figs. 2b and 2c.
- e. The training effect (Fig. 3a,b) obeyed a SG-like model.

$$H_{EX}^n = H_{EX}^\infty + A_f e^{-\frac{n}{P_f}} + A_i e^{-\frac{n}{P_i}} \quad (1)$$

consisting of the relaxation of two components of disordered spins at the Fe/FeO interfaces towards their equilibrium configuration: the uncompensated (1) low anisotropy interfacial (rotatable) AFM spins and (2) frozen AFM spins. Component (1) explains the observed H_c improvement, whereas (2) the EB shift, vertical shift, and open loop along the cooling direction field.

- f. The reduction of H_c (and wasp-wasting of the hysteresis loop), observed in the 5 – 300 K range after the FC measurement procedure (Fig. 3c,d), was tentatively assigned to the irreversible reconfiguration of a metastable FM state consisting in an increase of the fraction of low-coercivity relative to high-coercivity Fe nanoparticles.

Table 1: The calcination and annealing conditions. The degree of stability of the systems after annealing at 500 °C.

The as-prepared powders derived from Zn-Fe-carboxylate precursors		The samples studied in this work, derived from the as-prepared powders		
Sample	Calcination conditions (Final product: $\text{ZnFe}_2\text{O}_4 + \text{ZnO}$)	Sample	Annealing conditions. (Final product: $\text{Fe} + \text{FeO} + \text{ZnO}$)	The degree of stability (equilibrium) inferred from the processing conditions
ZF3-AP1	Heated with a 20 °C/min rate to 400 °C and calcined for 20 min	ZF3-500-15	Annealed at 500 °C for 15 min in Ar-5 %H ₂ (kept at 405 °C in the air for 60 min during heating)	3
ZF3-AP2	Heated with a rate of 1.5 °C/min to 400 °C, calcined for 20 min, then heat treated at 370 °C in the air for 30 min	ZF3-500-120	Annealed at 500 °C for 120 min in Ar-5 %H ₂	2
ZF20-AP	Heated with a rate of 1.5 °C/min to 400 °C, calcined for 20 min, then heat treated at 370 °C in the air for 60 min	ZF20-500-60	Annealed at 500 °C for 60 min in Ar-5 %H ₂	1 (most stable)
ZF60-AP	Heated with a 20 °C/min rate to 400 °C and calcined for 20 min	ZF60-500-30	Annealed at 500 °C for 30 min in Ar-5 %H ₂	4 (most unstable)

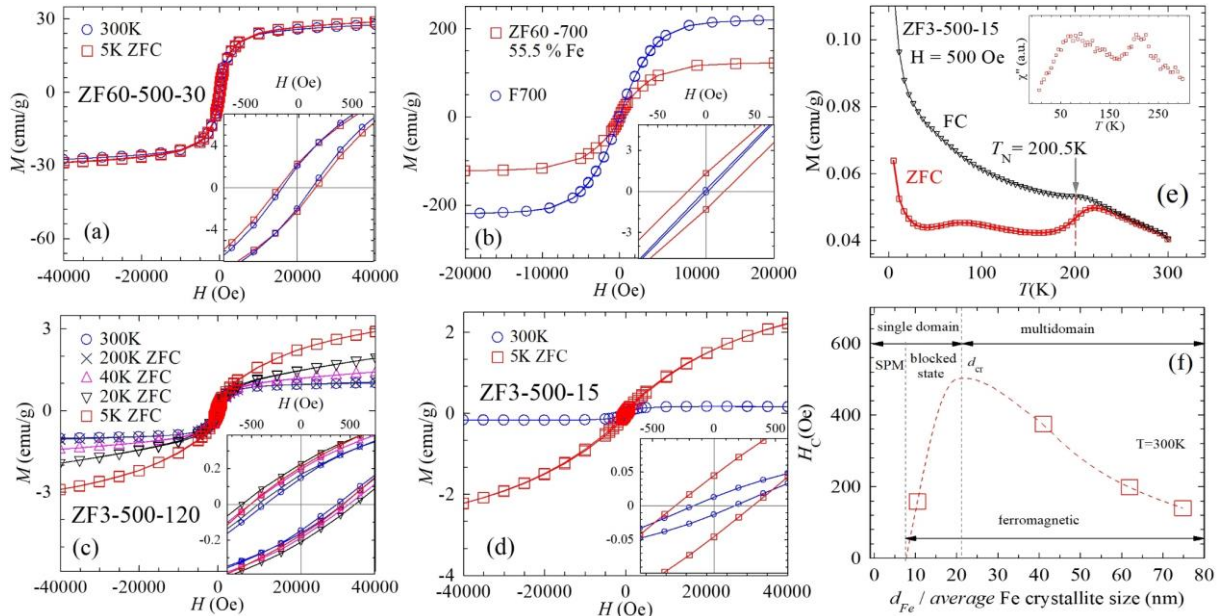


Fig. 1: M vs. H curves measured at/or between 5 K and 300 K for annealed samples: (a) ZF60-500-30; (b) ZF60-700 and F700; (c) ZF3-500-120; and (d) ZF3-500-15. Insets show magnified curves at the origin. (e) Zero-field-cooled (ZFC) and field-cooled (FC) magnetization curves measured between 5 K and 300 K for 500 °C annealed samples, with an example shown for sample ZF3-500-15. Inset: Imaginary component of AC magnetic susceptibility vs. temperature at a frequency of 2 Hz. (f) Dependence of the H_c on the average Fe particle size. Reproduced from Ref. [1].

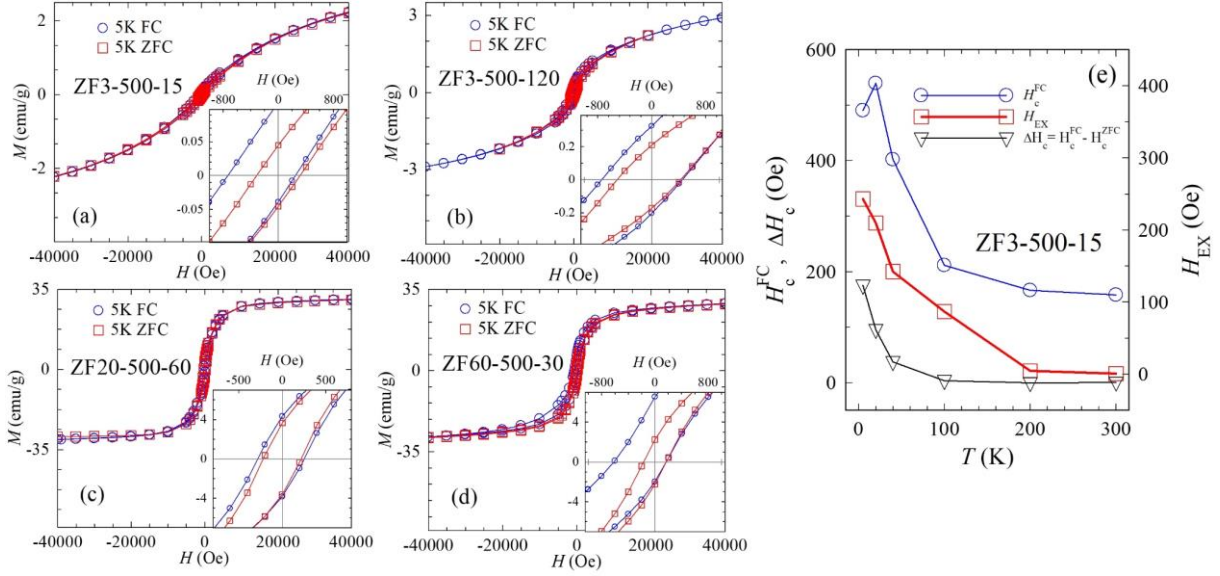


Fig. 2: (a–d) Hysteresis loops measured at 5 K in the ZFC and FC regime (in the applied field $H_{fc} = 4$ kOe) of the samples annealed at 500 °C. Insets: the magnified curves at the origin. (e) Hex vs. T , H_c -fc vs. T , and coercivity enhancement, ΔH_c vs. T , for sample ZF3-500-15. Reproduced from Ref. [1].

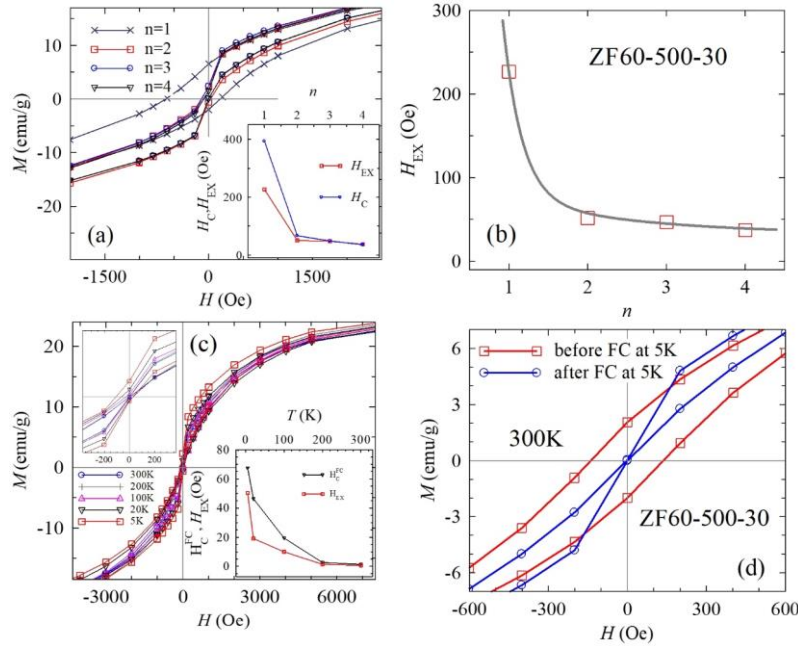


Fig. 3: (a) Consecutively cycled four hysteresis loops at 5 K after field-cooling in $H_{fc} = 40$ kOe for ZF60-500-30. Inset: H_{EX} and H_c vs. loop number, n . (b) The fit of H_{EX} vs. n using equation 1. (c) M vs. H for ZF60-500-30 cooled under $H_{fc} = 40$ kOe at different temperatures, the curves were measured after the first FC hysteresis loop at 5 K. Top inset: the magnified curves at the origin. Bottom inset: H_{EX} vs. T and H_{c-fc} vs. T . (d) The hysteresis loops measured at 300 K before and after the first FC cycle at 5 K for ZF60-500-30. Reproduced from Ref. [1].

References:

- [1] V. Mihalache, *Magnetic behaviors of exchange-biased Fe(FM)-FeO(AFM)-ZnO nanocomposites of different iron concentrations prepared under non-identical conditions with annealing in a reducing atmosphere*, Results Phys. 58 (2024) 107469–107483.
- [2] V. Mihalache, C. Negriřa, M. Secu, I. Mercioniu, N. Iacob, V. Kuncser, *Defect structures and (ferro)magnetism in $Zn_{1-x}Fe_xO$ nanoparticles with the iron concentration level in the dilute regime ($x = 0.001 - 0.01$) prepared from acetate precursors*, Results Phys. 51 (2023) 106644–106656.

Engineering optical and chemical properties of nitrogen-doped carbon quantum dots (NCQDs) through continuous hydrothermal flow synthesis (CHFS) processes

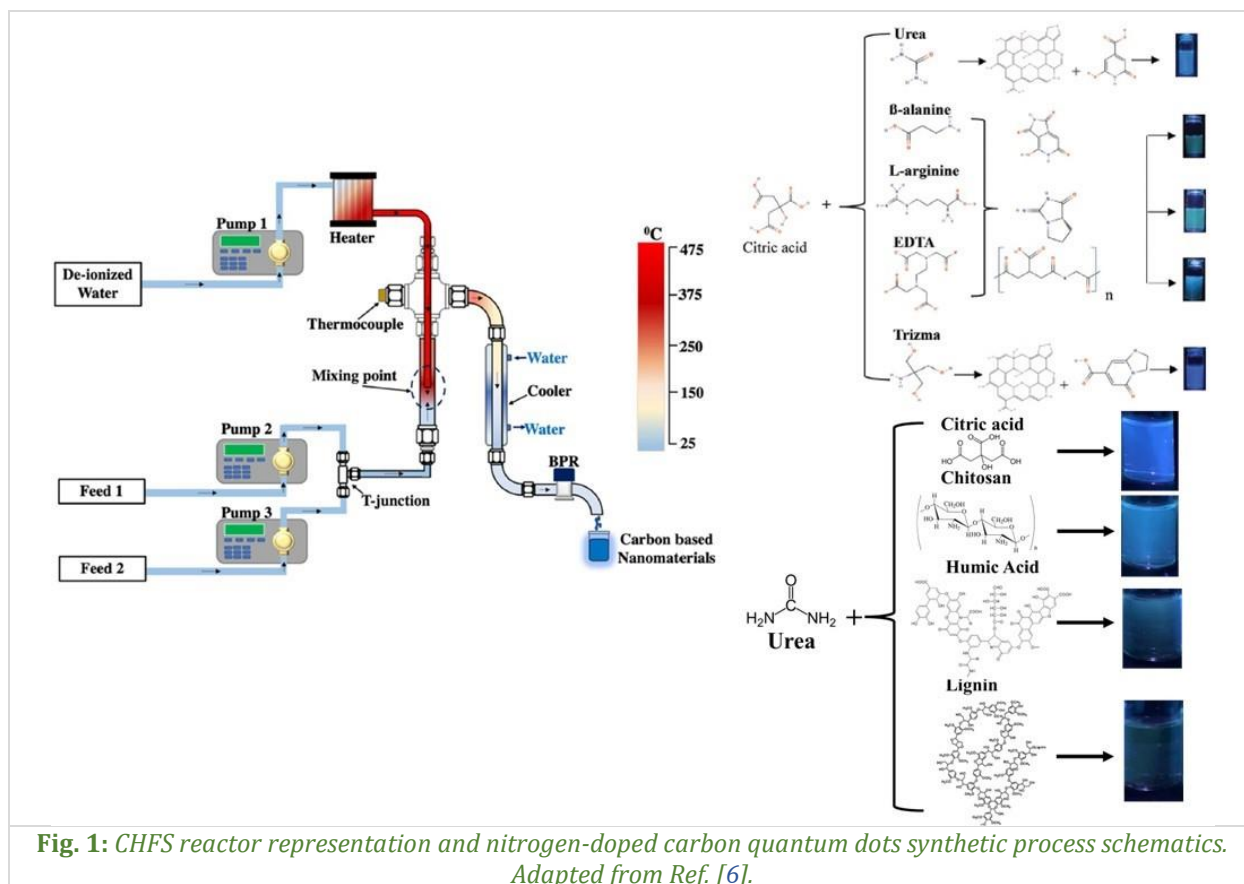
**K.G. Nguyen¹, M. Hus^{2,3,4}, I.A. Baragau^{1,5}, E. Puccinelli¹, J. Bowen⁶, T. Heil⁷,
A. Nicolaev⁵, L.E. Abramiuc⁵, A. Sapelkin⁸, D. Andrews¹, M. Tariq Sajjad¹,
S. Dunn¹, S. Kellici¹**

- 1) *School of Engineering, London South Bank University, SE1 0AA, London, United Kingdom*
- 2) *National Institute of Chemistry, Department of Catalysis and Chemical Reaction Engineering, SI-1000, Ljubljana, Slovenia*
- 3) *Association for Technical Culture of Slovenia (ZOTKS), SI-1000, Ljubljana, Slovenia*
- 4) *Institute for the Protection of Cultural Heritage of Slovenia (ZVKDS), SI-1000, Ljubljana, Slovenia*
- 5) *National Institute of Materials Physics, 077125, Măgurele, Romania*
- 6) *School of Engineering and Innovation, The Open University, Walton Hall, MK7 6AA, Milton Keynes, United Kingdom*
- 7) *Max Planck Institute for Solid State Research, 70569, Stuttgart, Germany*
- 8) *School of Physical and Chemical Sciences, Queen Mary University of London, E1 4NS, London, United Kingdom*

The current two studies recently reported are a continuation of previous synthetic explorations started in 2020 by Baragau *et al.* [1], when the continuous hydrothermal flow synthesis (CHFS) methodology was optimised for carbon quantum dots synthesis, being for the first report in the literature. This article was followed by three more studies using glucose as carbon source [2] also succeeding the sulphur [4] and nitrogen [4] doping of these glucose-derived carbon quantum dots *via* CHFS. The nitrogen doping process of carbon quantum dots is usually employed to enhance their physical and chemical properties, but there are no established requirements in the selection process of the nitrogen sources in producing high-quality nitrogen-doped carbon quantum dots (NCQDs). Also, the carbon source can play a key role in obtaining high quality nitrogen-doped carbon quantum dots. The current two studies explore the effect of nitrogen source nature when the carbon source was citric acid [5] and the influence of the carbon source when urea was used as nitrogen source dopant [6] (see the CHFS reaction setup and synthetic process schematics in Fig. 1).

The report from Small [5] explores the influence of various nitrogen dopants on the morphology, optical features, and band structure of NCQDs; citric acid is used as the carbon source, and urea, trizma base, beta-alanine, L-arginine, and EDTA are used as nitrogen sources. Notably, urea and trizma produced NCQDs with excitation-independent fluorescence, high quantum yields (up to 40%), and uniform dots with narrow particle size distributions. Density functional theory (DFT) and time-dependent DFT modelling established that defects and substituents within the graphitic structure have a more significant impact on the NCQDs' electronic structure than nitrogen-containing functional groups. Importantly, for the first time, this work demonstrates that the conventional approach of modelling single-layer structures is insufficient, but two layers suffice for replicating experimental data. This study, therefore, provides essential guidance on the selection of nitrogen precursors for NCQD customization for diverse applications. These findings highlight the critical role of precursor reactivity, solubility, and molecular structure in the carbonization process. Urea and trizma facilitated the decarboxylation and dehydration of citric acid, which proved crucial for the formation of an optimal graphitic carbon core. On the other hand, amino acids primarily led to polymerization pathways, resulting in a larger particle size distribution. Interestingly, we achieved excitation-independent emission for samples synthesized with urea and trizma, suggesting a uniform, single emissive state. A theoretical analysis further corroborated these findings, indicating that at least two layers of the graphitic structure need to be considered in any models to accurately reflect these experimental results. Functionalizing groups such as $-NH_2$, $-COOH$, $-CONH_2$, $-OH$, $-NO$, were found to have a relatively minor impact on the properties of NCQDs, suggesting that these groups can be utilized to fine-tune the emission properties, including

colour of the NCQDs. This effect was observed for a single-layer structure and is expected to remain consistent irrespective of the number of layers. Supporting this, electron analysis showed no significant activation or charge redistribution around the functionalizing groups upon excitation. In contrast, defects and substitutions, such as carbon vacancies or graphitic and pyrrolic nitrogen atoms, exerted a more pronounced influence on the properties of NCQDs.



The report from [Carbon](#) [6] explores the CHFS synthesis of nitrogen-doped carbon quantum dots (CQDs) from various biomass derived carbon sources, including high molecular weight polymeric sources like chitosan, lignin, and humic acid, observing that the carbon source structure significantly affects the size of the fabricated NCQDs and their optical properties. Citric acid, a low molecular weight precursor, yields NCQDs with excitation-independent emission, higher quantum yields, and low non-radiative losses, while NCQDs derived from polymeric precursors exhibit excitation-dependent, red-shifted, and lower efficiency emission. Theoretical calculations, performed to understand the configuration and distribution of nitrogen dopants within the NCQD structure, show that pyridinic and graphitic nitrogen atoms exhibit a strong preference to aggregate near the centre of the edge of the NCQD and not in the vertices nor in the graphitic core, thus affecting the HOMO and LUMO, bandgap, and light absorption and emission wavelengths. Comparing the distinct optical properties of the as-synthesised NCQDs provides key findings into their complex photoluminescence mechanisms and the role of molecular fluorophores. Citric acid stands out in producing NCQDs with excitation-independent emission, and higher quantum yield. In contrast, NCQDs derived from the polymeric precursors exhibit excitation-dependent, red-shifted, lower efficiency emission consistent with carbon core-confined states. These results highlight that the carbon source strongly influences the balance of molecular versus carbonized emitting states in NCQDs produced under same flow synthesis conditions. The optical properties of the NCQDs, including their fluorescence, depend on the particle size as well as the configuration of nitrogen dopants. Theoretical calculations show that the configuration of the nitrogen is not random. Instead, pyridinic and graphitic nitrogen atoms exhibit a strong preference to aggregate near the centre of the edge of the NCQDs and not in the vertices or the graphitic core. This is also shown to be the most active part of the NCQDs, as HOMO and LUMO are located there. Moreover, nitrogen dopants impact the work function and bandgap, thus influencing the light absorption and emission wavelengths, especially

pyridinic nitrogen. The weak fluorescence exhibited by these NCQDs correlates with their limited pyrrolic nitrogen content. Furthermore, the electronic structure of the NCQDs agrees with the other characterisation results and the principles of quantum confinement effects. Therefore, this study provides molecular-level insights into the interplay between carbon sources and unique NCQDs photoluminescence mechanisms. Also, the LCA analysis highlights CHFS's green advantages for producing NCQDs over batch methods. CHFS exhibits values below 20% for climate change, resource use, and freshwater eutrophication impacts, compared to over 60% for batch hydrothermal processes. Overall, this work demonstrates the power of continuous hydrothermal flow reactors to sustainably generate NCQDs from waste biomass streams with tailored properties based on the precursor chemistry.

References:

- [1] I.A. Baragau, N.P. Power, D.J. Morgan, T. Heil, R.A. Lobo, C.S. Roberts, M.M. Titirici, S. Dunn, S. Kellici, *Continuous hydrothermal flow synthesis of blue-luminescent, excitation-independent nitrogen-doped carbon quantum dots as nanosensors*, J. Mater. Chem. A 8 (2020) 3270–3279.
- [2] I.A. Baragau, N.P. Power, D.J. Morgan, R.A. Lobo, C.S. Roberts, M.M. Titirici, V. Middelkoop, A. Diaz, S. Dunn, S. Kellici, *Efficient continuous hydrothermal flow synthesis of carbon quantum dots from a targeted biomass precursor for on-off metal ions nanosensing*, ACS Sustain. Chem. Eng 9 (2021) 2559–2569.
- [3] I.A. Baragau, Z. Lu, N.P. Power, D.J. Morgan, J. Bowen, P. Diaz, S. Kellici, *Continuous hydrothermal flow synthesis of S-functionalised carbon quantum dots for enhanced oil recovery*, Chem. Eng. J. 405 (2021) 126631.
- [4] K.G. Nguyen, I.A. Baragau, R. Gromicova, A. Nicolaev, S.A.J. Thomson, A. Rennie, N.P. Power, M.T. Sajjad, S. Kellici, *Investigating the effect of N-doping on carbon quantum dots structure, optical properties and metal ion screening*, Sci. Rep. 12 (2022) 13806.
- [5] K.G. Nguyen, M. Huš, I.-A. Baragau, J. Bowen, T. Heil, A. Nicolaev, L.E. Abramiuc, A. Sapelkin, M.T. Sajjad, S. Kellici, *Engineering nitrogen-doped carbon quantum dots: Tailoring optical and chemical properties through selection of nitrogen precursors*, Small 20 (2024) 2310587.
- [6] K.G. Nguyen, M. Huš, I.-A. Baragau, E. Puccinelli, J. Bowen, T. Heil, A. Nicolaev, D. Andrews, M.T. Sajjad, S. Dunn, S. Kellici, *Controlling the optoelectronic properties of nitrogen-doped carbon quantum dots using biomass-derived precursors in a continuous flow system*, Carbon 230 (2024) 119623.

Crystallization processes of rare-earth doped GdF_3 nanocrystals in silicate glass matrix: dimorphism and photoluminescence properties

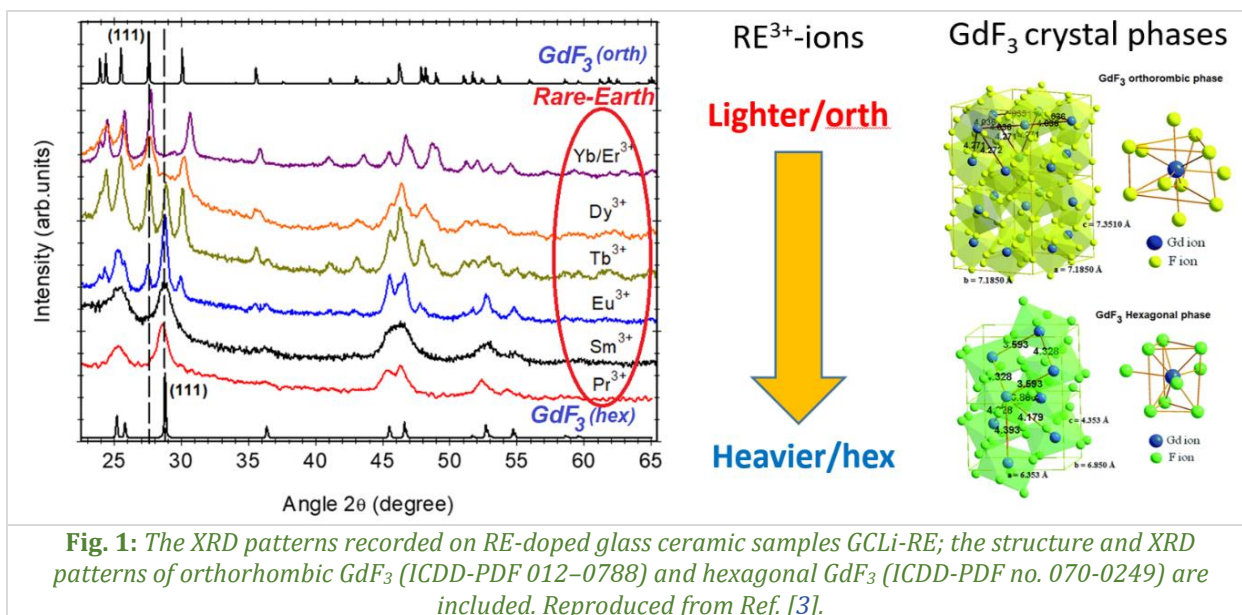
C.E. Secu, C. Bartha, C. Radu, M. Secu

National Institute of Materials Physics, 077125, Măgurele, Romania

A novel class of nanostructured materials are represented by the glassy nanocomposites where optically active nanocrystals are well dispersed within the amorphous matrix. They have high potential for various applications such as optical amplifiers, photovoltaic devices, scintillators, optical waveguides, optical refrigerator, and high-power white light-emitting diodes. Precipitation of a specific nanocrystalline phase within the amorphous glassy matrix is reached during a subsequent thermal processing [1]. Lanthanide doped GdF_3 present a special interest for multicolour emitting phosphors including white light applications. The overlapping between the 4f energy-levels of the Gd^{3+} and UV-excited states of RE^{3+} -ions, promote an efficient energy transfer between them [2].

For the preparation of RE^{3+} (1%)-doped 94SiO_2 - 5GdF_3 (mol%) glassy nanocomposites ($\text{RE}=\text{Pr}$, Sm , Eu , Dy , and Tb) and co-doped with Li we have used the sol-gel synthesis [3]; the glass-ceramisation was obtained after calcination of the dried xerogel at 530°C for 60 min.

The Li , RE -doped nanocomposites XRD patterns revealed the diffraction peaks assigned to the GdF_3 nanocrystalline phase precipitation. (Fig. 1). The GdF_3 exhibits two crystalline structures, orthorhombic (Pnma (No. 62)) and hexagonal (P63/mcm (No. 193)) which differ significantly in coordination number, lattice volume, etc. and the patterns showed both crystalline phases



XRD pattern analysis show a good correlation between the ionic radii of RE^{3+} ions [4] and structure of the GdF_3 nanocrystals. The structure is hexagonal for Pr^{3+} and Sm^{3+} ions, whose ionic radii are larger than that of Gd^{3+} , and orthorhombic the Dy^{3+} , Yb^{3+} , and Er^{3+} , whose ionic radii are smaller. A mixture of both phases was observed for Eu^{3+} and Tb^{3+} , where the ionic radii are close to that of Gd^{3+} . An estimation of the GdF_3 hexagonal/orthorhombic ratio from the XRD pattern analysis revealed a monotone transition between the nanocrystalline phases. This transition is dependent on the RE-ion size, with selective formation of the orthorhombic or hexagonal GdF_3 nanocrystalline phases. The observed phase stability is linked to the "lanthanide contraction" effect, which plays an important role in stabilizing the phase structure of the REF_3 nanocrystalline materials [5]. As can be seen, in the present case, the RE^{3+} dopant ions are responsible for the stabilization of the specific GdF_3 phase, whether orthorhombic or hexagonal. The RE^{3+} ions, whose ionic radii are larger than that of Gd^{3+} ions, expand the crystal lattice and increase the distance between fluoride anions. This results in a decrease in the repulsive energy between fluoride anions, ultimately favouring the formation of hexagonal GdF_3 nanocrystals.

Conversely, the doping of smaller RE^{3+} ions leads to the formation of orthorhombic phase GdF_3 nanocrystals [3].

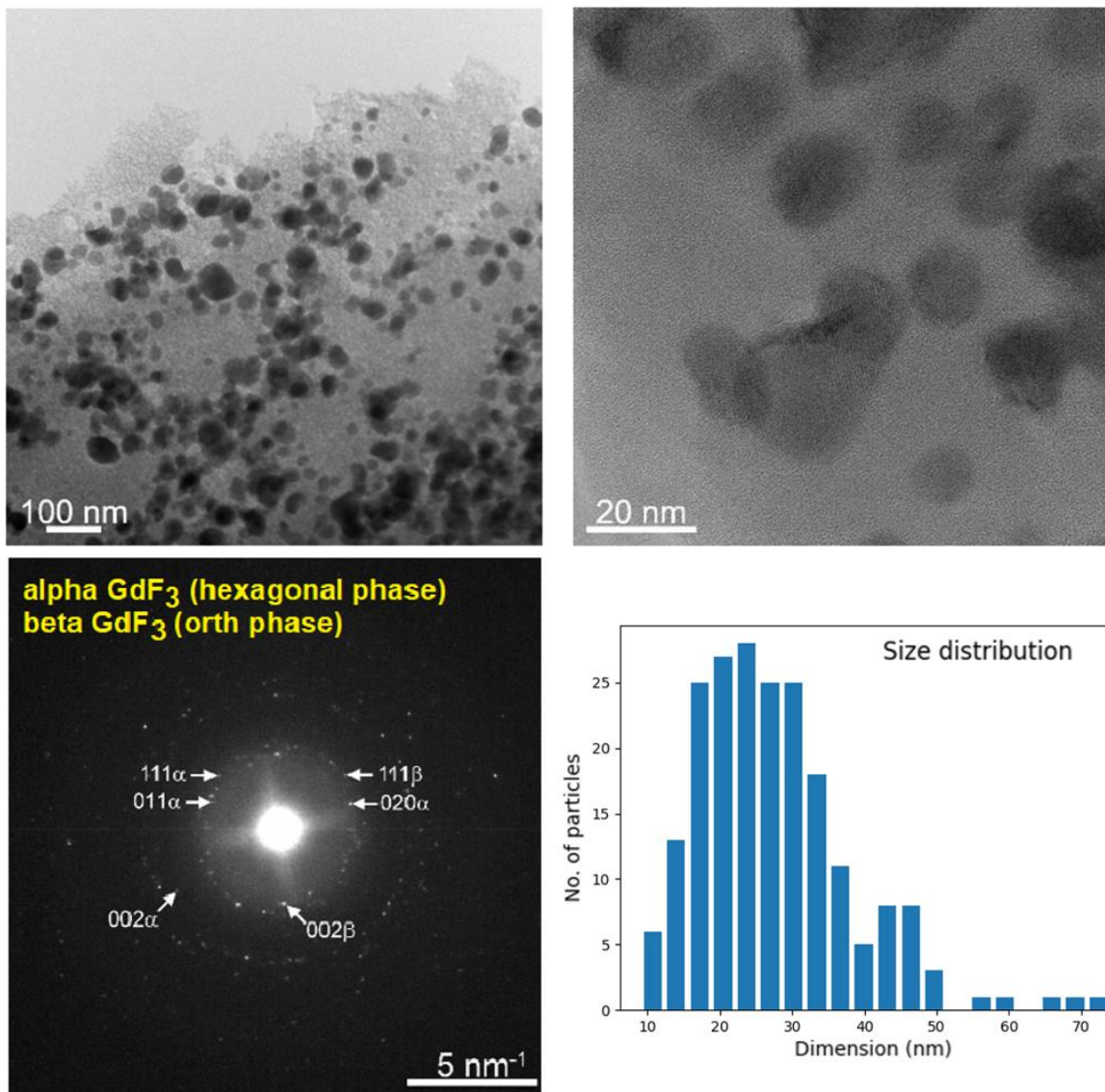


Fig. 2: Low magnification TEM image of Tb^{3+} -doped $\text{SiO}_2\text{-GdF}_3$ sample (GCLi-Tb) and the corresponding SAED pattern recorded on two different areas. The size distribution of the nanocrystals is showed in the bottom-right corner. Reproduced from Ref. [3].

The occurrence of the GdF_3 nanocrystals dispersed in the silica glassy matrix is revealed by the transmission electron microscopy (TEM) images recorded on Tb^{3+} -doped $\text{SiO}_2\text{-GdF}_3$ glass-ceramic sample (GCLi-Tb). These micrographs showed a large number of well-dispersed, quasi-spherical nanocrystals with size of tens of nanometres. The selected area electron diffraction (SAED) pattern confirmed the presence of dominant orthorhombic $\alpha\text{-GdF}_3$ nanocrystals, accompanied by hexagonal $\beta\text{-GdF}_3$ nanocrystals (Fig. 2).

Under UV-light excitation at 273 nm, we observed sharp Gd^{3+} UV luminescence at 310 nm ($8\text{S}7/2 \rightarrow 6\text{P}1$) accompanied by the typical RE^{3+} ions luminescence peaks, indicating an energy transfer (ET) process from Gd^{3+} sensitizer to RE^{3+} activator. The Stark splitting of the luminescence bands, due to the degeneracy lifting by the local crystal field (of GdF_3 nanocrystals) in which the RE^{3+} ions are incorporated, is also evident (Fig. 3). The efficiency of the $\text{Gd}^{3+} \rightarrow \text{RE}^{3+}$ energy transfer process (η_{ET}) has been evaluated from the Gd^{3+} luminescence lifetime at 310 nm in undoped (τ_{Gd}) and RE^{3+} -doped glass-ceramics. The highest $\eta_{\text{ET}} \cong 80\%$ was observed for the GCLiTb sample, and the lowest η_{ET} of $\cong 21\%$ for the GCLiSm sample.

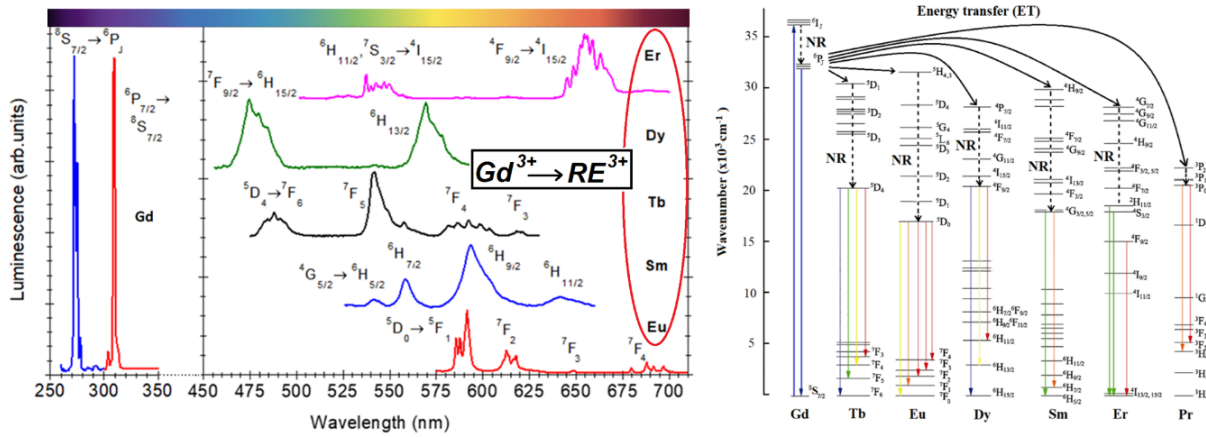


Fig. 3: Normalized photoluminescence spectra recorded on undoped and RE³⁺-doped glass ceramic samples recorded under Gd³⁺ ions 273 nm excitation. Possible energy transfer paths Gd³⁺ → RE³⁺ are shown. Reproduced from Ref. [3].

Finally, we observed that the relatively high ET values were not accompanied by intense luminescence signals, except for the Tb³⁺ ions, where the luminescence was weakly visible. We propose several contributing factors: (i) high absorption by the silica glass matrix in the UV region of the Gd³⁺ ions absorption; (ii) a high local RE-ions concentration within the nanocrystals (up to 20%), leading to a high rate of non-radiative transitions between close pairs and the luminescence concentration quenching; and (iii) effective matching between the Gd³⁺ and RE³⁺ energy levels, which occurs only for Eu and Tb dopant ions.

Hence, our experimental results demonstrated the precipitation of the GdF₃ nanocrystalline phase within the silica matrix, where the Li⁺ ions act as promoters of the crystallization process, and the RE-dopant ions drive the formation of the particular GdF₃ crystalline phase. The whole process can be described as an autocatalytic-type reaction, where a second metastable phase, LiF, acts as a catalyst by lowering the energy barrier for the crystallization of the GdF₃ nanocrystalline phase.

References:

- [1] C.B. de Araujo, L. Kassab, D.D. da Silva, *Optical properties of glasses and glass-ceramics for optical amplifiers, photovoltaic devices, color displays, optical limiters, and Random Lasers*, Opt. Mater. 131(2022) 112648.
- [2] H. Guan, Y. Sheng, C. Xu, Y. Dai, X. Xie, H. Zou, *Energy transfer and tunable multicolor emission and paramagnetic properties of GdF₃:Dy³⁺, Tb³⁺, Eu³⁺ phosphors*, Phys. Chem. Chem. Phys. 18 (2016) 19807–19819.
- [3] C.E. Secu, C. Bartha, C. Radu, M. Secu, *Crystallization processes of rare-earth doped GdF₃ nanocrystals in silicate glass matrix: Dimorphism and photoluminescence properties*, Ceram. Int. 20 (2024) 37518–37524.
- [4] R.D. Shannon, *Revised effective ionic radii and systematic studies of interatomic distances in halides and chalcogenides*, Acta Crystallogr. A 32(1976) 751–767.
- [5] M. Mansmann, *Die kristallstruktur von lanthantrifluorid*, Z. Kristallogr. Krist. 122 (1965) 375–398.

Investigation of the relationship between the pyro-phototronic effect and the crystalline structure of ZnO-based photodetectors for visible light detection

M.C. Istrate^{1,2}, C. Ghica¹, J.P.B. Silva³, E.M. Vieira⁴, K. Gwozdz⁵, N.E. Silva³, A. Kaim⁵, J.H. Correia⁴, M. Pereira³, L. Marques³, J.L. MacMannus-Driscoll⁶, R.L.Z. Hoyer⁷, M.J. Gomez³

1) National Institute of Materials Physics, 077125, Măgurele, Romania

2) University of Bucharest, Faculty of Physics, Măgurele 077125, Romania

3) University of Minho, 4710-057, Braga, Portugal

4) University of Minho, 4804-533, Guimarães, Portugal

5) Wrocław University of Science and Technology, 50-370, Wrocław, Poland

6) University of Cambridge, CB3 0FS, Cambridge, United Kingdom

7) University of Oxford, OX1 3QR, Oxford, United Kingdom

Broadband photodetectors (PDs) with ultrasensitive responses across the ultraviolet (UV), visible (Vis), and near-infrared (NIR) spectral ranges have extensive applications in optical communications, environmental monitoring, imaging systems, medicine, and multispectral detection [1]. Recently, self-powered PDs based on the photovoltaic (PV) effect in p-n junctions have gained significant attention, as they can operate without external power, reducing overall energy consumption [2]. The potential for self-driven PDs makes them highly attractive for applications in the Internet of Things and wearable electronics [3].

In particular, wide-bandgap semiconductor-based PDs for UV to visible (UV-Vis) detection offer advantages such as simple structures, easy miniaturization, and strong resistance to radiation in harsh environments [4]. Among them, metal oxides like ZnO, NiO, and TiO₂ have been extensively explored due to their non-toxicity, natural abundance, simple synthesis, and excellent stability, making them ideal for self-powered UV-Vis photodetection. Specifically, in ZnO-based PDs, the photovoltaic effect can be enhanced through the pyro-phototronic effect, which arises from the coupling of ZnO's pyroelectric properties with light absorption. Consequently, numerous studies have reported the UV detection capabilities of ZnO nanowires, thin films, and heterostructures. However, due to its wide bandgap, ZnO primarily absorbs UV light, posing a challenge for broadband photodetection applications.

Recent studies have demonstrated that integrating metal nanoparticles (NPs), such as gold (Au) or silver (Ag), with ZnO-based PDs can significantly enhance UV detection by leveraging the localized surface plasmon (LSP) effect alongside the pyroelectric effect. However, the impact of metal NPs on self-powered PDs for visible light detection remains unexplored. Given that plasmonic metal NPs strongly influence visible light absorption, our study investigates the role of Ag NPs of varying sizes at the interface of p-SnO and n-ZnO in an n-Si/p-SnO/n-ZnO heterojunction, aiming to enhance broadband photodetector performance [5]. The photoresponse of the fabricated photodetector under 650 nm pulsed laser illumination was systematically analysed. Compared to previously reported studies on Si-based heterojunctions, this work demonstrates a self-powered photodetector with superior responsivity, sensitivity, and rapid rise and fall times. A key aspect of our investigation is the interaction between the LSP effect and the pyro-phototronic effect, which significantly enhances the performance of the n-Si/p-SnO/Ag NPs/n-ZnO heterojunction.

To fabricate the Si/SnO/Ag NPs/ZnO structure, a thin Ag film was deposited with varying deposition times of 10, 20, 40, 80, and 160 seconds before the ZnO layer was applied. The deposition process was carried out using the ion beam sputter deposition (IBSD) technique on top of the pre-existing n-Si/p-SnO structure. In order to obtain both structural and spectroscopic information about the ZnO deposited thin films and Ag nanoparticles, transmission electron microscopy (TEM) studies have been performed. Moreover, by combining the structural and spectroscopic TEM techniques we can correlate the distribution and the size of the Ag nanoparticles with the quality of the photodetection properties.

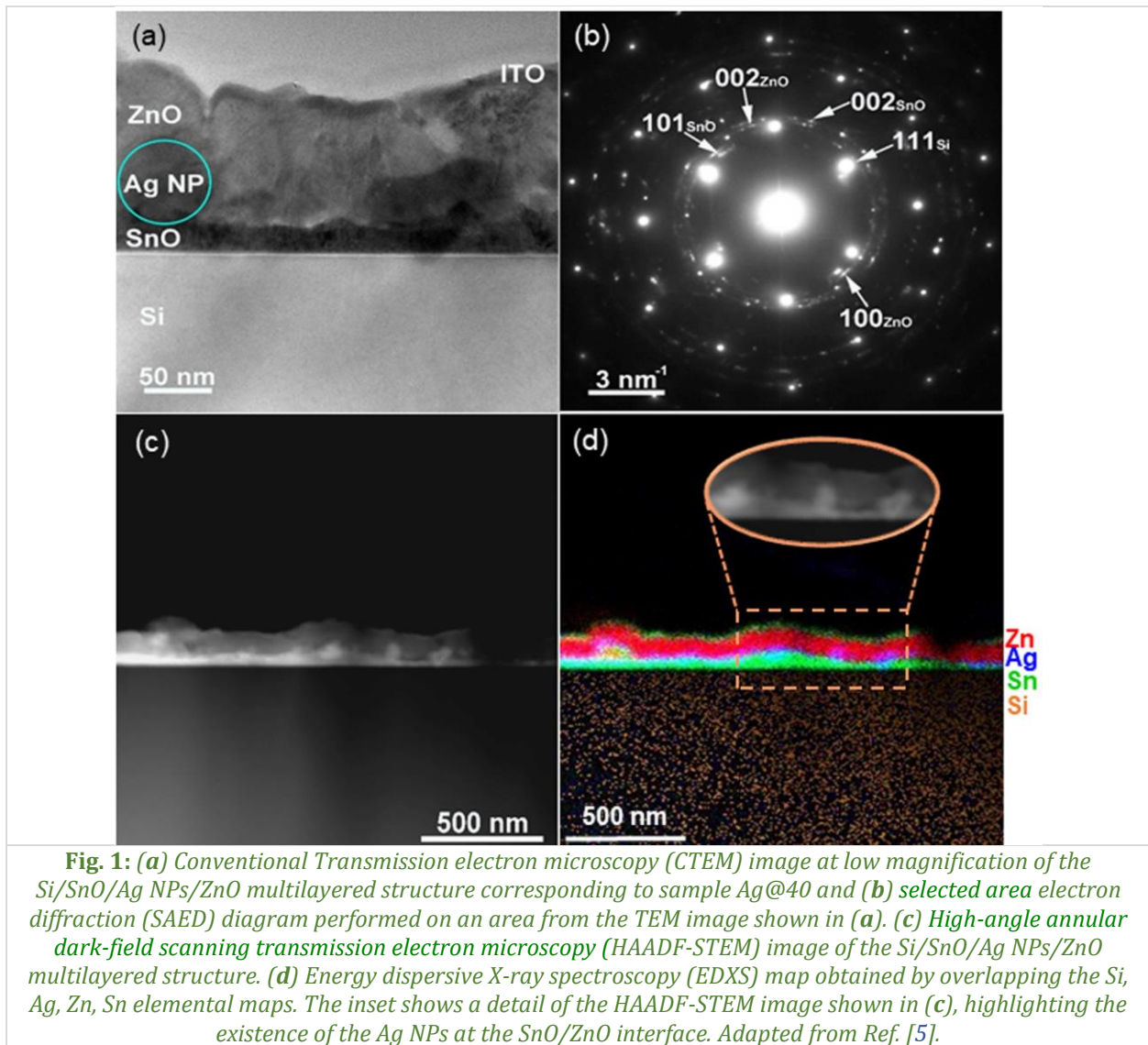


Fig. 1a is a low magnification CTEM image, displaying the morphology of the sample in diffraction contrast. The sample contains the following layers: ITO layer with an average thickness of 12 ± 3 nm, ZnO layer with an average thickness of 115 ± 5 nm, Ag nanoparticles, a SnO layer with a thickness of 22 ± 3 nm, and the Si substrate. Fig. 1b is a SAED pattern performed on the CTEM image from Fig. 1a, revealing the crystallinity of the sample. It contains a set of strong peaks assigned to the cubic Si structure of the substrate (space group Fd-3m), along with a series of diffraction rings, indicating the presence of polycrystalline materials. From the measurements performed on the SAED pattern, we indexed and assigned a set of diffraction rings as follows: two of them were assigned to the tetragonal SnO structure with space group P4/nmm and $a=b=0.3849$ nm, $c=0.4894$ nm lattice constants, with Miller indices (101) and (002) and the other two were assigned to the wurtzite structure (hexagonal structure) of ZnO with space group P6₃mc and $a=b=0.3237$ nm, $c=0.522$ nm lattice constants, with Miller indices (100) and (002).

In order to show the presence and the morphology of the Ag nanoparticles at the SnO/ZnO interface, we performed EDXS mapping on the HAADF-STEM image from Fig. 1c. This technique enables the acquisition of an EDXS spectrum at each pixel of the HAADF-STEM image, generating elemental maps that illustrate the spatial distribution of the elements present in the sample. Although the EDXS lines for Sn and Ag are quite close, this issue can be mitigated by selecting a weaker line for the Ag elemental map (L line) and the M line for the Sn elemental map. The EDXS map shown in Fig. 1d was obtained by overlapping the Si, Sn, Ag, and Zn maps and clearly indicates a sharp interface with no perceptible atomic interdiffusion between the layers, within the resolution limits of the EDXS spectrometer. In addition, the Ag NPs exhibited a spheroidal morphology with a diameter of around 60–70 nm, which is in good

agreement with the SEM measurements. The inset of the same figure shows a zoomed-in portion of the HAADF-STEM image from Fig. 1c, highlighting the formation of the Ag NPs at the SnO/ZnO interface. The enhanced pyro-phototronic effect can be understood as a result of the coupling between the photovoltaic effect at the Si/SnO junction, the pyroelectric effect in ZnO, and the plasmonic effect, which generates an additional electric field at the SnO/ZnO junction to facilitate charge separation. The PD exhibited a responsivity of 210.2 mA/W, a detectivity 54.7×10^8 Jones, and a sensitivity of 15.0×10^4 , along with rise and fall times of 2.3 and 51.3 μ s, respectively. This work demonstrated that the combination of plasmonic Ag NPs with a ZnO pyroelectric film and a n-Si/p-SnO heterojunction offers a promising solution for highly responsive, sensitive, and ultrafast photosensing.

References:

- [1] D. You, C. Xu, W. Zhang, J. Zhao, F. Qin, Z. Shi, *Photovoltaic-pyroelectric effect coupled broadband photodetector in self-powered ZnO/ZnTe core/shell nanorod arrays*, Nano Energy 62 (2019) 310–318.
- [2] S. Yang, M. Chen, X. Shen, Y. Yuan, Y. Liu, Q. Wang, D. Cao, *Self-powered narrowband visible-light photodetection enabled by organolead halide perovskite $\text{CH}_3\text{NH}_3\text{PbBr}_3$ /p-Si heterojunction*, Appl. Phys. Lett. 119 (2021) 121107.
- [3] J.P.B. Silva, E.M.F. Vieira, K. Gwozdz, A. Kaim, L.M. Goncalves, J.L. MacManus-Driscoll, R.L.Z. Hoyer, M. Pereira, *High-performance self-powered photodetectors achieved through the pyro-phototronic effect in Si/SnO_x/ZnO heterojunctions*, Nano Energy 89 (2021) 106347.
- [4] J.P.B. Silva, K. Gwozdz, L.S. Marques, M. Pereira, M.J.M. Gomes, J.L. MacManus-Driscoll, R.L.Z. Hoyer, *Large ferro-pyro-phototronic effect in $0.5\text{Ba}(\text{Zr}_{0.2}\text{Ti}_{0.8})\text{O}_3$ – $0.5(\text{Ba}_{0.7}\text{Ca}_{0.3})\text{TiO}_3$ thin films integrated on silicon for photodetection*, Carbon Energy 5 (2023) e297.
- [5] J.P.B. Silva, E.M.F. Vieira, K. Gwozdz, N.E. Silva, A. Kaim, M.C. Istrate, C. Ghica, J.H. Correia, M. Pereira, L. Marques, J.L. MacManus-Driscoll, R.L.Z. Hoyer and M.J.M. Gomes, *High-performance and self-powered visible light photodetector using multiple coupled synergetic effects*, Mater. Horiz. 11 (2024) 803–812.

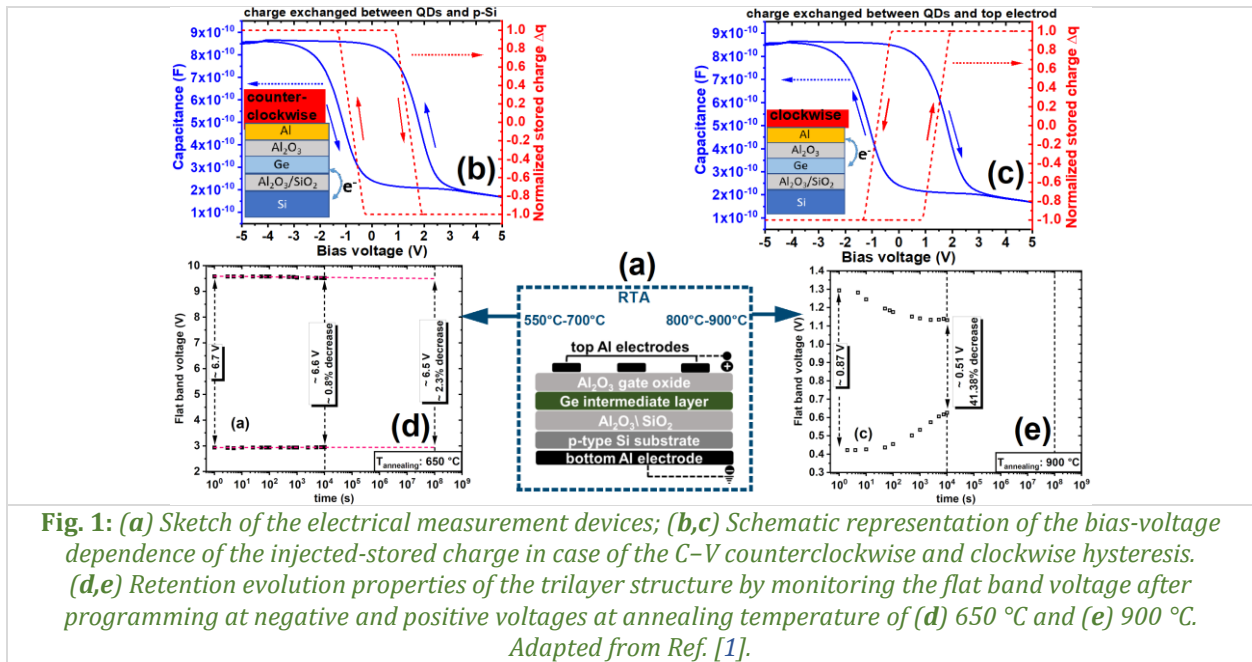
Annealing effects on charging-discharging mechanism in trilayer $\text{Al}_2\text{O}_3/\text{Ge}/\text{Al}_2\text{O}_3$ memory structures

I. Stavarache¹, C. Palade¹, V.A. Maraloiu¹, V.S. Teodorescu^{1,2},
T. Stoica¹, M.L. Ciurea^{1,2}

1) National Institute of Materials Physics, 077125, Măgurele, Romania

2) Academy of Romanian Scientists, 050094, Bucharest, Romania

For the development of memory devices and continued progress of IT engineering, a deep understanding of the charging–discharging mechanisms in nanocrystalline floating gate memories is crucial to overcoming the current limitations. The charging–discharging mechanism in $\text{Al}_2\text{O}_3/\text{Ge}/\text{Al}_2\text{O}_3$ trilayer memory structures, obtained by magnetron sputtering deposition, was investigated as a function of the post-deposition rapid annealing temperature, up to 900 °C [1]. The change in C–V hysteresis curves due to annealing was observed, transitioning from a clockwise type at low temperatures to a counter clockwise type in samples annealed in the intermediate temperature range of 550 to 650 °C, and then returning to a clockwise type for annealing at higher temperatures of 800–900 °C (Fig. 1). Up to 700 °C, memory performances constantly improved, with the 600 °C annealed samples achieving a memory window of 5.6 V for –1 to +15 V voltage sweep. The 650 °C annealed structures exhibited good retention characteristics, for which the charge loss is only ~2% after 10^8 s. When the annealing temperature was increased above 700 °C, a rapid decrease in the memory performance was observed. The annealing-induced changes are attributed to the Ge fast diffusion and nanocrystallisation process, in correlation with the morphological and structural high-resolution transmission electron microscopy results.



Reference:

- [1] I. Stavarache, C. Palade, V.A. Maraloiu, V.S. Teodorescu, T. Stoica, M.L. Ciurea, *Annealing effects on the charging-discharging mechanism in trilayer $\text{Al}_2\text{O}_3/\text{Ge}/\text{Al}_2\text{O}_3$ memory structures*, ACS Appl. Electron. Mater. 6 (2024) 978–986.

Atomically thin MoS₂ layers selectively grown on Mo patterned substrates for field-effect-controlled photosensors

I. Stavarache¹, C. Palade¹, A. Slav¹, I. Dascalescu¹, A.-M. Lepadatu¹,
L. Trupina¹, E. Matei¹, M.L. Ciurea^{1,2}, T. Stoica¹

1) National Institute of Materials Physics, 077125, Măgurele, Romania

2) Academy of Romanian Scientists, 050094, Bucharest, Romania

Selective growth of 2D MoS₂ layers on patterned substrates is highly desired for easy fabrication of devices. In this work [1], selectively grown 2D MoS₂ on Mo-patterned substrates, facilitating the formation of intimate metallic contact, was achieved using a Mo-CVD method. MoO₃ from the oxidized Mo pattern and S powder serves as the growth precursors. Mo films were deposited by magnetron sputtering onto SiO₂(300 nm)/c-Si substrates and subsequently patterned by photolithography techniques to obtain Mo strips and finger contact structures, with the gap between the strips and finger varied from 5 to 20 μm . The filling of the gap by selectively grown atomically thin MoS₂ plates of 1–2 monolayers (MLs) was demonstrated by scanning electron microscopy (SEM) and atomic force microscopy (AFM) imaging. Field effect devices for the characterization of the photosensitivity of selectively grown MoS₂ have been fabricated from finger contact structures. The dark current was drastically reduced from 10⁻⁹ to 10⁻¹³–10⁻¹⁴ A by varying the gate voltage from +7 to -7 V, showing the n-type semiconductor behaviour of the selectively grown 2D MoS₂. High photosensitivity of 10⁵ (%) was obtained for 4.5 \times 10⁻⁴ mW/cm² at 650 nm wavelength illumination. The spectral responsivity reached values of 15–25 A/W at 600 nm wavelength and showed an energy onset of 1.72–1.77 eV corresponding to about 2 ML MoS₂. The carrier-trapping effect, responsible for the slow part of the device response, can be attributed to structural defects as well as adsorbed molecules, similar to the behaviour observed in gas sensors (Fig. 1).

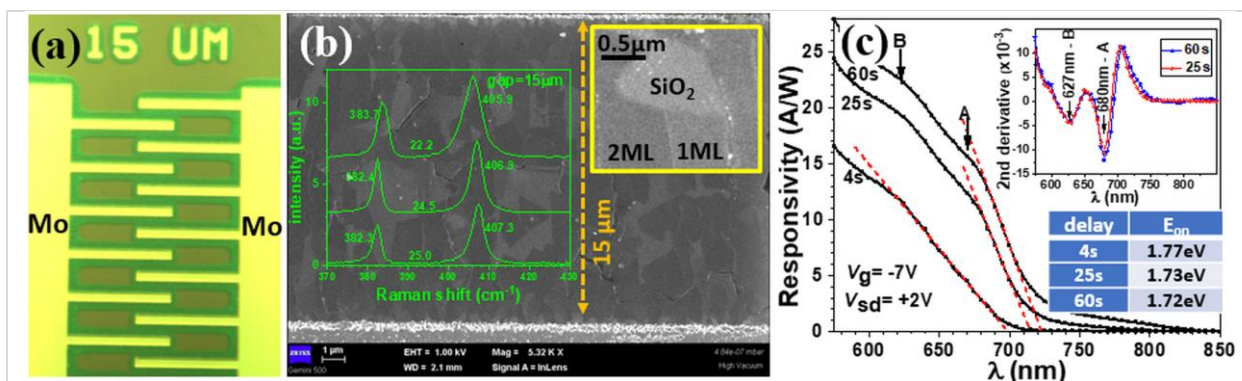


Fig. 1: Selective growth by Mo-CVD of 2D MoS₂ on substrates with Mo patterns of finger contact geometry: (a) optical image of a sample with 15 μm gap between finger; (b) SEM image acquired from the gap region with visible top and bottom small parts from Mo fingers covered by small MoS₂ crystallites (Insets: zoomed SEM image of a selected area with adjusted brightness and contrast to highlight regions of 1–2 MLs & Raman spectra acquired from different locations within the gap with MoS₂ flakes of 1–3 MLs); (c) Spectral responsivity obtained by normalization of the maximum values of $I_{ph}(\lambda)$ to the calibrated spectral light power and active MoS₂ area (Insets: second derivatives of 60 and 25 s spectral responsivity curves).

Adapted from Ref. [1].

Reference:

- [1] I. Stavarache, C. Palade, A. Slav, I. Dascalescu, A.-M. Lepadatu, L. Trupina, E. Matei, M.L. Ciurea, T. Stoica, Atomically thin MoS₂ layers selectively grown on Mo patterned substrates for field-effect-controlled photosensors, ACS Appl. Nano Mater. 7 (2024) 5051–5062.

Enhancing SiGeSn nanocrystals SWIR photosensing by high passivation in nanocrystalline HfO₂ matrix

I. Dascalescu¹, C. Palade¹, A. Slav¹, I. Stavarache¹, O. Cojocaru¹, V.S. Teodorescu^{1,2},
V.-A. Maraloiu¹, A.-M. Lepadatu¹, M.L. Ciurea^{1,2}, T. Stoica¹

1) National Institute of Materials Physics, 077125, Măgurele, Romania

2) Academy of Romanian Scientists, 050094, Bucharest, Romania

SiGeSn nanocrystals (NCs) in oxides are of considerable interest for photo-effect applications due to the fine-tuning of bandgap by quantum confinement in NCs. The increase in bandgap due to the quantum confinement effect can be compensated by Sn alloying. We thoroughly studied [1] SiGeSn NCs embedded in a nanocrystalline HfO₂ matrix, fabricated using magnetron co-sputtering deposition at room-temperature (RT) followed by rapid thermal annealing (RTA). The NCs were formed at temperatures in the range of 500–800 °C. RTA was performed to passivate the surfaces of SiGeSn NCs by embedding them in the HfO₂ matrix. The formation of NCs and β -Sn segregation was discussed in relation to the deposition and processing conditions, using HRTEM, XRD, and Raman spectroscopy studies. Spectral photosensitivity was extended to 2000 nm in the short-wavelength infrared (SWIR). Compared to similar results on GeSn NCs in SiO₂ matrix, the addition of Si enhances the thermal stability of SiGeSn NCs, while the use of HfO₂ matrix provides better passivation of the NCs increasing, thereby increasing the SWIR photosensitivity at RT. The high passivation offered by the HfO₂ matrix reduces recombination losses, enhancing device efficiency by the weak decrease of the photosensitivity from low (100 K) to RT. Furthermore, the increased thermal stability allows for higher processing temperatures without inducing Sn segregation, ensuring long-term reliability in practical applications. These results suggest that SiGeSn NCs embedded in an HfO₂ matrix are promising materials for SWIR optoelectronic devices (Fig. 1).

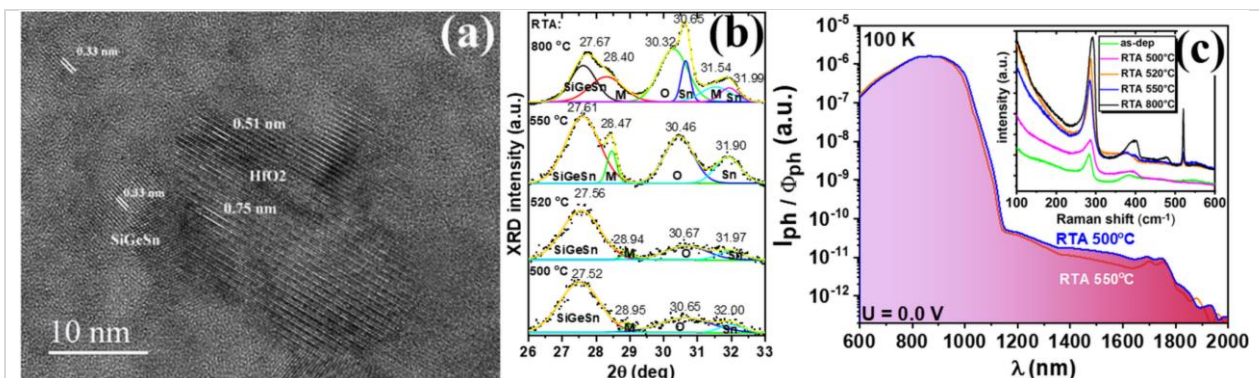


Fig. 1: (a) HRTEM image showing a 25 nm HfO₂ NC in contact with a smaller (10 nm) SiGeSn NC, in near [110] orientation; (b) Normalized deconvoluted XRD diffractograms for the samples annealed at different temperatures; (c) Spectral photosensitivity measured for zero bias voltage on ITO/SiGeSn-HfO₂/p-Si/Al diodes for RTA at 500 and 550 °C showing extended IR sensitivity to 2000 nm (Inset: Raman spectra of the laser-annealed as-deposited sample and the 500, 520, 550 and 800 °C RTA-treated films). Adapted from Ref. [1].

Reference:

- [1] I. Dascalescu, C. Palade, A. Slav, I. Stavarache, O. Cojocaru, V.S. Teodorescu, V.-A. Maraloiu, A.-M. Lepadatu, M.L. Ciurea, T. Stoica, *Enhancing SiGeSn nanocrystals SWIR photosensing by high passivation in nanocrystalline HfO₂ matrix*, Sci. Rep. 14 (2024) 3532.

Advances in Materials and Devices for Energy Systems, Extreme Environments, Space & Security

Versatile techniques based on the Thermionic Vacuum Arc (TVA) and laser-induced TVA methods for Mg/Mg:X thin films deposition: A review

R. Vladoiu^{1,2}, A. Mandes¹, V. Dinca¹, M. Tichy³, P. Kurdna³,
C.C. Ciobotaru⁴, S. Polosan^{2,4}

- 1) Dept of Physics, Faculty of Applied Sciences and Engineering, "Ovidius" University of Constanta, 900527, Constanta, Romania
- 2) Academy of Romanian Scientists, 050094, Bucharest, Romania
- 3) Department of Surface and Plasma Science, Faculty of Mathematics and Physics, Charles University, 180 00, Prague, Czech Republic
- 4) National Institute of Materials Physics, 077125, Măgurele, Romania

The recent developments in the Thermionic Vacuum Arc (TVA) and the Laser-Induced Thermoelectric Vacuum Arc (LTVA) technologies used for the deposition of magnesium (Mg) have been reviewed [1]. Mg and Mg-based alloy films deposited using a TVA method have multiple applications in the fields of metallic electrodes for diodes and batteries, as well as in active corrosion protection [1–4]. The improved laser-induced TVA (LTVA) method favours the crystallization processes of the deposited Mg-based films. This is because the interaction between laser and plasma discharge changes the thermal energy during photonic processes due to the local temperature variation. The morphology and surface properties of the obtained thin films differ between these two methods. While the amorphous character dominates in TVA thin films, resulting in a smooth surface, the LTVA method leads to rougher surfaces with pronounced crystallinity, and reduced surface energy. Both methods enable the production of uniform magnesium alloys, but the laser in the LTVA process, when interacting with the discharge plasma, plays a crucial role in controlling the ratio of added metals or elements. Thereby, the main advantage of methods based on TVA lies in the film's structure. TVA enables the formation of high-quality films with unique characteristics, such as smoothness and uniformity. In comparison, the thermal evaporation method provides a good evaporation rate but may not offer the same level of control over the structural features of the films. Increasing the evaporation rate results in more material reaching the sample surface within the same deposition time. This leads to a higher local temperature, which enhances the mobility of the atoms on the surface, promoting a more pronounced crystallization process. Consequently, films with better crystallinity and improved structural properties are obtained. Fig. 1a presents Scanning Electron Microscopy (SEM) micrographs of pure magnesium deposited on the Si/SiO₂ substrate using the LTVA method, while Fig. 1b displays micrographs of pure magnesium deposited on the same substrate by evaporation, both with a thickness of approximately 40 nm. At first glance, the evaporation method produces larger Mg hexagons, but without any apparent connection. In contrast, the LTVA sample exhibits a crystalline-amorphous structure with electrically conductive properties.

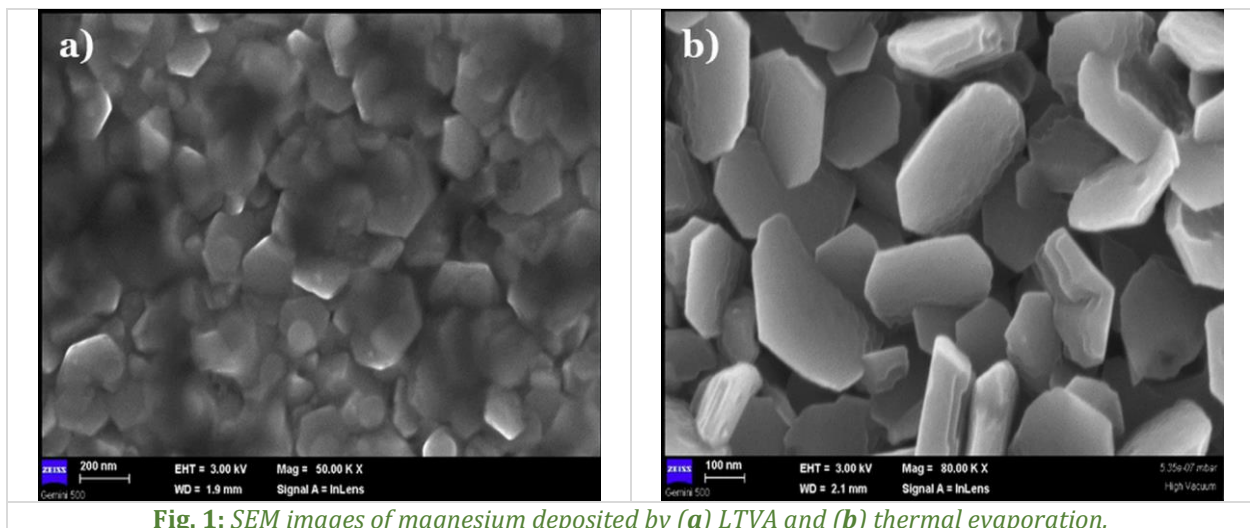


Fig. 1: SEM images of magnesium deposited by (a) LTVA and (b) thermal evaporation.

Fig. 2a shows the X-ray diffraction (XRD) patterns of Mg and Mg:Ag samples obtained by TVA and LTVA methods. The samples obtained by the TVA method confirm the formation of the Mg crystalline hexagonal phase P63/mmc (194) with the main peak 002 at $2\theta=34.62^\circ$, indicating the growth of the magnesium along the c -axis. The cell parameters for the Mg sample were refined using the hexagonal Mg structure as provided by the ICDD-PDF (card no. 35-0821), with $a = b = 3.19 \text{ \AA}$, $c = 5.18 \text{ \AA}$, $\alpha = \beta = 90^\circ$, and $\gamma = 120^\circ$. The mean crystallite size was evaluated to be in the range of 43–45 nm. For the sample obtained by LTVA, in addition to the two peaks corresponding to [002], the hump centered around 31° confirmed the partial amorphous character of these samples. The presence of Ag is indicated by the peak at 38.1° , which corresponds to the formation of the second crystalline phase, cubic silver (Fm3m) [106] or AgMg_3 crystalline structure. In this case, the mean crystallite is approximately 38 nm.

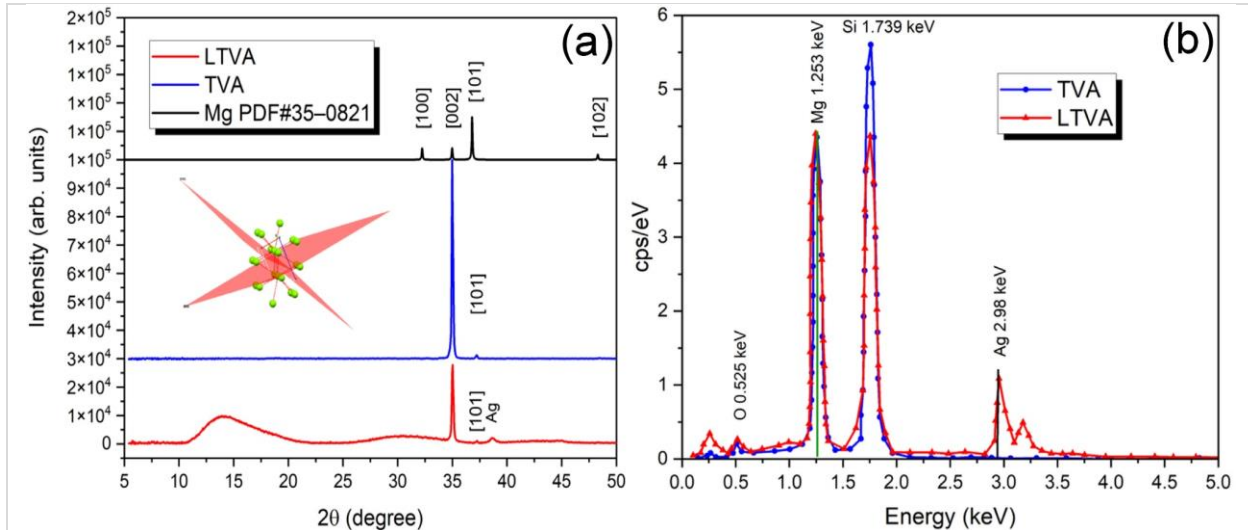


Fig. 2: (a) XRD patterns and (b) superposed EDXS spectra of the Mg:Ag deposited by TVA and LTVA methods. Adapted from Ref. [1].

For the LTVA sample, the hexagonal structure of Mg is slightly deformed, suggesting a mixture of hexagonal Mg with cubic Ag or AgMg_3 . This was further confirmed by energy dispersive X-ray spectroscopy (EDXS) analysis, where the composition shows significant intermixing between the Mg and Ag metals (Fig. 2b). The atomic composition determined by EDXS for the LTVA sample is provided in Table 1.

Table 1: EDXS results for the LTVA sample.

Element	At. number	Netto	wt. (%)	at. (%)
Ag	47	11076	62.18	27.03
Mg	12	25896	37.82	72.97

The samples' morphological structure was imaged using a SEM. From the SEM images, it is evident that the TVA sample exhibits higher crystallinity, with the dominant phase being the Mg structure (Fig. 3a, b). This result aligns with the hexagonal structures of metallic magnesium nanocrystals observed for this sample, which was the main finding from the XRD measurements.

The sheet resistance of magnesium and magnesium binary alloys could be crucial if used as thin-film electrodes in electroluminescent diodes or batteries. The dependence of the inner voltage vs. the applied current for TVA and LTVA is shown in Fig. 4. For a thickness of 100 nm, the resistivity is $\rho=71.5 \text{ n}\Omega\cdot\text{m}$ for the TVA sample and $\rho=83.6 \text{ n}\Omega\cdot\text{m}$ for the LTVA sample with a thickness of 197 nm. The higher resistivity of the TVA sample indicates a less electrically conductive thin film due to the structured Mg surface, whereas the lower resistivity of the Mg:Ag film suggests better conductivity owing to the presence of silver.

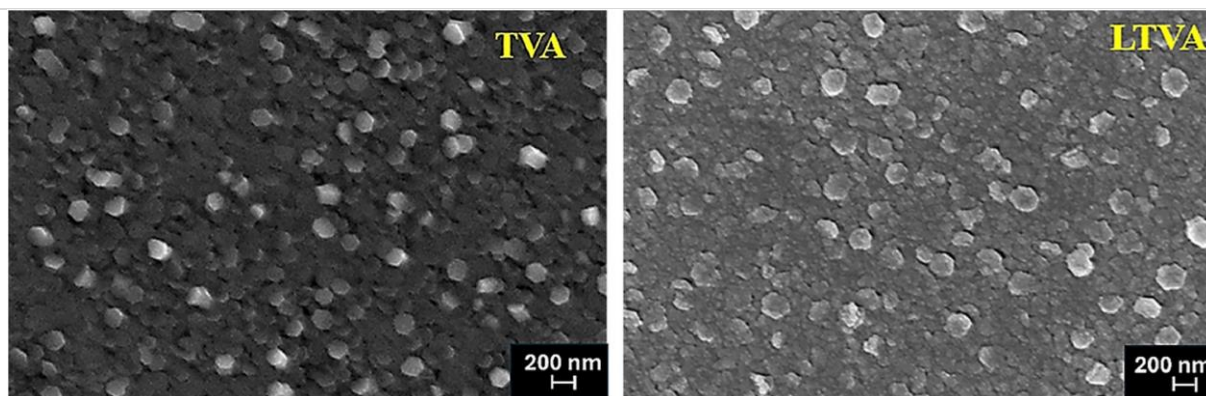


Fig. 3: SEM micrographs recorded on Mg:Ag samples deposited by TVA (left-hand side) and LTVA (right hand-side). Reproduced from Ref. [1].

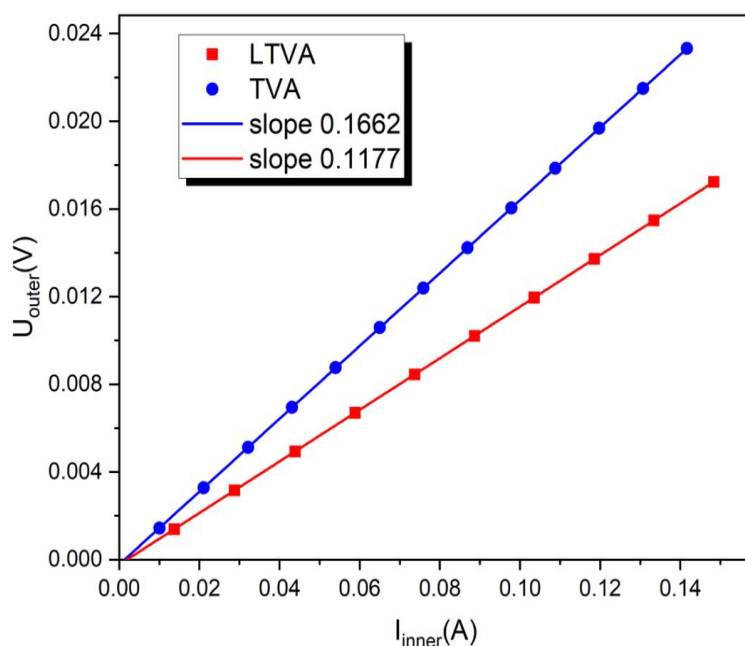


Fig. 4: Current-voltage characteristics of the Mg:Ag thin films. Reproduced from Ref. [1].

References:

- [1] R. Vladoiu, A. Mandes, V. Dinca, M. Tichy, P. Kudrna, C.C. Ciobotaru, S. Polosan, *Versatile techniques based on the Thermionic Vacuum Arc (TVA) and laser-induced TVA methods for Mg/Mg:X thin films deposition-A review*, J. Magnes. Alloy 12 (2024) 3115–3134.
- [2] R. Vladoiu, A. Mandes, V. Dinca, V. Ciupina, E. Matei, S. Polosan, *The synergistic effect of the laser beam on the thermionic vacuum arc method for titanium-doped chromium thin film deposition*, Coatings 12 (2022) 470.
- [3] V. Dinca, A. Mandes, R. Vladoiu, G. Prodan, V. Ciupina, S. Polosan, *Microstructural and morphological characterization of the cobalt-nickel thin films deposited by the Laser-Induced Thermionic Vacuum Arc Method*, Coatings 13 (2023) 984.
- [4] R. Vladoiu, A. Mandes, V. Dinca, P. Kudrna, M. Tichy, S. Polosan, *Magnesium-silver cathodes for efficient charge injection into Organic Light Emitting Diodes deposited by LTVA method*, J. Alloys Compd. 869 (2021) 159364.

A-site K-doped lanthanum manganite $\text{La}_{0.67}\text{Ba}_{0.33}\text{MnO}_3$ nanocrystallites for room-temperature micro-scale magnetic cooling

M. Oumezzine¹, A.M. Rostas², A.E. Bocirnea³, E.K. Hlil⁴, A.C. Galca³

- 1) *Faculty of Sciences of Monastir, University of Monastir, 5019, Monastir, Tunisia*
- 2) *National Institute for Isotopic and Molecular Technologies, 400293, Cluj-Napoca, Romania*
- 3) *National Institute of Materials Physics, 077125, Măgurele, Romania*
- 4) *Université Grenoble Alpes, CNRS, Grenoble INP, Institut Néel, 38000, Grenoble, France*

The mixed-valence perovskite-type lanthanum manganites $\text{La}_{1-x}\text{A}_x\text{MnO}_3$ ($\text{A} = \text{Sr}, \text{Ca}, \text{Ba}$) with strong electron-spin lattice correlations which leads to ferromagnetism, metallic conductivity, or colossal magnetoresistance, are proposed as emerging materials in magnetic refrigeration technology and applied spin-electronic devices. The double-exchange (DE) mechanism is the source of magnetic coupling in these materials, where the localized Mn t_{2g} spins are mediated by itinerant eg electrons hopping via oxygen-manganese metallic bonds ($\text{eg}(\text{Mn})-2p\sigma(\text{O})-\text{eg}(\text{Mn})$). The overlap between Mn 3d and O 2p orbitals depends on various parameters such as the oxidation state of the manganese ions, Mn–O–Mn bond angle, and the bond lengths of MnO_6 octahedra, which eventually affects the interactions between spin and lattice degrees of freedom. Stoichiometry, particle size, dimensionality, structure defects, and chemical disorder collectively impact the magnetic properties. Among the differently doped lanthanum manganites, whose properties can be influenced by B-site (divalent alkali metal) and A-site (trivalent alkali metal) substitutions in the ABO_3 perovskite structure, $\text{La}_{0.67}\text{Ba}_{0.33}\text{MnO}_3$ is of particular interest due to its ferromagnetic behaviour and significant magnetocaloric effect (MCE) above room-temperature (RT). Therefore, further exploration and research on optimizing this material through appropriate chemical substitution are needed to enhance its magnetic and MCE properties while tuning the transition temperature (Curie temperature, T_C) closer to RT.

Magnetic refrigeration (MR) may be quantitatively characterized in terms of the isothermal magnetic entropy change (ΔS_M) and cooling efficiency (the relative cooling power, RCP), which are typically found to be the highest across magnetic transitions, while a second-order magnetic phase transition (SMPOT) can also be an important criterion in deciding the practical use of these materials. Controlled doping of the A-site with simultaneous doping of monovalent, divalent, and trivalent elements is challenging, yet it holds the potential for outstanding results.

In our recent work [1], the modified Pechini method was used to prepare $\text{La}_{0.67}\text{Ba}_{0.33-x}\text{K}_x\text{MnO}_3$ material, where $\text{La}_{0.67}\text{Ba}_{0.33}\text{MnO}_3$ with T_C above RT was used as a matrix, and K-ions were doped into the A-site. Regarding the electronic structure, due to the valence difference in the A-site, the number of $\text{Mn}^{3+}/\text{Mn}^{4+}$ pairs in the materials is affected, leading to a significant change in the A-site ionic disorder of the crystal structure and the magnetic properties. The novelty of the presented report [1] lies in two key aspects: first, the correlation between the distortion of the MnO_6 octahedron, $\text{Mn}^{3+}/\text{Mn}^{4+}$ pairs, magnetic properties, and electron paramagnetic resonance as a function of the molar content of K-doping (x) (up to 20%). The second proposes a sample with optimized potassium doping concentration ($x = 0.20$) as a candidate for room temperature micro-scale magnetic cooling.

The $\text{La}_{0.67}\text{Ba}_{0.33-x}\text{K}_x\text{MnO}_3$ (with $x = 0, 0.05, 0.1$, and 0.2 ; in the following abbreviated with LBK0, LBK5, LBK10, and LBK20, respectively), belong to the R-3c (no. 167) space group having a crystallographic rhombohedral crystal structure, no secondary phases being discerned within the XRD limits (Fig. 1). The peaks shift to higher angles with increasing K content, indicating a decrease in the unit cell volume. Rietveld refinement of the experimental data showed that by substituting the Ba^{2+} ions with K^+ ($0.0 \leq x \leq 0.20$) increases the average A-site ionic radius from 1.299 to 1.316 Å and raises the A-site ionic disorder (σ^2) from 14.31×10^{-2} to 20.78×10^{-2} Å². The Mn–O–Mn bond angle θ decreases, whereas an inverse trend is seen in the bond length dMn–O. Increased randomness in the displacement of oxygen atoms from their average crystallographic positions due to lattice strains, more precisely, the increasing the distortion of the MnO_6 octahedra, favours the eg-electrons localization, while attenuating the strength of the double exchange (DE) interaction between Mn^{3+} and Mn^{4+} ions.

The temperature-dependent DC magnetization (M - T) at a 500 Oe applied magnetic field in the 3–400 K temperature range is measured in the field-cooled mode (Fig. 1). A transition from a low-temperature ferromagnetic phase to a high-temperature paramagnetic phase was evident. The T_C is the temperature corresponding to the derivative of the magnetization as a function of temperature, dM/dT . The values of T_C are lower when K concentration is larger, inferring that the existence of the K^+ ions in the A-site of the crystal lattice tends to weaken the double exchange (DE) magnetic interactions. The enhancement of the size mismatch of the A-cations induces the localization of eg-electrons, thereby decreasing the T_C values of the compounds.

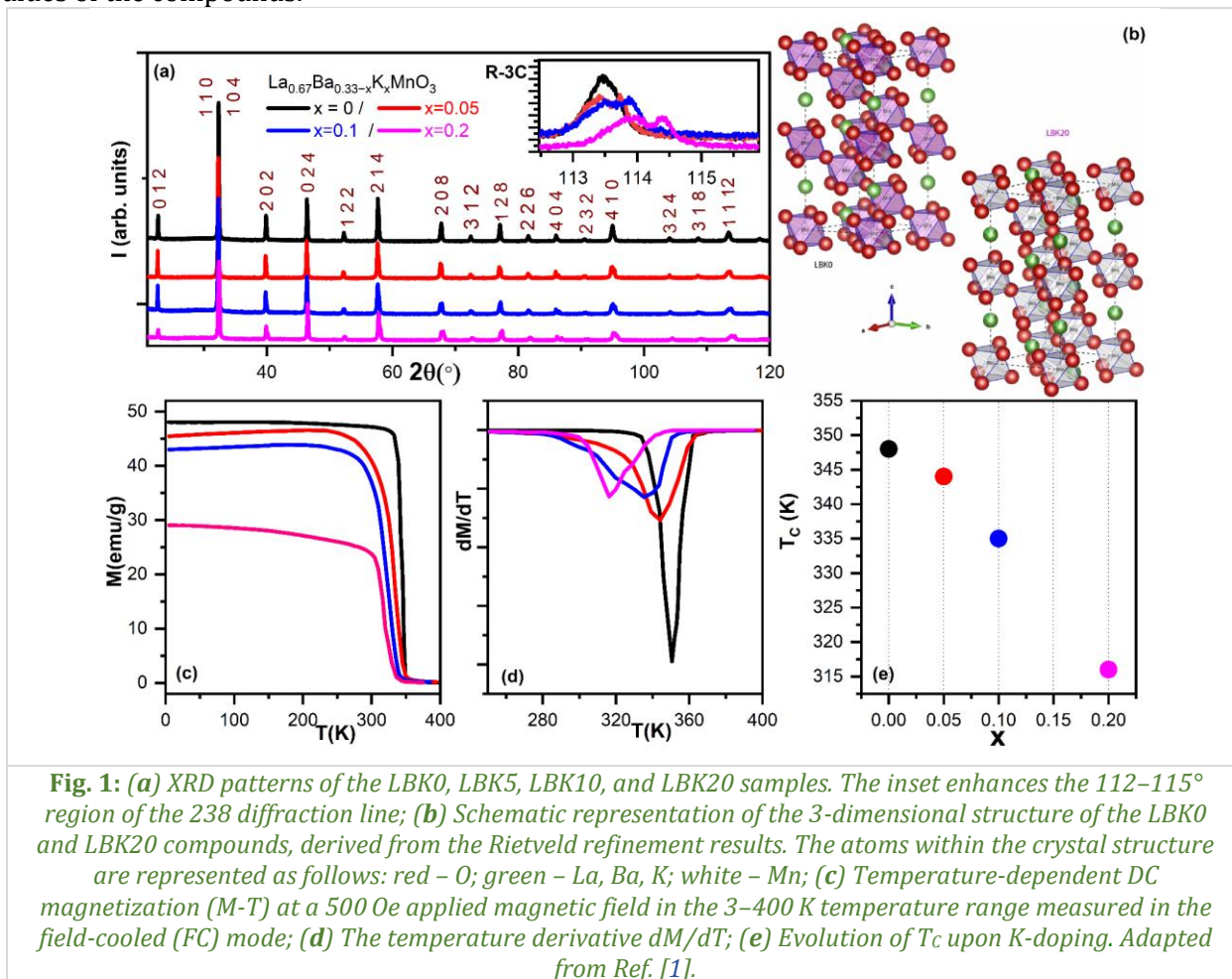
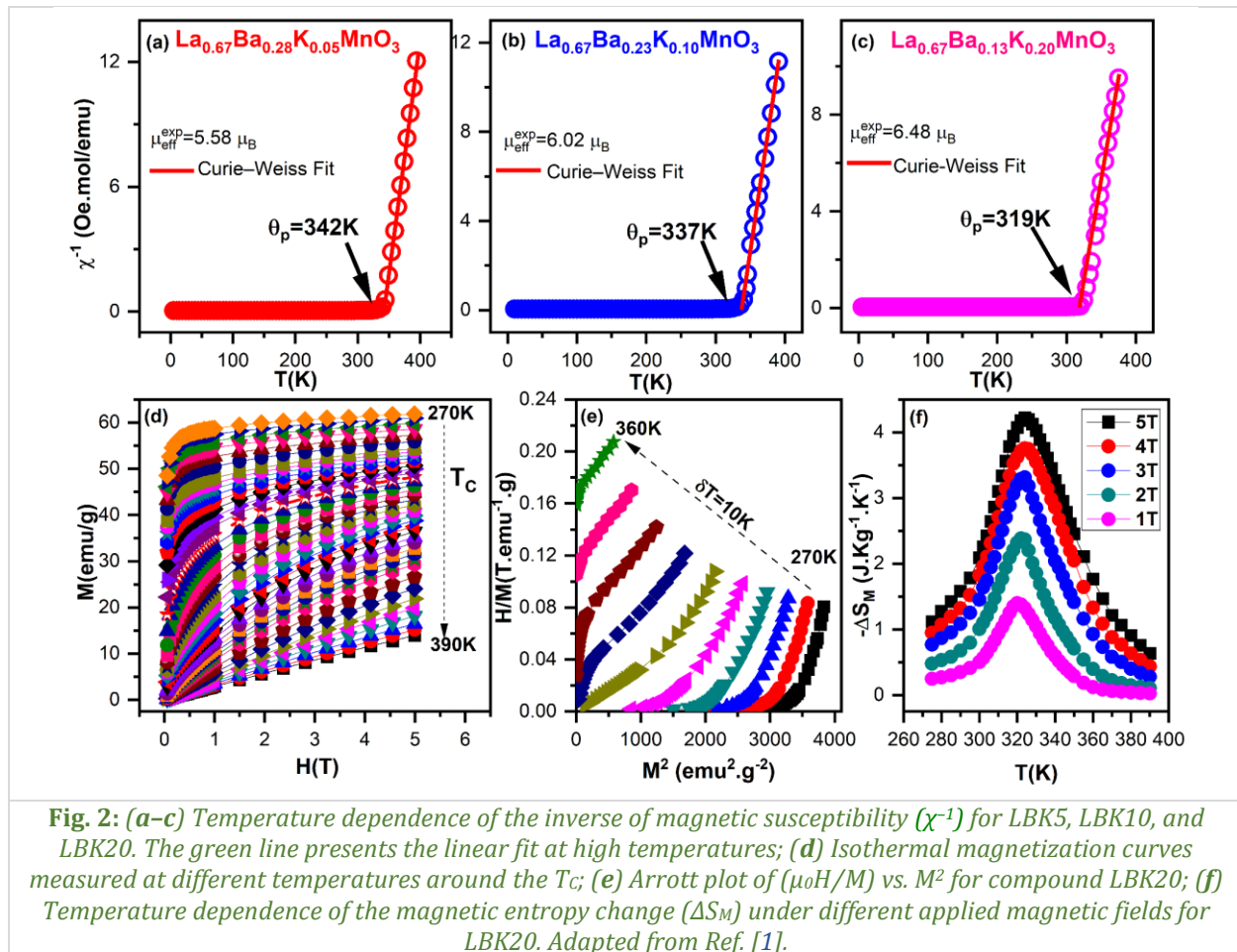


Fig. 1: (a) XRD patterns of the LBK0, LBK5, LBK10, and LBK20 samples. The inset enhances the 112–115° region of the 238 diffraction line; (b) Schematic representation of the 3-dimensional structure of the LBK0 and LBK20 compounds, derived from the Rietveld refinement results. The atoms within the crystal structure are represented as follows: red – O; green – La, Ba, K; white – Mn; (c) Temperature-dependent DC magnetization (M - T) at a 500 Oe applied magnetic field in the 3–400 K temperature range measured in the field-cooled (FC) mode; (d) The temperature derivative dM/dT ; (e) Evolution of T_C upon K-doping. Adapted from Ref. [1].

The inverse magnetic susceptibility (χ^{-1}) as a function of the temperature for the LBK5, LBK10, and LBK20 samples, along with the calculated curves deduced from the Curie-Weiss equation $1/\chi = (T - \Theta_p)/C$, and the Curie-Weiss parameters (Θ_p and C), as well as the experimental value of the effective paramagnetic moments, are presented in Fig. 2. The obtained effective magnetic moment values are considerably lower than the experimental ones (Table 1), underlying the presence of short-range FM interactions in the paramagnetic state (above T_C), which is commonly observed in manganites. Selecting the sample with T_C closest to RT is crucial for studying the effect of K^+ substitution of the MCE in the LBK system.



In a magnetic field of 5 T, the RCP value of the LBK20 sample is 225 J/kg (1400 mJ/cm³·K), which is 55% of that of pure Gd, the prototype magnetic refrigerant material (RCP = 410 J/kg). The obtained value is higher than that of polycrystalline manganites doped with K-ions at A sites. Our results indicate that the studied compound is promising for RT micro-scale magnetic cooling.

Table 1: Values of the Curie temperature (T_c), Curie-Weiss temperature (θ_p), experimental and theoretical effective paramagnetic moment, Mn–O bond length, Mn–O–Mn bond angle, Mn⁴⁺/Mn³⁺ ratio, and intrinsic size disorder (obtained from Rietveld refinement) for $\text{La}_{0.67}\text{Ba}_{0.33-x}\text{K}_x\text{MnO}_3$ (with $x = 0, 0.05, 0.1$, and 0.2).

Sample	T_c (K)	θ_p (K)	μ_{expeff} (μ_B)	μ_{theoreff} (μ_B)	$d_{\text{Mn-O}}$ (Å)	$\theta_{\text{Mn-O-Mn}}$ (°)	Mn ⁴⁺ /Mn ³⁺	σ^2 (10 ⁻² Å)
LBK0	348	352	5.43(2)	4.58(2)	1.959	173	0.4	14.31
LBK5	344	342	5.58(2)	4.53(2)	1.961	170	0.5	15.98
LBK10	335	337	6.02(2)	4.49(2)	1.965	167	0.6	17.61
LBK20	316	319	6.48(2)	4.17(2)	1.966	164	0.9	20.68

Reference:

- [1] M. Oumezzine, A.M. Rostas, A.E. Bocirnea, E.K. Hlil, A.C. Galca, A-site K-doped lanthanum manganite nanocrystalline $\text{La}_{0.67}\text{Ba}_{0.33}\text{MnO}_3$ for room-temperature micro-scale magnetic cooling, J. Alloys Compd. 976 (2024) 173257.

Kesterite to stannite phase transition and band gap engineering in $\text{Cu}_2\text{Zn}_{1-x}\text{Co}_x\text{SnS}_4$ thin films

E. El Mahboub¹, O. El Khouja², A.E. Bocirnea², S. Zakaria¹, A.C. Galca²,
M. Mansori¹, A. El Hichou¹

- 1) *Faculté des Sciences et Techniques Marrakech, Cadi Ayyad University, 4000, Marrakesh, Morocco*
- 2) *National Institute of Materials Physics, 077125, Măgurele, Romania*

The partial substitution of zinc in the CZTS crystal lattice could enhance the open circuit voltage (V_{oc}) in photovoltaic cells as consequence of a reduced density of point and defect clusters (CuZn and ZnCu). Cobalt (Co), a suitable environmentally friendly substitute for Zinc (Zn), has a stable +2 oxidation state and possesses different cation radii compared to Zn and copper (Cu). The incorporation of Co into the CZTS crystal lattice could favourably alter the band gap, potentially increasing light absorption and enhancing solar cell efficiency. The phase transition in the electronic structure from Kesterite to Stannite can also result from the partial substitution of Zn by transition metal ions, which induces a change in the ordering of cations in the tetragonal sublattice.

In a recent study [1], the phase transition from CZTS to CCTS, as well as the electronic structure transition (from Kesterite to Stannite), was investigated by exploring the effect of partial substitution of Zn with Co in $\text{CZn}_{1-x}\text{Co}_x\text{TS}$ thin films grown by spin coating, with x varying from 0 to 0.6.

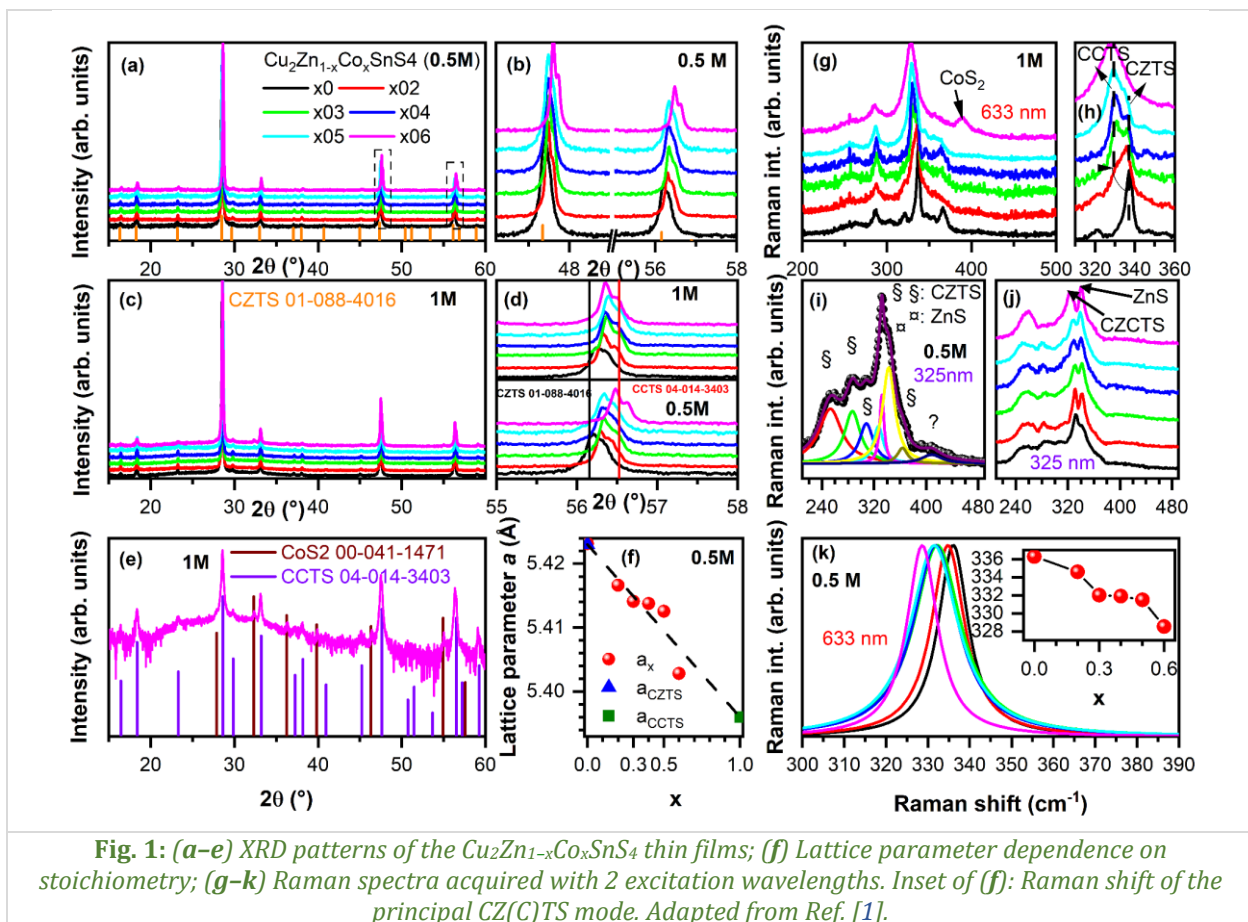


Fig. 1: (a–e) XRD patterns of the $\text{Cu}_2\text{Zn}_{1-x}\text{Co}_x\text{SnS}_4$ thin films; (f) Lattice parameter dependence on stoichiometry; (g–k) Raman spectra acquired with 2 excitation wavelengths. Inset of (f): Raman shift of the principal CZ(C)TS mode. Adapted from Ref. [1].

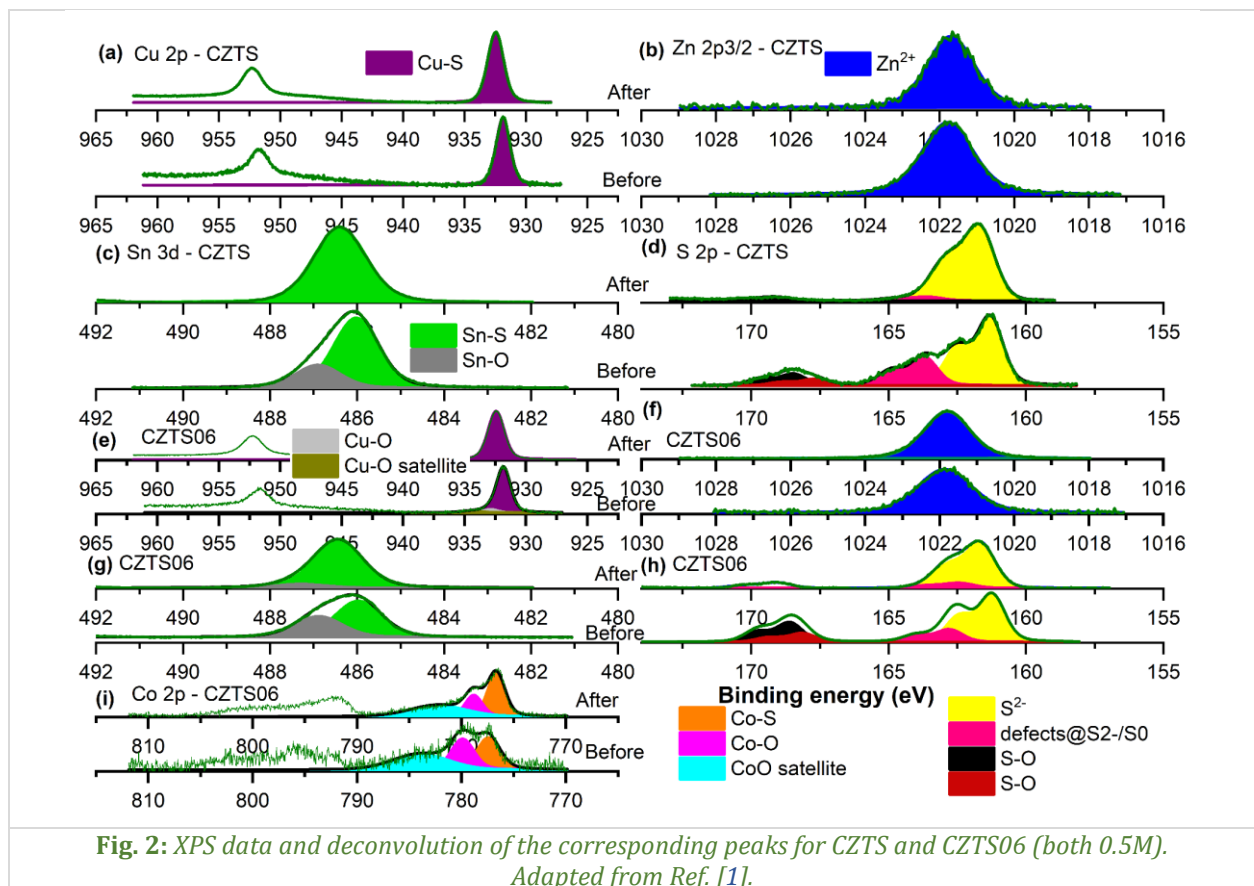
$\text{CuCl}_2 \cdot 2\text{H}_2\text{O}$ (99.0%), $\text{Co}(\text{CH}_3\text{COO})_2 \cdot 2\text{H}_2\text{O}$ (99.99%), $\text{Zn}(\text{CH}_3\text{COO})_2 \cdot 2\text{H}_2\text{O}$ (99.0%), $\text{SnCl}_2 \cdot 2\text{H}_2\text{O}$ (98.0%), and thiourea (99.0%) were added with 0.5 M and 1 M molarity into the solvent 2-methoxyethanol. The thiourea was solubilized separately and then mixed to obtain a yellow and homogenous solution. The resulting solution was kept under stirring at 60 °C for 30 min. The molar ratio used was $\text{Cu}:(\text{Zn}+\text{Co}):\text{Sn}:\text{S} = 2:1:1:8$. An excess of thiourea was added to potentially reduce oxidation and sulphur deficit in the

films. CZnCoTS Thin films were growth on cleaned glass substrates (soda lime glass) by spin coating at 3500 rpm for 30 s, followed by drying at 280 °C for 10 min to completely thermally decompose the metal-thiourea complexes and eliminate any organic remnants. This process was repeated four times to achieve a suitable thickness. Finally, all the thin films were sulfurized under nitrogen atmosphere with 0.6 g of sulphur powder at 550 °C for 1 h.

All $\text{Cu}_2\text{Zn}_{1-x}\text{Co}_x\text{SnS}_4$ thin films crystallized in tetragonal structure. Both series of thin films, with 0.5 M and 1 M molarity (Fig. 1), were polycrystalline and isotropic oriented. The shift of the 220 and 321 diffraction lines towards higher 2θ angles with increasing the Co concentration underscores the incorporation of Co into the CZTS lattice and the reduction of crystal lattice parameters due to the substitution of Zn^{2+} by Co^{2+} , which has a smaller ionic radius. The secondary phase CoS_2 was detected by both XRD and Raman spectroscopy only in films with higher Co concentration, obtained from the 1 M solution.

The most intense Raman peak, located around 336 cm^{-1} – 328 cm^{-1} , is attributed to the vibration of the sulphur atom surrounded by Zn/Co and Sn. The position of the characteristic A1 vibration mode as a function of cobalt doping (Fig. 1) followed the transition from Kesterite to Stannite. In the case where the 1 M solution was used in preparation of the films, the coexistence of the two phases is inferred from the Raman signature of the two different modes. Exciting with 325 nm, the Kesterite/Stannite split is not as visible due to larger line broadening, while the Raman mode of ZnS increased in intensity as the Co concentration rises, indicating that the formation of the Stannite phase becomes more favourable as Co is the preferred M^{2+} cation.

Fig. 2 shows the X-ray photoelectron spectroscopy (XPS) results for the CZTS and $\text{CZn}_{0.4}\text{Co}_{0.6}\text{TS}$ samples, respectively. All samples were measured before and after cleaning for 10 min of argon ion sputtering under vacuum, at a pressure of 10^{-5} mbar, with 3 keV energy and 10 mA current. The specific shake-up lines of Cu^{2+} were not visible for CZTS surface, indicating that Cu is in the +1-oxidation state, except for the as-introduced CZTS06 surface, which shows partial oxidation of copper near the top of the sample. The XPS profile of Sn $3d_{5/2}$ was deconvoluted with a peak at 486 eV, associated to the Sn-S bond, and a smaller component corresponding to the Sn-O bond. However, after the removal of the oxidized surface, tin oxide is less present or eventually absent. Thus, it can be concluded that surface oxidation is almost completely removed after argon ion sputtering.



The XPS profile of Co 2p presents three components: one at ~ 777 eV, another at ~ 779 eV, and a satellite specific to Co^{2+} at ~ 785 eV. The first component is associated to Co^{2+} in Co-S bonds, and the second one to Co^{2+} in Co-O.

From the optical characterization [1], the variation of the Urbach energy (E_u) as a function of Co concentration ranges from 223 meV for CZTS to 880 meV for CZTS04, with a plateau of 0.7 for other concentrations. This indicates an increase in lattice disorder with the introduction of Co, as well as a structural change from Kesterite to Stannite. The band gap (E_g) of the pure CZTS thin film was determined to be 1.47 eV, decreasing by Co incorporation to a minimum value of 1.17 eV at $x=0.4$. Beyond this point, the E_g increased to approximately 1.40 eV at $x=0.6$.

The results of these investigations provide a better understanding of cobalt alloying in CZTS. First, the change in metal precursor concentration affects both the concentration and microstructure of the films. Co is highly soluble in the CZTS lattice but significantly increases the disorder, leading to higher Urbach energies, which negatively impact the performance of the solar cells.

Another important aspect concerns the substrate as well as the thermal treatment conditions. In the present study, the sulfurization treatment was done in a quartz tube, while the best results are reported when using a confined space (e.g., a graphite box), where the evaporation of SnS and ZnS phases during the thermal treatment is suppressed by the vapor pressure created in a closed box. Additionally, an in-depth concentration gradient might be inhibited in such a setup. From our experience, under the same thermal treatment conditions as in the present study, Sn and Zn have higher concentrations at the surface than in the bulk and at the substrate/absorber interface. The nature of the substrate also plays a role. The diffusion of alkaline elements from the substrate (soda-lime glass) is inherent and impacts the microstructure as well as the formation of secondary phases. The use of different substrates, such as Mo/glass, might yield different results. It should also be noted that doping with alkaline elements is an uncontrolled process in this case.

Cationic substitution using isoelectronic elements from the same group of the Periodic Table is logically the preferred option, such as replacing Zn with Cd. However, less conventional options, such as transition metals (Fe, Co), are detrimental to the desired Kesterite lattice and, consequently, to the photovoltaic properties of the solar cells. These substitutions are still not competitive with other alternatives.

In conclusion, the incorporation of cobalt cation in the CZTS crystalline lattice, as well as the phase transition from Kesterite to Stannite, were confirmed by the XRD and Raman spectroscopy data. The XRD pattern showed peak shifting toward higher 2θ angles with increasing Co concentration, indicating a decrease in lattice parameters. The red shift of Raman peaks by increasing x from 0 to 0.6, confirmed the phase transition. The pure CZTS has a band gap of 1.47 eV, while for $\text{CZn}_{0.6}\text{Co}_{0.4}\text{TS}$, the gap was 1.17 eV, indicating that the incorporation of Co cations produces a red shift in the band-to-band transition energy.

Reference:

- [1] E. El Mahboub, O. El Khouja, A.E. Bocirnea, S. Zakaria, A.C. Galca, M. Mansori, A. El Hichou, *Investigation of kesterite to stannite phase transition and band gap engineering in $\text{Cu}_2\text{Zn}_{1-x}\text{Co}_x\text{SnS}_4$ thin films prepared by sol-gel spin coating*, Appl. Surf. Sci. 672 (2024) 160848.

Comprehensive study of chromium phosphates, dielectric properties and supercapacitor device

**Z. Mighri^{1,2}, R.E. Patru², I.D. Yildirim³, L.N. Leonat², O. El Khouja², E. Erdem³,
H. Nasri¹, A.M. Rostas⁴, A.C. Galca²**

1) *University of Monastir, Faculty of Sciences of Monastir, 5019, Monastir, Tunisia*

2) *National Institute of Materials Physics, 077125, Măgurele, Romania*

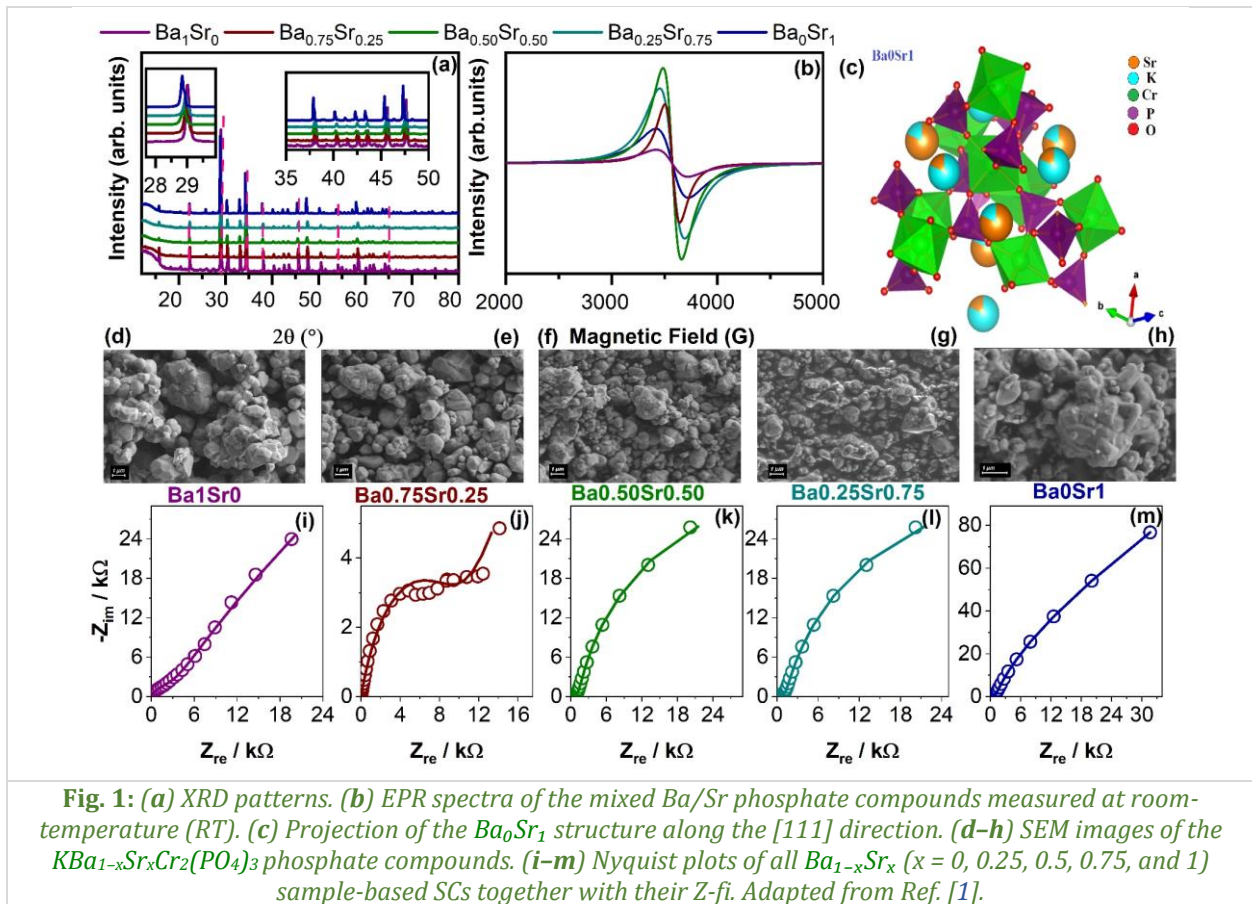
3) *Faculty of Engineering and Natural Sciences, Sabanci University, 34956, Tuzla, Istanbul, Turkey*

4) *National Institute for Isotopic and Molecular Technologies, 400293, Cluj-Napoca, Romania*

Energy storage is a critical issue in today's society, especially with the increase in reliance on renewable energy sources such as solar and wind power. Supercapacitors (SCs), which combine the advantages of electrical double layer capacitors (EDLCs), pseudo-capacitors (PCs), and hybrid Supercapacitors (HSCs) are emerging as promising solutions. While pseudo-capacitors rely on redox reactions, EDLCs store energy electrostatically at the electrode-electrolyte interface. There is great potential to achieve higher energy densities and improved cycling stability in hybrid devices that integrate both mechanisms, such as lithium-ion and sodium-ion capacitors. However, EDLCs suffer from limited ion-accessible surface area and poor carbon conductivity, restricting their capabilities. In contrast, redox SCs based on metal oxides, hydroxides, sulphides and phosphates have attracted attention for their superior electrochemical properties. In particular, metal phosphates have shown great promise for energy storage applications due to their unique structural characteristics and favourable electrochemical performance. The incorporation of strontium into Langbeinite phosphates has been shown to enhance electrical conductivity, improving their overall performance in capacitor applications [1].

Among the alkali metal ions, potassium (K^+) has attracted attention for its electrochemical properties, which are comparable to those of lithium and sodium. Potassium-ion batteries (PIBs) have emerged as a promising alternative to lithium-ion and sodium-ion batteries due to the environmental safety, high voltage operation and superior ionic conductivity of K^+ . The lower desolvation energy of K^+ ions, leads to faster diffusion, which improves the transport properties in such storage systems [2]. For this purpose, a comprehensive study was conducted, focusing on the synthesis and characterization of potassium transition metal phosphates with open framework structures, such as chromium-substituted Langbeinite phosphates, specifically $KBa_{1-x}Sr_xCr_2(PO_4)_3$, $KNiCr(PO_4)_2$, $KCoCr(PO_4)_2$, and $KCuCr(PO_4)_2$. This study investigates, on one hand, the effect of substituting barium with strontium and chromium with iron on the electrical properties of the materials. On the other hand, it also addresses the influence of ionic size on the structural and electrical properties of these materials by replacing Ni^{2+} cations with Co^{2+} and Cu^{2+} .

The synthesized samples were characterized by powder X-ray diffraction (XRD) using a Bruker-D8 Advance diffractometer in Bragg–Brentano geometry. Complete refinement of the powder XRD data was performed with the FullProf software using the Rietveld method to determine the structural model of the materials. First, the $KBa_{1-x}Sr_xCr_2(PO_4)_3$ compounds are closely related to the Langbeinite-type compounds identified as monophasic, cubic, with the $P 213$ space group (no. 198). The asymmetric unit has nine atomic positions, where the Cr atoms on axis 3 of the cubic lattice occupy two crystallographically independent sites labelled M(1) and M(2). The potassium and MII atoms ($M = Ba, Sr$) are statistically distributed with partial occupancy on two types of sites X(1) and X(2). The P atoms occupy just one type of site with tetrahedral coordination. A projection of this structure along the $[111]$ direction is represented in (Fig. 1).



Second, the $KMgCr(PO_4)_2$ materials have a monoclinic system with a $P2_1/n$ (no. 14) space group. These structures are an infinite assembly of $[MgCrP_2O_8]^-$ units, giving rise to large tunnels where K^+ cations are lodged. When Co^{2+} cations are replaced by Ni^{2+} and Cu^{2+} , the cell parameter " a " increases, while " b " decreases. This trend has been correlated with the ionic radius of each divalent cation. However, the " c " parameter shows a slight decrease, relating to the size of the monovalent A^+ cations ($A = Na, K, Rb$) located in the tunnels formed in the structure. This can be explained by the fact that only the K^+ cations occupy the tunnels in all the compounds (Fig. 2).

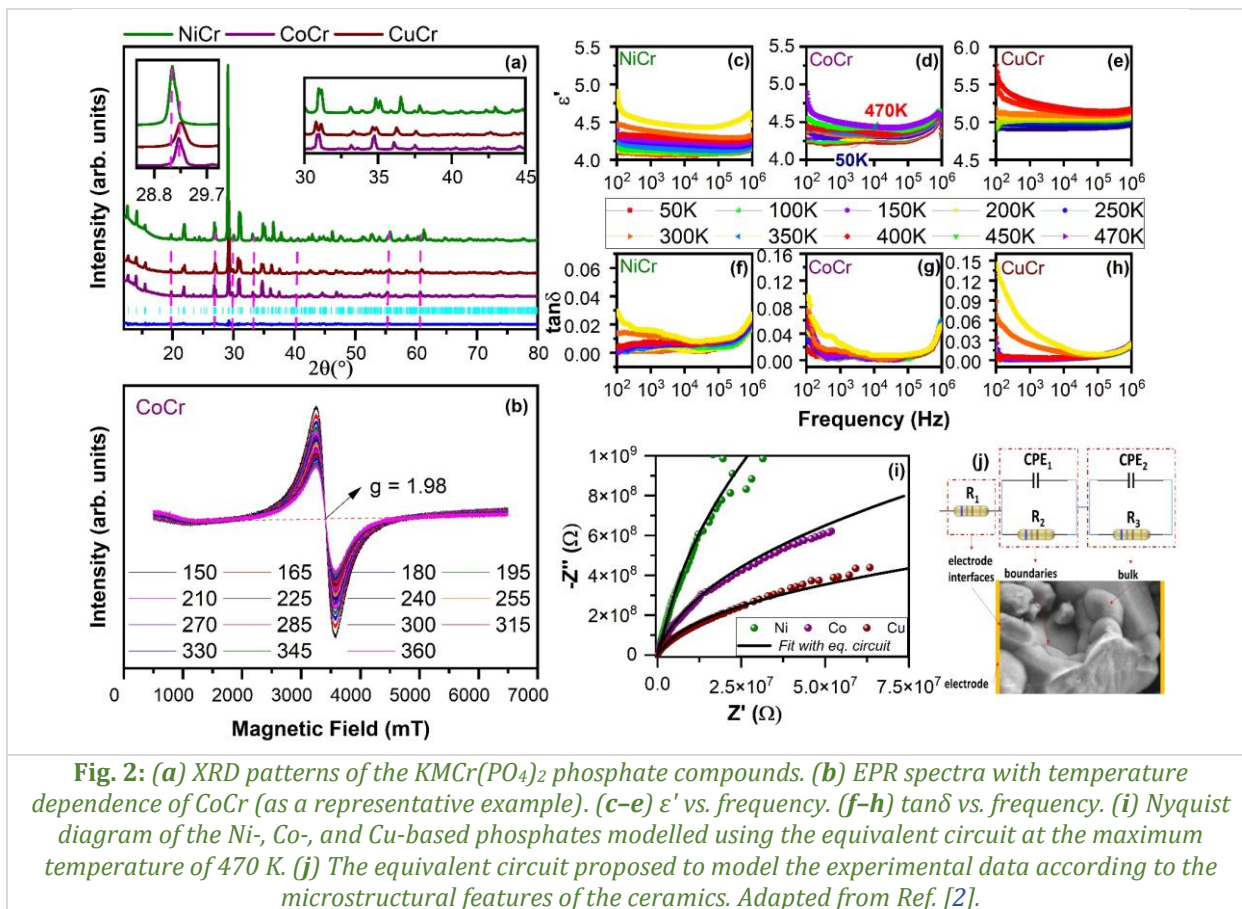
The EPR measurements carried out on the mixed Ba/Sr phosphate samples at RT present a single resonance line at $g_{eff} \sim 1.98$, characteristic of Cr^{3+} ($S = 3/2$) ions in an octahedral field. Only one broad EPR signal was observed. By substituting the Ba^{2+} ions with Sr^{2+} , the distortion of the CrO_6 octahedra decreases, leading to an increase of the EPR signal. At the same time, the distance between the Cr^{3+} centres decreases, which enhances the dipole–dipole interaction, broadening the EPR signal. The EPR results show that the compound $Ba_{0.5}Sr_{0.5}$ presents an equilibrium state of the MII+ centres, showing the highest EPR signal [1].

The EPR spectra of the CoCr, CuCr, and NiCr phosphates samples vary slightly in their line width, resonance field, and g -value. The peak-to-peak line width (H_{pp}) of the CoCr-based phosphate is around 32 mT, followed by CuCr with about 67 mT, and NiCr with the widest, approximately 115 mT. The g -values also vary for the different metal ions. The observed large line widths indicate strong exchange interactions, combined with high dipole-dipole interactions ($M^{2+}-M^{2+}$, $Cr^{3+}-Cr^{3+}$, and $M^{2+}-Cr^{3+}$), due to the high M^{2+} and Cr^{3+} contents [2].

The cyclic voltammetry (CV) technique was applied for all $KBa_{1-x}Sr_xCr_2(PO_4)_3$ samples to determine the charge storage mechanisms of the SCs. The CV shapes showed quasi-rectangular conically tapered shapes, displaying both EDLC and pseudocapacitive behaviour without clear redox peaks. The highest current values were achieved with the $Ba_{0.5}Sr_{0.5}$ sample. The calculated specific capacitance, shows that the highest values was achieved for $Ba_{0.5}Sr_{0.5}$ at 1 mV/s.

According to the Nyquist plots, $Ba_{0.5}Sr_{0.5}$ has the lowest impedance values, followed by $Ba_{0.75}Sr_{0.25}$. Also, in the high-frequency regions of the Nyquist plots, no semicircles have been observed, indicating fast-ion diffusion and negligible charge-transfer resistances (R_{ct}). From the galvanostatic charge–discharge

(GCD) curves, the $\text{Ba}_{0.50}\text{Sr}_{0.50}$ sample showed the best and most promising results among all samples. The performed electrochemical measurements were valuable in clearly demonstrating how the substitution with smaller Sr ions changes the electrochemical properties of the proposed material. The study of the dielectric properties of the developed $\text{KMCr}(\text{PO}_4)_2$ materials, showed that they exhibit a modest Maxwell-Wagner response, with stable permittivity values for NiCr and slightly higher values for CoCr and CuCr. The a.c. conductivity remained low across temperatures, with copper-based phosphates demonstrating the highest conductivity and the fastest charge movement, while nickel-based phosphates showed slower dielectric relaxation. Nickel-based phosphates tended to relax more slowly, whereas cobalt and copper-based phosphates enabled faster polarization and depolarization. Consequently, copper-based phosphates exhibited the most efficient charge movement and the highest a.c. conductivity compared to those with nickel or cobalt. The good stability and conductivity of the proposed phosphate-based materials make them ideal candidates for energy storage systems (Fig. 2).



References:

- [1] Z. Mighri, I.D. Yildirim, L.N. Leonat, O. El Khouja, E. Erdem, H. Nasri, A.C. Galca, A.M. Rostas, *Hybrid supercapacitors based on X-site Ba(II) ions substituted by Sr(II) in Langbeinite-type phosphates*, *Materialia* 36 (2024) 10214.
- [2] Z. Mighri, R.E. Patru, L.N. Leonat, O. El Khouja, H. Nasri, A.M. Rostas, A.C. Galca, *Effect of transition metal ions on the dielectric properties of chromium potassium phosphates*, *J. Alloys Compd.* 1009 (2024) 176870.

MnBi-FeSiB hard-soft magnetic nanocomposites

A. Alexandru-Dinu^{1,2}, C. Locovei^{1,2}, C. Bartha¹, M.A. Grigoroscuta¹, M. Burdusel¹, A. Kuncser¹, P. Palade¹, G. Schinteie¹, N. Iacob¹, W. Lu³, D. Batalu⁴, P. Badica¹, V. Kuncser¹

- 1) National Institute of Materials Physics, 077125, Măgurele, Romania
- 2) Faculty of Physics, University of Bucharest, 077125, Măgurele, Romania
- 3) Shanghai Key Lab. of D&A for Metal-Functional Materials, School of Materials Science & Engineering, Tongji University, 201804, Shanghai, China
- 4) Faculty of Materials Science and Engineering, National University of Science and Technology Politehnica Bucharest, 060042, Bucharest, Romania

RE-free permanent magnets of high performance are required in many technological domains. One candidate is MnBi. To enhance the energy of the magnet, composites with soft and hard magnetic components are of much interest. In our work [1], bulk nanocomposites of hard MnBi mixed with different amounts of soft FeSiB ($\text{Mn}_{55}\text{Bi}_{45} + x \text{ wt. \% of Fe}_{70}\text{Si}_{10}\text{B}_{20}$, $x = 0, 3, 5, 10, 20$) were prepared by spark plasma sintering. TEM image of MnBi-0 sintered sample show flake-like grains (up to 250 nm) which exhibit a compositional variation of the ratio Mn/Bi in the range 0.33 – 2.9, *i.e.*, larger than in the raw powder, in the range 0.5 – 1.65 (Fig. 1). Magnetically, these grains will perform in a different manner, due to different local mechanisms (Fig. 1). According to the XRD investigations, the main phases observed are MnBi and MnBi-nano.

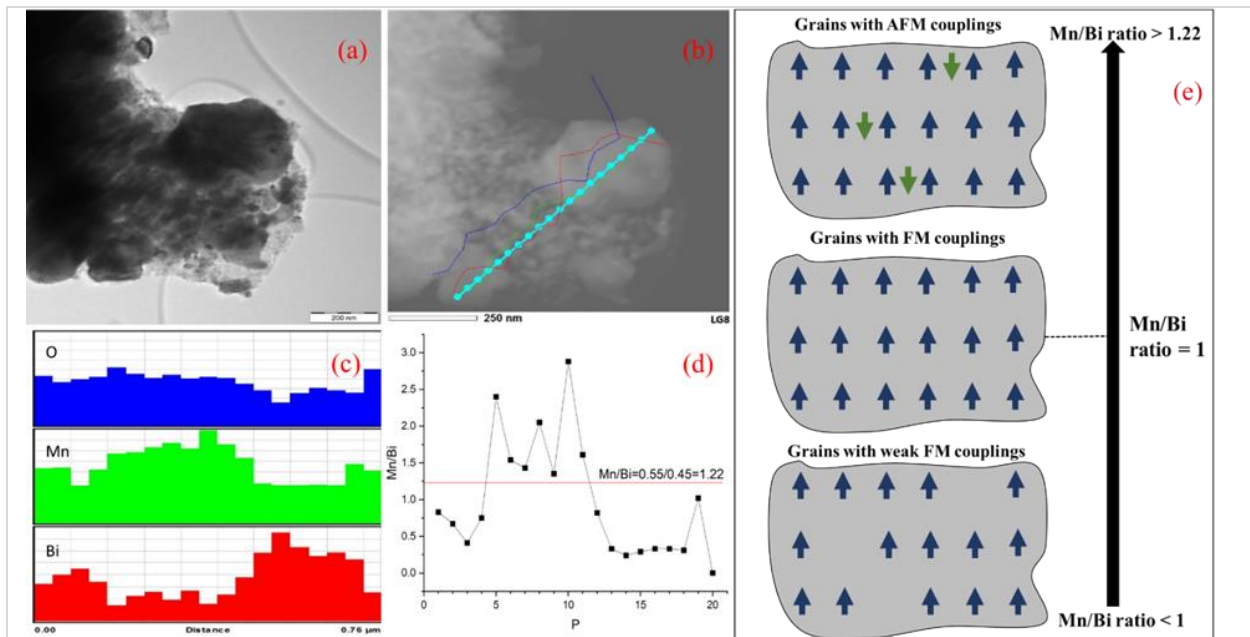


Fig. 1: (a) TEM image of SPSed MnBi-0 and (b) EDXS elemental composition measured along the indicated line; (c) Histograms of specific elements (Mn, Bi, and O) showing variation of composition along the EDXS line in (b); (d) Mn/Bi ratio determined along the EDXS composition line in (b) and using data from the histogram (d). In (d), the x-axis P shows the point number on the EDXS compositional line from (b), where P = 1 is the point on the left side and P = 20 is the point on the right side in (b). The designed atomic ratio $\text{Mn/Bi} = 55/45 = 1.22$, which approaches the average composition along the investigated micrometre size region, is indicated; (e) Schematic representation of Mn spins in Mn-Bi grains with MnBi ratio crossing the value of 1, *i.e.*, for Mn/Bi ratio lower than 1, weak ferromagnetic interactions are involved, whereas for Mn/Bi ratio higher than 1, a progressively increasing number of antiferromagnetic (AFM) interactions are involved.

Reproduced from Ref. [1].

The secondary phases were Bi and Bi_2O_3 . The lattice parameters of MnBi are not sensitive to FeSiB presence, suggesting no substitutional or interstitial site occupancy in the crystal lattice of MnBi (Table 1). However, the introduction of FeSiB reduced the decomposition of MnBi phases compared to the

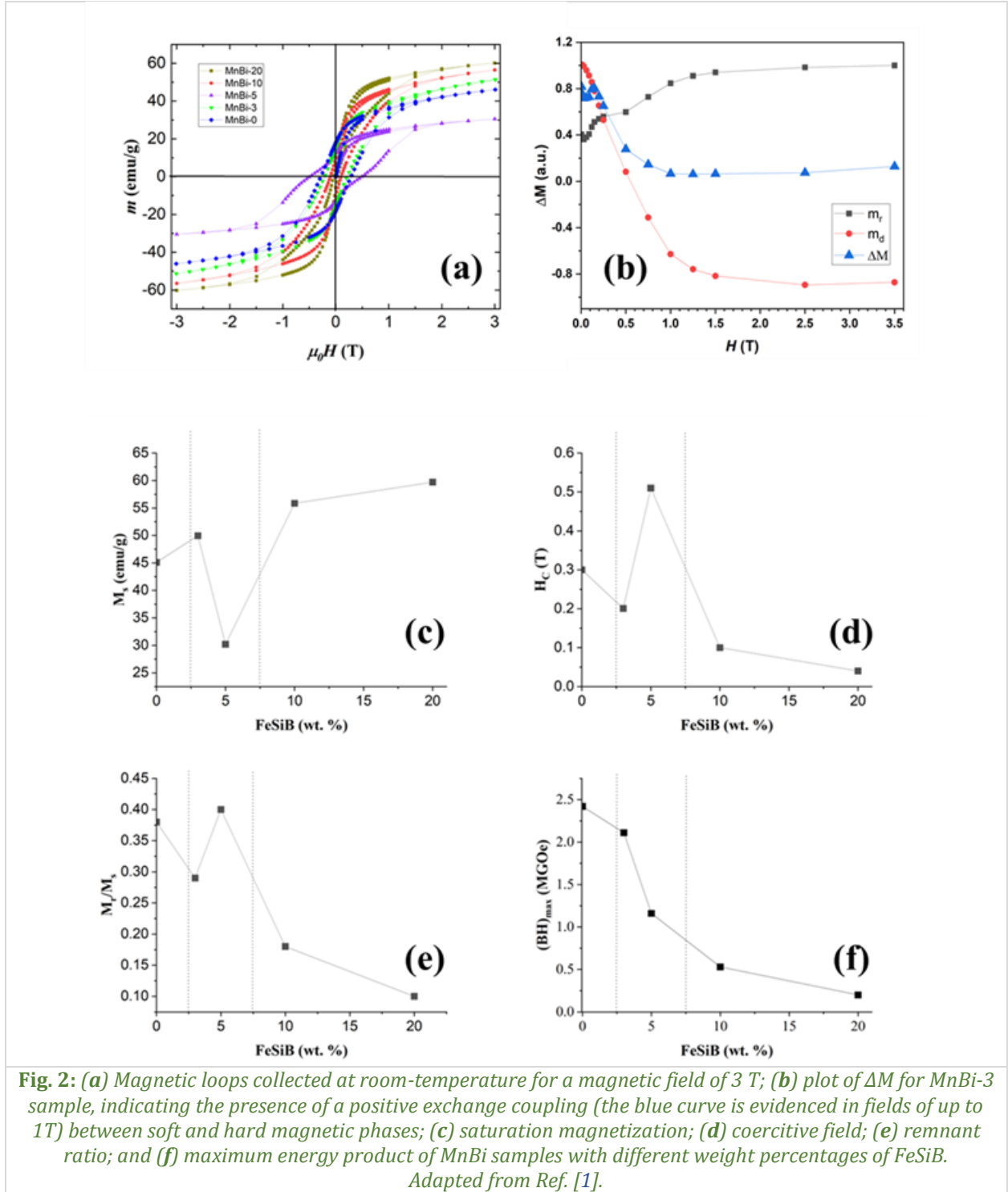
MnBi-0 sample, resulting in a lower overall amount of Bi or Bi₂O₃ in the composite samples. The two main effects of the FeSiB additive in the sintered composite samples are a reduced amount of Bi in the MnBi structure and an increased presence of the MnBi nanophase compared to MnBi-0.

Table 1: The constituent phases and their relative content of MnBi_x (where x = 3, 5, 10, 20 wt.% of FeSiB) as provided by the Rietveld refinements. Lattice parameters, crystal size, and lattice strain are also given.

Phase Sample	MnBi	Bi	MnBi-nano	Bi ₂ O ₃
MnBi-3	R = 79.9 wt.% a = 4.292 Å c = 6.112 Å D _{eff} = 144 nm $\langle \epsilon^2 \rangle^{\frac{1}{2}} = 2 \cdot 10^{-3}$	R = 14 wt.% a = 4.544 Å c = 11.867 Å D _{eff} = 61 nm $\langle \epsilon^2 \rangle^{\frac{1}{2}} = 2.3 \cdot 10^{-3}$	R = 6.1 wt.%	-
MnBi-5	R = 43.1 wt.% a = 4.289 Å c = 6.12 Å D _{eff} = 143 nm $\langle \epsilon^2 \rangle^{\frac{1}{2}} = 6 \cdot 10^{-4}$	R = 17.9 wt.% a = 4.546 Å c = 11.868 Å D _{eff} = 73 nm $\langle \epsilon^2 \rangle^{\frac{1}{2}} = 1.1 \cdot 10^{-3}$	R = 25.2 wt.%	R = 13.8 wt.% a = 7.740 Å c = 5.641 Å D _{eff} = 86 nm $\langle \epsilon^2 \rangle^{\frac{1}{2}} = 2.2 \cdot 10^{-3}$
MnBi-10	R = 61.6 wt.% a = 4.289 Å c = 6.119 Å D _{eff} = 147 nm $\langle \epsilon^2 \rangle^{\frac{1}{2}} = 8 \cdot 10^{-4}$	R = 26.3 wt.% a = 4.544 Å c = 11.868 Å D _{eff} = 75 nm $\langle \epsilon^2 \rangle^{\frac{1}{2}} = 2 \cdot 10^{-3}$	R = 12.1 wt.%	-
MnBi-20	R = 50 wt.% a = 4.288 Å c = 6.119 Å D _{eff} = 166 nm $\langle \epsilon^2 \rangle^{\frac{1}{2}} = 7 \cdot 10^{-4}$	R = 23.3 wt.% a = 4.545 Å c = 11.86 Å D _{eff} = 76 nm $\langle \epsilon^2 \rangle^{\frac{1}{2}} = 1.5 \cdot 10^{-3}$	R = 19.2 wt.%	R = 7.5 wt.% a = 7.744 Å c = 5.646 Å D _{eff} = 78 nm $\langle \epsilon^2 \rangle^{\frac{1}{2}} = 1.5 \cdot 10^{-3}$

As the FeSiB content increases, the saturation magnetization (Fig. 2c) increases for MnBi-3, MnBi-10, and MnBi-20 with values of 49.96 emu·g⁻¹, 55.85 emu·g⁻¹, and 59.71 emu·g⁻¹, respectively, compared to the corresponding magnetization of MnBi-0 (46 emu·g⁻¹). This is connected, on one hand, to the high saturation magnetization of the FeSiB, and, on the other hand, to a lower level of MnBi phase decomposition in the composite samples. On the contrary, with the M_s enhancement, H_c at room-temperature decreased with the increase of x. The samples exhibit exchange spring behaviour. For example, in Fig. 2b, the positive ΔM variation up to ~1 T for sample MnBi-3 indicates a ferromagnetic coupling between hard and soft magnetic components. An out of trend magnetic behaviour is displayed by MnBi-5 sample, resulting from the interplay between the higher MnBi nanophase content, which has larger coercivity, and the reduced exchange coupling effects.

The present study [1] demonstrates that fabrication of MnBi based nanocomposites by spark plasma sintering of powder mixtures rather than by melting techniques is a promising approach towards fabrication of high performance RE-free permanent magnets. For further progress, studies should focus on identifying optimal processing conditions and methods to refine the control of the magnetic properties of such nanomaterials. This includes utilizing exchange spring phenomena through the optimization of composition, morphology, grain size, crystallinity, and the design of specific grain boundaries.



Reference:

- [1] A. Alexandru-Dinu, C. Locovei, C. Bartha, M.A. Grigoroscuta, M. Burdusel, A. Kuncser, P. Palade, G. Schinteie, N. Iacob, W. Lu, D. Batalu, P. Badica, V. Kuncser, *Microstructure and coupling mechanisms in MnBi-FeSiB nanocomposites obtained by spark plasma sintering*, Sci. Rep. 14 (2024) 17029.

New growth mechanism of rhombohedral ZrO₂ thin film deposited on (111) Nb:STO

M.C. Istrate¹, C. Ghica¹, V. Lenzi², J.P.B. Silva², B. Šmíd³, V. Matolín³,
J.L. MacManus-Driscoll⁴, L. Marques²

- 1) National Institute of Materials Physics, 077125, Măgurele, Romania
- 2) University of Minho, 4710-057, Braga, Portugal
- 3) Charles University, 18000, Prague, Czech Republic
- 4) University of Cambridge, CB3 0FS, Cambridge, United Kingdom

Defect engineering has emerged as a powerful strategy for advancing ferroelectric thin films across various applications [1–4]. For example, the electromechanical response of ferroelectric BaTiO₃ thin films has been shown to improve with the presence of oxygen vacancies (OVs) [3]. Similarly, enhancing the concentration of intrinsic point defects (*e.g.*, Pb, Ti, OVs) has been demonstrated to boost the energy storage performance of 0.68Pb(Mg_{1/3}Nb_{2/3})O₃-0.32PbTiO₃ (PMN-PT) thin films [1]. Moreover, ferroelectric and ferroelastic domain walls have emerged as novel 2D topological defects with promising functionalities, potentially enabling the transition from nanoscale to atomic-scale electronics [5].

Since 2011, orthorhombic-phase (o-phase) Hf_xZr_{1-x}O₂ (HZO) thin films, with *x* varying from 0 to 1, have gained significant attention due to their remarkable ferroelectric properties at the nanoscale. These oxides are compatible with existing complementary metal-oxide-semiconductor (CMOS) technology while offering robust ferroelectric polarization. As a result, they have been widely explored for ferroelectric memory, field-effect transistors, energy storage, energy harvesting, and sensor applications. However, the presence of OVs is commonly linked to the "wake-up" effect, where pre-cycling is required to induce stable ferroelectric behavior. This poses challenges for integrating these materials into reliable memory technologies. Consequently, defect engineering, particularly the reduction or elimination of OVs has been employed to achieve wake-up-free HZO-based thin films.

In 2018, Y. Wei *et al.* reported a novel wake-up-free ferroelectric rhombohedral (r-phase) in Hf_{0.5}Zr_{0.5}O₂ thin films [6]. This phase was later observed in ZrO₂ films by Silva *et al.* [7]. However, the origin of the large ferroelectric polarization in these materials remains unclear, as strain-based theoretical models predict only moderate polarization [6,7]. More recently, direct oxygen imaging combined with oxygen voltammetry experimentally confirmed that OVs play a critical role in stabilizing the rhombohedral phase in Hf_{0.5}Zr_{0.5}O₂, suggesting that OVs engineering could be a key strategy for designing new ferroelectric phases and functionalities. Additionally, theoretical studies have shown that charged OVs contribute to the stabilization of rhombohedral Hf_{0.5}Zr_{0.5}O₂ films on ZnO substrates.

In this work, we first provide experimental evidence of the presence of VO in r-phase thin films of ZrO₂ deposited on a Nb:STO substrate in the (111) orientation, showing the influence of OVs on the ferroelectric response [8]. Transmission electron microscopy (TEM) studies corroborated with X-ray diffraction (XRD) analysis revealed a novel growth mechanism for ZrO₂ thin films, domain matching epitaxy, which occurs in highly misfit structures.

Fig. 1a shows a cross-sectional HRTEM image of the ZrO₂ films grown on (111) Nb:SrTiO₃ (Nb:STO) substrates, revealing a crystalline ZrO₂ layer and a sharp interface between the 8-nm thick ZrO₂ layer and the Nb:STO substrate. The high crystallinity quality as well as the existence of the r-phase in ZrO₂ films were discussed in detail in an earlier study. In the HRTEM image of Fig. 1a, a ~68.8° angle was observed between the [111] and [11-1] directions of the imaged grain. The 68.8° angle is an indicative of the R3m r-phase. The distance between the (111) planes (*d*₁₁₁) of the r-phase ZrO₂ films was measured to be *d*₁₁₁ = 2.98 ± 0.06 Å, which compares to the bulk theoretical value of 2.94 Å. This corresponds to an estimated out-of-plane tension of ~1.3%, and thus in-plane compression of ~1%.

In order to better describe the thin film-substrate orientation relationship we processed Fast Fourier Transform (FFT) patterns on a HRTEM picture which includes both the STO substrate and the r-phase ZrO₂ thin film. In the FFT pattern from Fig. 1b a well-defined set of peaks are emerging from the zone axis oriented ZrO₂ grain and from the STO substrate. After the measurements performed on the FFT pattern two peaks were indexed and assigned as indicated by the subscripts in Fig. 1b. Analysing the distribution of the peaks the following crystallographic relationship between the oriented ZrO₂ grain

and the STO substrate can be derived: $[11\bar{1}]\text{ZrO}_2 \parallel [110]\text{STO}$ for the in-plane direction. The interplanar distances of the $(11\bar{1})\text{ZrO}_2$ planes ($d_{11\bar{1}}=0.294\text{ nm}$) and the $(110)\text{STO}$ planes ($d_{110}=0.275\text{ nm}$) give a lattice mismatch of around -6.9% , which rules out epitaxy in conventional terms for the observed orientation relationship. In this case, the epitaxial relationship can be explained *via* a near coincidence lattice model or domain matching epitaxy (DME), with the formation of geometrical dislocations. The image in Fig. 1c, obtained with the $(11\bar{1})\text{ZrO}_2$ and $(110)\text{STO}$ peaks from the FFT diagram, is a Fourier filtered image and shows the formation of the misfit dislocations at the ZrO_2 -STO interface with epitaxy domains of variable lateral size. Therefore, *r*-phase ZrO_2 films can be grown on $(111)\text{Nb:STO}$ substrates through DME.

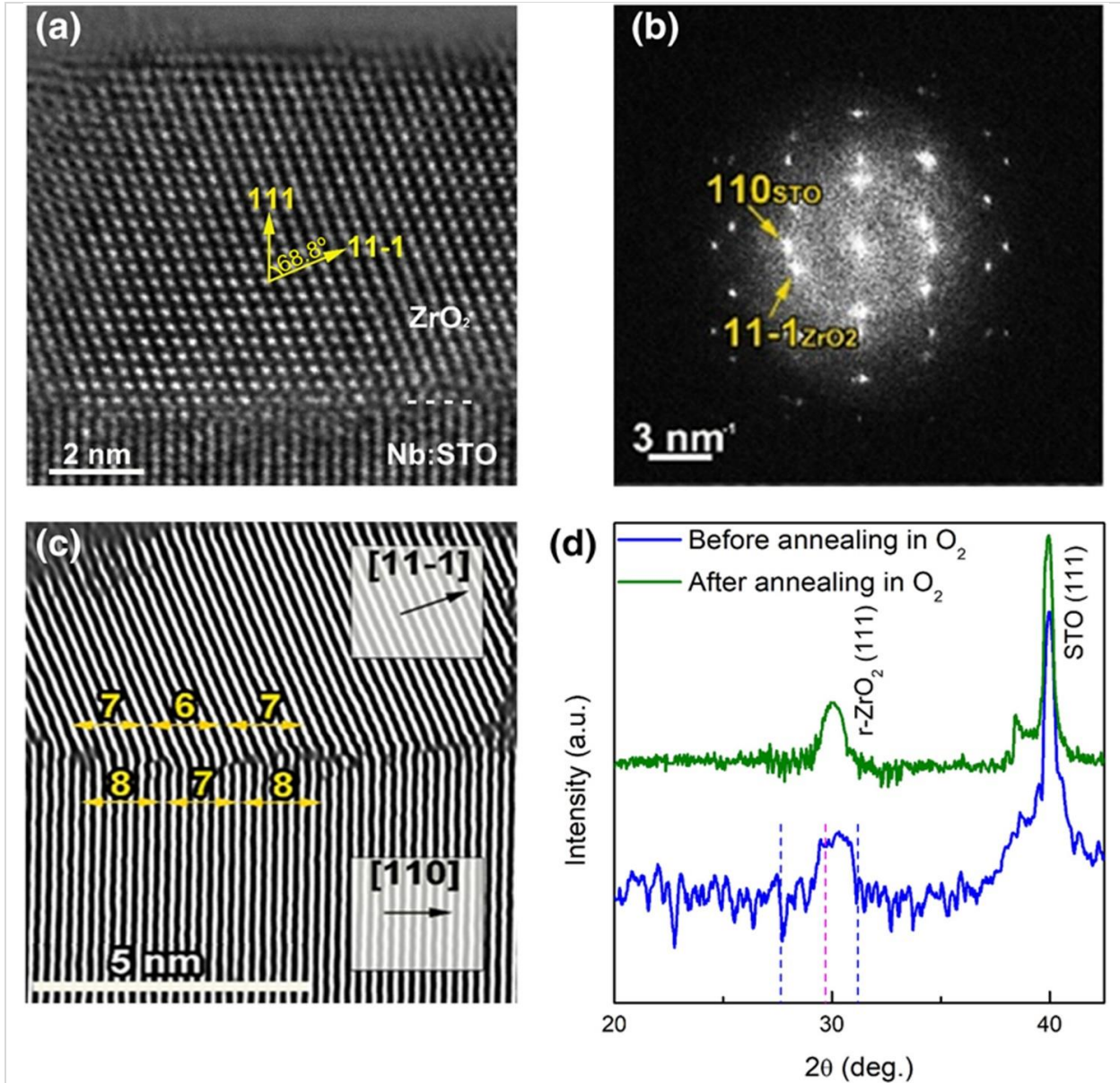


Fig. 1: (a) HRTEM image showing a crystallite in the ZrO_2 thin films, with the $[111]$ and $[11\bar{1}]$ directions marked. The 68.8° angle between the $[111]$ and $[11\bar{1}]$ directions is an indicative of a rhombohedral (*r*) structure in the films. (b) FFT pattern corresponding to micrograph (a). (c) Fourier-filtered micrograph of an *r*-phase ZrO_2 crystallite Fourier filtered micrograph in (b) obtained with the $(11\bar{1})\text{ZrO}_2$ and $(110)\text{STO}$ spots in the FFT diagram (b); the numbers indicate the number of planes in the film (6,7) continued into the substrate (7,8) between the cores of successive mismatch dislocations (endings of the supplementary half-planes in ZrO_2) showing domains of epitaxial growth with a variable lateral size. (d) XRD analysis performed on the *r*-phase ZrO_2 films, performed before and after annealing in an oxygen-rich atmosphere. Adapted from Ref. [8].

Fig. 1d shows the XRD patterns for the ZrO_2 films grown on $(111)\text{Nb:STO}$ substrates. Besides the Bragg peak approximately centred at $2\theta = 39.97^\circ$, originating from the (111) planes of the STO substrate, one

significant diffraction peak centred at $2\theta = 30.27^\circ$ ($d = 2.95 \text{ \AA}$) is observed, which was previously attributed to the r-phase ZrO_2 .

To investigate the role of OV's on the crystallinity quality and ferroelectric response of the r-phase ZrO_2 films, the films were annealed in an oxygen-rich atmosphere ($p\text{O}_2 = 10 \text{ mbar}$) at a moderate temperature (400°C) for 3 h so as to oxidize them. Fig. 1d shows also the XRD pattern of the film after the annealing process. No significant differences were observed in the XRD pattern before and after the annealing process, thereby suggesting that the crystalline phase structure remains the same.

Using HRTEM, we have demonstrated the domain matching epitaxy growth mechanism of ZrO_2 thin film as a driving force in stabilizing the rhombohedral phase of ZrO_2 .

References:

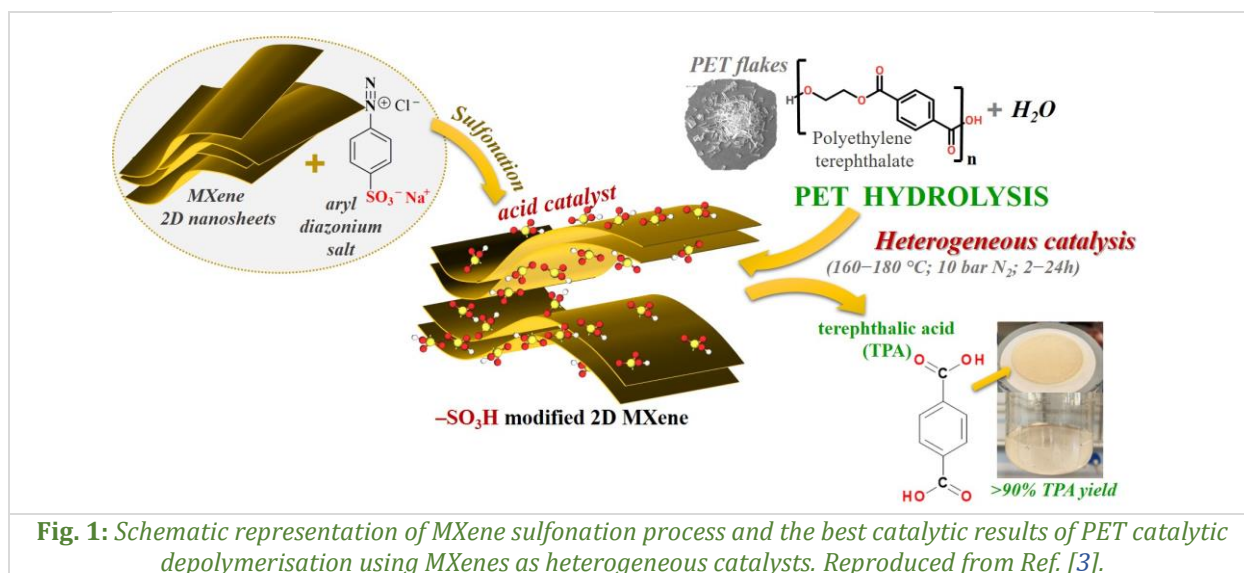
- [1] J. Kim, S. Saremi, M. Acharya, G. Velarde, E. Parsonnet, P. Donahue, A. Qualls, D. Garcia, L.W. Martin, *Ultrahigh capacitive energy density in ion-bombarded relaxor ferroelectric films*, Science 369 (2020) 81–84.
- [2] A. Kashir, S. Oh, H. Hwang, *Defect engineering to achieve wake-up free HfO_2 -based ferroelectrics*, Adv. Eng. Mater. 23 (2021) 2000791.
- [3] K.P. Kelley, A.N. Morozovska, E.A. Eliseev, V. Sharma, D.E. Yilmaz, A.C.T. van Duin, P. Ganesh, A. Borisevich, S. Jesse, P. Maksymovych, N. Balke, S.V. Kalinin, R.K. Vasudevan, *Oxygen vacancy injection as a pathway to enhancing electromechanical response in ferroelectrics*, Adv. Mater. 34 (2022) 2106426.
- [4] D.-S. Park, M. Hadad, L.M. Rimer, R. Ignatans, D. Spirito, V. Esposito, V. Tileli, N. Gauquelin, D. Chezganov, D. Jannis, J. Verbeeck, S. Gorfman, N. Pryds, P. Muralt, D. Damjanovic, *Induced giant piezoelectricity in centrosymmetric oxides*, Science 375 (2022) 653–657.
- [5] G.F. Nataf, M. Guennou, J.M. Gregg, D. Meier, J. Hlinka, E.K.H. Salje, J. Kreisel, *Domain-wall engineering and topological defects in ferroelectric and ferroelastic materials*, Nat. Rev. Phys 2 (2020) 634–648.
- [6] Y. Wei, P. Nukala, M. Salverda, S. Matzen, H. J. Zhao, J. Momand, A. S. Everhardt, G. Agnus, G. R. Blake, P. Lecoeur, B. J. Kooi, J. Íñiguez, B. Dkhil, B. Noheda, *A rhombohedral ferroelectric phase in epitaxially strained $\text{Hf}_{0.5}\text{Zr}_{0.5}\text{O}_2$ thin films*, Nat. Mater. 17 (2018) 1095–1100.
- [7] J.P.B. Silva, R.F. Negrea, M.C. Istrate, S. Dutta, H. Aramberri, J. Íñiguez, F.G. Figueiras, C. Ghica, K.C. Sekhar, A.L. Kholkin, *Wake-up free ferroelectric rhombohedral phase in epitaxially strained ZrO_2 thin films*, ACS Appl. Mater. Interfaces 13 (2021) 51383–51392.
- [8] V. Lenzi, J.P.B. Silva, B. Šmíd, V. Matolín, C.M. Istrate, C. Ghica, J.L. MacManus-Driscoll, L. Marques, *Ferroelectricity induced by oxygen vacancies in rhombohedral ZrO_2 thin films*, Energy Environ. Mater. 7 (2024) e12500.

Acid-modified Ti_3C_2 -based MXene as catalysts for enhanced polyethylene terephthalate up-cycling

I.M. Chirica^{1,2}, A.G. Mirea¹, T. Șuteu², A. Kuncser¹, Ș. Neațu¹, M. Florea¹,
M.W. Barsoum³, F. Neațu¹

- 1) National Institute of Materials Physics, 077125, Măgurele, Romania
- 2) Faculty of Physics, University of Bucharest, 077125, Măgurele, Romania
- 3) Department of Materials Science & Engineering, Drexel University, PA 19104, Philadelphia, USA

The recycling of plastics, particularly polyethylene terephthalate (PET), is essential to reduce environmental pollution and support a circular economy. Chemical recycling methods [1], such as hydrolysis, can break PET into its monomers, terephthalic acid (TPA) [2] and ethylene glycol (EG), for reuse. However, current processes face challenges, including high energy requirements, by-product generation, and catalyst inefficiencies [2]. This study [3] explores the potential of sulfonated Ti_3C_2 MXene ($\text{Ti}_3\text{C}_2\text{Tx-SO}_3\text{H}$) as a recoverable, solid acid catalyst to overcome these limitations, achieving high TPA yields at moderate reaction conditions. MXenes, a family of two-dimensional (2D) transition metal carbides/nitrides [4,5], were synthesized from Ti_3AlC_2 by selectively etching the aluminium layers using LiF and HCl. Sulfonic acid ($-\text{SO}_3\text{H}$) groups were grafted onto the $\text{Ti}_3\text{C}_2\text{Tx}$ surface using aryl diazonium salts derived from sulfanilic acid (Fig. 1). The resulting materials ($\text{Ti}_3\text{C}_2\text{Tx-SO}_3\text{H-1}$, $\text{Ti}_3\text{C}_2\text{Tx-SO}_3\text{H-3}$, and $\text{Ti}_3\text{C}_2\text{Tx-SO}_3\text{H-5}$) were characterized using techniques such as X-ray diffraction (XRD), X-ray photoelectron spectroscopy (XPS), transmission electron microscopy (TEM), Raman spectroscopy, and thermogravimetric analysis (TGA). Their acidity was quantified by temperature-programmed desorption of NH_3 (NH_3 -TPD). Catalytic depolymerisation of PET by hydrolysis route was performed in a stainless-steel autoclave using 0.02–0.06 g of $\text{Ti}_3\text{C}_2\text{Tx-SO}_3\text{H}$ catalysts with 0.1 g of PET flakes in 10 mL of water at 160–180 °C for up to 24 h. The TPA yield was confirmed by nuclear magnetic resonance (NMR) spectroscopy. Sulfonation process successfully grafted $-\text{SO}_3\text{H}$ groups onto the MXene surface, increasing interlayer spacing and enhancing accessibility to catalytic sites.



XRD and TEM analyses confirmed the 2D structure's integrity and the intercalation of sulfonic groups. NH_3 -TPD measurements demonstrated a direct correlation between the number of sulfonic acid groups and the catalyst's acidity, with $\text{Ti}_3\text{C}_2\text{Tx-SO}_3\text{H-5}$ exhibiting the highest acidity. The catalytic performance displays that $\text{Ti}_3\text{C}_2\text{Tx}$ exhibited no catalytic activity while $\text{Ti}_3\text{C}_2\text{Tx-SO}_3\text{H-5}$ achieved a 99% TPA yield at 180°C in 24 h, significantly outperforming other catalysts (e.g., $\text{Ti}_3\text{C}_2\text{Tx-SO}_3\text{H-1}$ and $\text{Ti}_3\text{C}_2\text{Tx-SO}_3\text{H-3}$). Lower reaction temperatures (160 °C) rendered the catalyst inactive, while moderate temperatures (170 °C) achieved a 44% yield, demonstrating the temperature dependency of PET hydrolysis. The

catalytic activity of $\text{Ti}_3\text{C}_2\text{Tx-SO}_3\text{H}$ materials in PET hydrolysis was evaluated by analysing key influencing factors. The results are summarized in Table 1. To confirm that no reaction occurs under the specified conditions, blank experiments (without a catalyst) were conducted at 160, 170, and 180 °C for 24 h, showing no PET conversion, in our reaction conditions. To further validate the catalytic results, the as-synthesized MXene was tested as catalyst. As expected, no depolymerization products were detected under these conditions (Table 1, entry 1), confirming that the catalytic activity arises from the sulfonated MXene. The introduction of sulfonic groups significantly enhanced PET depolymerization at 180 °C (Table 1, entries 2–4).

A key aspect for industrial application is reducing the depolymerization temperature, given that PET hydrolysis is an endothermic reaction. Among the three sulfonated MXenes, a direct correlation was observed between the PET depolymerization yield and the concentration of sulfonic groups. According to TPD- NH_3 analysis, a higher sulfonation degree corresponds to a greater number of acidic surface sites. Specifically, the $\text{Ti}_3\text{C}_2\text{Tx-SO}_3\text{H-5}$ sample exhibits 1.25 times more acidic sites than $\text{Ti}_3\text{C}_2\text{Tx-SO}_3\text{H-1}$, reinforcing the importance of sulfonic groups for catalytic activity.

To assess the effect of temperature, PET depolymerization was performed using $\text{Ti}_3\text{C}_2\text{Tx-SO}_3\text{H-5}$. At 170 °C, the TPA yield reached 44% (Table 1, entry 5). However, lowering the reaction temperature to 160 °C rendered the catalyst inactive (Table 1, entry 6), likely due to the temperature dependency of PET depolymerization. This suggests that $\text{Ti}_3\text{C}_2\text{Tx-SO}_3\text{H-5}$ alters the activation energy for PET depolymerization, requiring a minimum threshold temperature for catalytic activity. The inactivity at 160 °C indicates that this threshold is not met, preventing the reaction from occurring. Increasing catalyst loading from 0.02 g to 0.06 g improved TPA yields, highlighting the importance of catalyst concentration in scaling reaction efficiency (Table 1, entry 7–8).

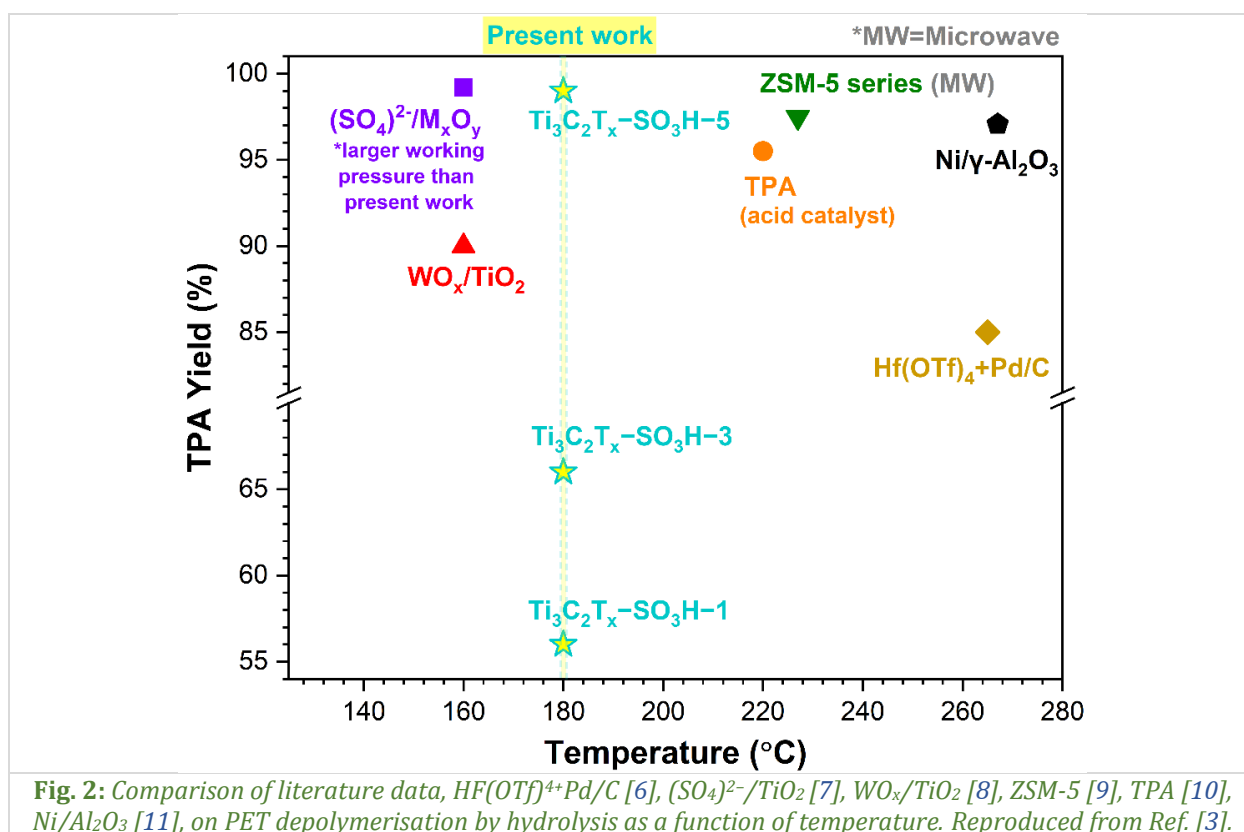
Table 1: Catalytic results of PET hydrolysis using materials synthesized herein.

Entry	Catalyst	Temperature (°C)	TPA yield (%)
1	$\text{Ti}_3\text{C}_2\text{Tx}$	180	0
2	$\text{Ti}_3\text{C}_2\text{Tx-SO}_3\text{H-1}$	180	56
3	$\text{Ti}_3\text{C}_2\text{Tx-SO}_3\text{H-3}$	180	66
4	$\text{Ti}_3\text{C}_2\text{Tx-SO}_3\text{H-5}$	180	72
5	$\text{Ti}_3\text{C}_2\text{Tx-SO}_3\text{H-5}$	170	44
6	$\text{Ti}_3\text{C}_2\text{Tx-SO}_3\text{H-5}$	160	0
7	$\text{Ti}_3\text{C}_2\text{Tx-SO}_3\text{H-5}$ (i)	180	55
8	$\text{Ti}_3\text{C}_2\text{Tx-SO}_3\text{H-5}$ (ii)	180	99

Reaction conditions: stainless-steel batch reactor equipped with a magnetic stirrer and a manometer, 0.1 g PET flakes from a white bottle, 0.04 g catalyst in 10 mL water, 24 h; TPA product confirmed by ^1H NMR and ^{13}C NMR; (i) 0.02 g catalysts; (ii) 0.06 g catalyst.

$\text{Ti}_3\text{C}_2\text{Tx-SO}_3\text{H}$ catalysts maintained their structure and activity over three reaction cycles, achieving consistent TPA yields (~54%). XRD and TGA confirmed the catalyst's thermal and structural stability under reaction conditions. Transparent PET bottles gave the highest TPA yields (66%), while green bottles (31%) and T-shirts (37%) showed reduced activity due to additives interference, suggesting a pure material source dependence.

$\text{Ti}_3\text{C}_2\text{Tx-SO}_3\text{H-5}$ operates at 180 °C, a temperature ~40 °C lower than other heterogeneous catalysts reported in the literature, making it more energy-efficient. The catalyst avoids the harsh conditions (high pressures, supercritical fluids) required by other systems, emphasizing its practicality and scalability (Fig. 2).



This study [3] establishes acid-modified Ti_3C_2 -based MXenes as efficient and recoverable catalysts for PET upcycling. The combination of high acidity, a flexible 2D structure, and stability enables near-complete depolymerization of PET under moderate conditions. These findings position $\text{Ti}_3\text{C}_2\text{Tx}-\text{SO}_3\text{H}$ as a promising candidate for scalable and sustainable PET recycling, aligning with circular economy principles.

References:

- [1] T. Hundertmark, M. Mayer, C. McNally, T.J. Simons, C. Witte, *How plastics-waste recycling could transform the chemical industry*, McKinsey on Chemicals, (2018).
- [2] K. Ghosal, C. Nayak, *Recent advances in chemical recycling of polyethylene terephthalate waste into value added products for sustainable coating solutions – Hope vs. hype*, Mater. Adv. 3 (2022) 1974–1992.
- [3] I.M. Chirica, A.G. Mirea, T. Şuteu, A. Kuncser, Ş. Neaţu, M. Florea, M.W. Barsoum, F. Neaţu, *Acid-modified, Ti_3C_2 -based MXene as catalysts for upcycling polyethylene terephthalate*, ACS Sustain. Chem. Eng. 12 (2024) 9766–9776.
- [4] I. Vollmer, M.J.F. Jenks, M.C.P. Roelands, R.J. White, T. van Harmelen, P. de Wild, G.P. van der Laan, F. Meirer, J.T.F. Keurentjes, B.M. Weckhuysen, *Beyond mechanical recycling: Giving new life to plastic waste*, Angew. Chem. Int. Ed. 59 (2020) 15402–15423.
- [5] M. Naguib, M.W. Barsoum, Y. Gogotsi, *Ten years of progress in the synthesis and development of MXenes*, Adv. Mater. 33 (2021) 2103393.
- [6] Y. Kratish, T.J. Marks, *Efficient polyester hydrogenolytic deconstruction via tandem catalysis*, Angew. Chem. Int. Ed. 61 (2022) e202112576.
- [7] X. K. Li, H. Lu, W.Z. Guo, G.P. Cao, H.L. Liu, Y.H. Shi, *Reaction kinetics and mechanism of catalyzed hydrolysis of waste PET using solid acid catalyst in supercritical CO_2* , AIChE J. 61 (2015) 200–214.
- [8] W.Z. Guo, H. Lu, X.K. Li, G.P. Cao, *Tungsten-promoted titania as solid acid for catalytic hydrolysis of waste bottle PET in supercritical CO_2* , RSC Adv. 6 (2016) 43171–43184.
- [9] M.J. Kang, H.J. Yu, J. Jegal, H.S. Kim, H.G. Cha, *Depolymerization of PET into terephthalic acid in neutral media catalyzed by the ZSM-5 acidic catalyst*, Chem. Eng. J. 398 (2020) 125655.
- [10] W. Yang, R. Liu, C. Li, Y. Song, C. Hu, *Hydrolysis of waste polyethylene terephthalate catalyzed by easily recyclable terephthalic acid*, Waste Manag. 135 (2021) 267–274.
- [11] M. Yan, Y. Yang, F. Chen, D. Hantoko, A. Pariatamby, E. Kanchanatip, *Development of reusable $\text{Ni}/\gamma\text{-Al}_2\text{O}_3$ catalyst for catalytic hydrolysis of waste PET bottles into terephthalic acid*, Environ. Sci. Pollut. Res. 30 (2023) 102560–102573.

Healthcare & Environmental Applications: Materials and Devices

Electrospun nanofibrous scaffolds for biomedical engineering

M. Beregoi, D. Oprea, M.C. Bunea, M. Enculescu, I.C. Ciobotaru,
I. Enculescu, T.A. Enache

National Institute of Materials Physics, 077125, Măgurele, Romania

Cells are remarkable living systems, equipped with intricate molecular machinery that enables them to generate energy, synthesize proteins, and communicate with their surroundings. Their ability to sense and respond to environmental changes through sophisticated signalling pathways and gene regulation makes them highly adaptable. This dynamic nature not only sustains essential biological functions but also plays a crucial role in health and disease. By integrating cellular signalling biomarkers into advanced smart technologies, researchers can gain deeper insights into disease mechanisms, enhance early diagnosis, and develop more precise, personalized treatments [1]. As in any scientific field, the optimum experimental conditions in terms of sensitivity and minimization of undesirable effects requires the appropriate model. Thus, the electrochemical sensing of cells biomarkers requires the cultivation of the cells at/near the (bio)sensor surface, maintaining an appropriate electroactive available surface, and avoiding the passivation. This can be achieved using electrospun nanofiber polymer scaffolds, which allow the cell cultivation in desired condition that allow further integration in biosensing devices for biomarkers monitoring or in systems that promote cellular processes. These scaffolds may have a dual-role, serving as polymeric support for cell culture and as platform for induce cellular differentiation, the later requiring their metallization and functionalization with conductive polymers. Based on this, at National Institute of Materials Physics the fibroblast differentiation into myofibroblasts, an important process in wound healing, was achieved using nylon electrospun nanofibres modified with poly(styrene sulfonate) doped poly(3,4-ethylenedioxythiophene) (PEDOT:PSS) whereas the melanin exocytosis was successfully quantified using a commercial electrode as electrochemical transducer integrated with an electrospun scaffold based on nanometric nylon fibres. The preparation procedure is presented in Fig. 1 for both cellular scaffolds utilized in tissue engineering (Fig. 1a) [2] and biosensing (Fig. 1b) [3]. First, a 17% (w/v) nylon 6/6 solution was prepared by dissolving the polymer in formic acid. The solution was loaded into a syringe equipped with a blunt needle, connected to a pumping system to control the flow rate. A high voltage source was linked to the needle, with a grounded collector positioned 200 mm away. The electrospinning process was conducted under controlled conditions: applied voltage: 25 kV, solution flow rate: 0.1 mL/h, temperature: 21–24 °C, relative humidity: 35–40%. To remove residual solvent traces, the freestanding meshes or attached on commercial membranes were heated in an oven at 100 °C for 2 h. The second step involved the coating of the freestanding nanofiber meshes with a gold layer in order to perform the electrochemical synthesis. The deposition time was adjusted to achieve a metal thickness of approximately 39 nm.

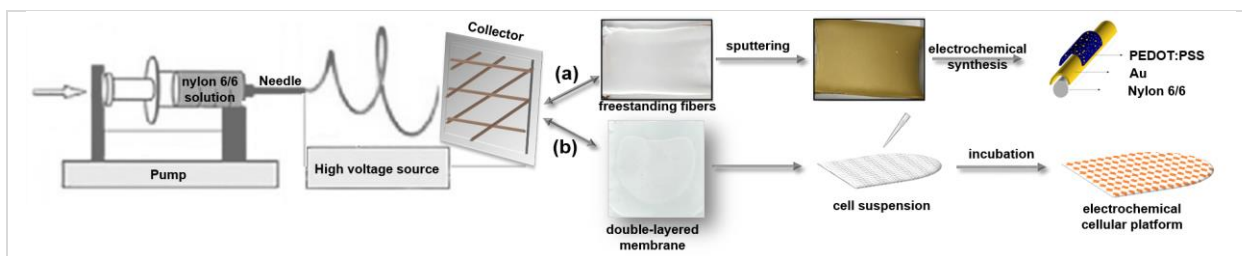


Fig. 1: Schematic representation of the scaffold preparation for both targeted applications: (a) tissue engineering and (b) biosensing. Adapted from Ref. [3].

For the development of the polymeric scaffolds in order to induce cellular differentiation, the PEDOT:PSS-coated nanofiber meshes involved electrochemical deposition, a process that enhances the electrical conductivity and biocompatibility of the nanofibers (Fig. 1a). The electrochemical deposition was achieved using the following procedure: (i) firstly, the metallized nanofiber meshes were mechanically gripped between two stainless steel frames, serving as the working electrode, while a platinum mesh and a commercial saturated calomel electrode were used as the counter and reference

electrodes; (ii) secondly, the precursor aqueous solution, containing 10 mM 3,4-ethylenedioxythiophene (EDOT) monomer and 100 mM sodium polystyrene sulfonate (NaPSS) as the dopant, was prepared; (iii) the electrochemical polymerization was achieved by cyclic voltammetry sweeping the potential between -0.2 V and $+1.4$ V for 20 cycles at a scan rate of 100 mV/s; (iv) after deposition, the freestanding PEDOT:PSS-coated nanofiber meshes were rinsed with ultrapure water to remove residual electrolyte and dried at room temperature. Likewise, the development of cellular scaffolds to be integrated in electrochemical biosensing systems, enhancing cell adhesion is crucial. Applying a poly-L-lysine (PLL) coating is an effective method to improve cell attachment due to its positive charge, which facilitates electrostatic interactions with the negatively charged cell membranes. The double-layered membranes (Fig. 1b) were functionalized with approximately 70 μ L of this solution which was evenly distributed over the membranes and left to dry overnight, allowing the PLL to form a uniform layer on the nanofibers. Following this step, UV sterilization was applied for 3 h, and the scaffolds were ready to be used. Two cellular systems were investigated, L929 fibroblasts were tested for differentiation and B16-F10 melanoma cells for biomarker detection capacity. Scanning electron microscopy (SEM) evidences the uniformity of PEDOT:PSS deposition (Fig. 1a) and fibre distribution on commercial membranes (Fig. 1b), as well as their cytocompatibility.

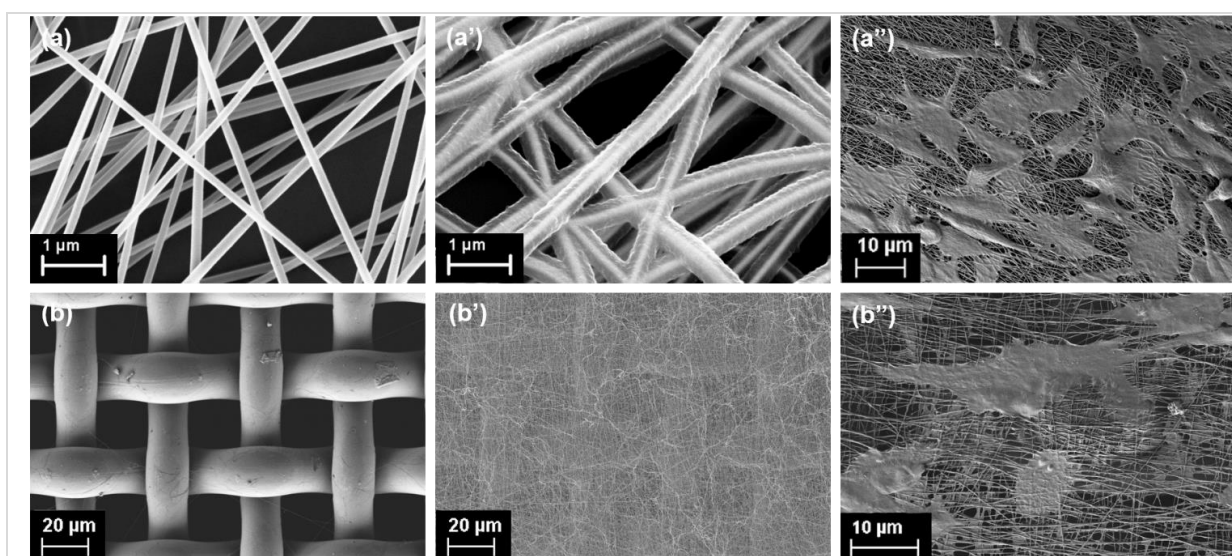


Fig. 2: SEM images of: (a') as spun and (a') PEDOT:PSS coated nanofibers; (a'') L929 fibroblast cells onto PEDOT:PSS mesh; (b) commercial polymeric membrane; (b') double-layered membrane; and (b'') B16 melanoma cells onto double-layered membrane. Adapted from Refs. [2,3].

The use of electrospun nanofibers in biosensing devices for biomarkers monitoring was demonstrated using B16 melanoma cell line and a commercial planar three-electrode system, from DropSens, as sensor for melanin detection after UV irradiation of B16 cell culture (Fig. 3a). The advantage of the proposed system is to avoid the growth of cells at the sensor surface, a process that can lead to the passivation of the surface due to the adsorption of chemical species from the medium, rendering the biosensor non-functional. Furthermore, the flow of charges between the electrodes may damage the cells and induce the formation of interfering molecular species. The choice of the B16 cell line and melanin was driven by the fact that, although melanin expression in cell culture is well known, its tendency to aggregate presents a significant challenge. In the proposed methodology, the cell culture is in close proximity to the electrode surface, allowing for the electrochemical detection of melanin released after UV stimulation to occur before polymerization (Fig. 3b).

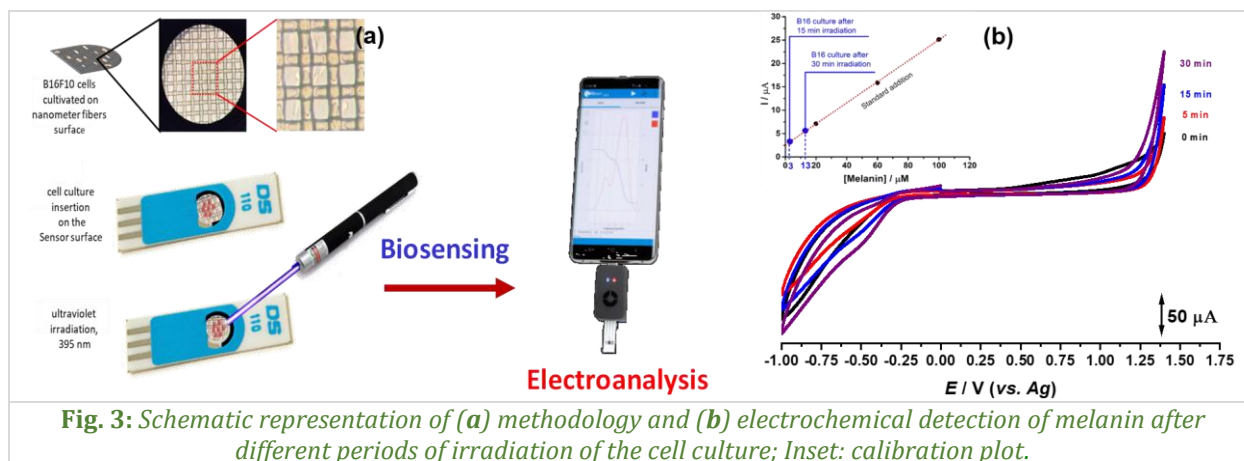


Fig. 3: Schematic representation of (a) methodology and (b) electrochemical detection of melanin after different periods of irradiation of the cell culture; Inset: calibration plot.

To confirm the differentiation process, fluorescence images were captured for fibroblast cells seeded and incubated for 72 h on all sample types. The cells were immunochemically labelled with an α -SMA antibody, the α -SMA antigen being a specific biomarker of the differentiation process. For comparison, the cells were also stained with DAPI and Phalloidin to highlight the nucleus and actin filaments, respectively. To facilitate a clearer interpretation of the results, the mean fluorescence intensity of selected individual cells was analysed. Fig. 4 reveals that the highest degree of differentiation was observed in cells seeded and incubated on PEDOT:PSS-coated fibres. This differentiation process may result from the interaction between the conductive PEDOT:PSS layer and the gold layer with the cells, local modifications in the surrounding microenvironment, or mechanical stimulation.

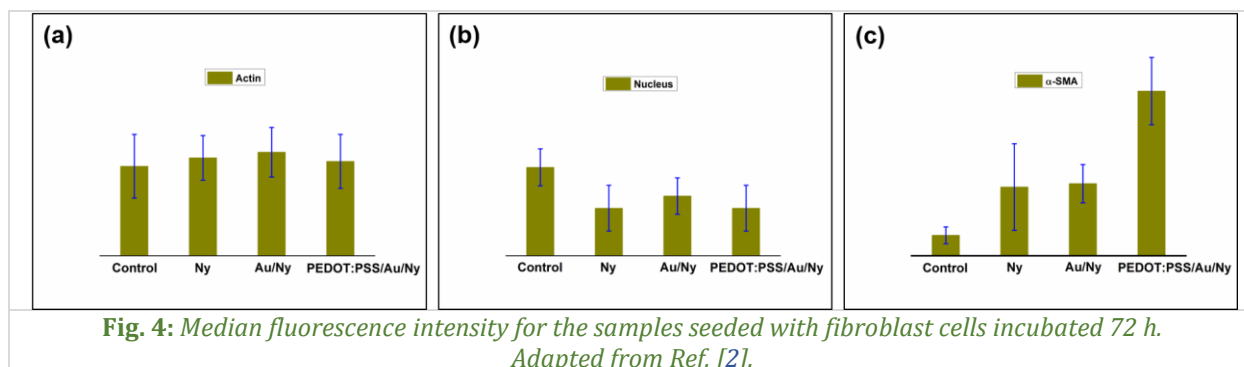


Fig. 4: Median fluorescence intensity for the samples seeded with fibroblast cells incubated 72 h. Adapted from Ref. [2].

The electrospun nanofibrous scaffolds developed in this study demonstrated dual functionality, both promoting cellular differentiation and serving as platforms for real-time biomarker detection. These findings highlight the versatility of electrospun scaffolds in biomedical applications, particularly in tissue engineering and biosensing. By combining cellular support with functional properties, these scaffolds contribute to the development of advanced biomedical devices with improved performance.

References:

- [1] J. Su, Y. Song, Z. Zhu, X. Huang, J. Fan, J. Qiao, F. Mao. *Cell-cell communication: new insights and clinical implications*, Signal Transduct. Target Ther. 9 (2024) 196.
- [2] M. Beregoi, T.A. Enache, D. Oprea, M. Enculescu, I.C. Ciobotaru, C. Busuioc, I. Enculescu. *PEDOT:PSS based electrospun nanofibres used as trigger for fibroblasts differentiation*, Smart Mater. Struct. 33 (2024) 015009.
- [3] M. Beregoi, D. Oprea, M.C. Bunea, M. Enculescu, T.A. Enache. *Electrospun fibrillary scaffold for electrochemical cell biomarkers detection*, Mikrochim. Acta 191 (2024) 435.

Palladium coated submicron electrospun polymeric fibers with immobilized uricase for uric acid determination in body fluids

R.J.B. Leote, D.N. Crisan, E. Matei, I. Enculescu, V.C. Diculescu

National Institute of Materials Physics, 077125, Măgurele, Romania

Uric acid (UA) is the final product of purine metabolism in humans, and abnormal UA levels are associated with various health conditions, including gout, kidney disease, and Lesch-Nyhan syndrome. Continuous UA monitoring can significantly enhance patient management, akin to the benefits experienced by diabetics using glucometers. Real-time tracking of UA could facilitate early detection and treatment of infections through wearable sensing devices [1].

Sweat analysis provides a non-invasive means of extracting valuable biochemical information [2–4]. Wearable biosensors have garnered interest in biomedical technology due to their ability to offer continuous, real-time health monitoring without interruptions. For these devices to be effective, they must withstand mechanical stress, function at body temperature, and deliver rapid, selective responses to analyte concentration changes. Flexible materials have been extensively used in wearable sensing platforms, with polymeric fibres emerging as promising support structures. Electrospinning is a widely employed technique for fabricating flexible polymeric fibres, allowing precise control over their physical and chemical properties down to the nanometre scale. However, the inherent conductivity limitations of polymeric scaffolds present a challenge, which can be addressed through direct metallization with transition or noble metals. Palladium, in particular, has proven effective in biosensing applications due to its ability to facilitate hydrogen peroxide reduction near 0.0 V vs. Ag/AgCl, minimizing interference. This study presents a novel approach involving electrospun poly(methyl methacrylate) (PMMA) fibres coated with a gold layer, adhered to polyethylene terephthalate (PET) foils, and subsequently subjected to palladium electrodeposition (Fig. 1). These flexible electrodes were characterized using cyclic voltammetry and electrochemical impedance spectroscopy to analyse interfacial processes. Scanning electron microscopy (SEM) was employed to examine the morphological features of the nanostructured palladium-modified electrodes. The electrodes were tested for hydrogen peroxide detection, followed by the development of a UA biosensor through urate oxidase (UroX) immobilization. The biosensor was initially evaluated using artificial sweat analysis, with additional tests in artificial urine and blood serum to assess its feasibility for point-of-care applications.

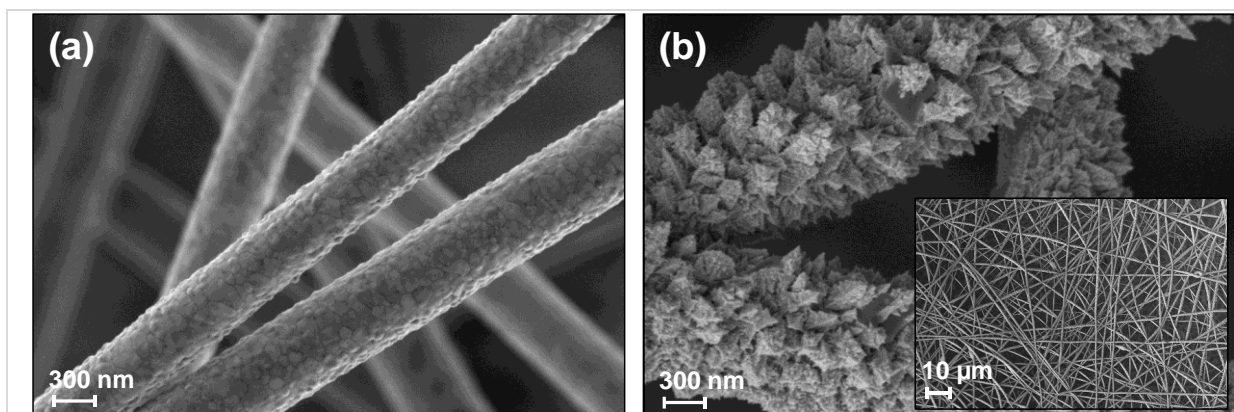


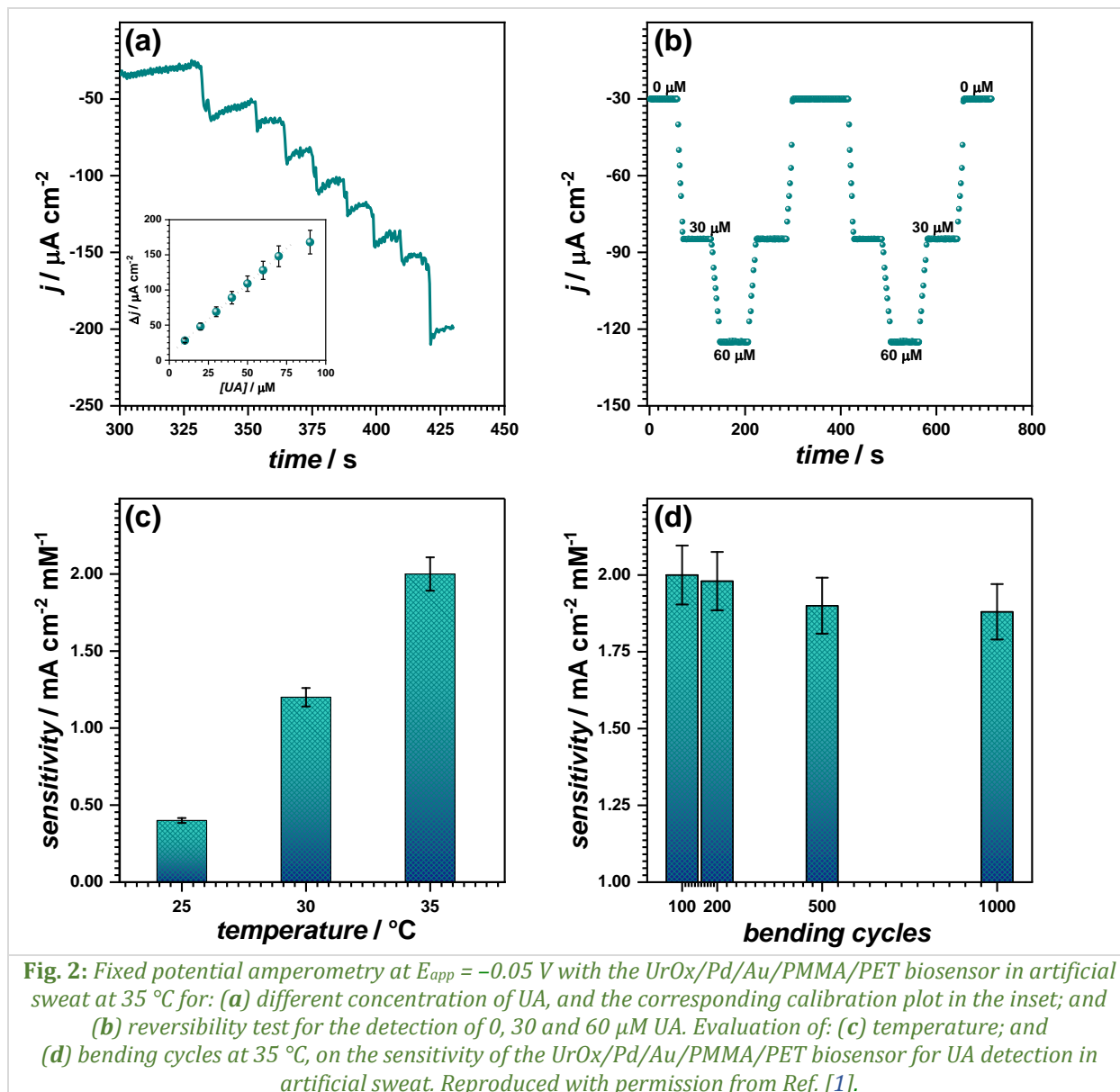
Fig. 1: SEM images of (a) Au/PMMA/PET and (b) Pd/Au/PMMA/PET electrodes at 100,000× and (inset) 1,000× magnification. Adapted with permission from Ref. [1].

The uric acid biosensor was obtained by immobilization of UroX at the surface of the Pd/Au/PMMA/PET electrode through cross-linking in glutaraldehyde vapours. Optimal conditions such as pH, applied potential and enzyme loading for the detection of UA were determined [1]. The analytical performance of the UroX/Pd/Au/PMMA/PET biosensor was initially investigated for the determination of UA in buffer solutions, by fixed potential amperometry at $E_{app} = -0.05$ V, with successive additions of UA in artificial sweat (Fig. 2a). The working principle of the biosensor is based on the detection of H_2O_2 produced during the enzymatic reaction (Eq. 1). H_2O_2 reacts on the Pd surface, resulting in the formation

of PdO (Eq. 2). At the same time, at $E_{app} = -0.05$ V the reduction of PdO occurs (Eq. 3), which correlates with the concentration of H_2O_2 from the enzymatic reaction and consequently with that of UA.



The biosensor displayed a sensitivity of 2.02 ± 0.10 mA cm⁻² mM⁻¹ (RSD = 2.4%, n = 3) and a detection limit $LoD = 2.20 \pm 0.01$ μ M (RSD = 4.1, n = 3), determined as $3 \times \text{standard deviation} \times (\text{sensitivity})^{-1}$. A linear behaviour was observed in concentration range between 10 and 90 μ M which is larger than the usual uric acid content in sweat of hyperuricemic patients, thus demonstrating its suitability for UA detection in sweat analysis.



For continuous monitoring, biosensors must present a high degree of reversibility. In this regard, the reversibility of the UrOx/Pd/Au/PMMA/PET biosensor in artificial sweat was investigated by increasing and decreasing the UA concentration in artificial sweat at 35 °C. Amperometric measurements were performed with the same biosensor at 0, 30 and 60 μ M UA in artificial sweat for increasing and decreasing concentrations (Fig. 2b). The biosensor displayed a reversible behaviour and a RSD = 2.5% between equivalent concentration steps.

Wearable biosensors need to withstand severe mechanical stress due to body movement. Moreover, they can be exposed to different temperatures due to a lack of control of the environment at which they are exposed. These altering conditions affect the stability of bioreceptors, and in order to address these issues, a study of the mechanical resistance and temperature influence was conducted. The effect of temperature on the sensitivity to UA detection in artificial sweat was evaluated for on-body measurements (Fig. 2c). It was observed that with increasing temperature, the UrOx/Pd/Au/PMMA/PET biosensor sensitivity to UA increased linearly, displaying a maximum sensitivity value of $2.02 \text{ mA cm}^{-2} \text{ mM}^{-1}$ at 35°C .

Also, the effect of consecutive bending cycles on the biosensor sensitivity was tested by bending the UrOx/Pd/Au/PMMA/PET biosensor for 50, 100, 200, 500, 1000 times and measuring the response to $10 \mu\text{M}$ UA after each cycle at 35°C (Fig. 2d). The decrease of the current response after 1000 bending cycles was approx. 4.1%, demonstrating the mechanical resistance of the UrOx/Pd/Au/PMMA/PET biosensor when subjected to aggressive treatment.

The UrOx/Pd/Au/PMMA/PET biosensor was applied to the determination of UA in spiked/fortified samples of different body fluids (Table 1). The percentage of recovery was between 98% and 110%, confirming that the detection of UA can be carried out with the UrOx/Pd/Au/PMMA/PET biosensor. The response from the biosensor method was compared with the HPLC analysis of the same type of samples (Table 1). The results obtained using the biosensor were in good agreement with the HPLC analysis, indicating that the newly developed biosensor is reliable and validated.

Table 1: Uric acid detection in complex samples with UrOx/Pd/Au/PMMA/PET biosensor and comparison with HPLC. Reproduced with permission from Ref. [1].

Sample	Added (μM)	Found (μM)		Recovery (%)	
		Biosensor	HPLC	Biosensor	HPLC
Artificial sweat	20	22	20	110	100
	40	39	40	98	100
	60	62	60	103	100
Urine	1000	1020	1010	102	101
	1500	1550	1520	103	101
	2000	2090	2090	105	101
Blood serum	–	147	140	–	–

The analytical performance of the biosensor under harsh mechanical deformations and physiological temperatures demonstrated its potential for applications in wearable sensing platforms.

References:

- [1] R.J.B. Leote, D.N. Crisan, E. Matei, I. Enculescu, V.C. Diclescu, *Palladium-coated submicron electrospun polymeric fibers with immobilized uricase for uric acid determination in body fluids*, ACS Appl. Polym. Mater. 6 (2024) 2274–2283.
- [2] V.C. Diclescu, M. Beregoi, A. Evanghelidis, R.F. Negrea, N.G. Apostol, I. Enculescu, *Palladium/palladium oxide coated electrospun fibers for wearable sweat pH-sensors*, Sci. Rep. 9 (2019) 8902.
- [3] A. Aldea, E. Matei, R.J.B. Leote, I. Rau, I. Enculescu, V.C. Diclescu, *Ionophore-NafionTM modified gold-coated electrospun polymeric fibers electrodes for determination of electrolytes*, Electrochim. Acta 363 (2020) 137239.
- [4] A. Aldea, R.J.B. Leote, E. Matei, A. Evanghelidis, I. Enculescu, V.C. Diclescu, *Gold coated electrospun polymeric fibres as new electrode platform for glucose oxidase immobilization*, Microchem. J. 165 (2021) 106108.

Development and evaluation of metal-doped hydroxyapatite thin films with enhanced physicochemical properties and antifungal capabilities for potential biomedical applications

D. Predoi¹, S.L. Iconaru¹, C.S. Ciobanu¹, L. Ghegoiu¹, S. Talu², M.V. Predoi³, R.S. Matos⁴, H.D. da Fonseca Filho⁵, S.-A. Predoi^{6,7,8}, N. Buton⁹, G.Q. Ramos¹⁰, M. Motelica-Heino¹¹

- 1) *National Institute of Materials Physics, 077125, Măgurele, Romania*
- 2) *The Directorate of Research, Development and Innovation Management (DMCDI), Technical University of Cluj-Napoca, 400020, Cluj-Napoca, Romania*
- 3) *Department of Mechanics, National University of Science and Technology Politehnica Bucharest, 060042, Bucharest, Romania*
- 4) *Amazonian Materials Group, Physics Department, Federal University of Amapá (UNIFAP), 68903-419, Macapa, Amapa, Brazil*
- 5) *Laboratory of Synthesis of Nanomaterials and Nanoscopy (LSNN), Physics Department, Federal University of Amazonas (UFAM), 69067-005, Manaus, Amazonas, Brazil*
- 6) *École Normale Supérieure Paris-Saclay, Département de Physique, 91190, Gif-sur-Yvette, France*
- 7) *Université Paris-Saclay, 911190, Gif-sur-Yvette, France*
- 8) *École des Hautes Études Commerciales de Paris, 78350, Jouy-en-Josas, France*
- 9) *HORIBA Jobin Yvon S.A.S., 91165, Longjumeau, France*
- 10) *Centro Multiusuario para Analise de Fenomenos Biomedicos of Universidade Do Estado Do Amazonas (CMABio), Universidade Do Estado Do Amazonas (UEA), 69065-001, Manaus, Amazonas, Brazil*
- 11) *Institut des Sciences de la Terre d'Orléans (ISTO), UMR 7327 CNRS, Université d'Orléans, 45071, Orleans, France*

Thin films of hydroxyapatite (HAp) doped with chromium (20CrHAp) were applied onto silicon substrates using the spin coating technique [1]. We employed Minkowski Functionals and fractal/multifractal analysis to examine the properties of the studied films [1]. The Ag/Mg doped HAp nanocomposites coatings were deposited on Si substrate using the dip-coating technique [2]. The resulting coatings were characterized SEM, EDXS, FTIR-ATR spectroscopy, AFM, and XPS [2]. The antifungal evaluation of AgMgHAp coatings was carried out using the *Candida albicans* ATCC® 10231 fungal strain [2]. Cu-doped hydroxyapatite (CuHAp) thin films were obtained using spin-coating method [3]. The thin films were characterized by XRD, EDXS, XPS, FTIR spectroscopy, AFM, and SEM [3]. The cytotoxicity of CuHAp thin films was assessed using human gingival fibroblasts (HGF-1) cells [3]. The synthesis methods of doped HAp and their characterization techniques were described in detail in our works [1–3]. The AFM images of pre-incubation coating (Fig. 1a) display an exceptionally smooth surface with a consistently uniform topographic height distribution [1]. Fig. 1b confirms this uniformity through a normal height distribution, indicating a platykurtic behaviour [1]. The Abbott-Firestone curve [1] for this coating exhibits a typical S-type pattern (Fig. 1c), indicating a strong tendency for centralized data, reaffirming the minimal variation in topographic heights [1].

The FTIR spectroscopy results (Fig. 1e) obtained for the 20CrHAp thin films revealed the presence of large bands associated with (PO₄)³⁻ groups, observed around 1028 cm⁻¹ (ν₃), 556 cm⁻¹ (ν₄), and at 466 cm⁻¹ (ν₂) [1]. The SEM studies conducted on the 20CrHAp thin films highlighted the surface morphology, which consists of conglomerates of nanoparticles unevenly distributed across the surface (Fig. 1d) [1]. The results of the EDXS studies (Fig. 1d) revealed only the presence of the Cr K, O K, P K, and Ca K lines [1], specific to 20CrHAp. The graphical representation of the antifungal activity of the 20CrHAp showed that the CFUs values decreased considerably with the increase of the incubation time compared to the control (C+) (Fig. 1f) [1]. The results of the quantitative antifungal assays, which showed that the

inhibition rate increases with prolonged exposure time, can be attributed to the gradual release of chromium ions from the HAp matrix over time [1].

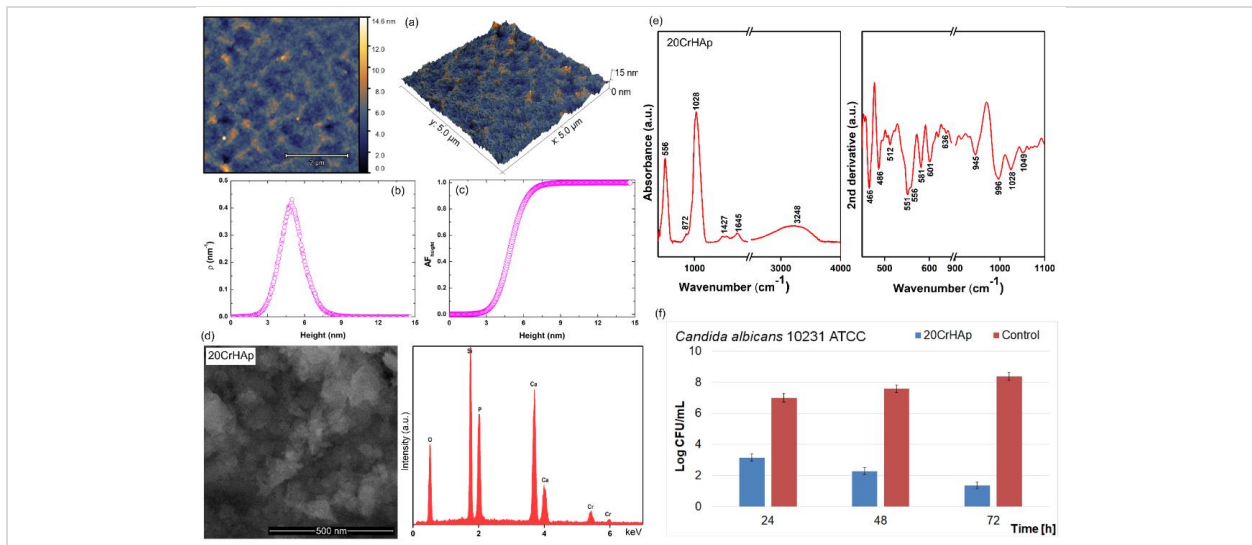


Fig. 1: (a) 2D and 3D representation of the AFM surface topography of 20CrHAp coating before incubation and its (b) height histogram and (c) Abbot-Firestone curve. (d) SEM images and EDXS spectra of 20CrHAp thin films. (e) FTIR and second derivative spectra of 20CrHAp thin films. (f) Graphical representation of the antifungal activity of 20CrHAp thin films against *C. albicans* ATCC® 10231. Adapted from Ref. [1].

XPS studies were carried out to study the chemical composition of AgMgHAp nanocomposites (Figs. 2a–d) [2]. Fig. 2a–d illustrates both the overall XPS spectrum and the high-resolution XPS spectra for Ag 3d, Mg 1s, and Mg 2p [2]. The XPS survey spectrum shows the main peaks associated with Ca 2p, P 2s, and O 1s, characteristic of HAp, as well as Ag 3d, Mg 1s, and Mg 2p, characteristic of the dopants (Fig. 2a) [2]. The SEM images confirmed that the AgMgHAp coatings were continuous, homogeneous, and crack-free, demonstrating the effectiveness of the dip-coating technique in achieving excellent surface coverage on the Si substrate (Fig. 2e) [2]. The adhesion and growth of *C. albicans* cells on the surface of AgMgHAp coatings were investigated using AFM analysis (Fig. 2f) [2]. The AFM images of the 2D surface topography of AgMgHAp coatings revealed their effective inhibition of *C. albicans* fungal cell adhesion and growth, even during the early developmental stage [2]. Notably, the coatings demonstrated the ability to prevent biofilm formation on their surface [2]. Both the 2D topography and its 3D representation suggested a time-dependent correlation with the antifungal activity of the coatings, showing a rapid reduction in the number of attached cells over time [2].

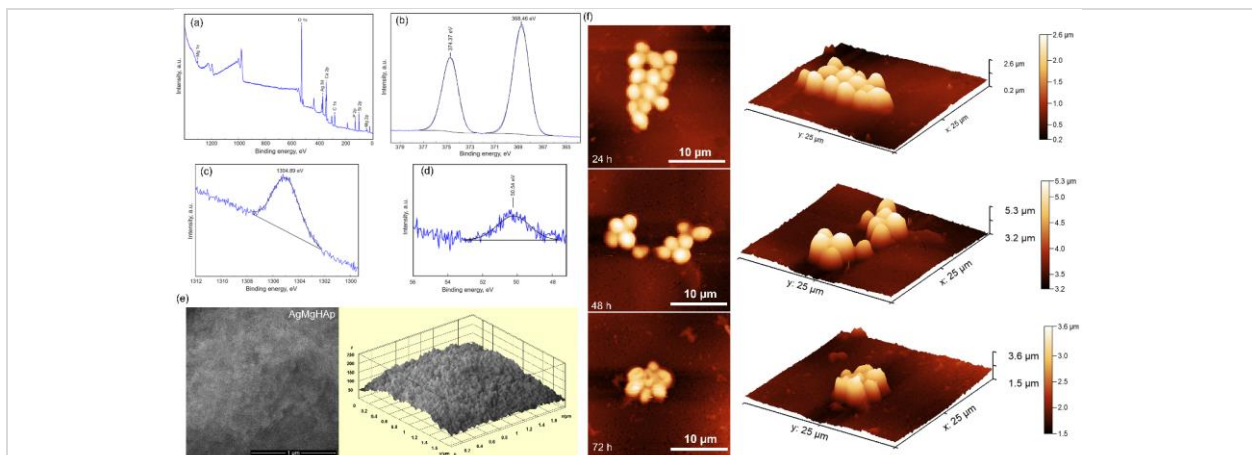


Fig. 2: (a) The XPS survey spectrum of the Ag and Mg doped hydroxyapatite nanocomposite (AgMgHAp). The high-resolution XPS spectra for (b) Ag 3d, (c) Mg 1s, and (d) Mg 2p core electron levels. (e) Characteristic SEM image and the derived 3D topographical representation for the AgMgHAp coating. (f) AFM surface topography of *C. albicans* ATCC® 10231 cells, following incubation with AgMgHAp coatings for 24, 48, and 72 h, depicted in both 2D and 3D representations. Adapted from Ref. [2].

The XRD pattern of the CuHAp thin film showed maxima associated with pure hexagonal HAp in accordance with ICDD-PDF no. 09-0432 reference file (Fig. 3a) [3]. Peaks associated with impurities were not observed. The 2D AFM images (Fig. 3b) revealed that the surface of the CuHAp thin films is homogenous and continuous without presenting any signs of unevenness, cracks or any other discontinuities [3]. The 2D AFM topographies of the CuHAp thin film surfaces after incubation for 24, 48, and 72 h with HGF-1 cells are depicted in Fig. 3c. The 2D AFM topographies revealed that HGF-1 cells adhered to the entire surface of the CuHAp thin films [3]. The 2D AFM images highlighted that the adhered cells exhibited the typical cellular morphology of normal, healthy gingival fibroblasts, with flattened and elongated shapes [3]. The results of the AFM investigation emphasized that the HGF-1 cells showed good adherence to the CuHAp thin film surfaces, with clear evidence of their spread across the entire surface, even at the early stage of adhesion [3]. The AFM studies further demonstrated that the CuHAp thin films favoured the adhesion and development of HGF-1 cells, making them promising candidates for the future development of novel biocompatible devices for biomedical applications [3].

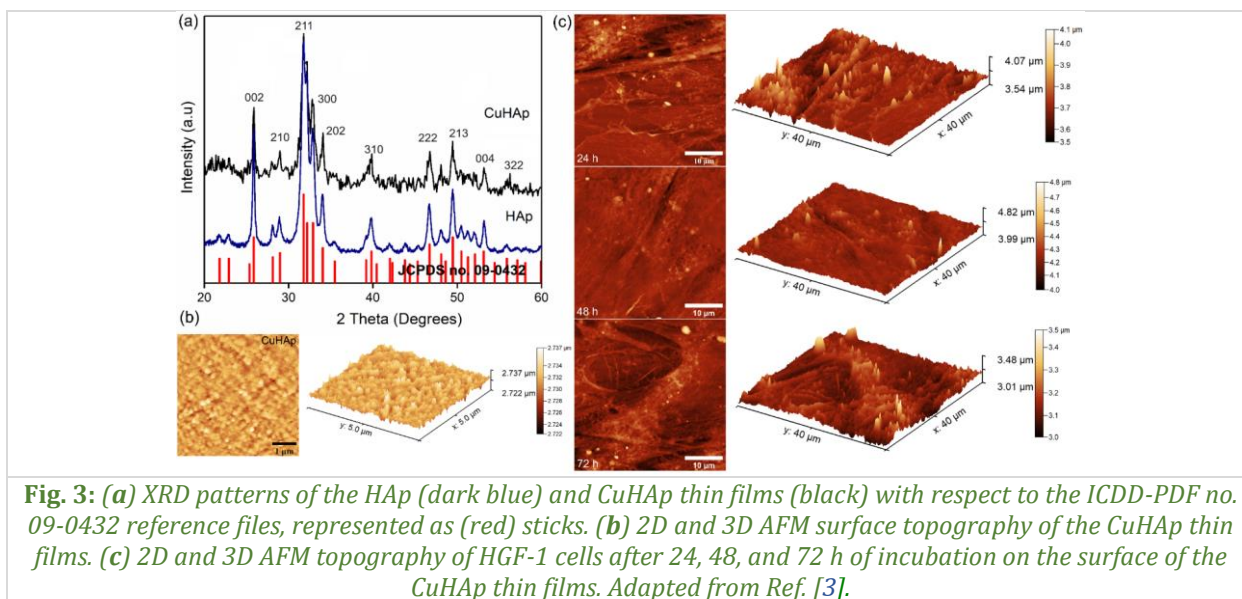


Fig. 3: (a) XRD patterns of the HAp (dark blue) and CuHAp thin films (black) with respect to the ICDD-PDF no. 09-0432 reference files, represented as (red) sticks. (b) 2D and 3D AFM surface topography of the CuHAp thin films. (c) 2D and 3D AFM topography of HGF-1 cells after 24, 48, and 72 h of incubation on the surface of the CuHAp thin films. Adapted from Ref. [3].

In conclusion, it can be stated that 20CrHAp, AgMgHAp, and CuHAp coatings enhance the physicochemical and biological properties of HAp, making them promising candidates for biomedical applications [1–3].

References:

- [1] D. Predoi, S.L. Iconaru, S.C. Ciobanu, Ș. Țălu, S.A. Predoi, N. Buton, G.Q. Ramos, H.D. da Fonseca Filho, R.S. Matos, *Synthesis, characterization, and antifungal properties of chrome-doped hydroxyapatite thin films*, Mater. Chem. Phys. 324 (2024) 129690.
- [2] D. Predoi, Ș. Țălu, S.C. Ciobanu, S.L. Iconaru, R.S. Matos, H.D. da Fonseca Filho, *Exploring the physicochemical traits, antifungal capabilities, and 3D spatial complexity of hydroxyapatite with Ag⁺-Mg²⁺ substitution in the biocomposite thin films*, Micron 184 (2024) 103661.
- [3] C.S. Ciobanu, D. Predoi, S.L. Iconaru, M.V. Predoi, L. Ghegoiu, N. Buton, M. Motelica-Heino, *Copper doped hydroxyapatite nanocomposite thin films: Synthesis, physico-chemical and biological evaluation*, BioMetals 37 (2024) 1487–1500.

Sodium bicarbonate-hydroxyapatite used for removal of lead ions from aqueous solution

**S.A. Predoi^{1,2,3}, S.C. Ciobanu⁴, C.M. Chifiriuc^{3,5,6}, S.L. Iconaru⁴, D. Predoi⁴,
C.C. Negri⁴, I.C. Marinas³, S. Raaen⁷, K. Rokosz⁸, M. Motelica-Heino⁹**

- 1) *École Normale Supérieure Paris-Saclay, Département de Physique, 91190, Gif-sur-Yvette, France*
- 2) *Université Paris-Saclay, 911190, Gif-sur-Yvette, France*
- 3) *Life, Environmental and Earth Sciences Division, Research Institute of the University of Bucharest (ICUB), University of Bucharest, 060023, Bucharest, Romania*
- 4) *National Institute of Materials Physics, 077125, Măgurele, Romania*
- 5) *Department of Microbiology, Faculty of Biology, University of Bucharest, 060101, Bucharest, Romania*
- 6) *Biological Sciences Division, The Romanian Academy, 010071, Bucharest, Romania*
- 7) *Department of Physics, Norwegian University of Science and Technology (NTNU), NO 7491, Trondheim, Norway*
- 8) *Faculty of Electronics and Computer Science, Koszalin University of Technology, PL 75-453. Koszalin, Poland*
- 9) *Institut des Sciences de la Terre d'Orléans (ISTO), UMR 7327 CNRS, Université d'Orléans, 45071, Orleans, France*

One of the toxic metals that can be found in the polluted surface or underground waters is lead (Pb) [1,2]. In the last years, numerous studies regarding the harmful effects of Pb against humans and environment have been reported. In this context, this study [2] focused on developing a novel hydroxyapatite/sodium bicarbonate (HAp-SB) biocomposite for environmental remediation, specifically for removing lead ions (Pb^{2+}) from contaminated water. The XRD patterns of HAp-SB powder before and after decontamination are depicted in Fig. 1a,b. Fig. 1a presents the XRD pattern of HAp-SB before decontamination, along with the ICDD-PDF no. 09-0432 reference file of hexagonal HAp. The XRD pattern of the HAp-SB powder indicated good crystallinity of the structure. The XRD pattern of the powder recovered after decontamination (PbHAp-SB) is presented in Fig. 1b. The XRD peaks of PbHAp-SB were slightly shifted to higher diffraction angles compared to HAp-SB. The presence of additional peaks corresponding to calcium lead phosphate hydroxide (ICDD-PDF no. 10-3163) and lead hydrogen phosphate (ICDD-PDF no. 12-0005) was observed. In addition, a noticeable decrease in the peaks associated with HAp can be observed in the XRD pattern of PbHAp-SB, while peaks corresponding to $Ca_{0.805}Pb_{4.195}(PO_4)(OH)$ and $PbH_2P_2O_7$ like phases appeared. This behaviour suggests the occurrence of ion exchange during Pb^{2+} adsorption by HAp-SB. The obtained results are in good agreement with previously reported data [3], which indicated that Ca^{2+} ions replaced Pb^{2+} ions from the environment. This result highlights that HAp-SB powder has significant potential for removing pollutants from contaminated water.

The XPS survey spectra of the HAp-SB composite are presented both before (Fig. 1f) and after being used in the process of removing lead ions from the contaminated solution (Fig. 1g). The XPS survey spectrum of HAp-SB (Fig. 1f) shows the binding energies of C 1s, O 1s, Ca 2p, P 2p, and Na 1s. The XPS survey spectrum recorded after the adsorption of lead ions (PbHAp-SB) also highlights the binding energy of Pb 4f (Fig. 1g). In Fig. 1h the high-resolution XPS spectrum of Pb 4f is presented. Peaks A and B at 138.99 eV and 143.86 eV, respectively, were assigned to Pb 4f_{7/2} and Pb 4f_{5/2}. The morphology of HAp-SB and PbHAp-SB samples was evaluated using SEM (Fig. 2a,b). The results of the SEM studies revealed that, after the lead decontamination experiments, the morphology of the PbHAp-SB was slightly altered. In both EDXS spectra, the presence of Ca, P, and O peaks can be noticed, which arise from the presence of HAp. For the powders recovered after the lead decontamination experiments (PbHAp-SB), the EDXS spectra showed the Pb (M and L) lines, confirming the efficient adsorption of Pb^{2+} by the HAp-SB samples. Additional information regarding the chemical composition of the HAp-SB and PbHAp-SB powders was obtained through elemental cartography, and the results are depicted in Fig.

2e,f. The main elemental cartographies obtained for the HAp-SB correspond to Ca, P, O, and Na, which are the chemical elements present in the HAp-SB composition (Fig. 2e). For the PbHAp-SB powders recovered and analysed after the lead decontamination experiments, in addition to the cartographies of the chemical elements found in the structure of the HAp-SB sample, a specific cartography of adsorbed Pb was also obtained (Fig. 2f).

FTIR spectroscopy measurements were employed to highlight the functional groups present in both HAp-SB and PbHAp-SB nanopowders, with the results shown in Fig. 3a–d. It was observed that the FTIR spectra of the powders recovered after lead decontamination experiments (PbHAp-SB) closely resemble those of the initial powders (HAp-SB). However, a slight displacement and a broadening of the vibrational peaks can be noticed.

The capacity of HAp-SB nanoparticles to remove Pb^{2+} ions from contaminated water was determined through batch adsorption experiments, and the results are depicted in Fig. 3e–h. Fig. 3e presents a graphical representation of the removal efficiency (R%) as a function of the initial Pb^{2+} concentration in the contaminated solutions. The results demonstrated that the R% for Pb^{2+} removal using HAp-SB nanoparticles was above 88%. Additionally, the findings indicated that the R% value was influenced by the initial Pb^{2+} concentration in the contaminated solution.

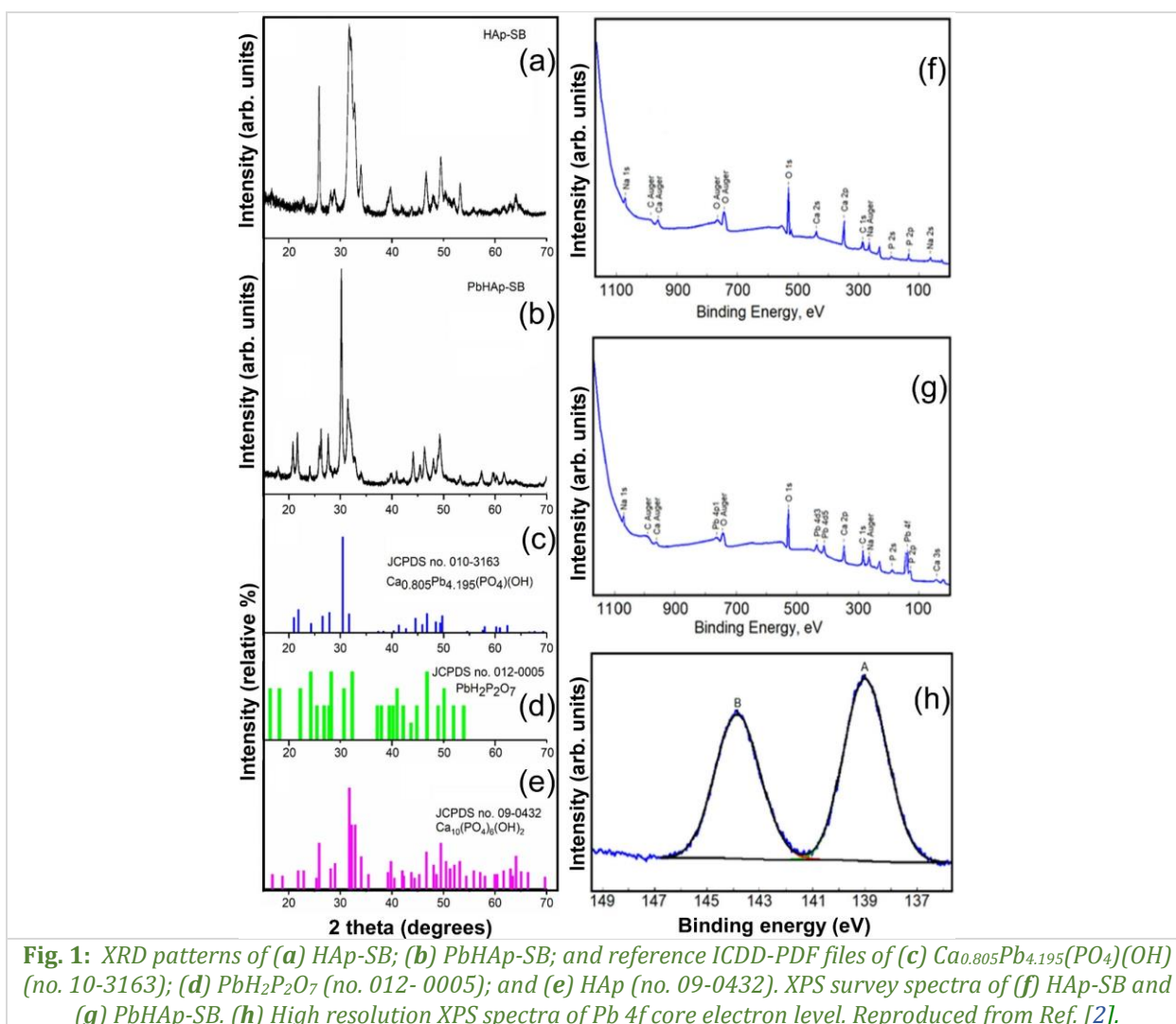
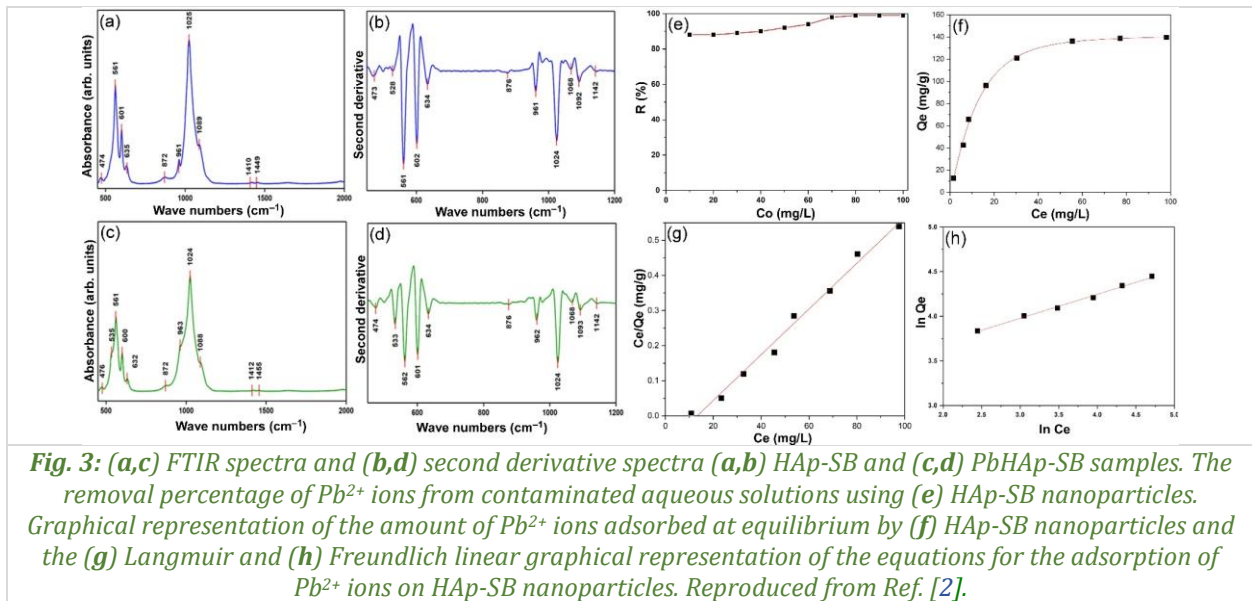
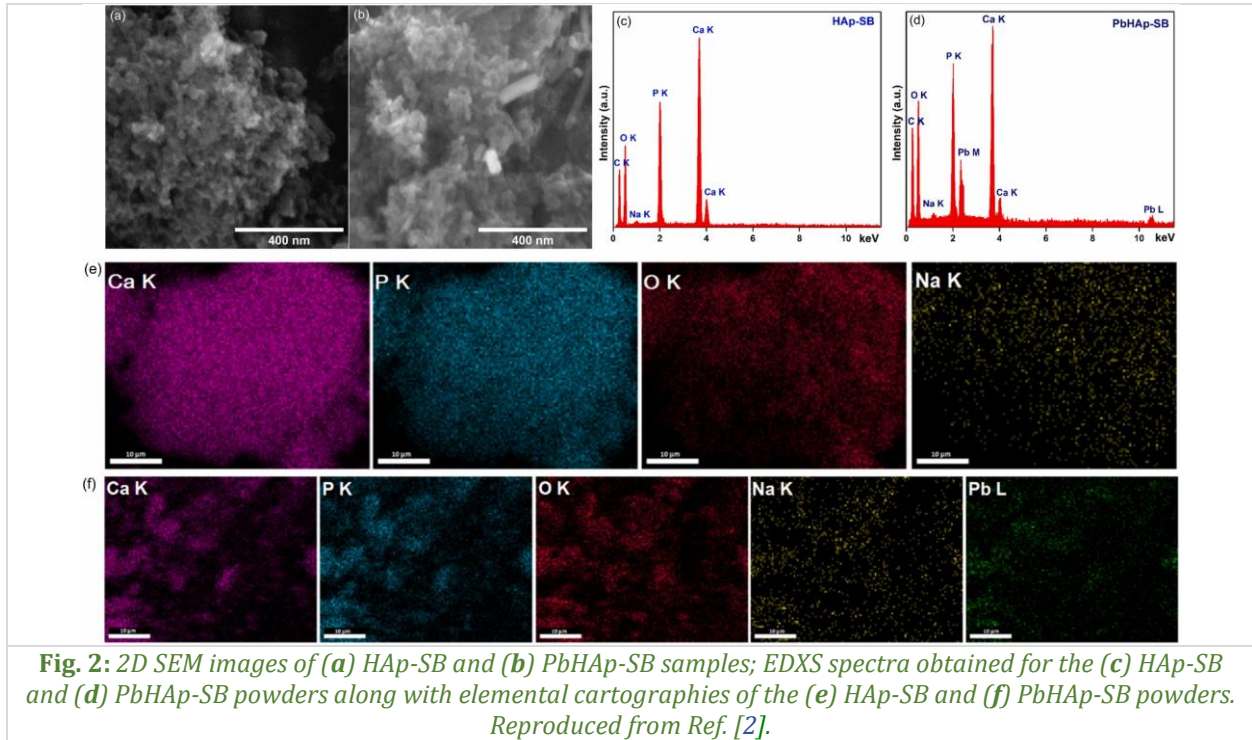


Fig. 1: XRD patterns of (a) HAp-SB; (b) PbHAp-SB; and reference ICDD-PDF files of (c) $\text{Ca}_{0.805}\text{Pb}_{4.195}(\text{PO}_4)(\text{OH})$ (no. 10-3163); (d) $\text{PbH}_2\text{P}_2\text{O}_7$ (no. 012-0005); and (e) HAp (no. 09-0432). XPS survey spectra of (f) HAp-SB and (g) PbHAp-SB. (h) High resolution XPS spectra of Pb 4f core electron level. Reproduced from Ref. [2].

The results highlighted the capability of HAp-SB nanoparticles in removing Pb^{2+} from contaminated water, demonstrating a high affinity for Pb^{2+} ions. The data from the batch experiments, when fitted to both Langmuir and Freundlich isotherm models, showed R^2 values equal to or above 0.99. This suggests that both models were suitable for describing the adsorption of Pb^{2+} onto HAp-SB nanoparticles. However, the results indicated that the Langmuir model ($R^2 = 0.995$) provided a better fit to the experimental data from the batch adsorption experiments compared to the Freundlich model ($R^2 =$

0.994). The adsorption kinetic parameters were also calculated using the linear forms of the equations for Pb^{2+} adsorption on HAp-SB nanoparticles, as shown in Fig. 3g,h. All the results obtained in this study demonstrated that the HAp-SB powders, synthesized through the co-precipitation method, were effective in removing Pb^{2+} ions from contaminated solutions.



References:

- [1] Y. Zhu, Z. Zhu, X. Zhao, Y. Liang, Y. Huang, *Characterization, dissolution, and solubility of lead hydroxypyromorphite $[Pb_5(PO_4)_3OH]$ at 25–45 °C*, J. Chem. 2015 (2015) 269387.
- [2] S.A. Predoi, S.C. Ciobanu, C.M. Chifiriuc, S.L. Iconaru, D. Predoi, C.C. Negrila, I.C. Marinas, S. Raaen, K. Rokosz, M. Motelica-Heino, *Sodium bicarbonate-hydroxyapatite used for removal of lead ions from aqueous solution*, Ceram. Int. 50 (2024) 1742–1755.
- [3] Y. Zhu, B. Huang, Z. Zhu, H. Liu, Y. Huang, X. Zhao, M. Liang, *Characterization, dissolution and solubility of the hydroxypyromorphite-hydroxyapatite solid solution $[(Pb_xCa_{1-x})_5(PO_4)_3OH]$ at 25 °C and pH 2–9*, Geochem. Trans. 17 (2016) 2.

Recent breakthroughs in the field of magnetron-sputtered bioactive glass thin films

**G.E. Stan¹, M. Montazerian^{2,3}, A. Shearer³, B.W. Stuart⁴, F. Baino⁵,
J.C. Mauro³, J.M.F. Ferreira⁶**

- 1) *National Institute of Materials Physics, 077125, Măgurele, Romania*
- 2) *Northeastern Laboratory for Evaluation and Development of Biomaterials, Federal University of Campina Grande, 58429-900, Campina Grande, PB, Brazil*
- 3) *Department of Materials Science and Engineering, The Pennsylvania State University, 16802, University Park, PA, USA*
- 4) *Advanced Materials Research Group, Faculty of Engineering, University of Nottingham, NG7 2RD, Nottingham, United Kingdom*
- 5) *Institute of Materials Physics and Engineering, Department of Applied Science and Technology, Politecnico di Torino, 10129, Torino, Italy*
- 6) *CICECO Aveiro Institute of Materials, Department of Materials and Ceramics Engineering, University of Aveiro, 3810-193, Aveiro, Portugal*

Load-bearing endosseous implants are typically manufactured from medical-grade metallic alloys, with titanium-based variants currently dominating the global market. Despite their proven biocompatibility and excellent mechanical performance, metallic implants require long healing times due to their lack of bioactivity, osteointegration, and therapeutic functionality. Consequently, they do not actively contribute to the bonding and healing processes. To address these limitations, current research focuses on coating endosseous implants with bioactive and functional materials [1].

Bioactive glasses (BGs) are recognized for their selective ability to (i) form a mechanically strong interfacial bond with hard or soft tissues, as seen in silica-, silica-phosphate-, phosphate-, borate-phosphate-, or silica-phosphate-borate-based BGs; or (ii) serve as reservoirs for the rapid release of therapeutic ions with osteogenic, angiogenic, anticarcinogenic, or antimicrobial properties, as in phosphate- and borate-based BGs. The biomineralization capacity and resorbability of BGs are influenced by the ratio of network formers to modifiers, depending on the specific case.

BGs offer excellent biocompatibility but are biomechanically suboptimal for load-bearing applications due to their lower fracture toughness and higher elastic modulus. A promising strategy to address this limitation is the development of BG coatings on load-bearing endosseous implants.

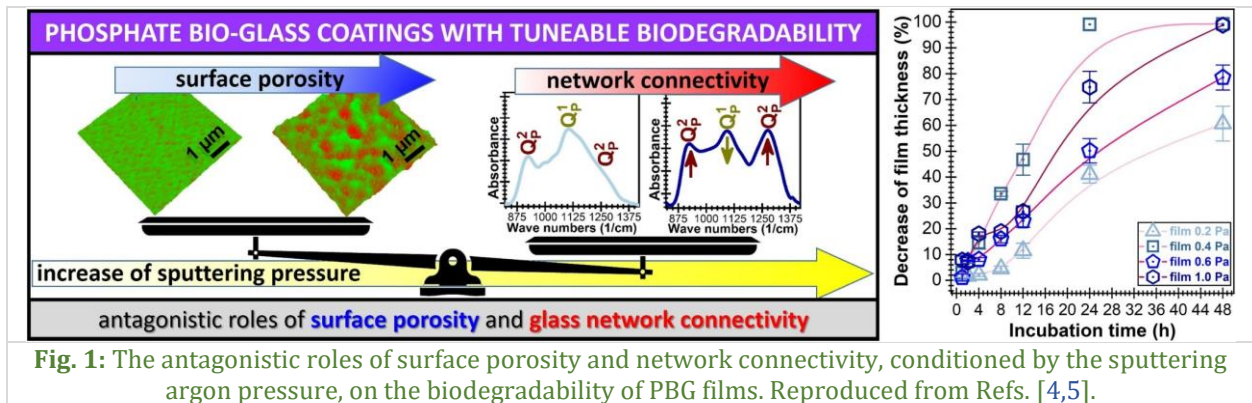
Currently, commercially available implants are coated with thick hydroxyapatite (HA) layers (>50 µm) using plasma spraying (PS), the most widely employed technique for HA deposition [2]. Notably, this remains the only FDA-approved process for coating clinical-ready endosseous implants [3]. Despite their suitable biological performance, PS HA coatings often face challenges with proper adhesion to the substrate, which remains a key limitation to their widespread adoption.

Alternatively, various deposition methods have been explored for both thick coatings (>5 µm) and thin films (<5 µm), including enamelling/glazing, electrophoretic deposition, sol-gel, pulsed laser deposition, pulsed electron deposition, ion-beam sputtering, and radio-frequency magnetron sputtering (RF-MS) [4]. Although many studies have explored implant coatings, research on BG coatings for 3D-profiled endosseous implants is still limited.

Noteworthy, the advancements made in RF-MS deposition of BGs, including the coating of implants with complex geometries, particularly over the last decade, have accelerated their progress. This makes it essential to provide an analytical review of their rapid development toward real-life biomedical applications. In this regard, this work [4] critically evaluates BG thin films produced by RF-MS, offering insights into their future potential. RF-MS, an industry-ready large-scale physical vapor deposition (PVD) technology, has been developed primarily by researchers from the National Institute of Materials Physics (Romania), the University of Nottingham (UK), and the University of Aveiro (Portugal), both independently and in collaboration.

In addition to its proven ability to be translated to industry, this deposition technology's versatility and flexibility have enabled protocols that address key development challenges, including bonding strength,

composition and structure replication, "line-of-sight" deposition (poor step coverage), low deposition rate, control over degradability (Fig. 1), and cost-effective manufacturing.



The adhesion of BG films deposited by RF-MS is no longer a concern, surpassing the ISO 13779-2:2018 minimum (15 MPa) and often exceeding the FDA's recommendation (50.8 MPa) [3] for low coefficient of thermal expansion BG systems [4]. Strategies to enhance bonding strength for more demanding BGs have been successfully applied, including thin-layer insertion with graded BG-Ti composition and atomic interdiffusion through post-deposition annealing treatments [4].

Early criticisms of RF-MS, particularly regarding its inability to accurately replicate the composition of complex materials like BGs due to the expulsion of lighter species, have been addressed through systematic studies [4]. These studies revealed that the issue is no longer a major challenge, as it has been overcome by adjusting process methodologies. Sputtering pressure has been identified as the most effective parameter for accurately tailoring the composition and structure, with higher pressures proving preferable [4]. Additionally, a long target pre-sputtering step (~45–60 min) significantly improves the atomic transfer from target to substrate, ensuring a more consistent and accurate deposition.

Of course, there is no one-size-fits-all RF-MS processing regime, as each target composition requires specific adjustments. However, the key influencing factors have now been identified, allowing for precise tailoring of film properties. The wide array of RF-MS parameters, such as sputtering pressure, working ambient, target-to-substrate distance, electrical power, and driving radio-frequency, enables optimization of mechanical and biological performance with a single target composition. This flexibility makes RF-MS an economically attractive and versatile technique.

Additionally, challenges related to step and 3D feature coverage, particularly for complex geometries like dental implants, have been overcome by simple solutions like substrate rotation [4] (Fig. 2), with many of these advancements already incorporated into commercial systems.

The use of powder targets, as advocated by Stan & Ferreira and colleagues [4], offers several clear advantages over traditional compact targets (such as those made from melt-quenched pre-forms or sintered powders). These advantages include: (i) the ability to employ higher target powers without risking irreversible damage or cracking to the compact targets, and (ii) the potential for reproducible coatings, as powder targets can be easily reassembled before each deposition session, ensuring a fresh target surface each time and preventing the surface composition of compact targets from altering during use [4].

Altogether, RF-MS is a promising method for bio-functionalizing endosseous implants with BG layers, but further developments are needed. Key areas for advancement include:

1. Optimizing BG coating characteristics, such as surface topography and wettability, to enhance cell adhesion and osseointegration.
2. Using larger magnetron cathode deposition systems for industrial-scale applications.
3. Investigating post-deposition annealing treatments to improve the mechanical properties and degradation of SBGs and PBGs, and exploring BBG deposition by RF-MS.
4. Defining technical specifications for BG coatings, including the effects of sterilization and critical coating thickness.
5. Expanding the antimicrobial range of BGs by identifying new ionic therapeutic agents.
6. Increasing deposition rates to improve manufacturability and clinical translation.

7. Exploring ionized physical vapor deposition methods for better coverage of high-aspect ratio substrates.

These developments will support the transition of BG coatings from research to clinical use. We believe that the future lies in pushing the boundaries of manufacturing compatibility with these methods and making novel advancements to enable the industrialization of BG coatings.

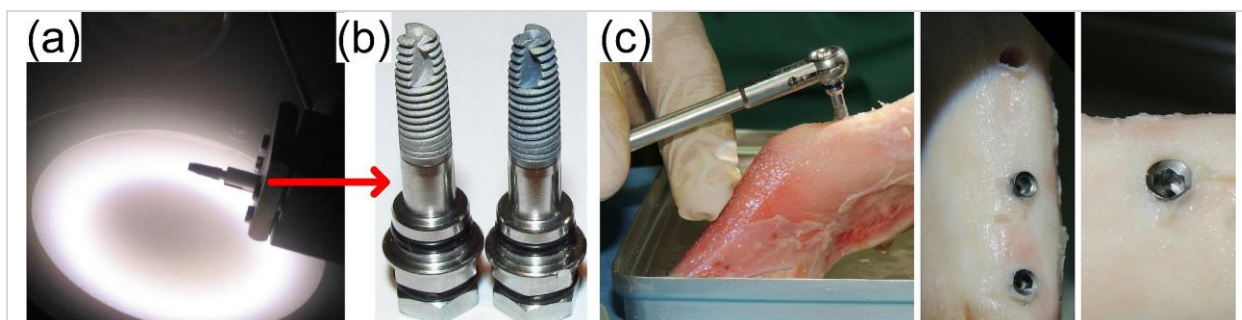


Fig. 2: (a) Snapshot taken during the RF-MS coating process of a dental screw with BG. (b) Comparative images of simple (left-hand side) and BG functionalized (right-hand side) dental implants. (c) Representative images acquired during the implantation-extraction procedure of the dental screws biofunctionalized by RF-MS with BG coatings. Reproduced from Refs. [4,6].

References:

- [1] M. Montazerian, F. Hosseinzadeh, C. Migneco, M.V.L. Fook, F. Baino, *Bioceramic coatings on metallic implants: An overview*, *Ceram. Int.* 48 (2022) 8987–9005.
- [2] R.B. Heimann, *Plasma-sprayed hydroxylapatite coatings as biocompatible intermediaries between inorganic implant surfaces and living tissue*, *J. Therm. Spray Technol.* 27 (2018) 1212–1237.
- [3] [STP25193S – Calcium phosphate \(Ca-P\) coating draft guidance for preparation of Food and Drug Administration \(FDA\) submissions for orthopedic and dental endosseous implants.](#)
- [4] G.E. Stan, M. Montazerian, A. Shearer, B.W. Stuart, F. Baino, J.C. Mauro, J.M.F. Ferreira, *Critical advances in the field of magnetron sputtered bioactive glass thin-films: An analytical review*, *Appl. Surf. Sci.* 646 (2024) 158760.
- [5] T. Tite, A.C. Popa, I.M. Chirica, B.W. Stuart, A.C. Galca, L.M. Balescu, G. Popescu-Pelin, D.M. Grant, J.M.F. Ferreira, G.E. Stan, *Phosphate bioglass thin-films: Cross-area uniformity, structure and biological performance tailored by the simple modification of magnetron sputtering gas pressure*, *Appl. Surf. Sci.* 541 (2021) 148640.
- [6] A.C. Popa, G.E. Stan, M. Enculescu, C. Tanase, D.U. Tulyaganov, J.M.F. Ferreira, *Superior biofunctionality of dental implant fixtures uniformly coated with durable bioglass films by magnetron sputtering*, *J. Mech. Behav. Biomed. Mater.* 51 (2015) 313–327.

Challenges and solutions in developing barium titanate–hydroxyapatite ceramics with optimal piezoelectric and biological properties

M. Cioangher¹, L. Amarande¹, G.E. Stan¹, L. Nedelcu¹, I. Pasuk¹, L. Leonat¹,
A.C. Popa¹, L.C. Miclea^{2,3}, T. Savopol^{2,3}, M.G. Moisescu^{2,3}, I. Tivig^{2,3}

- 1) *National Institute of Materials Physics, 077125, Măgurele, Romania*
- 2) *Biophysics and Cellular Biotechnology Department, Faculty of Medicine, Carol Davila University of Medicine and Pharmacy, 050474, Bucharest, Romania*
- 3) *Excellence Centre for Research in Biophysics and Cellular Biotechnology, Carol Davila University of Medicine and Pharmacy, 050474, Bucharest, Romania*

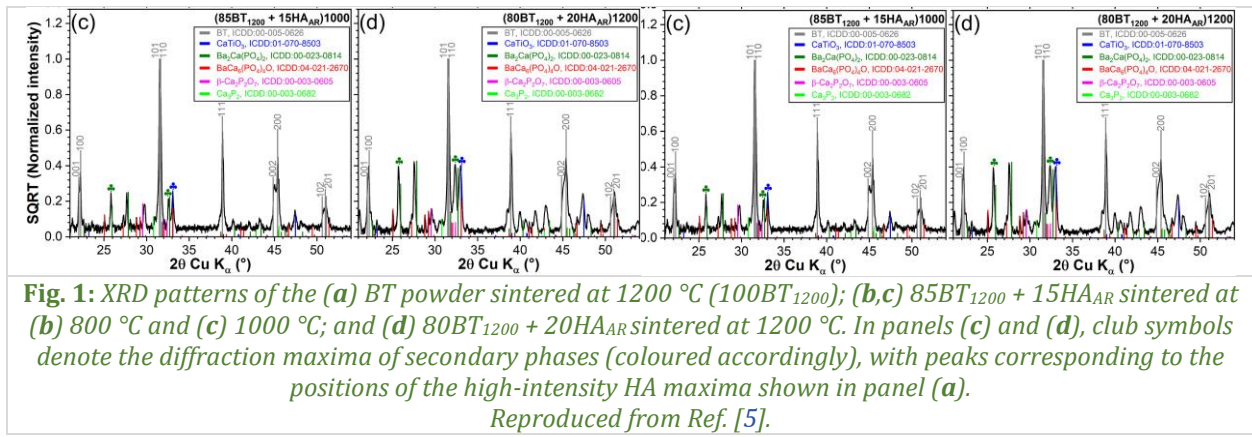
The biomedical research community is focused on developing competitive alternatives to bone repair solutions, utilizing new synthetic biomaterials or material combinations with enhanced osteogenic properties, as substitutes for (i) autografts, (ii) allografts, and (iii) xenografts [1,2]. To date, calcium orthophosphates (hydroxyapatite [HA, $\text{Ca}_{10}(\text{PO}_4)_6(\text{OH})_2$] and beta-tricalcium phosphate [$\beta\text{-Ca}_3(\text{PO}_4)_2$]) and silica-based bioactive glasses have been extensively studied for the design of synthetic bone graft substitutes (SBGSs) and bio-functionalization coatings for implant [3]. Barium titanate (BT, BaTiO_3) is considered a promising piezoceramic candidate for bone tissue regeneration due to its bio-inertness, biocompatibility, and significant piezoelectric effect [4]. In this context, our research aimed to explore whether the reactivity of BT-HA during conventional ceramic fabrication could be mitigated by altering the BT/HA ratio, crystalline quality, particle size, and sintering temperature [5]. Structural, electrical, and in-vitro biological investigations were conducted.

The sintering of BT-HA mixtures was performed using a stratified approach to investigate the effects of: (i) sintering temperature, varied within the 800 – 1300 °C range; (ii) bioactive HA phase content (5–20 wt.%); and (iii) pre-sintering heat-treatment temperatures of BT (1100, 1200, and 1300 °C) and HA (500, 1100, and 1300 °C) powders.

The BT and HA components remain unreacted only during the 800 °C sintering. This is evidenced by the unchanged diffraction peaks of BT, both in terms of position and width, as well as the definitive identification of all the prominent maxima of hexagonal HA, except for those overlapped by the BT peaks (Fig. 1a,b). Another indication of the preservation of HA upon sintering the BT-HA mixtures at 800 °C is the largely conserved mean crystallite sizes along the *c*- and *a*-axes, with $D_{002} \approx 101$ nm and $D_{300} \approx 47$ nm, similar to those of pure HA discs sintered at 800 °C. However, the sintered products were brittle and, therefore, unsuitable for SBGS applications.

At 1000 °C, the BT and HA phases react (Fig. 1c), resulting in the formation of new crystalline phases: CaTiO_3 , two barium calcium phosphates $\text{Ba}_2\text{Ca}(\text{PO}_4)_2$ and $\text{BaCa}_6(\text{PO}_4)_4\text{O}$, β -calcium pyrophosphate, and calcium phosphide. Thereby, both BT (partially) and HA (apparently completely) react, leading to the formation of CaTiO_3 , with the minuend Ba forming the two barium calcium phosphates (*i.e.*, $\text{Ba}_2\text{Ca}(\text{PO}_4)_2$; $\text{BaCa}_6(\text{PO}_4)_4\text{O}$). The supplemental advent of the of calcium pyrophosphate and phosphide phases may be induced by a Ca/P molar ratio significantly lower than the stoichiometric ratio of HA (1.67) in the remaining available Ca and P atoms, as well as the favourable transformation of $\beta\text{-Ca}_3(\text{PO}_4)_2$ into the calcium phosphide phase. Increasing the sintering temperature to 1200 °C resulted in an augment of the CaTiO_3 and barium calcium phosphate phases (Fig. 1d).

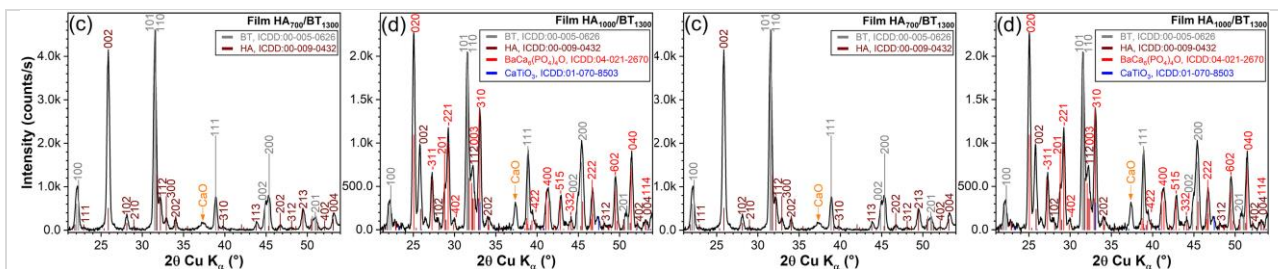
Despite efforts to vary the powder particle size and crystallinity, the ratio of constituent phases, and the sintering regime at temperatures ≥ 1000 °C, BT reacts with HA, resulting in severe-to-total decomposition of HA and partial decomposition of BT. This reaction leads to the formation of CaTiO_3 , various Ba and Ca phosphates, $\beta\text{-Ca}_2\text{P}_2\text{O}_7$, and Ca_3P_2 as secondary phases, which significantly compromises the piezoelectric and bioactive properties originally expected from the BT-HA composite.



To overcome the reactivity issues between BT and HA and preserve the intrinsic properties of both phases, a novel functional coupling approach was explored: coating the BT bulk ceramic with radio-frequency magnetron sputtered (RF-MS) HA layers. This method allows the use of sintering temperatures suitable for BT, which is manufactured separately from HA in this scenario, while also enabling the processability of HA (*i.e.*, deposition and *ex-situ* crystallization at lower temperatures in a second step). This approach prevents HA's thermal decomposition and reactivity with BT, enabling high-quality BT-HA products that combine BT's mechanical and piezoelectric properties with an osteogenic interface from the HA coating.

HA films were deposited by RF-MS on the surface of BT discs sintered at 1300 °C for 2 h. In their as-deposited form, the HA films were amorphous at the XRD apparatus's sensitivity limit, necessitating an *ex-situ* post-deposition thermal treatment in air. In the first experiment, thin (~200 nm) HA films were deposited on BT discs and annealed at 550 °C for 1 h in air. These samples underwent GIXRD analysis at grazing angles between 0.25° and 5°, corresponding to penetration depths of ~0.2 to 3.5 μm. The annealing process fully crystallized the as-deposited HA film, with no BT-HA chemical reactions or diffusivity phases detected, regardless of the grazing angle.

In a second experiment, thick (~2000 nm) HA films were deposited on BT discs to assess the structural features and piezoelectric response of the HA-BT couple as a function of post-deposition annealing at 550, 700, and 1000 °C. GIXRD analysis (Fig. 2) revealed that the as-deposited (AD) HA film was amorphous, as indicated by the broad hump in the 2θ range of ~25–35° (Fig. 2a). Annealing at 550 °C resulted in the complete crystallization of the HA film (Fig. 2b). The crystallized HA films displayed a *c*-axis preferred orientation, with a significantly intensified 002 peak compared to the corresponding line in the reference ICDD file, a characteristic feature of many hexagonal compounds deposited by RF-MS. A minor secondary CaO phase was detected, but no BT-HA reaction occurred. Similar results were obtained after annealing the HA/BT samples at 700 °C (Fig. 2c). However, at 1000 °C, strong BT-HA reactivity was observed, marked by the formation of BaCa₆(PO₄)₄O and CaTiO₃ phases (Fig. 2d). However, compared to the BT-HA powder mixtures sintered at 1000 °C (Fig. 1c), the HA-coated BT discs annealed at 1000 °C show a notable preservation of HA, with a significant reduction in the number of secondary phases (Fig. 2d) when compared to the conventional sintering of the admixed BT-HA at 1000 °C.



Altogether, post-deposition annealing at 550 °C in air was found to be sufficient to induce complete crystallization of the applied HA coating, yielding a crystalline quality comparable to HA discs sintered

at 1100 °C, with a mean crystallite size along the *c*-axis of approximately 340 nm. Furthermore, SEM analysis of the 550 °C-annealed films showed that they were well-compacted and conformed closely to the BT surface.

The HA films post-annealed at 550 and 700 °C did not significantly alter the P-E loops of the BT ceramics. However, the film post-annealed at 1000 °C exhibited an increased coercive field and a slightly reduced maximum polarization, likely due to the partial reaction between BT and HA.

All BT-HA mixtures sintered at temperatures below 1300 °C were found to be cytotoxic to fibroblast cells. This toxicity resulted from factors such as the high solubility of the constituent phases, which led to alkalisation of the cell culture medium, and the presence of Ba-based phosphates, known to be harmful to cell viability. In turn, the cell viability and proliferation in both fibroblast and osteoblast cell cultures for the 550 °C-annealed HA coatings were similar to those of the bulk sintered HA discs.

In conclusion, this multi-parameter study, demonstrated that in a conventional sintering regime, the reactivity of BT-HA mixture constituents cannot be avoided at temperatures exceeding 800 °C, regardless of their ratio, crystalline quality, or particle size. To address this issue, a simple and cost-effective solution was proposed and validated to mitigate BT-HA reactivity, while preserving the piezoelectric properties of BT and the osteogenic potential of HA: deposition of HA coatings on the surface of pre-sintered BT discs by the industrial-ready RF-MS deposition technology.

A comprehensive evaluation of the complementarity of BT-HA for accelerated bone regeneration applications will be pursued as a future step, addressing both (i) the comparative osteogenic responses of bare and HA-coated BT surfaces, and (ii) the exploration of the correlation between the magnitude of the piezoelectric effect, generated under dynamic mechanical stress (a rarely explored subject to date), and the speed of osseointegration.

References:

- [1] S.S. Lee, X. Du, I. Kim, S.J. Ferguson, *Scaffolds for bone-tissue engineering*, Matter 5 (2022) 2722–2759.
- [2] A.P. Francis, A.R. Augustus, S. Chandramohan, S.A. Bhat, V.V. Priya, R. Rajagopalan, *A review on biomaterials-based scaffold: An emerging tool for bone tissue engineering*, Mater. Today Commun. 34 (2023) 105124.
- [3] G.E. Stan, M. Montazerian, A. Shearer, B.W. Stuart, F. Baido, J.C. Mauro, J.M.F. Ferreira, *Critical advances in the field of magnetron sputtered bioactive glass thin-films: An analytical review*, Appl. Surf. Sci. 646 (2024) 158760.
- [4] M. Acosta, N. Novak, V. Rojas, S. Patel, R. Vaish, J. Koruza, G.A. Rossetti, J. Rödel, *BaTiO₃-based piezoelectrics: Fundamentals, current status, and perspectives*, Appl. Phys. Rev. 4 (2017) 041305.
- [5] M. Cioanher, L. Amarande, G.E. Stan, L. Nedelcu, I. Pasuk, L. Leonat, A.C. Popa, L.C. Miclea, T. Savopol, M.G. Moisesescu, I. Tivig, *Hindrances and solutions on the path towards adjoined barium titanate–hydroxyapatite ceramics with uncompromised piezoelectric and biological responses*, Ceram. Int. 50 (2024) 29711–29728.

Reticulated mesoporous TiO₂ scaffold for self-cleaning surfaces

**C. Besleaga¹, A.G. Tomulescu¹, I. Zgura¹, A. Stepanova¹, A.C. Galca¹, S. Laafar¹,
F.L. Zorila^{2,3}, M. Alexandru², I. Pintilie¹, M. Iliescu^{4,5}**

- 1) *National Institute of Materials Physics, 077125, Măgurele, Romania*
- 2) *Horia Hulubei National Institute of Physics and Nuclear Engineering, 077125, Măgurele, Romania*
- 3) *Faculty of Biology, University of Bucharest, 050095, Bucharest, Romania*
- 4) *Institute of Solid Mechanics, Romanian Academy, 030167, Bucharest, Romania*
- 5) *S.C. Optoelectronica-2001 S.A., 35 Lacului, 077125, Măgurele, Romania*

The growing interest in self-cleaning coatings arises from their potential to enhance quality of life and comfort, particularly in large urban areas where pollution is a major concern. By applying these coatings to surfaces such as window glass, the reliance on chemical cleaners, often harmful and environmentally polluting, can be significantly reduced. This approach is also highly beneficial in the solar panel industry, where keeping large-scale solar plants or roof-mounted panels clean is both challenging and costly. Neglecting maintenance can lead to significant performance losses. By utilizing UV light from the sun and rainwater for cleaning, self-cleaning coatings offer a sustainable and cost-effective solution for maintaining efficiency.

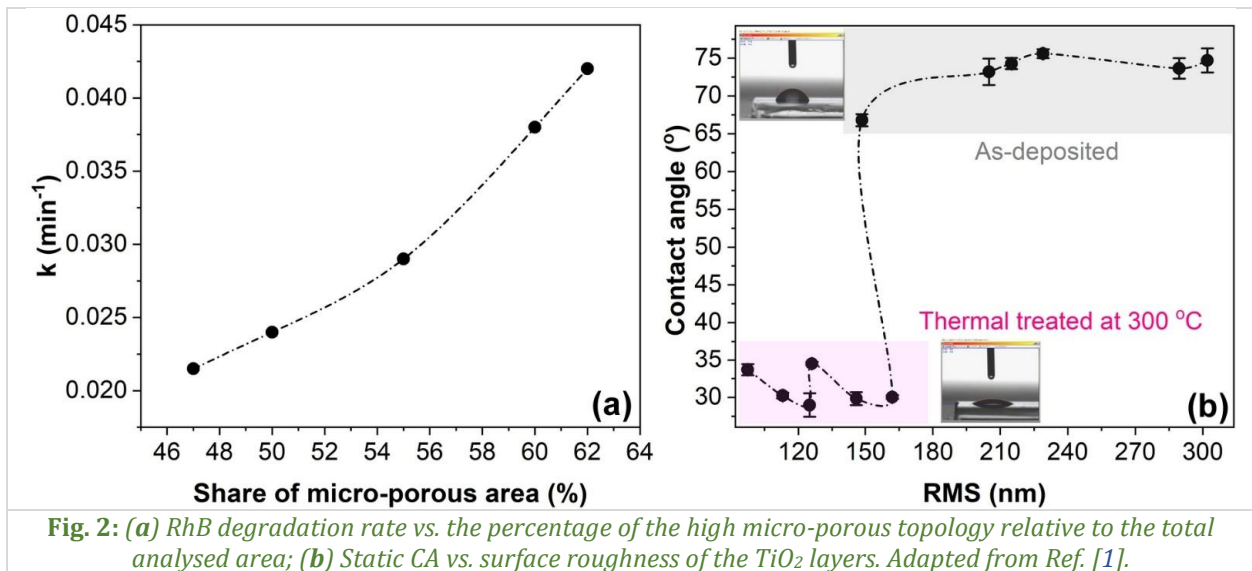
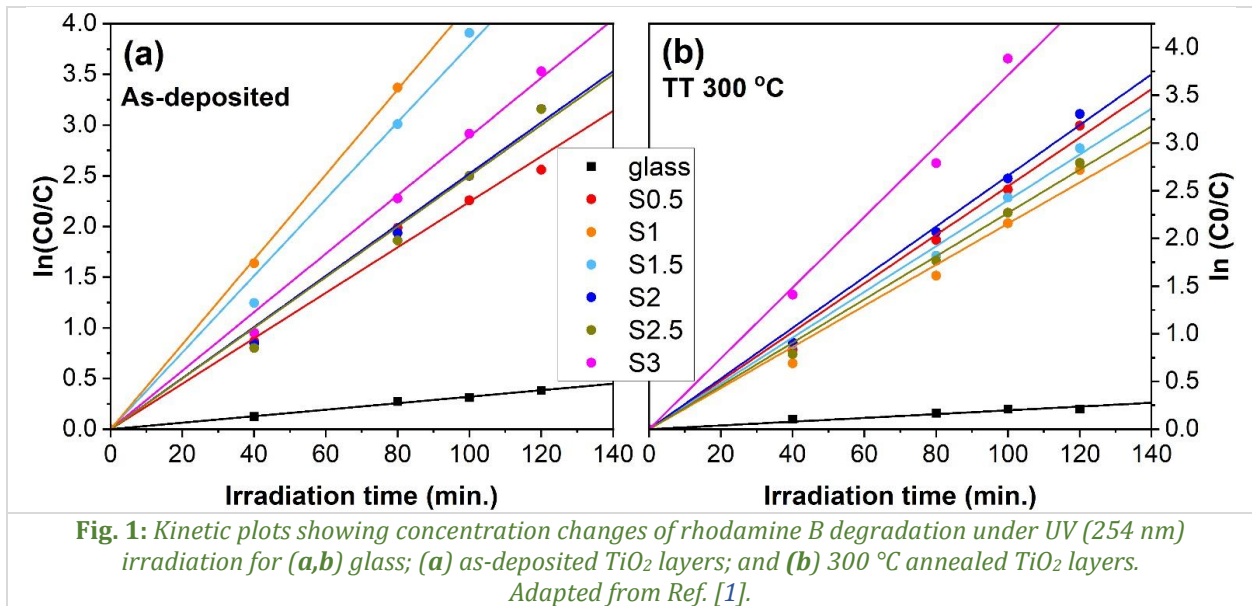
We engineered passive substrates (*e.g.*, window glass) with TiO₂ nanoparticles in the form of reticulated mesoporous coatings applied by spray deposition. The goal was to enhance efficacy in both organic dirt degradation and achieve self-cleaning and antimicrobial effects. We hypothesized that these TiO₂ reticulated mesoporous scaffolding coatings, with their unique textural characteristics, would improve photocatalytic efficiency and self-cleaning capacity. The mesoporous structure, with its extensive porous network, is designed to facilitate light penetration, and thus maintain transparency, while enabling pollutants to interact with the catalytic surface, thereby maximizing degradation. Various coating architectures were produced and analysed using multiple techniques, with results cross-referenced and discussed. Preliminary evidence suggests that this innovative approach, utilizing affordable materials (*i.e.*, TiO₂) and deposition methods (*i.e.*, spray deposition), could effectively address the limitations of conventional self-cleaning coatings, potentially leading to more effective and durable self-cleaning and self-decontamination solutions.

The TiO₂ layers were deposited on preheated supports, at 100 °C, with nitrogen carrier gas pressure changed from 0.5 to 3 kgf/cm² in 0.5 kgf/cm² increments. More details about the fabrication processes can be found in the source article [1].

The as-deposited TiO₂ layers demonstrated notable photocatalytic activity in the degradation of RhB, with the highest degradation rate of 0.045 min⁻¹ achieved by sample S1, which degraded 97.3% of a 25 mL of RhB solution in 80 minutes (Fig. 1a). Sample S1.5 exhibited the second-best degradation rate of 0.039 min⁻¹, degrading 98% of the RhB solution after 100 min of 254 nm irradiation. Thus, for as-deposited samples, the optimal deposition pressure for achieving good photocatalytic efficiency is between 1 and 1.5 kgf/cm², conditions that correspond to high roughness values. The best activity among the annealed samples was observed for S3-TT 300 °C sample, deposited at the highest pressure of 3 kgf/cm², with a corresponding degradation rate (*k*) of 0.037 min⁻¹ (Fig. 1b).

AFM images revealed that the peaks correspond to particle aggregates with a fractal-like appearance, compact at the microscale, while the valleys exhibit high microporosity. The area percentage of the high micro-porous topology relative to the total analysed area was evaluated using Gwyddion2.62 software and then plotted against the RhB degradation rate (Fig. 2a).

At the nanometric scale, both the tall and valley regions of the tested samples exhibit similar nanoporosity, as indicated by the FE-SEM investigations. Therefore, in our case, the measured photocatalytic degradation rate is directly related to the micro-porosity. Empirical evidences showed that the micro-porous surfaces can perform as well as nano-porous ones [2]. The enhanced photocatalytic performance associated with the increased porosity is well documented and attributed to the larger specific surface area, which increases the contact between the photocatalytic material and the pollutant [3].



The CA measurements indicated that all the samples are hydrophilic. Post-deposition annealed samples have CAs close to superhydrophilic ($\sim 30^\circ$), whereas the as-deposited samples show CA values of $\sim 75^\circ$ (Fig. 2b), placing them near to hydrophobic boundary (*i.e.*, 90°). The wettability properties of the TiO_2 reticulated surfaces are directly related to their surface roughness, which can be adjusted by varying the spraying pressure or through post-deposition thermal treatment at low temperatures. A step-like dependence of CA on RMS was observed, with a threshold RMS value of ~ 165 nm. This behaviour is consistent with regular arrays of microstructures [4] and can be theoretically explained using the Wenzel and Cassie-Baxter models [5,6]. The dynamic wetting behaviour tests revealed that the water droplets maintain their spherical cap shape even when tilted in vertical position (90°) with volume of $10 \mu\text{L}$. As tilt angle increases, the receding CA is linearly decreasing, from $\sim 39^\circ$ to $\sim 20^\circ$, while the advancing CA increases, from $\sim 47^\circ$ to $\sim 70^\circ$, irrespective of the droplet volume used (*i.e.*, 1, 8, or $10 \mu\text{L}$). According to Yeh *et al.* [7], in the Wenzel model, advancing CAs increase with surface roughness, while receding CAs decrease. In contrast, the Cassie-Baxter model suggests that both advancing and receding CAs are independent of surface roughness. However, the results of the dynamic wetting do not align with either of these models. Instead, both the advancing and receding CAs are increasing with RMS. This observation supports the static CA data from Fig. 3, indicating that the reticulated TiO_2 surfaces do not conform to either Wenzel or Cassie-Baxter models.

For the self-cleaning tests, a bare glass substrate was used as reference sample. The cleaning efficiency for the bare glass substrate was of $\sim 82\%$ after 3 h and of $\sim 94.5\%$ after 22 h of 254 nm UV exposure. In

contrast, all the post-deposition treated TiO_2 samples demonstrated significantly improved self-cleaning efficiency, achieving 100% cleaning within just 3 h of UV exposure (Fig. 3). This is notably better than the as-deposited samples, which either reached 100% cleaning only after a much longer duration of 22 h or achieved a maximum 36% cleaning under the same UV exposure conditions.

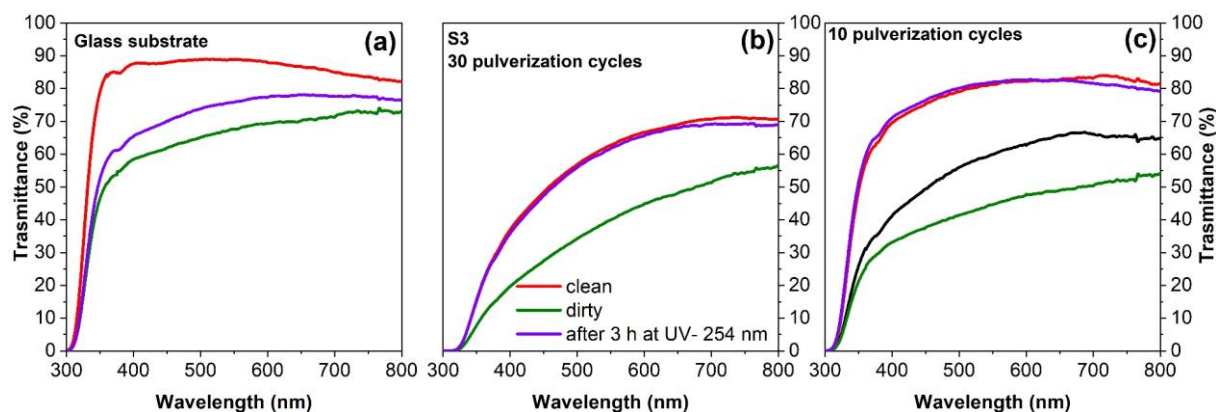


Fig. 3: Transmittance spectra before and after dirt self-cleaning for the 300 °C annealed samples – UV 254 nm: (a) glass; (b) S3 – 30 pulverization cycles; and (c) S3 – 10 pulverization cycles. Adapted from Ref. [1].

Beside self-cleaning properties, the reticulated TiO_2 coating showed promising results for the elimination of pathogen microorganisms and surface disinfection.

These findings contribute to a deeper understanding of TiO_2 surface properties and open new avenues for developing highly efficient and versatile functional coatings for self-cleaning and antimicrobial decontamination applications.

References:

- [1] C. Besleaga, A.G. Tomulescu, I. Zgura, A. Stepanova, A.C. Galca, A. Laafar, F.L. Zorila, M. Alexandru, I. Pintilie, M. Iliescu, *Reticulated mesoporous TiO_2 scaffold for self-cleaning surfaces*, *Ceram. Int.* 50 (2024) 42264–42275.
- [2] T. Dikici, S. Yildirim, M. Yurddaskal, M. Erol, R. Yigit, M. Toparli, E. Celik, *A comparative study on the photocatalytic activities of microporous and nanoporous TiO_2 layers prepared by electrochemical anodization*, *Surf. Coat. Technol.* 263 (2015) 1–7.
- [3] M.V. Roldán, P. de Oña, Y. Castro, A. Durán, P. Faccendini, C. Lagier, R. Grau, N.S. Pellegrini, *Photocatalytic and biocidal activities of novel coating systems of mesoporous and dense TiO_2 -anatase containing silver nanoparticles*, *Mater. Sci. Eng. C* 43 (2014) 630–640.
- [4] B. D'Urso, J.T. Simpson, M. Kalyanaraman, *Emergence of superhydrophobic behavior on vertically aligned nanocone arrays*, *Appl. Phys. Lett.* 90 (2007) 044102.
- [5] J. Drelich, E. Chibowski, D.D. Meng, K. Terpilowski, *Hydrophilic and superhydrophilic surfaces and materials*, *Soft Matter* 7 (2011) 9804.
- [6] A. Sabbah, A. Youssef, P. Damman, *Superhydrophobic surfaces created by elastic instability of PDMS*, *Appl. Sci.* 6 (2016) 152.
- [7] K.-Y. Yeh, L.-J. Chen, J.-Y. Chang, *Contact angle hysteresis on regular pillar-like hydrophobic surfaces*, *Langmuir* 24 (2008) 245–251.

Local structure and magnetic interactions in non-stoichiometric $\text{Mg}_{0.5}\text{Ca}_{0.5}\text{Fe}_2\text{O}_4$ nanoferrites by magnetometry and Mössbauer spectroscopy

C. Comanescu^{1,2}, N. Iacob¹, V. Kuncser¹, S. Tiwari³, V.K. Salvi³, S. Kumar³

1) National Institute of Materials Physics, 077125, Măgurele, Romania

2) Faculty of Physics, University of Bucharest, 077125, Măgurele, Romania

3) Magnetism Laboratory, Department of Physics, Mohanlal Sukhadia University, 313002, Udaipur, India

Soft nanocrystalline spinel ferrites [1] are versatile materials with wide applicability as microwave absorbing materials, humidity sensors, gas sensors, antibacterial materials, magnetic hyperthermia, drug delivery vehicles, and MRI contrast agents [2]. The synthesis of such materials involves methodologies such as sol-gel, hydrothermal, solid-state, solvothermal, and green synthesis, enabling the production of high-quality mixed-valence spinel nanoferrites with diverse morphologies.

MgFe_2O_4 is an interesting soft spinel ferrite that also exhibits n-type semiconducting behaviour, while CaFe_2O_4 is a soft p-type semiconducting ferrite and its nanometric miniaturization leads to superparamagnetism at 300 K with a decent saturation magnetization. Mg and Ca can serve as model dopants for ferrites to investigate defects and lattice contraction induced structural transformation. Hyperthermia and photothermal therapy are alternative cancer treatments that target cancer cells through localized heat. Research into biocompatible ferrites has identified $\text{Mg}_{1-x}\text{Ca}_x\text{Fe}_2\text{O}_4$ ferrites as promising candidates, exhibiting high saturation magnetization (up to 65.33 emu/g) and a notable specific absorption rate (up to 556.73 W/g).

A comprehensive investigation of magnetic inhomogeneities was undertaken in collaboration with Indian partners in non-stoichiometric $\text{Mg}_{0.5}\text{Ca}_{0.5}\text{Fe}_2\text{O}_4$ (MCNF) nanoferrite through detailed DC-magnetization, AC-susceptibility, and 57Fe Mössbauer spectroscopic measurements [3]. The polycrystalline sample of $\text{Mg}_{0.5}\text{Ca}_{0.5}\text{Fe}_2\text{O}_4$ nanoferrite was synthesized using the citrate-metal nitrate self-ignition technique. Rietveld refinement of XRD data confirmed the formation of the expected spinel fcc phase of MCNF with a minor calcite impurity, while the Scherrer analysis and HRTEM investigations revealed a broad size distribution with an average nanocrystallite size of ~15 nm. 57Fe Mössbauer and DC-magnetization studies at 300 K indicated the coexistence of ferrimagnetic (67%) and superparamagnetic (33%) states, with $M_s = 22$ emu/g, $M_r = 4$ emu/g, and $H_c = 130$ Oe, and blocking of most MCNF nanoparticles. The coercivity followed the size-modified Kneller law, and the saturation magnetization obeyed the Bloch law. AC-susceptibility studies uncovered two magnetic transitions: a high-temperature transition (~330 K) linked to the relaxation of larger blocked superparamagnetic particles and a low-temperature anomaly associated with surface spin glass freezing. The presence of surface spin glass was further confirmed through aging experiments and dynamic scaling analysis, though the slower spin-flip dynamics precluded a conventional spin glass state. These results suggest that MCNF consists of a soft ferrimagnetic core enveloped by a disordered spin-glass-like surface layer. Additionally, exchange bias at 30 K and training effects at 6 K confirmed an FM core-SG shell system.

The variation of magnetic parameters *i.e.*, H_c , M_r , M_s , K_{eff} , and S is summarized in Table 1. It can be seen that M_s , M_r , H_c , and K_{eff} increased with cooling and MCNFs exhibited soft ferrimagnetic character on a wide temperature range from 20 to 300 K. Isomer shift obtained in room-temperature Mössbauer measurement indicate that Fe is in high spin 3+ state in MCNFs. On the basis of cationic distribution $(\text{Mg}_{0.32}\text{Fe}_{0.68})\text{A}[\text{Mg}_{0.18}\text{Ca}_{0.5}\text{Fe}_{1.32}]\text{BO}_4$, the theoretical value of magnetic moment comes out to be $3.78\mu_B$ per formula unit which significantly differs from experimentally obtained value of $1.154\mu_B$ at 6 K. This difference between experimental and theoretical values indicates the possibility of non-collinear spin structure explained by Yafet Kittel (YK) Model, which suggests formulation of magnetic moment per formula unit as $\mu_B = M_B \cos \alpha_{\text{YK}} - M_A$ (M_A , M_B are the moments of A and B sites respectively in Bohr Magneton).

The ZFC-FC magnetization recorded under low field further asserts that average blocking temperature of assembly of MCNFs must be beyond 300 K.

Table 1: Magnetic parameters for MCNFs (remanent and saturation magnetization, coercive field, squareness, spin dispersion by Yafet Kittel angle, and effective anisotropy).

T (K)	Mr (emu/gm)	Ms (emu/g)	Hc (Oe)	S	α_{YK} (degree)	keff (103 erg/cc)	Ms ($\mu\text{B}/\text{f.u.}$)
6	11.0	31.00	302	0.37	48.48	9.55	1.15
20	9.8	29.40	280	0.35	49.07	8.16	1.09
30	9.2	29.20	272	0.31	49.56	8.00	1.04
50	8.7	27.57	235	0.32	49.72	6.47	1.03
100	7.1	26.75	194	0.27	50.02	5.17	0.99
200	5.2	24.57	156	0.21	50.79	3.84	0.91
300	3.9	22.05	130	0.18	51.67	2.88	0.82

In SPM nanoparticles, spin flips or direction of magnetization fluctuates between easy axes with a relaxation time (τ) in accordance to Néel-Brown relation $\tau = \tau_0 e^{\frac{K_{\text{eff}} V}{k_{\text{BT}}}}$, with V the volume of NPs and K_{eff} the effective anisotropy constant. If τ is much less than Mössbauer measurement time window (τ_m), then the spectrum will be a doublet arising from the superparamagnetic relaxation otherwise if $\tau \gg \tau_m$ then a sextet characteristic of ferrimagnet is observed. Fe^{2+} and Fe^{3+} ions can be distinguished by Mössbauer measurements, specifically from isomer shift and quadrupole splitting values. Mössbauer measurements in the range 6–300 K to understand the cationic distribution and magnetic behaviour of MCNFs were performed. From Fig. 1 it can be observed that at low temperatures (6 K) there are only two components in the spectrum: two sextets along with a central doublet (of 1.5% relative contribution). It can be inferred that at 6 K, MCNFs display ferrimagnetic ordering; although, due to wide size distribution, some ultra-fine nanoparticles relax even at such low temperatures. However, most of the nanoparticles in the MCNFs assembly remain blocked, leading to two sextets, which also indicates the presence of Fe^{3+} at both octahedral and tetrahedral sites. The two magnetic components are characterized by a hyperfine field of about 53 T (the outer one) and 50 T (the inner one). Their isomer shifts are of 0.46 mm/s and 0.39 mm/s, respectively, with negligible QS in both cases (Table 1). IS confirmed the presence of Fe^{3+} and ruled out the possibility of Fe^{2+} , while the negligible QS suggested an overall cubic symmetry between Fe^{3+} and the surroundings.

Temperature dependent magnetization measurements (under zero field cooling (ZFC) and in-field cooling (FC) protocols) were done at low fields of 50 Oe & 100 Oe to assess the magnetic phase transition in the range 15 – 300 K. The magnetization recorded under ZFC protocol did not exhibit a well-defined maximum, and the ZFC -FC curves did not overlap up to 300 K. This behaviour suggests that anisotropic barriers at low fields dominate over the externally applied thermal energy, preventing the majority of the spins from relaxing in a superparamagnetic (SPM) fashion, resulting in them remaining blocked. This result can be expected owing to the wide size distribution of nanoparticles. HRTEM analysis revealed a wide size distribution of the nanoparticles, which results in a broad distribution of anisotropic barriers. This, in turn, leads to a wide range of blocking temperatures, which is reflected as a hump in the ZFC protocol of the magnetization vs. temperature (MT) measurements.

Coercive fields below blocking temperature for ideal non-interacting single domain nanoparticles with uniaxial anisotropy must adhere to the Kneller's law $H_c(T) = H_c(0) \left[1 - \left(\frac{T}{T_B} \right)^{\alpha_K} \right]$. Zener suggested temperature dependent modification for anisotropy of cubic ferromagnets should be incorporated to model the temperature evolution of coercive fields. Effective anisotropy was found using the law of approach to saturation: $M = M_s \left(1 - \frac{b}{H^2} \right) + kH$ where $b = \frac{4K_{\text{eff}}^2}{15M_s^2}$.

The presence of disordered surface spins has been apparent from flattening of FC curves and appreciable increment in coercive field at low temperatures due to increase in surface anisotropy owing to randomly frozen surface spins.

In summary, the comprehensive evaluation of the local structure and magnetic properties in sol-gel derived nonstoichiometric $\text{Mg}_{0.5}\text{Ca}_{0.5}\text{Fe}_2\text{O}_4$ nanoferrites (MCNFs) over a wide range of temperature down to 6 K, suggest magnetic inhomogeneity comprised of superparamagnetism, ferrimagnetism, and disordered surface spin glass state in a FM core-SG shell-like system.

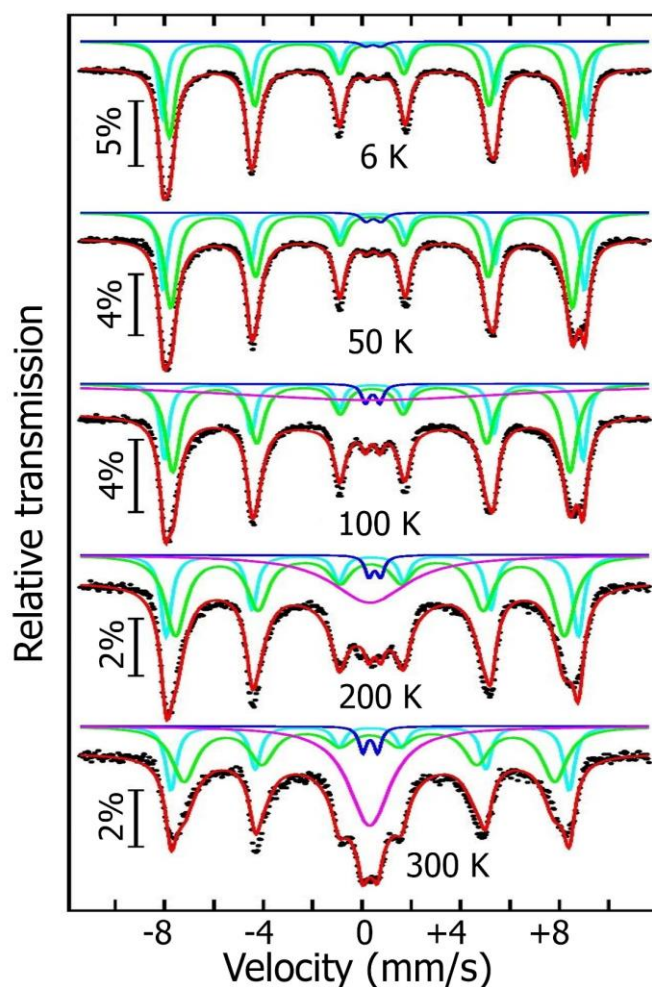


Fig. 1: Mössbauer spectra at various temperatures for MCNFs. Adapted from Ref. [3].

References:

- [1] P. Palade, C. Comanescu, A. Kuncser, D. Berger, C. Matei, N. Iacob, V. Kuncser, *Mesoporous cobalt ferrite nanosystems obtained by surfactant-assisted hydrothermal method: Tuning morpho-structural and magnetic properties via pH variation*, *Nanomaterials* 10 (2020) 476.
- [2] V. Kuncser, P. Palade, A. Kuncser, S. Greculeasa, G. Schinteie, *Engineering magnetic properties of nanostructures via size effects and interphase interactions*. In: *Size Effects in Nanostructures*. V. Kuncser, L. Miu (Eds.). Springer Series in Materials Science Vol. 205, Springer, Berlin, 2014, pp. 169–237.
- [3] S. Tiwari, C. Comanescu, N. Iacob, V. Kuncser, V.K. Salvi, S. Kumar, *Evaluation of magnetic inhomogeneities in non-stoichiometric $Mg_{0.5}Ca_{0.5}Fe_2O_4$ nanoferrite*, *Ceram. Int.* 50 (2024) 6025–6041.

Interplay between ferroelectricity and molecular adsorptions on (001) barium titanate

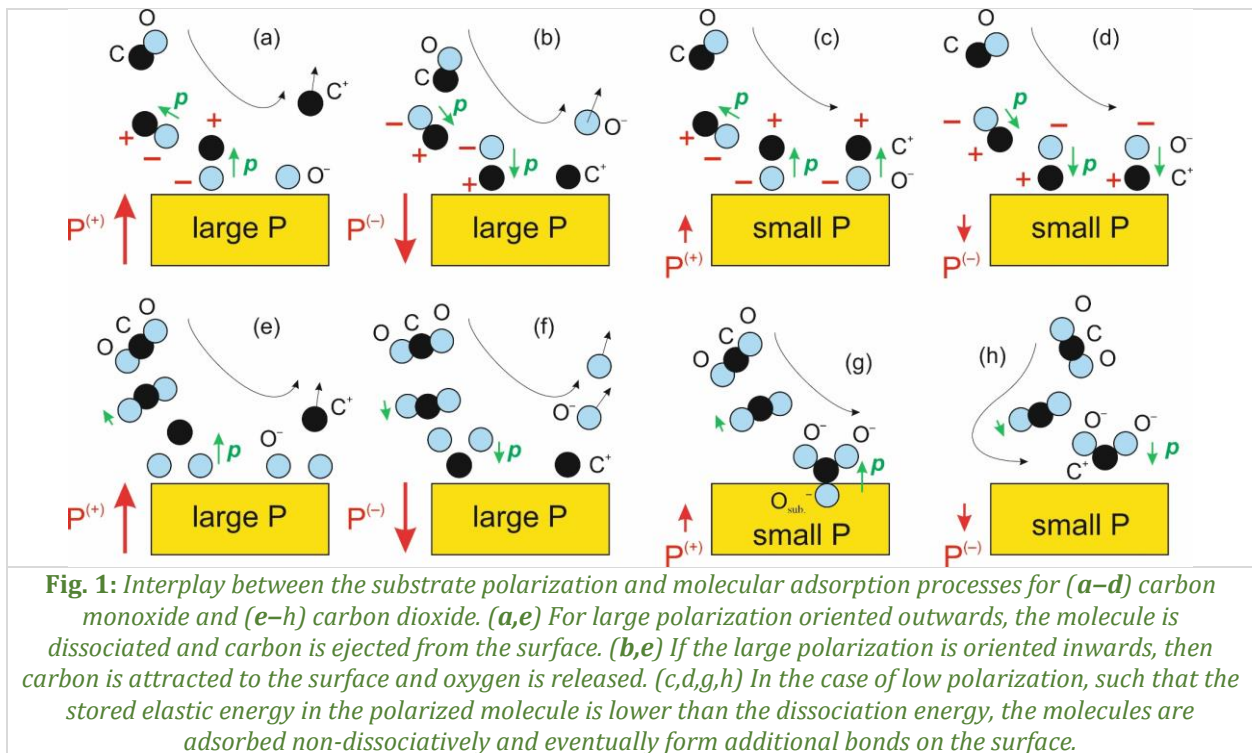
**A.-C. Iancu^{1,2}, N.G. Apostol¹, A. Nicolaev¹, L.E. Abramiuc¹, C.F. Chirila¹, D.G. Popescu¹,
G.A. Lungu¹, C.A. Tache¹, C.M. Teodorescu¹**

1) *National Institute of Materials Physics, 077125, Măgurele, Romania*

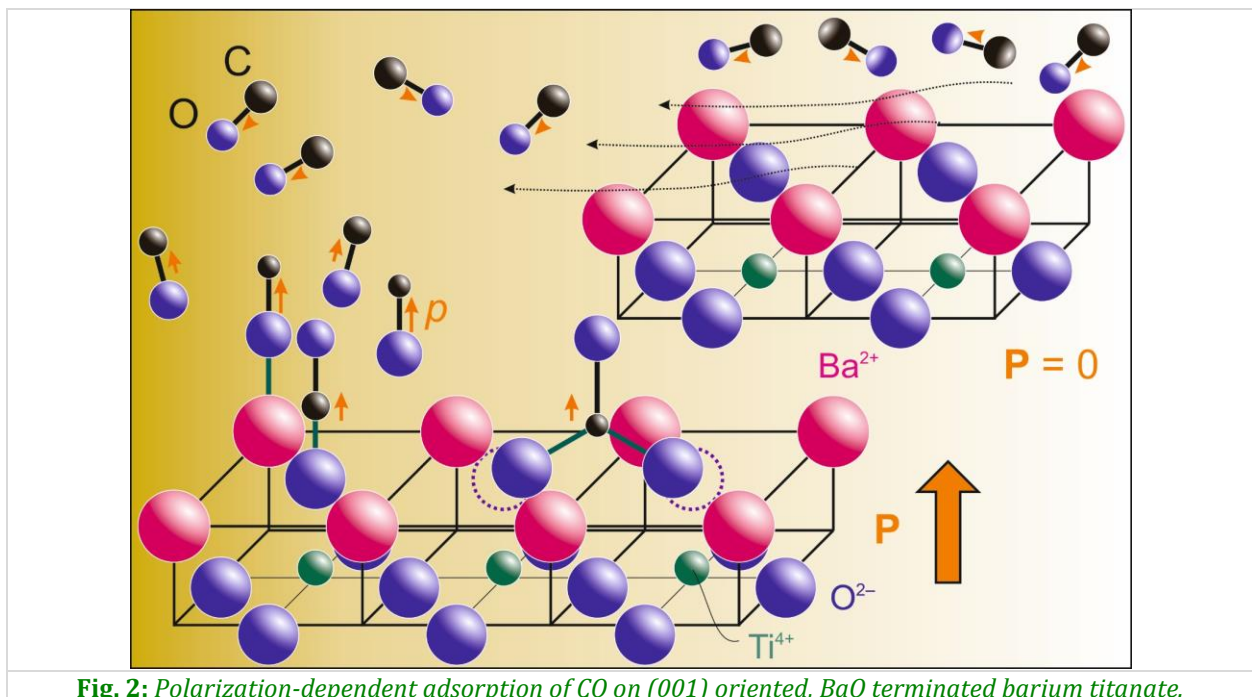
2) *Faculty of Physics, University of Bucharest, 077125, Măgurele, Romania*

Although in the last years there was increasing evidence of the remarking catalytic properties of ferroelectric materials, the fundamental processes involved are still under debate. Since an essential step of these processes consists in molecular adsorption, the studies presented in this contribution concentrate on the influence of the ferroelectric state of the adsorption processes. A pre-requisite for such studies is the cleanness of the sample surface, together with its good crystallinity, in order to work on a system as close as possible on the ones supposed by theoretical modelling. This was achieved for the first time almost one decade ago, on lead zirconate titanate (PZT) thin films, where a cleaning procedure involving extended annealing in oxygen allowed one to synthesize surfaces with no carbon contamination as investigated by synchrotron radiation X-ray photoelectron spectroscopy (SRXPS) in an enhanced surface sensitivity regime and crystallinity revealed by low energy electron diffraction (LEED) [1]. This film was in a well-defined polarization state oriented inwards and it was found that carbon monoxide is adsorbed and partly dissociated on this surface. Carbon is then desorbed in form of carbon dioxide when the substrate is heated above the Curie temperature. Therefore, these experiments indicate the clear interplay between the polarization state and adsorption/desorption processes. Since carbon monoxide has a very low dipole moment (about 0.1 Debye), a mechanism involving the polarizability of the molecule by the field generated by the ferroelectric surface had to be established. Since the induced dipole moment on the adsorbate is proportional to the polarization and the interaction of this dipole with the external field is equal to (minus) the scalar product of the dipole moment with the electric field produced by the material, the adsorption binding energy is therefore proportional to the square of the polarization and so is also the elastic energy stored in the molecule subject to the external field. A simple estimate of this energy (in eV) is about 4.5 times the molecular polarizability (in Ångström cubed) times the square of the polarization (in Coulomb per square meter, CSM). For carbon monoxide with polarizability of about 2 Ångström cubed adsorbed on a strong ferroelectric such as PZT featuring polarization of more than 1 CSM, the interaction energy exceeds the dissociation energy of the molecule, and this is the reason for the observed dissociation.

The drawback of these processes is that when one tries to get rid of the adsorbate by heating the substrate above the Curie temperature, carbon uptakes oxygen from the substrate. Therefore, the surface is depleted in oxygen and is not stable upon several cycles of adsorption/desorption. On the contrary, for a substrate with lower polarization, such as barium titanate (BTO) with about one quarter of the polarization of PZT, the interaction energy is lower than the dissociation energy and therefore molecules are adsorbed without dissociation. Upon heating the substrate, molecules are adsorbed without affecting the substrate. All these processes are schematized for both carbon monoxide and carbon dioxide in Fig. 1. It is shown in which cases the molecules are adsorbed and dissociated (as observed on PZT [1]) or not (as observed on BTO, see in the following), how for dissociated molecules some atoms/ions are ejected or attracted to the surface, and how molecules adsorbed in non-dissociated states form additional bonds with atoms from the first layer of the ferroelectric surface. It follows that exploring the use of BTO is highly desirable, since this material is abundant, non-toxic, relatively cheap, and can provide the ability of reversible molecular adsorption/desorption of carbon-containing molecules from the ambient atmosphere.



A first study involved a similar experiment with carbon monoxide on a 12.5 nm thick BTO film with outwards polarization and BaO termination [2]. The clean substrate was characterized by LEED and SRXPS, then adsorption and desorption processes were followed-up by ultrafast SRXPS. The complete XPS characterization allowed one to propose adsorption mechanisms and sites (Fig. 2), while the carbon monoxide was completely desorbed upon heating above the Curie temperature, with full recovery of the BTO substrate.



The next step was to investigate by the same methods a molecule without permanent dipole moment in the gas phase, ethylene [3]. The results were consistent with the findings for carbon monoxide, i.e., a clear influence of the ferroelectric state on molecular adsorption. Moreover, the molecule is oxidized in its last adsorption steps and, upon heating at moderate temperatures (since the Curie temperature of

the BTO(001) thin film is about 420 K), the oxidation process is reversed and ethylene is desorbed in its reduced state, while the substrate is recovered.

The last and most important study from this contribution is the adsorption of carbon dioxide by the polarized BTO(001) substrate with Ba termination. Adsorption geometries are again determined, together with a clear interplay of the substrate polarization on the adsorption processes (Fig. 3). The unexpected and encouraging result was that the amount of adsorbed carbon approaches one monolayer (one carbon atom for a surface BaO unit cell) at room-temperature. This promotes BTO as a valid candidate for decarbonization.

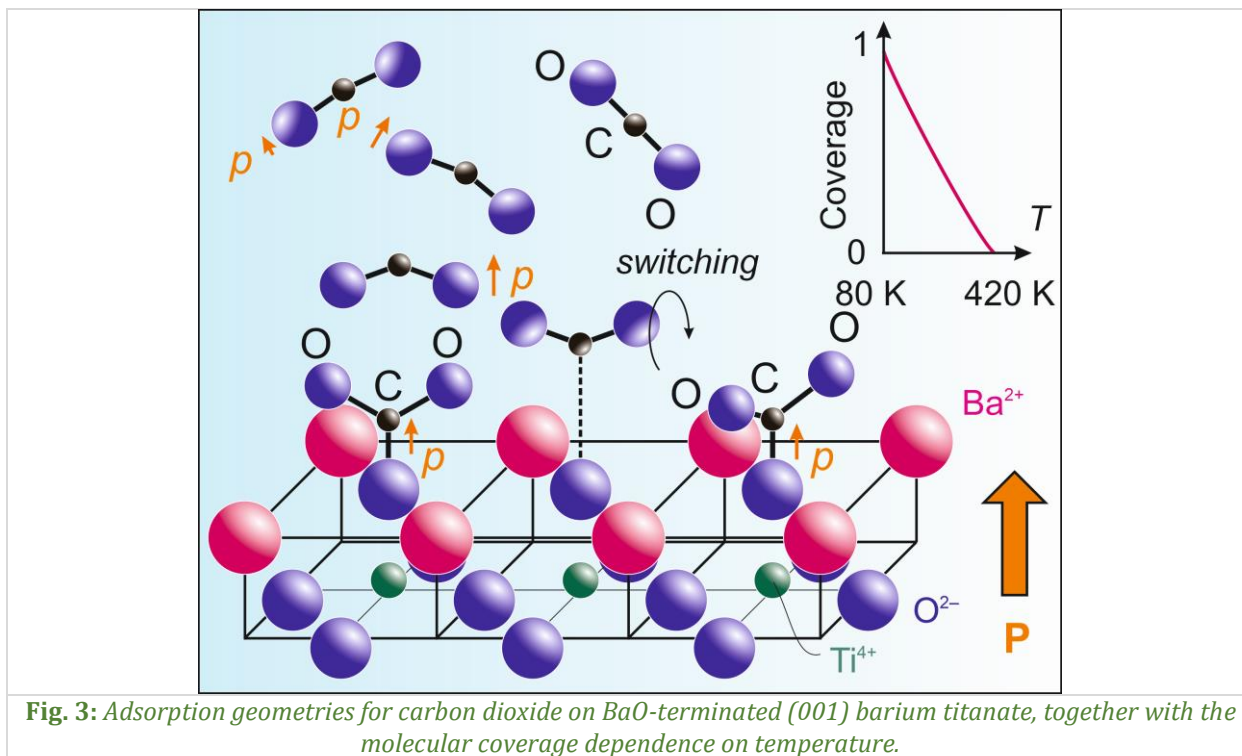


Fig. 3: Adsorption geometries for carbon dioxide on BaO-terminated (001) barium titanate, together with the molecular coverage dependence on temperature.

In Ref. [4], where this work was presented, an estimate of carbon dioxide adsorption ability based on this experiment yielded a capacity of about 8 mg per g of material for 20 nm sized barium titanate powder, by supposing that the ferroelectric properties are similar to the bulk. A scale-up of this finding yields a necessary of about 1.2 million tons BTO with an initial price of 2–3 billion USD to remove 10 billion tons carbon dioxide per year, by using a total power of about 40 GW (30 billion USD per year). Complete decarbonization could then be achieved in about 20 years.

References:

- [1] L.C. Tanase, N.G. Apostol, L.E. Abramiuc, C.A. Tache, L. Hrib, L. Trupina, L. Pintilie, C.M. Teodorescu, *Ferroelectric triggering of carbon monoxide adsorption on lead zirco-titanate (001) surfaces*, Sci. Rep. 6 (2016) 35301.
- [2] A.-C. Iancu, N.G. Apostol, A. Nicolaev, L.E. Abramiuc, C.F. Chirila, D.G. Popescu, C.M. Teodorescu, *Molecular adsorption–desorption of carbon monoxide on ferroelectric BaTiO₃(001)*, Mater. Adv. 5 (2024) 5709–5723.
- [3] A.-C. Iancu, A. Nicolaev, N.G. Apostol, L.E. Abramiuc, C.M. Teodorescu, *Reversible oxidation of ethylene on ferroelectric BaTiO₃(001): An X-ray photoelectron spectroscopy study*, Heliyon 10 (2024) e35072.
- [4] A.-C. Iancu, G.A. Lungu, C.A. Tache, C.M. Teodorescu, *Ferroelectric-enabled significant carbon dioxide molecular adsorption on BaTiO₃(001)*, Mater. Adv. 5 (2024) 8798–8811.

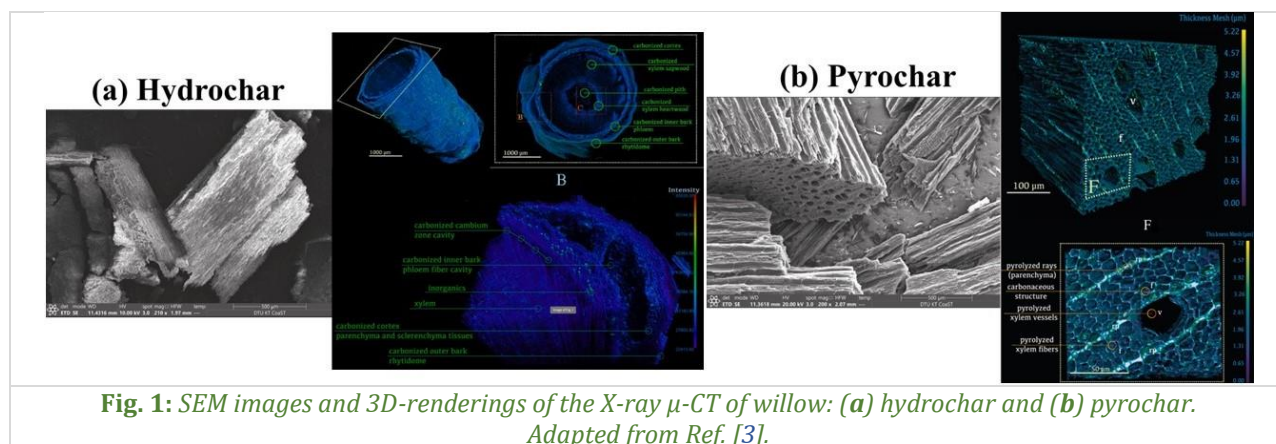
Hydrothermal carbonization and pyrolysis of willow resources from engineered wetland systems (EWS) for carbon sequestration and phosphorus recovery

A.C. Acosta^{1,2,3,9}, C.A. Arias^{2,9}, P. Biller^{1,9}, N.K. Wittig⁴, I.-A. Baragau⁵, M.J. Alhnidi⁶, G. Ravenni⁷, Z. Sarossy⁷, L. Benedini⁷, L.E. Abramiuc⁵, D.G. Popescu⁵, W. Negassa^{8,11}, V.F. Marulanda¹⁰, D.S. Müller-Stover⁸, H. Brix^{2,9}

- 1) *Department of Biological and Chemical Engineering, Aarhus University, 8200, Aarhus, Denmark*
- 2) *Department of Biology, Aarhus University, 8000, Aarhus, Denmark*
- 3) *Deutsches Biomassforschungszentrum gemeinnützige GmbH [DBFZ], 04347, Leipzig, Germany*
- 4) *Department of Chemistry and iNANO, Aarhus University, 8000, Aarhus, Denmark*
- 5) *National Institute of Materials Physics, 077125, Măgurele, Romania*
- 6) *Department of Conversion Technologies of Biobased Resources, University of Hohenheim, 70599, Stuttgart, Germany*
- 7) *Department of Chemical Engineering, Technical University of Denmark, 2800, Kongens Lyngby, Denmark*
- 8) *Department of Plant and Environmental Sciences, University of Copenhagen, 1172, Copenhagen, Denmark*
- 9) *WATEC, Aarhus University Centre for Water Technology, 8600, Silkeborg, Denmark*
- 10) *Chemical Engineering School, Universidad del Valle, Cali, Colombia*
- 11) *The James Hutton Institute, AB15 8QH, Aberdeen, United Kingdom.*

Environmental and climate crises are major outcomes of intensive human activities, leading to widespread and uncontrollable pollution of the atmosphere, surface and underground waters, and soil. Simultaneously, there is a global race to secure natural resources, with the pressing challenge of identifying or developing new sustainable and renewable sources to extract vital resources, including various biomass-derived hydrocarbons, organic compounds, minerals, and fuels. Developing novel systems and processes which can address multiples global issues are ideal approaches to speed up solving environmental and climate recovery, assuring a safe, clean and sustainable future for the next generation of humans, animals, and plants on Planet Earth. For example, willow is a fast-growing tree, naturally found primarily in the northern hemisphere. It is an important source of biomass, recognized for its bioenergy value, and possesses significant potential as a source of phosphorus [1]. Willows from engineered wetland systems (EWS) offer a sustainable approach to wastewater treatment and biomass production [2]. The current study [3] assesses the potential of willow for nutrient recovery and carbon sequestration through slow pyrolysis (600 °C) and hydrothermal carbonization (250 °C). Our study proposes EWS-pyrochars as a ready-to-integrate opportunity for soil amendment, as they exhibit predominant CO₂ release and the absence of harmful compounds in pyrolysis chromatograms, indicating higher stability than hydrochars. Using sequential phosphorus extractions, we observed a high bioavailability in the willow-woodchips and a significant phosphorus retention in EWS chars up to 92% in pyrochars and near-complete retention in hydrochars, along with a higher labile-P fraction of 21% in hydrochars than 5% in pyrochars. Utilizing X-ray-based techniques, Raman spectroscopy, scanning electron microscopy, and gas physisorption, we characterized the structures of the EWS-chars. We revealed innovative 3D visualizations, which transcend previous literature by providing insights into the chars' internal porosity and quantifying, for the first time, their carbonaceous structural thickness using a meshing algorithm and the mean Feret diameter. EWS-pyrochars exhibit remarkable aromaticity with a higher concentration of overall sp² carbon atoms at 63% vs. 43 % in hydrochars. Moreover, unlike hydrochars, which depict occluded porosity, EWS pyrochars exhibited 92% water storage-like pores. Although hydrochars exhibited lower carbonization and thermal stability than pyrochars, their higher carbon retention (55% vs. 41% in pyrochar) suggested superior annual benefits

on a 10 ha EWS scale, with 80 tons of carbon sequestration and 334 kg of phosphorus recovery, compared to 60 tons of carbon and 298 kg of phosphorus with pyrochars. Our findings suggest innovative materials for resource recovery, advancing the engineered wetland systems field, shifting their traditional use, and opening opportunities for future integration into biorefineries. Utilizing X-ray μ -CT, high-resolution X-ray photoelectron spectroscopy (HRXPS), X-ray diffraction, Raman spectroscopy, SEM, and gas physisorption analysis (N_2 and CO_2), we investigated the carbonaceous structures of hydrochars and pyrochars derived from EWS willows. We aimed to provide detailed 3D visualizations to reveal the morphology of these as-yet unexplored EWS-chars (see Fig. 1). Our approach innovates by quantifying the carbonaceous chars' structures *via* a thickness mesh and the mean Feret diameter, to elucidate their internal architecture and porosity. Additionally, sequential chemical extractions and thermal decomposition analysis are conducted on the willow woodchips and chars, with the overall goal of evaluating phosphorus densification, bioavailability, and thermal stability.



References:

- [1] C.I. Aragón-Briceño, A.K. Pozarlik, E.A. Bramer, L. Niedzwiecki, H. Pawlak-Kruczek, G. Brem, *Hydrothermal carbonization of wet biomass from nitrogen and phosphorus approach: A review*, Renew. Energy 171 (2021) 401–415.
- [2] D. Istenič, G. Božič, *Short-rotation willows as a wastewater treatment plant: Biomass production and the fate of macronutrients and metals*, Forests 12 (2021) 554.
- [3] A.C. Acosta, C.A. Arias, P. Biller, N.K. Wittig, I.-A. Baragau, M.J. Alhnidi, G. Ravenni, Z. Sárossy, L. Benedini, L.E. Abramiuc, D.G. Popescu, W. Negassa, V.F. Marulanda, D.S. Müller-Stöver, H. Brix, *Hydrothermal carbonization and pyrolysis in wetland engineering: Carbon sequestration, phosphorus recovery, and structural characterization of willow-based chars with X-ray μ -computed tomography*, Chem. Eng. J. 492 (2024) 151916.

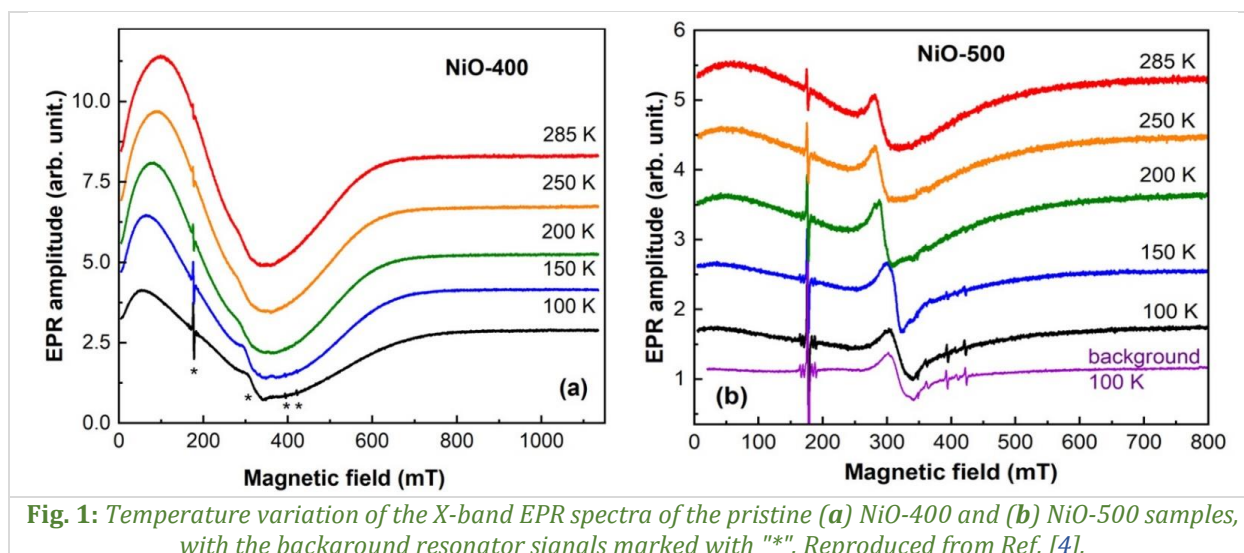
In-depth insight into the structural properties of nanoparticulate NiO for CO sensing

C.G. Mihalcea^{1,2}, M. Stefan¹, C. Ghica¹, O.G. Florea¹, A. Stanoiu¹, C.E. Simion¹,
S. Somacescu³, D. Ghica¹

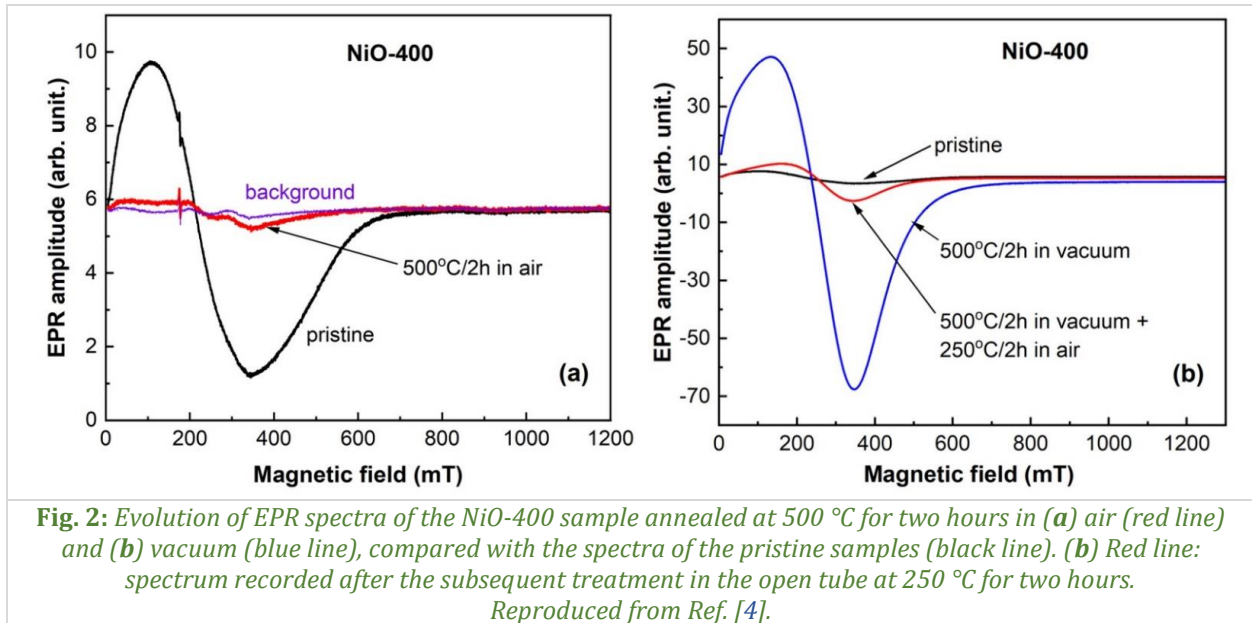
- 1) National Institute of Materials Physics, 077125, Măgurele, Romania
- 2) Faculty of Physics, University of Bucharest, 077125, Măgurele, Romania
- 3) "Ilie Murgulescu" Institute of Physical Chemistry, Romanian Academy, 060021, Bucharest, Romania

NiO, a wide band-gap ($E_g = 3.6\text{--}4.0$ eV) antiferromagnetic semiconductor with a p-type behaviour due to the cation deficit non-stoichiometry, is a multifunctional material with a wide range of applications which include chemical gas sensors. The selective sensitivity and sensor response strongly depend on the chemical synthesis route, the thermal history of the samples, the nature and concentration of unintended impurities in precursors, *etc.* Among the strategies explored to improve these properties were tailoring the structural and morphological properties and varying the concentration and nature of the defects and/or dopants. In cation deficient oxides the usual charge compensation for the cation vacancy is the oxygen vacancy (OV), but in bulk NiO the Ni^{3+} ions are considered to act as charge compensator. The presence of paramagnetic defects such as Ni^{3+} ions and ionized OV, even in low concentrations (tens of ppm), their localization in the volume, the superficial layer or in minority phases can be determined by electron paramagnetic resonance (EPR) spectroscopy [1,2]. Also, agglomerated paramagnetic defects in local high concentration, forming minority phases which often affect the electrical and magnetic properties of the material, can be detected by EPR.

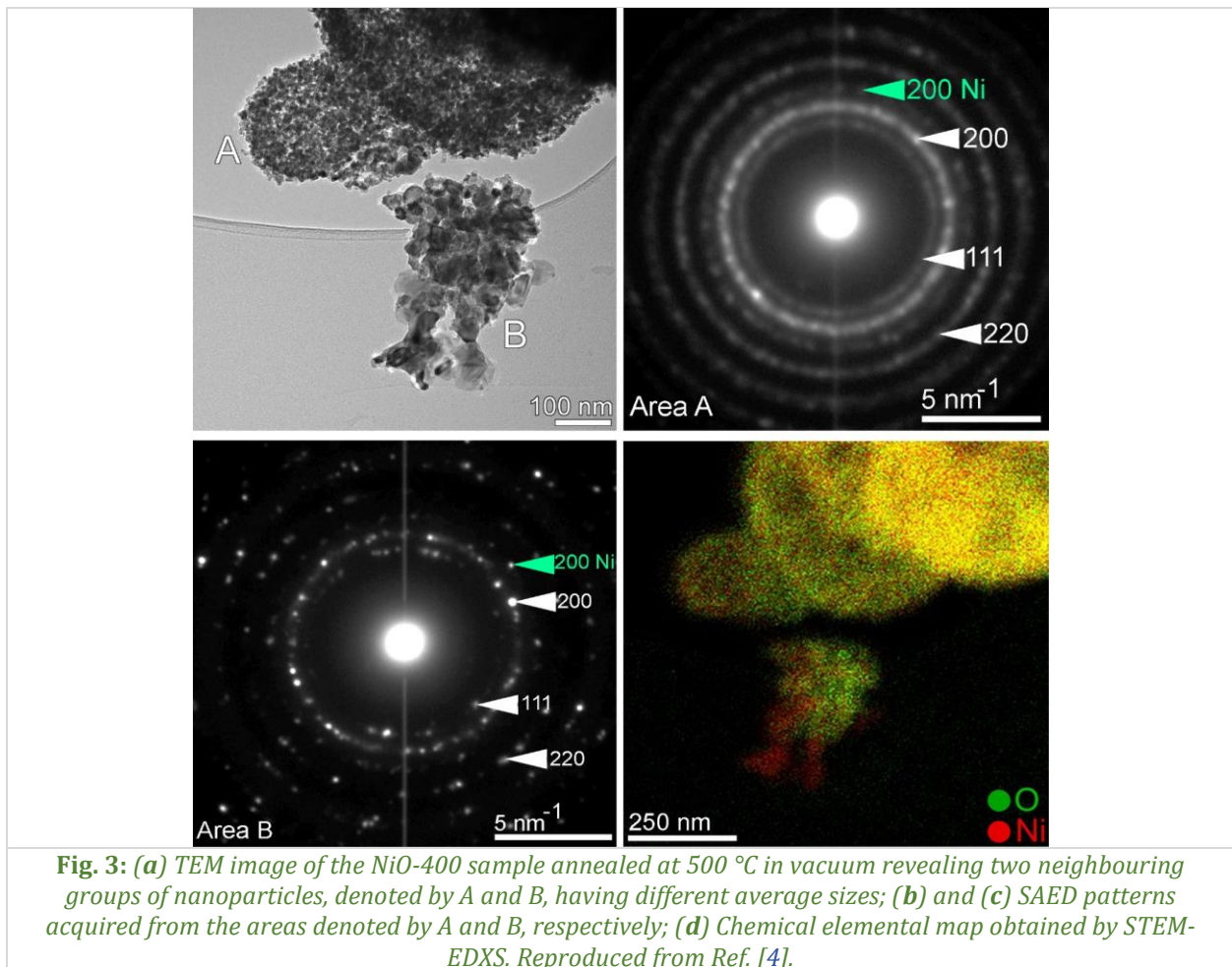
We have shown [3] that NiO nanoparticles with different size and morphology have almost similar CO sensing properties under in-field conditions – an intriguing result that warranted further investigation. Therefore, the present study [4] was focused on the complex characterization by EPR of similar NiO nanoparticulate samples calcined at 400 °C and 500 °C, correlated with analytical transmission electron microscopy (TEM) and X-ray photoelectron spectroscopy (XPS), accompanied by CO-sensing measurements. The EPR investigation of the pristine NiO-400 and NiO-500 samples calcined at 400 °C and 500 °C, respectively, evidenced the presence of a ferromagnetic phase (Fig. 1) [4].



To elucidate the nature of this phase, the NiO-400 sample was annealed at 500 °C in air and in vacuum (Fig. 2). The evolution of the EPR spectra under annealing was explained by the presence of dispersed Ni clusters in the NiO nanoparticles, close to the surface. Annealing in air at 500 °C lead to the oxidation of the Ni clusters, as reflected by the considerable decrease in the EPR intensity, while the vacuum annealing at 500 °C increased the size and number of the Ni clusters close to the surface.

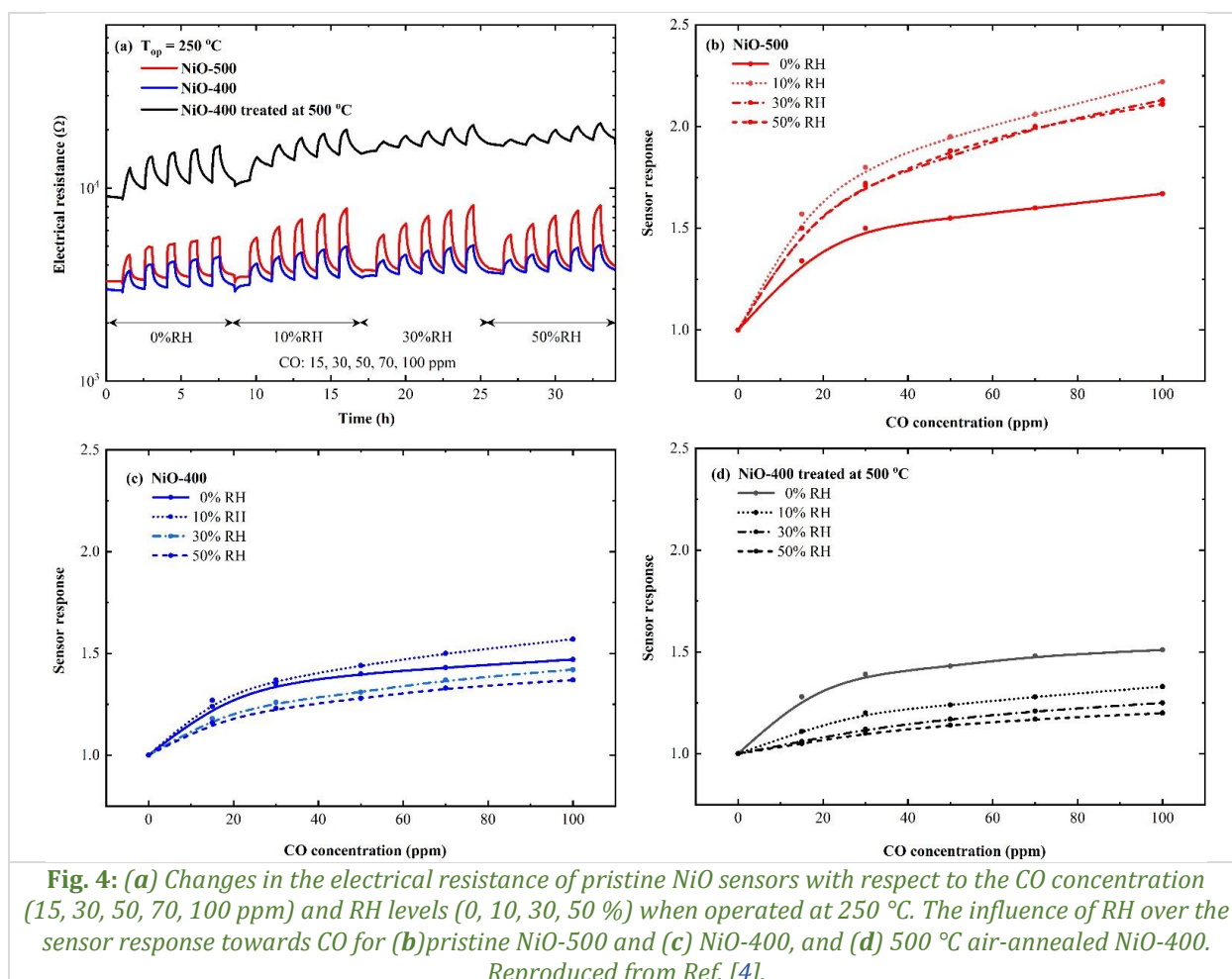


The presence of the Ni clusters with a non-uniform distribution was confirmed by the electron diffraction (SAED) patterns of both pristine samples and of the vacuum annealed NiO-400 sample (Fig. 3). The chemical elemental (STEM-EDXS) mapping of the vacuum annealed NiO-400 sample also evidenced nickel rich regions, in line with the local formation of a metallic Ni phase [4].



The amount of metallic Ni phase was estimated to be less than 1%. The analytical TEM investigations also evidenced morpho-structural changes induced by annealing at 500 °C in the NiO-400 sample, such as nanoparticles growth and enhanced faceting. The XPS analysis confirmed the presence of the Ni²⁺ oxidation state in NiO with different crystallization degrees, as well as the formation of a tiny amount of metallic Ni on the surface/near surface [4].

The CO sensing tests performed on the pristine NiO-400 and NiO-500 samples and air annealed at 500 °C NiO-400 sample evidenced an increase in the baseline resistance of the air annealed NiO-400 sample, explained by the decrease of free charge carriers induced by the dissolution of the Ni clusters (Fig. 4). The three investigated samples exhibited different CO sensor responses and selectivity, with the NiO-500 sample having the highest sensitivity to CO and the air annealed NiO-400 sample showing an increased sensitivity towards CO₂, without cross-sensitivity to various other gases. The morpho-structural, spectroscopic and gas sensing data support the conclusion that the sensor response of the NiO nanoparticles is affected by the interplay of nanoparticle size, morphology, and the shallow defects near the grain surface, correlated with the thermal history of the samples [4].



References:

- [1] D. Ghica, I.D. Vlaicu, M. Stefan, V.A. Maraloiu, A.C. Joita, C. Ghica, *Tailoring the dopant distribution in ZnO:Mn nanocrystals*, Sci. Rep. 9 (2019) 6894.
- [2] I.D. Vlaicu, M. Stefan, C. Radu, D.C. Culita, D. Radu, D. Ghica, *Atomic scale insight into the decomposition of nanocrystalline zinc hydroxynitrate toward ZnO using Mn²⁺ paramagnetic probes*, Front. Chem. 11 (2023) 1154219.
- [3] A. Stanoiu, C. Ghica, C.G. Mihalcea, D. Ghica, S. Somacescu, O.G. Florea, C.E. Simion, *Effects of calcination temperature on CO-sensing mechanism for NiO-based gas sensors*, Chemosensors 10 (2022) 191.
- [4] C.G. Mihalcea, M. Stefan, C. Ghica, O.G. Florea, A. Stanoiu, C.E. Simion, S. Somacescu, D. Ghica, *In-depth insight into the structural properties of nanoparticulate NiO for CO sensing*, Appl. Surf. Sci. 651 (2024) 159252.

InS nanosheet-based sensors for superior NO₂ sensitivity and selectivity

**C. Ghica¹, M.C. Istrate¹, G. D'Olimpio², D. B. Boukhvalov³, V. Galstyan⁴, J. Occhiuzzi²,
M. Vorochta⁵, M. Amati⁶, Z. Milosz⁶, L. Gregoratti⁶, C.N. Kuo⁷,
C.S. Lue⁷, E. Comini⁴, A. Politano²**

1) *National Institute of Materials Physics, 077125, Măgurele, Romania*

2) *University of L'Aquila, 67100, L'Aquila, Italy*

3) *Nanjing Forestry University, 210037, Nanjing, China*

4) *University of Brescia, 25133, Brescia, Italy*

5) *Charles University, 18000, Prague, Czech Republic*

6) *Elettra – Sincrotrone Trieste SCpA, 34149, Trieste, Italy*

7) *National Cheng Kung University, 70101, Tainan, Taiwan*

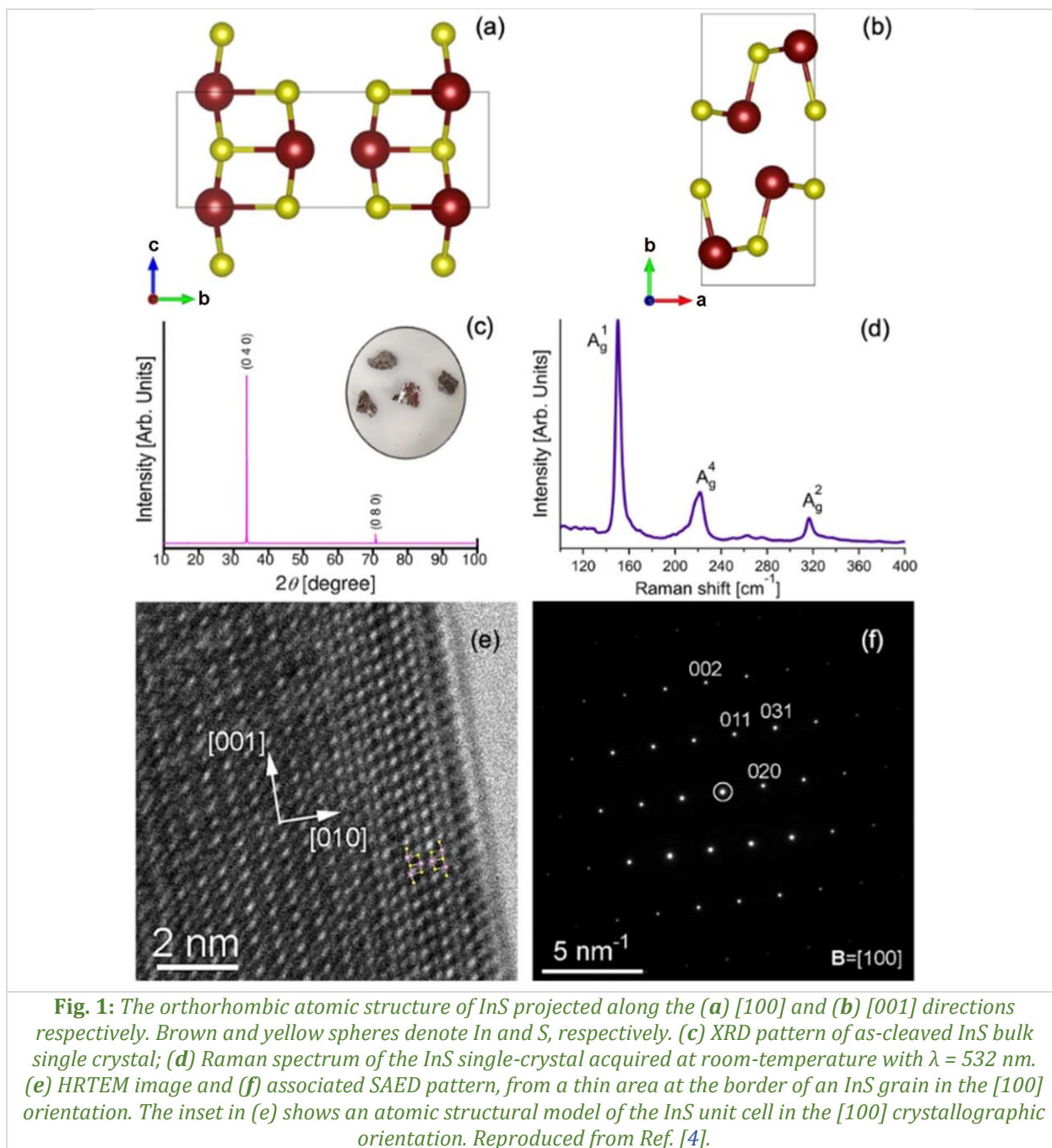
In today's world, marked by rapid industrial expansion and the escalating effects of climate change, the need for efficient air quality monitoring has become critical. Chemoresistive gas sensors, predominantly based on metal-oxide semiconductors [1–3], have gained a widespread adoption due to their compact design, user-friendliness, and sensitivity to changes in the electrical properties of metal oxides upon gas adsorption. However, achieving optimal gas detection remains a complex endeavour, with key obstacles including the need for enhanced sensitivity, improved sticking coefficients, and effective control over conductance variations. These persistent challenges highlight the urgent necessity for the development of advanced functional materials designed to meet the evolving requirements of cutting-edge gas sensing technologies.

In recent years, there has been a significant shift in focus towards 2D semiconductors, which are gaining recognition for their extensive surface areas, outstanding charge transport properties, and distinctive surface physicochemical characteristics. Despite their potential, these materials have yet to surpass metal oxides in terms of sensitivity, selectivity, response and recovery times, and long-term stability. Therefore, further investigation into the diverse range of 2D semiconductors for gas sensing applications is necessary.

Indium sulfide (InS) possesses a direct bandgap and exists in multiple phases, each exhibiting unique electronic and structural properties. Previously, InS has been proposed as a promising material for nonlinear optics and photovoltaics. In this work [4], we demonstrate the potential of InS as a viable platform for hazardous gas detection by developing innovative sensors based on solution-processed InS nanosheets. These sensors demonstrate remarkable selectivity and sensitivity for NO₂ detection, achieving a detection limit of 180 ppb at 350 °C. To understand the specific gas sensing properties of InS, we analysed its atomic structure by correlating simulated atomic models of InS with results from transmission electron microscopy (TEM) and X-ray diffraction (XRD) analysis [4].

InS is a III–VI family semiconductor, closely related to its parent compounds GaS, GaSe, and InSe. Like its counterparts, InS features tetrahedral coordination geometry for its constituent atoms. However, what sets InS apart is its asymmetric atomic layering: two sulphur atoms and one indium atom are positioned in a single plane, with an additional sulphur atom residing in an adjacent layer. This unique three-dimensional network structure necessitates advanced characterization techniques.

Raman spectroscopy plays a crucial role in this characterization, particularly for evaluating stoichiometry and intra-domain variations. In Fig. 1d, we present the room-temperature Raman spectrum of InS, with mode assignments closely aligning with previously reported findings. Our analysis focuses on the most prominent Ag intralayer optical modes (A¹g, A²g, A⁴g), occurring at frequencies of 150, 222, and 317 cm⁻¹. In the A¹g and A²g modes, atomic oscillations occur parallel to the direction of bond stretching, whereas the A⁴g mode involves atomic bending vibrations. These vibrational modes not only provide insights into the material's properties, but also contribute to an ongoing discussion regarding the atomic structure of InS. Previous studies have proposed both monoclinic and orthorhombic structures for equiatomic InS.



To resolve this ambiguity, we conducted single-crystal X-ray diffraction (XRD) analysis, which yielded lattice parameters of $a = 4.45$ Å, $b = 10.65$ Å, $c = 3.94$ Å, and $\alpha = \beta = \gamma = 90^\circ$, confirming an orthorhombic structure (indexed according to CIF file no. 1540925). Fig. 1c presents the Laue diffraction pattern of the bulk crystal, further validating the orthorhombic symmetry through cleavage along the (010) plane. Complementing these spectroscopic and diffraction insights, Fig. 1e display a high-resolution transmission electron microscopy (HRTEM) micrograph along the [100] zone axis orientation. The small-area electron diffraction (SAED) pattern in Fig. 1f further confirmed this orientation, with the [010] direction aligned towards the crystal border and the [001] direction parallel to it. An overlay of the InS unit cell atomic model on the HRTEM image (inset of Fig. 1e) provides additional structural validation. Notably, the grain's outer edge exhibits a distinct HRTEM pattern due to the formation of a native oxide layer upon air exposure, which is further corroborated by the low oxygen peak observed in the EDXS spectrum (Fig. 2).

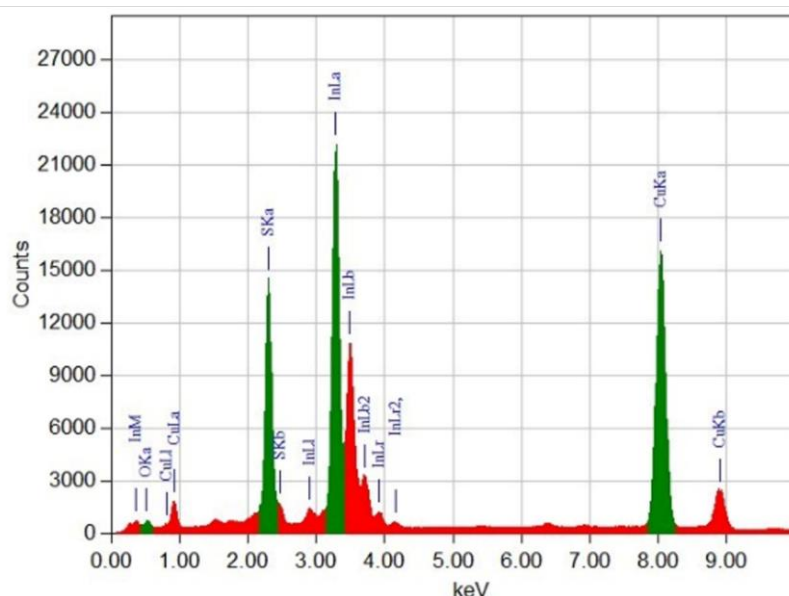


Fig. 2: EDXS spectrum indicating the presence of oxygen along with the main elements In and S.

References:

- [1] C. Badie, J.H. Lee, A. Mirzaei, H.W. Kim, S. Sayegh, M. Bechelany, L. Santinacci, S.S. Kim, *Enhanced sensitivity towards hydrogen by a TiN interlayer in Pd-decorated SnO₂ nanowires*, J. Mater. Chem. A 11 (2023) 12202–12213.
- [2] J. Yan, X. Guo, Y. Zhu, Z. Song, L.Y.S. Lee, *Solution-processed metal doping of sub-3 nm SnO₂ quantum wires for enhanced H₂S sensing at low temperature*, J. Mater. Chem. A 10 (2022) 15657–15664.
- [3] N. Barsan, D. Koziej, U. Weimar, *Metal oxide-based gas sensor research: How to?*, Sens. Actuat. B-Chem. 121 (2007) 18–35.
- [4] G. D'Olimpio, D.W. Boukhvalov, V. Galstyan, J. Occhiuzzi, M. Vorochta, M. Amati, Z. Milosz, L. Gregoratti, M.C. Istrate, C.N. Kuo, C.S. Lue, C. Ghica, E. Comini, A. Politano, *Unlocking superior NO₂ sensitivity and selectivity: The role of sulfur abstraction in indium sulfide (InS) nanosheet-based sensors*, J. Mater. Chem. A 12 (2024) 10329–10340.

Theoretical and Computational Materials Physics

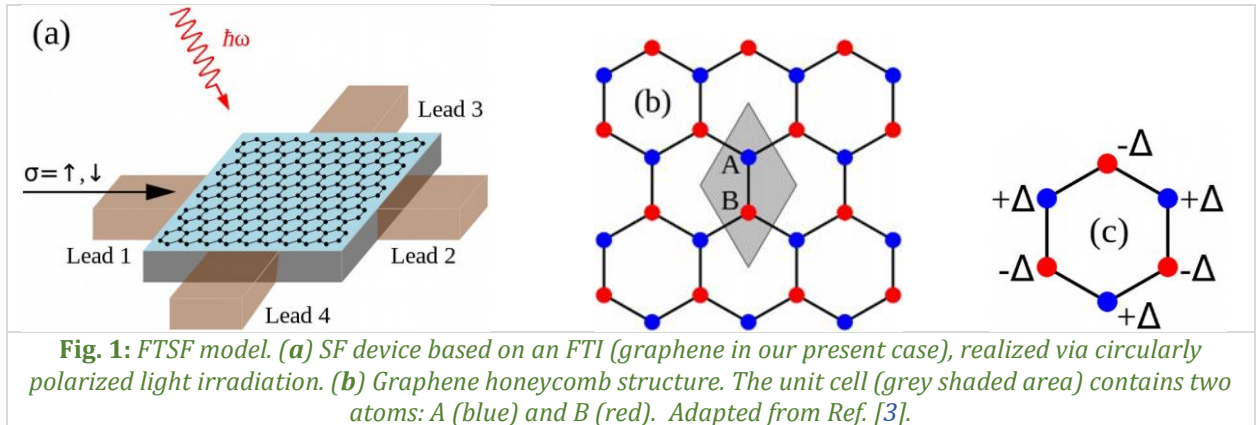
Spin filter devices based on Floquet topological insulators

A. Pena, C. Radu

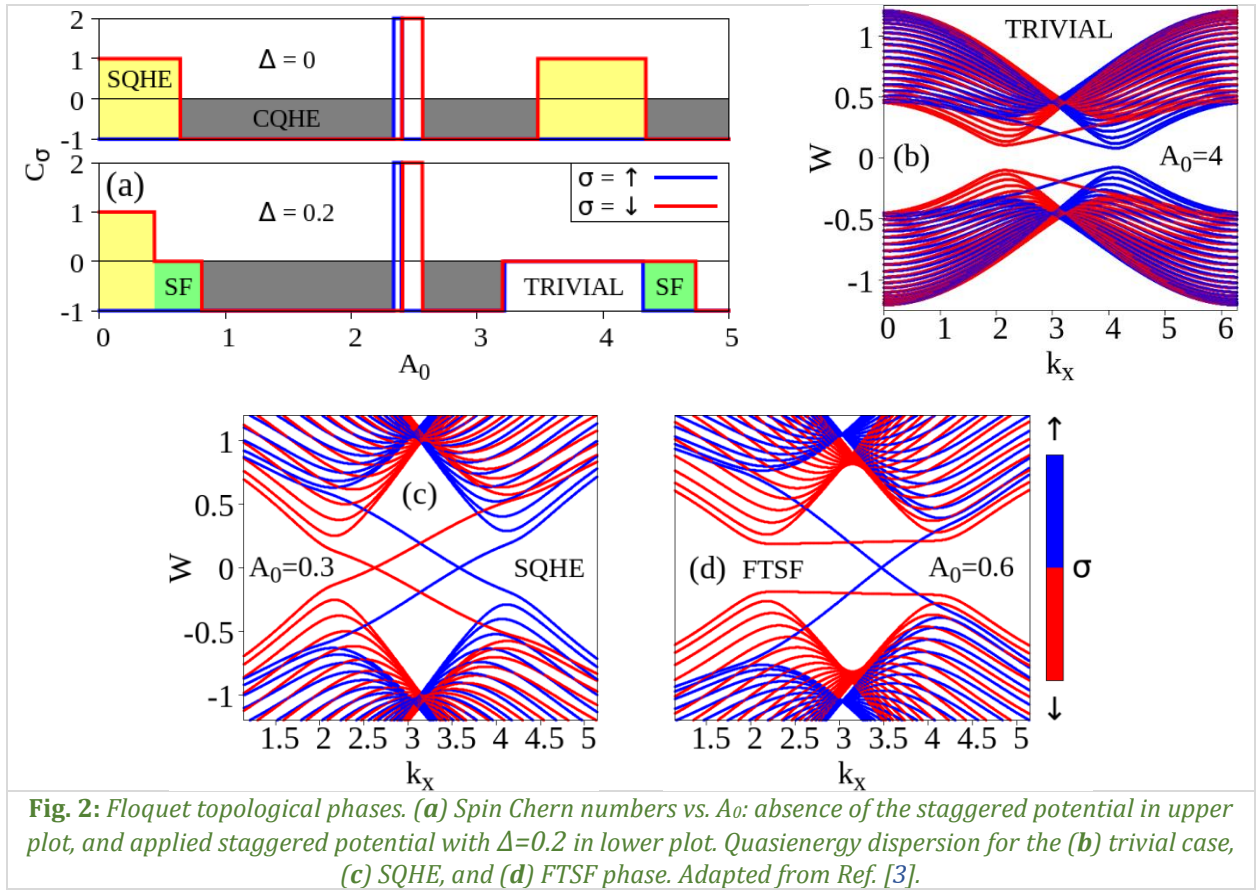
National Institute of Materials Physics, 077125, Măgurele, Romania

Circularly polarized light is known to induce topological phases *via* time reversal symmetry (TRS) breaking in so-called *Floquet topological insulators* (FTIs) [1]. Thus, under circularly polarized light irradiation, in a quantum Hall transport experiment, one expects to highlight quantized Hall resistance plateaus. Moreover, if the intrinsic spin-orbit coupling is present, an intricate interplay between two topological phases will take place, namely charge quantum Hall effect (CQHE) and spin quantum Hall effect (SQHE) [2].

First, we discuss here the appearance of a third topological phase, that is *Floquet topological spin filter* (FTSF) [3]. Second, based on FTSF phase, we propose a spin filter (SF) device. The SF is schematically described in Fig. 1a. We deal with a topological insulator (graphene in the present case) under circularly polarized light irradiation, giving rise to an FTI. From the left side (Lead 1), the current is injected, going outside the device through Lead 2. The spin-filtered Hall signal will be measured between Lead 3 and Lead 4. The main ingredient of our proposed idealized model is the presence of an on-site staggered potential. To be more explicit, in Fig. 1b, we show the graphene structure. The lattice in question is constructed by a bi-atomic unit cell, as indicated by the grey shaded area, which contains two atoms: A (blue) and B (red). As shown in Fig. 1c, the staggered potential acts independently on the two atomic sites as a potential energy $+\Delta$ on A sites, and $-\Delta$ on B sites, respectively.

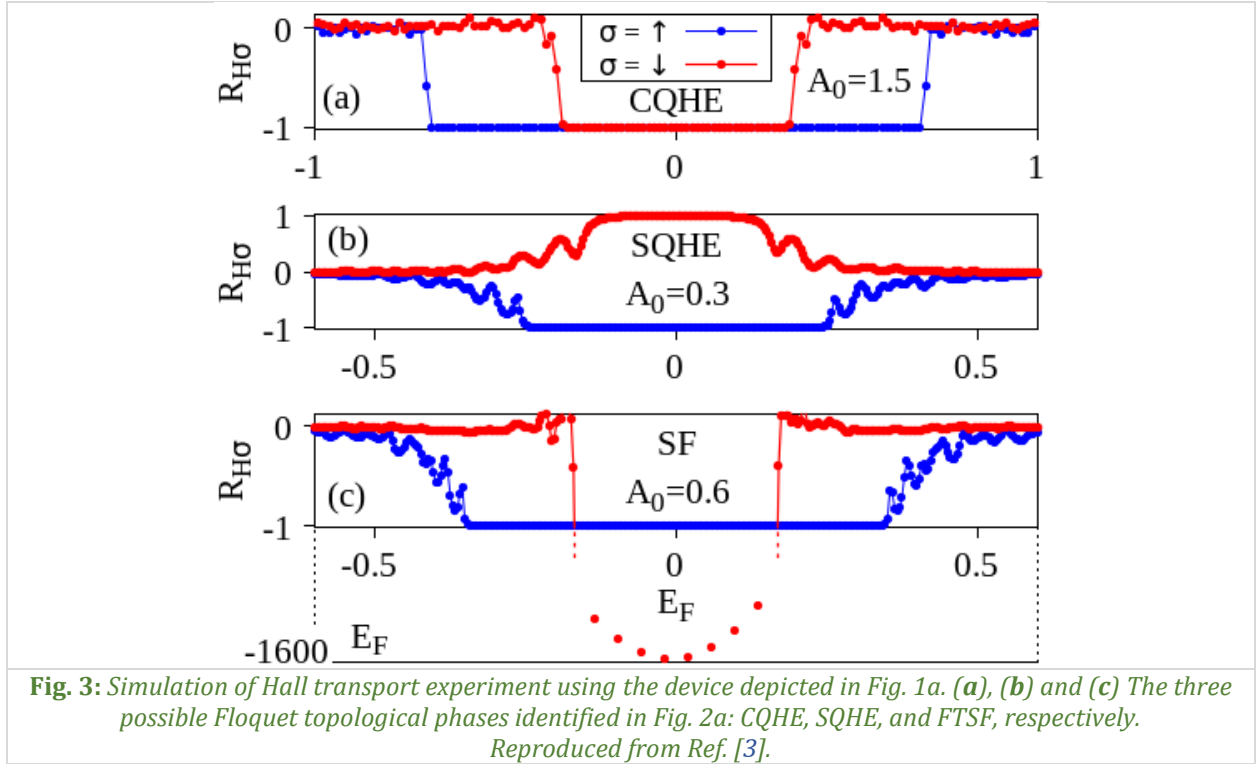


Going further, to highlight the appearance of FTSF phase, we investigated the system in terms of spin Chern numbers (C_σ) as topological invariants, with σ being the spin quantum number. In Fig. 2a, we show the values vs. A_0 which represents a measure of light intensity. The top plot shows the case without staggered potential ($\Delta=0$), and the bottom one shows the case in the presence of the staggered potential with $\Delta=0.2$. In the first case, we distinguish (i) the SQHE (yellow areas) with $C_\uparrow=-1$ and $C_\downarrow=+1$; and (ii) the CQHE (black areas) with $C_\uparrow=C_\downarrow=-1$. In the second case, where the staggered potential is applied, we observe the appearance of the FTSF phase (green areas). To achieve this special topological phase, one of the two spin Chern numbers should vanish, while the other takes a non-zero value. In our example, the two invariants are $C_\uparrow=-1$ and $C_\downarrow=0$. For $C_\uparrow=C_\downarrow=0$, the system lies in trivial phase.



Further, we discuss how each identified topological phase reflects in the system spectral properties, for a zigzag terminated ribbon, see Fig. 1b (infinite on horizontal direction). We start with the trivial case, see Fig. 2b. Here, one may observe a gap in the quasienergy spectrum for both spin states. In SQHE (Fig. 2c) and similarly in CQHE phase, inside the gap, chiral edge states arise for both spin states, giving rise to conduction channels localized at the ribbon edges [2]. In FTSF phase (Fig. 2d) a peculiar property arises. That is, for $\sigma=\downarrow$, a gap takes place, indicating a trivial phase, while for $\sigma=\uparrow$, a pair of crossed chiral bands arises. In this configuration, only $\sigma=\uparrow$ states lie in a topological phase. In this configuration, in a Hall transport experiment, only $\sigma=\uparrow$ states will be transmitted across the device. In other words, $\sigma=\uparrow$ spin states are filtered.

Next, we simulate a Hall experiment, considering the device depicted in Fig. 1a. In Fig. 3, we present the Hall resistance R_H vs. Fermi level E_F , for each topological phase identified in Fig. 2a, as indicated on each plot. The values are expressed in terms of h/e^2 constant, with h being the Planck constant, and e the elementary charge. First, in CQHE [panel (a)], we observe the formation of two plateaus for both spin states with $R_H=-1$, for a E_F range according to the topological gap shown in Fig. 2c. In this case, the system transports a net amount of charge. Second, in SQHE [panel (b)], the plateaus emerge at $R_H=\pm 1$. In this case, the system transports spin states, but no charge. Third and the most interesting, we highlight the FTSF phase [panel (c)]. As one may notice, here, a plateau $R_H=-1$ appears for $\sigma=\uparrow$ states, with a width in accordance with the topological gap bounded by the red bands shown in Fig. 2d. For the other spin state $\sigma=\downarrow$, the R_H values reach up to -1600 , evidently in our numerical limitations. In the real case of such a device, the Hall resistance is actually $R_H \rightarrow \pm\infty$. In this topological configuration, the $\sigma=\uparrow$ spin state is purely filtered. Now, it is worth noting that changing the light polarization (helicity), the filtered spin state is also reversed.



Despite our proposed model is based on the presence of idealized on-site staggered potential, there are some classes of topological materials which mimic the staggered potential needed to achieve the FTSF phase, such as buckled 2D topological insulators, graphene/hexagonal boron nitride structure, or twisted bilayer topological insulators.

In conclusion, we have presented a SF device based on an FTI realized in graphene via circularly polarized light irradiation. Depending on the light intensity, expressed in our case through A_0 amount, we have identified three possible Floquet topological phases: CQHE, SQHE, and FTSF. In FTSF phase, one of the two existing spin states is purely filtered, and may be selected via light polarization state.

References:

- [1] N. H. Lindner, G. Refael, V. Galitski, *Floquet topological insulator in semiconductor quantum wells*, Nat. Phys. 7 (2011) 490–495.
- [2] A. Pena, C. Radu, *Floquet topological insulators with spin-orbit coupling*, Phys. Rev. B 109 (2024) 075121.
- [3] A. Pena, C. Radu, *Floquet topological spin filters*, Phys. Rev. B 110 (2024) L241113.

Stacking model of a 3D second-order topological insulator exhibiting the quantum anomalous Hall effect

B. Ostahie, A. Aldea

National Institute of Materials Physics, 077125, Măgurele, Romania

The study of topological properties in condensed matter began with the quantum Hall effect and 2D materials like graphene. Extending to 3D systems introduced higher-order topological phases (HOTI), where an N -th-order topological insulator (TI) in D dimension hosts $(D-N)$ -dimensional states. Second-order topological insulators (SOTI) ($N=2$) feature hinge states, while third-order topological insulators ($N=3$) exhibit corner states. These topological states arise from crystalline symmetries combined with time-reversal symmetry, ensuring their robustness [1–3].

Different possible 3D trajectories of chiral 1D hinge states in a 3D structure could lead to a quantum 3D Hall effect with distinct properties. Despite being a recent field, several theoretical models and experiments confirm the existence of higher-order topological states. Identified materials include chalcogenide crystals such as Bi_2Se_3 , a strong 3D TI with a 0.3 eV band gap, as well as Bi_1Te_1 , Bi_2Te_1 , and Bi_4Br_4 , where topological hinge states have been observed. Beyond real materials, the HOTI phase has also been demonstrated in metamaterials like acoustic, phononic, and electrical circuit systems [4,5].

The aim of the work [6] was to develop a 3D SOTI model with broken time reversal (TR) symmetry, linked to the 3D quantum anomalous Hall effect (QAHE). While the traditional QHE arises in a 2D electron gas under a strong perpendicular magnetic field due to Landau levels, the discovery of the 3D QHE marked a major advancement, observed in materials like Cd_3As_2 Weyl semimetals and ZrTe_5 crystals. Typically, the 3D QHE requires an external magnetic field to influence Weyl orbits or induce hinge states. In contrast, our model achieves TR symmetry breaking without an external field, relying instead on an intrinsic Haldane-type phase.

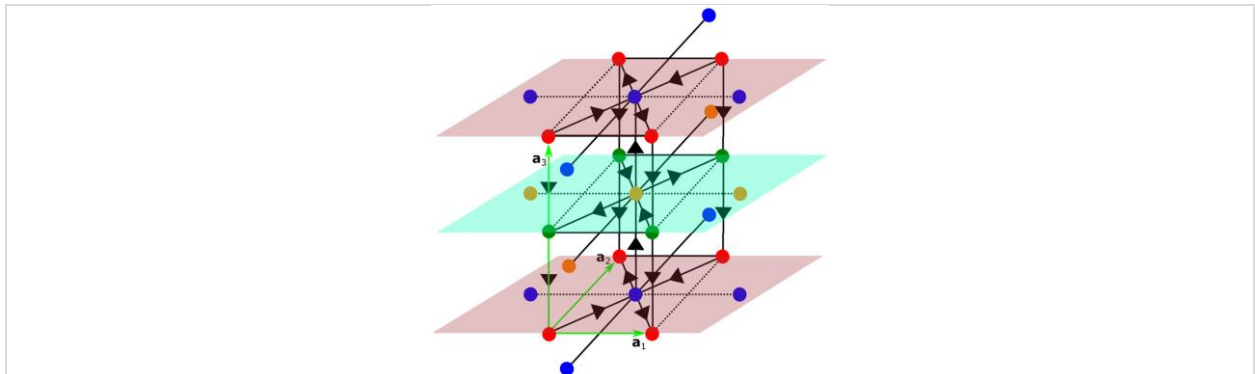


Fig. 1: Sketch of a cubic lattice formed by stacking three layers. The red and blue layers exhibit opposite Haldane-type phases, represented by in-plane arrows, resulting in a unit cell with four atoms: red (A), blue (B), green (C), and orange (D). The in-plane arrows correspond to the hopping element t_1 , while the vertical arrows correspond to t_1 . Dashed and solid lines represent next-nearest-neighbor hopping t_2 between atoms of the same type. The primitive vectors \mathbf{a}_1 , \mathbf{a}_2 , and \mathbf{a}_3 are aligned along the O_x , O_y and O_z directions, respectively. Reproduced from Ref. [6].

The 3D model is constructed by stacking layers with Chern properties in an alternating chirality sequence (see Fig. 1). This stacking approach, commonly used in theoretical models, enables independent tuning of intralayer and interlayer couplings. Unlike other methods, our model introduces a phase in the interlayer hopping, referred to as the vertical phase. This phase, combined with sufficiently strong interlayer coupling, leads to chiral hinge states that support the QAHE. Notably, the effect strongly depends on whether the number of layers is odd or even, as the hinge currents close differently in each case. This stacking results in a unit cell containing four atoms: A (red), B (blue), C (green), and D (orange), with primitive vectors \mathbf{a}_1 , \mathbf{a}_2 , and \mathbf{a}_3 .

In the following, we introduce the Hamiltonian of our model in momentum space:

$$\mathcal{H}(k_x, k_y, k_z) = \begin{pmatrix} -2t_2 f(k_x, k_y) & t_1 g(k_x, k_y, \gamma) & t_\perp h(k_z, \gamma_\perp) & 0 \\ t_1 g^*(k_x, k_y, \gamma) & 2t_2 f(k_x, k_y) & 0 & t_\perp h(k_z, -\gamma_\perp) \\ t_\perp h^*(k_z, \gamma_\perp) & 0 & -2t_2 f(k_x, k_y) & t_1 g(k_x, k_y, -\gamma) \\ 0 & t_\perp h^*(k_z, -\gamma_\perp) & t_1 g^*(k_x, k_y, -\gamma) & 2t_2 f(k_x, k_y) \end{pmatrix}, \quad (1)$$

where the notations $f(k_x, k_y)$, $g(k_x, k_y, \gamma)$ and $h(k_z, \gamma_\perp)$ are:

$$\begin{aligned} f(k_x, k_y) &= \cos(k_x) - \cos(k_y); \\ g(k_x, k_y, \gamma) &= \exp(-i\gamma) \{1 + \exp[-1(k_x + k_y)]\} \\ &\quad + \exp(i\gamma) \{\exp(-ik_x) + \exp(-ik_y)\}; \\ h(k_z, \gamma_\perp) &= \exp(i\gamma_\perp) + \exp(-i\gamma_\perp) \exp(ik_z). \end{aligned} \quad (2)$$

The energy spectrum is obtained by directly diagonalizing the Hamiltonian in momentum space. As shown in Fig. 2, the energy dispersion reveals two distinct phases: a semimetallic phase (for $t_2 = 0$ at any γ_\perp) and an insulating phase (for $t_2 \neq 0$, independent of γ_\perp). In Eq. (2), the Hamiltonian matrix includes the parameter t_2 on the diagonal, which controls the mass term. When t_2 is nonzero, electrons acquire mass, leading to an energy gap opening. This transition from the semimetallic to the insulating phase is crucial for understanding the system's behaviour. Under appropriate hard-wall boundary conditions, this insulating gap is expected to host hinge states, confirming the topological nature of the models.

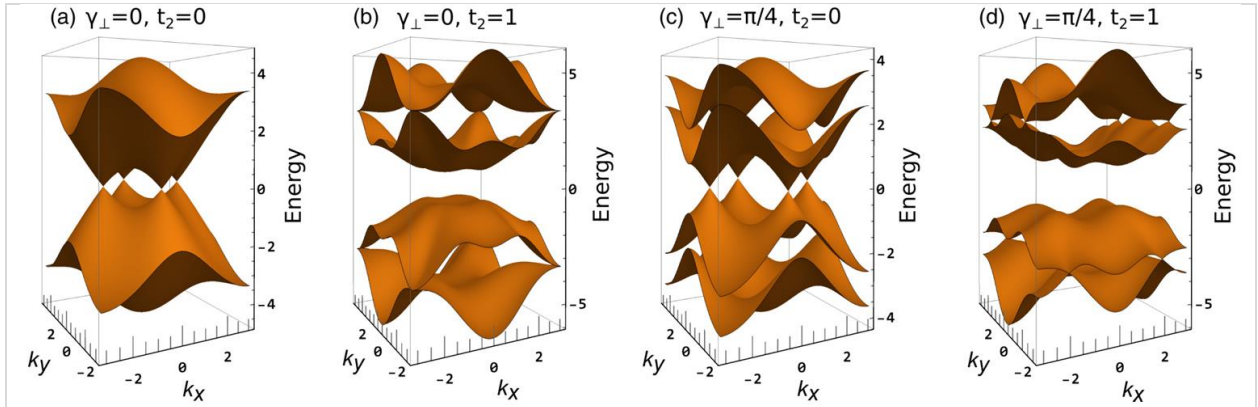


Fig. 2: The energy spectrum is shown for different parameter values (t_2, γ_\perp) with a fixed momentum $k_z = \pi/4$. When $t_2 = 0$, the system remains in a semimetallic phase for any γ_\perp [see (a) and (c)]. In contrast, as illustrated in (b) and (d), the presence of $t_2 \neq 0$ induces an insulating phase. Reproduced from Ref. [6].

To verify this, we construct a nanowire by imposing hard-wall boundary conditions along the O_x direction while preserving some geometry on the surface. As a result, the energy spectrum depends only on the k_z momentum. The energy spectrum is computed under conditions where the energy gap is maximized: $t_2 = 1$, $t_\perp = 1$, and $\gamma_\perp = \pi/4$. Our expectation of chiral hinge states is confirmed in Fig. 3a, where the energy gap is filled with gapless states. To further validate the 1D nature of these states, we numerically calculate the local density of states $|\langle \psi(k_z) | n, m \rangle|^2$ and the result is presented in Fig. 3b. By positioning the Fermi level at the centre of the gap, two intersection points emerge at specific k_z values, marked by red and blue dots. These degenerate states propagate along opposite edges of the wire, as depicted in Fig. 3b. Notably, the velocities $v_{k_z} = dE(k_z)/dk_z$ at these intersections are nonzero. The sign of the derivative indicates the presence of counter-propagating currents along the hinges. To calculate the Hall effect, one needs to attach four leads, which we arrange in the cross configuration. Obviously, to point out this effect in 3D, two of them (say, the current leads) should be attached to the lower face of the parallelepiped, while the other two leads (necessary to measure the Hall voltage) are attached to the upper face, as in Fig. 3d. Then the well-known Landauer-Büttiker formalism will be used to calculate the transmission coefficients between the four leads and the Hall resistance.

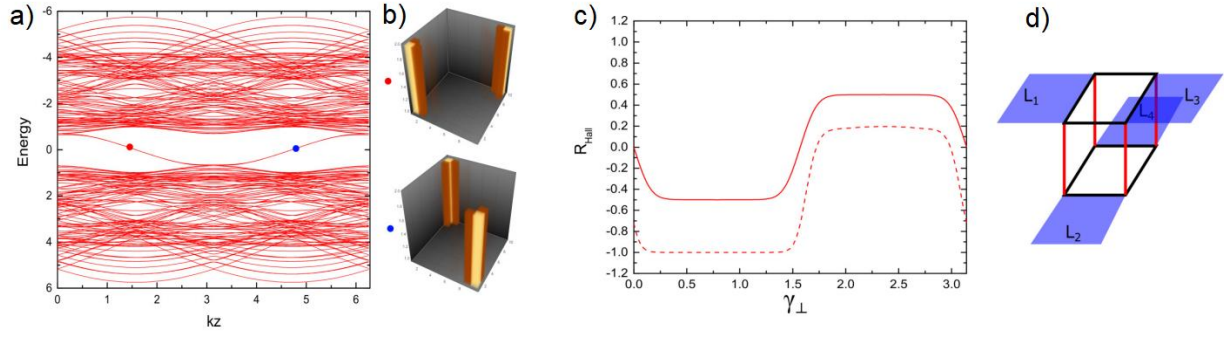


Fig. 3: (a) Energy spectrum of the nanowire in the SOTI phase, with red and blue points marking gapless hinge state intersections with the Fermi level. (b) The eigenfunctions confirm the 1D nature of hinge states. (c) Hall resistance as a function of perpendicular phase γ_{\perp} at zero Fermi energy for two system sizes with odd (red dashed line) and even (red solid line) number of layers. (d) Schematic of the Hall device with four leads.

Adapted from Ref. [6].

Even without an external magnetic field, the Hall effect remains nonzero due to TR symmetry breaking from the intralayer γ and interlayer phases γ_{\perp} . Fig. 3c shows the quantum Hall resistance dependence on γ_{\perp} , where quantum anomalous Hall plateaus appear. Their numerical accuracy improves with system size, using odd and even layers, respectively. For odd layers and $\gamma_{\perp} \in (0, \pi/2)$, the only integer plateau occurs, with $R_H = -1$ (h/e^2) from summing Chern numbers. For even layers, hinge states form two disjoint channels, resulting in $R_H = \pm 1/2$ (h/e^2).

We developed a 3D tight-binding model that captures the spectral properties of a SOTI and the transport behaviour of the anomalous quantum Hall effect [6]. Built by stacking Chern-insulating diatomic layers, the model features four atoms per unit cell and key parameters: next-nearest hopping t_2 , intralayer phase γ , and interlayer phase γ_{\perp} . The number of layers affects hinge state paths, with odd-layer systems forming two separate hinge channels and even-layer systems forming a single one, leading to fractional Hall resistance plateaus [6].

References:

- [1] J. Langbehn, Y. Peng, L. Trifunovic, F. von Oppen, P.W. Brouwer, *Reflection-symmetric second-order topological insulators and superconductors*, Phys. Rev. Lett. 119 (2017) 246401.
- [2] Z. Song, Z. Fang, C. Fang, *(d - 2)-dimensional edge states of rotation symmetry protected topological states*, Phys. Rev. Lett. 119 (2017) 246402.
- [3] W.A. Benalcazar, B.A. Bernevig, T.L. Hughes, *Electric multipole moments, topological multipole moment pumping, and chiral hinge states in crystalline insulators*, Phys. Rev. B 96 (2017) 245115.
- [4] M. Eschbach, M. Lanius, C. Niu, E. Młyńczak, P. Gospodarič, J. Kellner, P. Schüffegen, M. Gehlmann, S. Döring, E. Neumann, M. Luysberg, G. Mussler, L. Plucinski, M. Morgenstern, D. Grützmacher, G. Bihlmayer, S. Blügel, C.M. Schneider, *Bi₁Te₁ is a dual topological insulator*, Nat. Commun. 8 (2017) 14976.
- [5] N. Avraham, A.K. Nayak, A. Steinbok, A. Norris, H. Fu, Y. Sun, Y. Qi, L. Pan, A. Isaeva, A. Zeugner, C. Felser, B. Yan, H. Beidenkopf, *Visualizing coexisting surface states in the weak and crystalline topological insulator Bi₂TeI*, Nat. Mater. 19 (2020) 610–616.
- [6] B. Ostahie, A. Aldea, *Stacking model of a three dimensional second-order topological insulator manifesting quantum anomalous Hall effect*, Phys. Rev. Res. 6 (2024) 023168.

QED-DFT-TP approach to cavity-quantum dot arrays

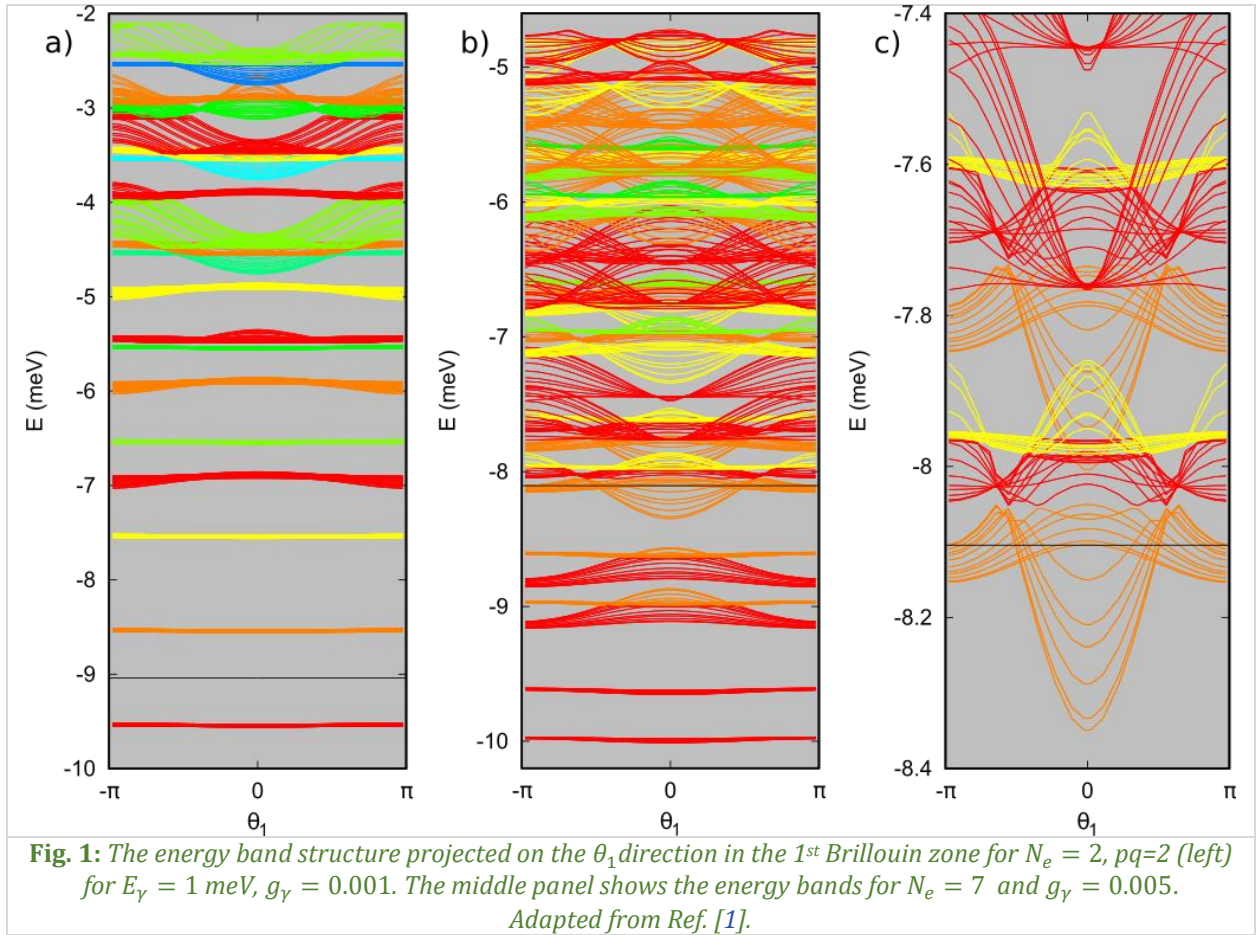
**V. Moldoveanu¹, V. Gudmundsson², V. Mughnetsyan³, H.-S. Goan^{4,5,6}, J.-D. Chai^{4,5,6},
N.R. Abdullah⁷, C.-S. Tang⁸, A. Manolescu⁹**

- 1) *National Institute of Materials Physics, 077125, Măgurele, Romania*
- 2) *Science Institute, University of Iceland, IS-107, Reykjavik, Iceland*
- 3) *Department of Solid State Physics, Yerevan State University, Alex Manoogian 1, 0025 Yerevan, Armenia*
- 4) *Department of Physics and Center for Theoretical Physics, National Taiwan University, 106319, Taipei, Taiwan*
- 5) *Centre for Quantum Science and Engineering, National Taiwan University, 106319, Taipei, Taiwan*
- 6) *Physics Division, National Centre for Theoretical Sciences, 106319, Taipei, Taiwan*
- 7) *Physics Department, College of Science, University of Sulaimani, Kurdistan Region, Iraq*
- 8) *Department of Mechanical Engineering, National United University, 36003, Miaoli, Taiwan*
- 9) *Department of Engineering, Reykjavik University, IS-102, Reykjavik, Iceland*

In two recent papers [1,2] we adapted the so-called QED-DFT-TP theoretical method [3] to investigate the equilibrium properties and the excitation spectrum of a square quantum dot array embedded in a cylindrical cavity. The array is etched in a GaAs heterostructure and subject to an external homogeneous perpendicular magnetic field. The interdot and intradot Coulomb interactions are introduced *via* Hartree and exchange-correlation potentials and an iteration scheme is used to plug the current and the charge densities in the paramagnetic and the diamagnetic terms of the electron-photon interaction (EPI). The QED-DFT-TP methods allows the calculation of various quantities which unravel non-trivial effects of the EPI whose strength is denoted by g_γ : the mean energy in the system, the mean photon number, charge and spin densities of orbital magnetization.

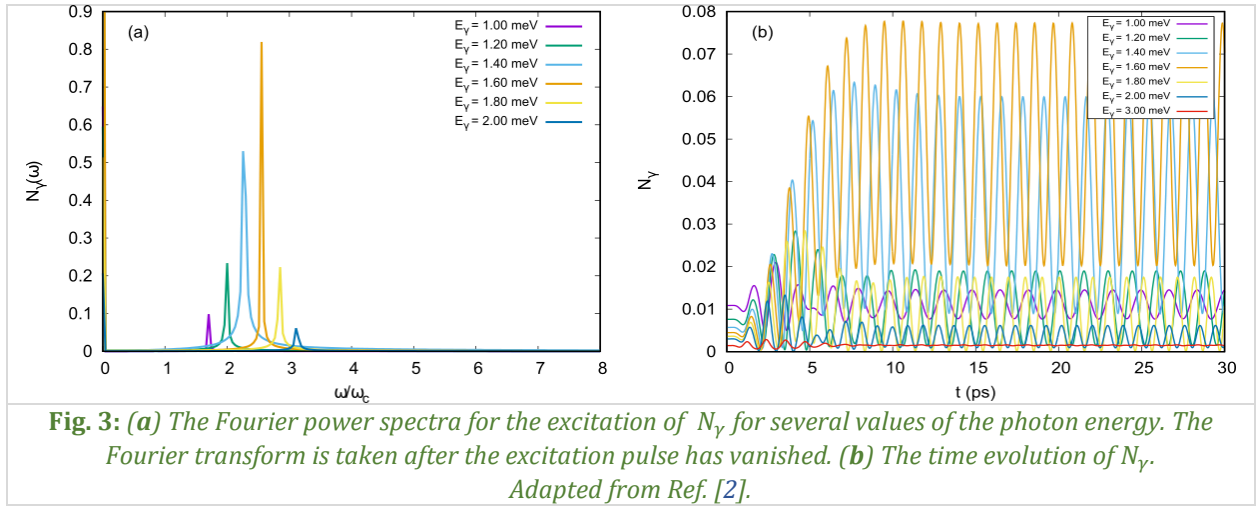
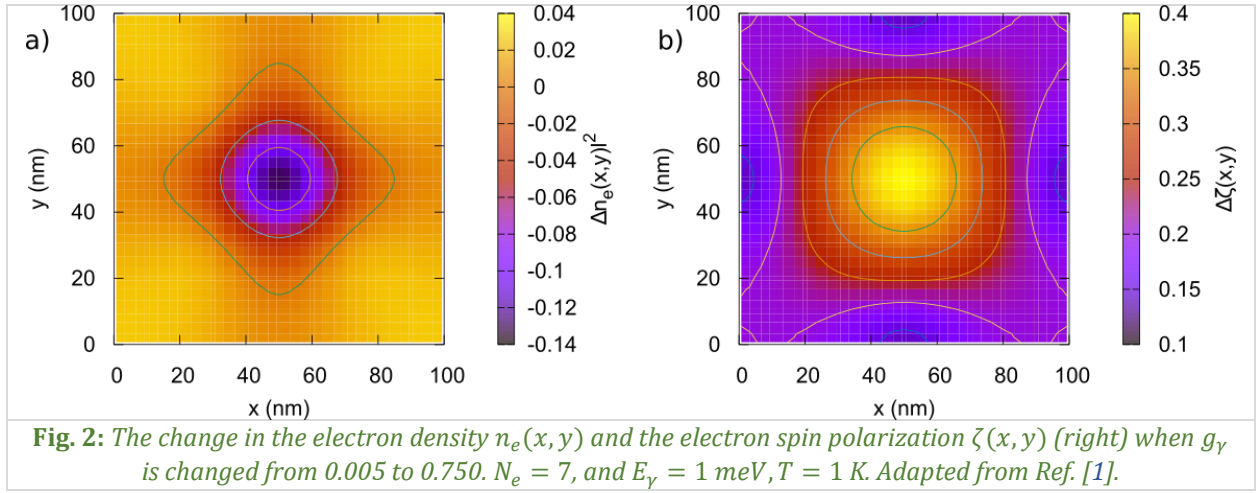
Let us stress that the arrays of QDs placed in photon cavities studied here are actually large and extended hybrid quantum systems (HQS), in contrast to much smaller qubit-like devices (*e.g.*, QDs coupled to MW cavities or colour centres coupled by phononic modes). Note that in the case of large HQS the theoretical tools and modelling are more involved. The standard QEDFT approach is built on an explicit functional for the electron-photon interactions [4]. The main feature of this functional is that it does not lead to any photon replicas of electron states in the energy spectra. In contrast, the QED-DFT-TP formalism brings back the photon replicas. We omit the complicated formal details which can be found in Refs. [1,2] and briefly present few results.

Two such QED-DFT-TP spectra are shown in Fig. 1 for $N_e = 2$ and $N_e = 7$ electrons in each dot. The 2D spectrum is projected on the θ_1 direction in reciprocal space. The photon content of the Landau subbands is encoded in their colour with red for zero, or a very low photon number, and deep blue for 12 photons. The low electron-photon coupling in the left panel results in the total average photon number $N_\gamma \approx 0.006$ for the two-electron states. The low external magnetic field $B \approx 0.82$ T lead to a spin singlet with no enhancement of the exchange energy, and the spin splitting is thus not discernible. The chemical potential indicated with a black horizontal line in the figure is $\mu \approx -9$ meV. As g_γ is small, one can identify photon replicas of the two states below the chemical potential located at almost regular intervals of $\hbar\omega_\gamma = 1$ meV above them (see the first photon replica orange subbands around -8.5 meV and the second replica yellow subbands around -7.5 meV). The higher energy spectrum displays complex structures hinting at resonances and interactions.



The situation changes in the middle panel which corresponds to $N_e = 7$. The right panel shows a clear anticrossing of bands close to μ . The closeness of this structure to the chemical potential means it influences most properties of the system. In addition to the Rabi-splitting and anticrossing of the subbands an enhanced spin splitting is seen. In Fig. 2 we also show that the EPI leads to local changes on the charge and spin densities of the 2DEG-cavity system. In Fig. 2a it is seen how the polarizing power of the photons lowers the charge density in the centre of each dot and moves it on the diagonals between the dots to minimize the Coulomb interaction energy. Note that the densities are compared for two very different values of the g_γ . The change in the spin polarization is displayed in the right panel of Fig. 2b and shows a concentration of one spin direction in the QDs as g_γ increases. Note that a variation in the electron density does imply a variation of the cavity photon density in the system; this information is not available in the QEDFT 2DEG model.

In the 2nd paper [2] we add a time-dependent excitation to the same system and model the magnetically active photon processes controlling the para- and diamagnetic transitions. The Fourier power spectra for the photon number N_γ is presented in Fig. 3a for selected values of the photon energy E_γ . The location of an excitation peak can be interpreted in terms of the energy of the cavity photons and a shift caused by the electron-photon interactions. The height of the peaks can be related to the parameters of the excitation pulse which has a broad frequency range with a maximum around $\hbar\omega = 3.5$ meV corresponding to $\omega/\omega_c \approx 2.5$. In Fig. 3b we show the time-dependent evolution of the total mean photon number. The results are outside the regime of linear response as energy is clearly pumped into the system (see Fig. 3a in Ref. [2]). We find that after the excitation the mean total energy stays constant, but the photon number oscillates steadily.



References:

- [1] V. Gudmundsson, V. Mughnetsyan, H.-S. Goan, J.-D. Chai, N. R. Abdullah, C.-S. Tang, V. Moldoveanu, A. Manolescu, *Magneto-optical properties of a quantum dot array interacting with a far-infrared photon mode of a cylindrical cavity*, Phys. Rev. B 109 (2024) 235306.
- [2] V. Gudmundsson, V. Mughnetsyan, H.-S. Goan, J.-D. Chai, N. R. Abdullah, C.-S. Tang, V. Moldoveanu, A. Manolescu, *The tuning of para- and diamagnetic cavity photon excitations in a square array of quantum dots in a magnetic field*, Phys. Rev. B 110 (2024) 205301.
- [3] J. Malave, A. Ahrens, D. Pitagora, C. Covington, K. Varga, *Real-space, real-time approach to quantum-electrodynamical time-dependent density functional theory*, J. Chem. Phys. 157 (2022) 194106.
- [4] J. Flick, *Simple exchange-correlation energy functionals for strongly coupled light-matter systems based on the fluctuation dissipation theorem*, Phys. Rev. Lett. 129 (2022) 143201.

